
Controlling friction by multi-scale surface patterning inside and outside the contact zone

Dissertation

zur Erlangung des Grades
des Doktors der Ingenieurwissenschaften
der Naturwissenschaftlich-Technischen Fakultät
der Universität des Saarlandes



UNIVERSITÄT
DES
SAARLANDES

von

Philipp Grützmaker

Saarbrücken

April 2019

Tag des Kolloquiums: 17.10.2019
Dekan: Prof. Dr. rer. nat. Guido Kickelbick
Berichterstatte: Prof. Dr.-Ing. Frank Mücklich
Prof. Dr.-Ing. Dirk Bähre
Vorsitz: Prof. Dr.-Ing. Matthias Nienhaus
Akad. Mittelbau: Dr.-Ing. Florian Schäfer

„Die Wissenschaft, richtig verstanden, heilt den Menschen von seinem Stolz; denn sie zeigt ihm seine Grenzen.“

(Albert Schweitzer)

TABLE OF CONTENTS

ACKNOWLEDGEMENTS	VI
ZUSAMMENFASSUNG	VIII
ABSTRACT	IX
ABBREVIATIONS AND SYMBOLS	X
1 MOTIVATION AND OBJECTIVES	1
2 STATE OF THE ART	7
2.1 Techniques for designing surface patterns	7
2.1.1 Laser surface patterning	7
2.1.2 Micro- and roller-coining	12
2.1.3 Photochemical patterning	14
2.2 Surface patterning to control friction and wear in lubricated systems	15
2.2.1 Single-scale surface patterns	17
2.2.2 Multi-scale surface patterns	22
2.3 Lubricant migration	24
2.3.1 Reasons for lubricant migration	25
2.3.2 Chemical modification to improve lubricant migration	28
2.3.3 Topographical modification to improve lubricant migration	29
3 OVERVIEW	33
4 INCLUDED PAPERS	42
4.0 Outline	42
I The influence of centrifugal forces on friction and wear in rotational sliding	44
II How to guide lubricants – Tailored laser surface patterns on stainless steel	45
III Guiding lubricant on stainless steel surfaces by channel-like structures fabricated by roller- and micro-coining	46

IV	Lubricant migration on stainless steel induced by bio-inspired multi-scale surface patterns	47
V	Effects of Multi-Scale Patterning on the Run-In Behavior of Steel–Alumina Pairings under Lubricated Conditions	48
VI	From lab to application - Improved frictional performance of journal bearings induced by single- and multi-scale surface patterns	49
VII	Surface texturing in machine elements - a critical discussion for rolling and sliding contacts	50
5	CONCLUSIONS AND OUTLOOK	51
6	NOT INCLUDED PAPERS	56
	REFERENCES	58
	FIGURES	66

ACKNOWLEDGEMENTS

First and foremost, I want to express my sincere gratitude to my scientific supervisor, Prof. Dr. Frank Mücklich, for providing me with the possibility to carry out this research work at his institute. I am very grateful for his mentoring and constructive feedback. It was he who guided me through my first steps of pursuing a scientific career, and I will never forget it.

Besides I want to thank Prof. Dr. Dirk Bähre for being my scientific advisor throughout my thesis, the fruitful discussions, and for his role as second reviewer of my thesis.

Regarding my scientific output and my professional and scientific development, there is one person in particular to mention. Prof. Dr. Andreas Rosenkranz is undoubtedly one of the persons I owe the most profound gratitude to. He helped me a lot by discussing my research with me, motivating me, and pushing me towards finding the right answers. In times where I was doubtful or unmotivated, he helped me to keep going. I am very impressed by his work and his attitude to science. Since the beginning of my PhD, we have not only been colleagues but also friends. I am looking forward to many more exciting and joyful encounters.

Of course, I also want to thank Prof. Dr. Carsten Gachot who started my interest in pursuing a scientific career and convinced me to start my master thesis and later my PhD thesis at the chair of functional materials. I am deeply grateful not only for his impact on my professional life but also for his friendship.

Special thanks also go out to Dr. Sebastian Suarez, who helped me in developing many interesting research ideas and was never tired in discussing my research with me. I am fortunate to be able to work with such a motivating and interested person.

Furthermore, I want to thank the students of the materials science and engineering department, who significantly contributed to my research work and made my thesis possible: Emre Atalay, Sebastian Rammacher, Cedric Mathieu and Kevin Murzyn.

A big part of my thesis was also performed in cooperation with the universities RWTH Aachen and FAU Erlangen-Nürnberg within the scope of the DFG project SPP 1551. I want to thank my colleagues from there for the perfect teamwork and cooperation: Prof. Dr. Gerhard Hirt, Prof. Dr. Georg Jacobs, Prof. Dr. Sandro Wartzack, Adam Szurdak, Markus Grüber, Florian König, and Max Marian. At this point, I also want to acknowledge the Deutsche Forschungsgemeinschaft (DFG, project: MU 959/27-2) for their financial support.

Additionally, my thanks go to all of my colleagues from FuWe which made my time at the institute not only fruitful but a lot of fun too. Of course, the “Kicker” group should be mentioned in particular: Daniel Müller, Timothy MacLucas, Christian Schäfer, Flavio Soldera, Sebastian Suarez, and Leander Reinert. Many of whom I became close friends during my time at the institute. Also, I will never forget

Flavio Soldera and his EUSMAT team, who started my interest in studying materials science and engineering in Saarbrücken and who are continuously working hard to help students coming from all over the world to be able to study AMASE. Go AMASE! Prof. Dr. Rosenkranz and Dr. Sebastian Suarez are especially acknowledged for proofreading this thesis.

Right at the beginning of my PhD, I met my future wife, Aura. With her at my side, I never had any doubt that we could accomplish anything. She made the time of my PhD the most enjoyable time of my life. I am impressed by your energy, your kindness, and your ability to transmit it to people. I am grateful every day to have you!

Last but not least, I want to express my deepest gratitude to my parents, Elisabeth and Hansjörg, who made all my accomplishments possible. Thank you for your never-ending support, your advice, and your belief in me. Finally, I want to thank my grandparents, who are idols for me and whom I could always talk to and find comfort.

ZUSAMMENFASSUNG

Tribologische Probleme in Maschinenelementen tragen wesentlich zum Energieverbrauch bei und haben somit einen großen Einfluss auf die Wirtschaftlichkeit und den CO₂-Ausstoß. Um Einfluss auf die tribologischen Eigenschaften von Oberflächen zu nehmen, werden in der vorliegenden Arbeit bio-inspirierte Multiskalen-Oberflächenstrukturen entwickelt und innerhalb und außerhalb der Kontaktzone von technologisch relevanten Stahloberflächen eingesetzt. Für die Erzeugung von multi-skaligen Strukturen werden größere mikrogeprägte Muster mit kleineren Lasermustern kombiniert.

Strukturen außerhalb der Kontaktfläche können Schmiermittel über die Oberfläche leiten oder die Schmiermittelmigration aus dem Kontakt heraus aufhalten, welche durch Zentrifugalkräfte, sowie Temperaturgradienten verursacht wird. Im Hinblick auf die Entwicklung effektiver Strukturen wurden multi-skalige Strukturen als besonders wirksam sowohl innerhalb als auch außerhalb der Kontaktzone identifiziert. Somit können die tribologischen Eigenschaften direkt und indirekt durch den Einsatz von multi-skaligen Oberflächenmustern verbessert werden. Für ein effektives Design der Strukturen müssen vor allem strukturelle Parameter wie Tiefe und Periodizität berücksichtigt werden. Als effektive befundene einzel- und multi-skalige Strukturen werden auf die Wellen von Gleitlagern übertragen. Die Reibuntersuchungen zeigen eine gute Vergleichbarkeit zwischen Laborversuchen und Anwendung. Im Vergleich zur unstrukturierten Welle kann die Reibung der Welle mit einer multi-skaligen Struktur um den Faktor 4 reduziert werden.

Abschließend wird die Verwendung von Oberflächenstrukturen in Maschinenelementen kritisch diskutiert und allgemeine Designrichtlinien für die Oberflächenstrukturierung in Maschinenelementen abgeleitet.

ABSTRACT

Tribological problems in machine elements contribute significantly to energy consumption and thus have a major impact on economic efficiency and CO₂ emissions. To influence the tribological properties of surfaces, bio-inspired multi-scale surface patterns are developed in the present dissertation and applied inside and outside the contact zone of technologically relevant steel surfaces. For the generation of multi-scale patterns, larger micro-coined patterns are combined with smaller laser patterns.

Patterns outside the contact zone can guide lubricants over the surface or prevent lubricant migration out of the contact caused by centrifugal forces or temperature gradients. With respect to the development of effective surface patterns, multi-scale patterns have been identified as particularly effective both inside and outside the contact zone. Thus, the tribological properties can be improved directly and indirectly by the use of multi-scale surface patterns. For an effective design of the patterns, structural parameters like depth and periodicity have to be considered. Suitable single- and multi-scale surface patterns are selected and successfully transferred to the shafts of journal bearings. The frictional investigations show an excellent comparability between laboratory tests and application. Compared to the non-patterned shaft, the friction of the shaft with a multi-scale pattern can be reduced by a factor of 4.

Finally, the use of surface patterns in machine elements is critically discussed, and general design guidelines for surface patterning in machine elements are derived.

ABBREVIATIONS AND SYMBOLS

COF	Coefficient of friction	α	Absorption coefficient
d	Structural depth	β	Channel angle
DLIP	Direct laser interference patterning	γ	Surface tension
DLW	Direct laser writing	γ_{SL}	Solid-liquid interfacial tension
EHL	Elastohydrodynamic lubrication	γ_{SG}	Solid-gas interfacial tension
F_N	Normal force	γ_{LG}	Liquid-gas interfacial tension
F_c	Centrifugal force	θ	Contact angle
h_0	Lubricant film thickness	θ_a	Advancing contact angle
I	Intensity	θ_r	Receding contact angle
I_0	Initial intensity	κ	Thermal diffusivity
K	Geometric term	λ	Lambda parameter
l	Length of channel's wetted portion	λ'	Wavelength
l_d	Thermal penetration depth	μ	Dynamic viscosity
m	Mass	σ	Combined surface roughness
P	Periodicity	τ_p	Laser pulse duration
PAO	Polyalphaolefin oil	ϕ	Edge angle
R	Radius		
SEM	Scanning electron microscope		
SD	Sliding distance		
T	Temperature		
ΔT	Temperature gradient		
t	Time		
UV	Ultraviolet		
v	Migration velocity		
v_r	Rotational speed		
x	Position		
z	Depth		

1. MOTIVATION AND OBJECTIVES

Tribology, the science that describes the ubiquitous phenomena friction, wear, and lubrication can be found everywhere around us, from daily activities to automotive applications, nature, and the human body ^[1]. In general, whenever two contacting surfaces are brought into contact and set into relative motion there will be friction and, as a result of this, wear. In machine elements, this might be the relative motion between piston and cylinder or shaft and bearing, whereas in nature some examples of friction are the blink of the eyelid or the movement of head and cup in a hip joint ^[2,3].

Since friction is all around us and greatly affects our daily life as well as the reliability, the efficiency and the lifetime of machine elements, humankind has gathered plentiful information about friction and how to reduce it. It is, therefore, no wonder that this knowledge has been used for centuries, for example in the form of wheels, to reduce friction in translational motion ^[4]. However, the science of friction has not been investigated until the 15th century when Leonardo da Vinci experimented with rectangular blocks sliding over a flat surface and came up with the idea of the coefficient of friction (COF), which is defined as the ratio of the frictional force and the normal force. Since then, extensive research has been conducted in the field of tribology, and fundamental rules have been deduced. Especially Amontons and Coulomb rediscovered these fundamentals and found that the friction force is directly proportional to the normal load, independent of the nominal area of contact and after the initiation of motion independent of velocity ^[4].

In the context of tribological processes in machine elements, it is important to stress that sometimes high friction is desirable, as it is the case for brakes or bolts ^[4]. The same holds true for high wear, which is essential in production steps such as machining and polishing ^[4]. Nevertheless, most of the times, friction and wear can be named as processes, which greatly reduce the efficiency and the lifetime of machine components. Holmberg and Erdemir calculated the energy losses in tribological contacts and concluded that 23 % of the world's total energy consumption is used to overcome friction (20 %) and wear (3 %) ^[5]. Taking a passenger car as an example, the frictional losses account for about 28 % of the initially supplied fuel energy ^[6]. Moreover, Holmberg and Erdemir concluded that by utilizing modern technologies the energy losses caused by friction and wear could be reduced by 40 % within 15 years, which accounts for 8.7 % of the total energy consumption ^[5]. Taking the passenger car as an example again, the authors estimated that about 60 % of the energy used in tribological contacts could be potentially saved leading to economic and fuel savings of 576 000 million euros or 385 million liters, respectively ^[6]. Also, CO₂ emissions could be reduced by improving the energy efficiency of tribological contacts. This is especially important since CO₂ emissions have been steadily rising resulting from an ever-growing demand for energy due to an increasing population as well as worldwide economic growth and development ^[7]. As can be seen from **Fig. 1**, the electricity and heat production sector, as well as the transportation sector, have a major share in the production of CO₂. In

both of these sectors, technological progress in the field of tribology could contribute to decrease CO₂ production. Considering the increase in CO₂ emissions and linking it to global warming, dwindling resources, and stricter regulations, it is evident that drastic changes need to be made to slow down these processes. The most significant impact on reducing CO₂ emissions is estimated to be achieved from end-use energy efficiency, in which tribology plays a major role [5].

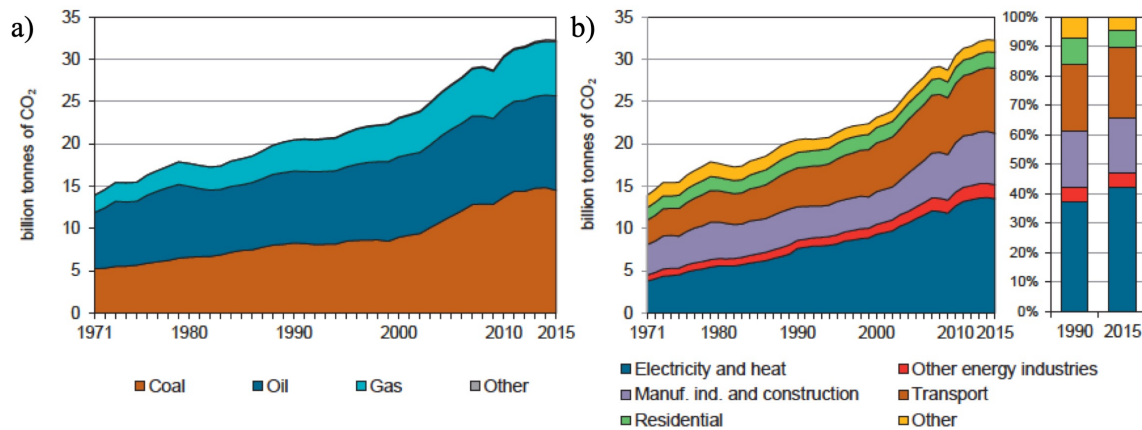


Figure 1: a) Increasing worldwide CO₂ emissions in tons of CO₂ since 1971 due to the growth in world energy demand from fossil fuels. In b) the CO₂ emissions are broken down by sector. Two-thirds of global emissions are produced by two sectors of which electricity and heat generation is by far the largest with 42 %, followed by transport, accounting for 24 % [7].

The most common approach to reduce friction between rubbing surfaces is to use a lubricant, which separates both surfaces thus reducing friction and wear greatly [4]. Other approaches to improving the tribological efficiency have been the substitution of materials, the application of coatings and new lubricants as well as surface engineering [5]. In this context, surface engineering also comprises tailoring the topography of the contacting surfaces, which is called surface patterning. The influence of the surface roughness on dry friction was discovered as early as 1699 by Amontons, who concluded that smooth surfaces show less friction [8]. In this context, friction depends on the interplay between surface roughness and lubricant film thickness. According to the relation between film thickness and surface roughness, three main lubrication regimes can be defined: boundary, mixed and hydrodynamic lubrication. Under boundary lubrication, the lubricant film thickness is small compared to the surface roughness, and thus there is intimate contact between both surfaces. In mixed lubrication, the lubricant film thickness is in the range of the surface roughness, and the load is partially carried both by the surface asperities and the lubricant. Finally, under hydrodynamic lubrication, the load is carried by a thick lubricant film completely separating the surfaces, and there is no contact between the surface asperities [4]. As friction generated during sliding of surface contacts is usually greater than the friction generated by shearing a lubricant film, friction increases with the number of contacting surface asperities [9]. Despite the fact that according to this theory friction increases with increasing surface roughness, the discovery that friction can be influenced by surface topography has led to the intended usage

of surface patterning to improve the tribological performance of sliding surfaces. The first applications of such surface patterns were the cylinder-liner interface and rotary shaft seals ^[10,11].

Especially in the last three decades, the operating conditions in machine elements have become more severe due to an increasing demand for power density. The ongoing trend towards more fuel-efficient and compact car engines, for example, leads to increasing loads, speeds, and temperatures within the main components of the engine, namely the valve train, the piston assembly, and the journal bearings ^[12]. In combination with the use of lower viscosity oils this ultimately results in a decrease of the lubricant film thickness inside the components down to the height of the surface roughness ^[12–15]. As a consequence, more machine elements operate under boundary and mixed lubrication where there is contact of the surfaces. This underlines the necessity to tailor the surface topography in order to render the surfaces more wear resistant, improve the frictional behavior and increase the components' lifetime.

Over the years many different patterning methods have been developed to modify the surface topography and hence to improve the tribological behavior. Among those, lithographic methods ^[11,16], diamond cutting ^[17], embossing or coining ^[18,19], and laser patterning ^[20,21] have been widely used. In this context, laser patterning is a versatile, fast, precise and environmentally friendly tool ^[20]. For bigger surface patterns, particularly micro-coining is an interesting method since it is cost-effective and offers the possibility for up-scaling to mass production ^[18].

Depending on the acting lubrication regime (from boundary to hydrodynamic lubrication), surface patterns can have different functions, which contribute to improved tribological behavior. Under boundary lubrication, the patterns may trap generated wear particles and thus reduce abrasion. In addition, the real area of contact is decreased, resulting in a reduction of adhesion and ultimately friction ^[22]. Even though friction is independent of the nominal area of contact, it is well known that the real area of contact has a significant impact on friction ^[23]. According to Bowden and Tabor, for plastically deforming contacts the friction force is proportional to the real area of contact, which in turn is directly proportional to the normal load ^[23]. Regarding mixed lubrication, the surface patterns can be used to trap wear particles, reduce the real area of contact, and additionally to act as reservoirs for lubricant and increase the hydrodynamic pressure ^[20,22,24,25]. Finally, under hydrodynamic lubrication, surface patterns help to create an additional hydrodynamic pressure thus increasing the load carrying capacity ^[20,22,26].

Typically, surface patterns are applied directly within the tribologically loaded contact zone where the above-described mechanisms can contribute to improved friction and wear behavior. The major issue with surface patterns applied inside the contact zone is that they might be subjected to substantial wear upon contact of the moving surfaces, which leads to the destruction of the surface patterns and hence to the loss of their effectiveness ^[21,27]. This holds especially true for starved lubrication conditions where there is not enough lubricant available in the contact zone to sufficiently lubricate the

contact over time. As a result, the lubricant film thickness is drastically decreased leading to high friction and/or wear.

Upon contact between the surface asperities of the rubbing surfaces, most of the energy is dissipated in the form of heat resulting in an increase of the interfacial temperature [28,29]. Outside of the contact zone, where no friction occurs, the temperature remains low and constant. If there is a liquid like a fluid lubricant on the surface, the resulting temperature gradient on the tribologically loaded surface induces a variation of the surface tension whereby the surface tension is higher for lower temperatures [30,31]. This gradient in surface tension drives the lubricant from high-temperature regions to the cooler surroundings without any external force, resulting in the loss of lubricant in the contact zone and finally starved lubrication [32–35]. This lubricant migration behavior on surfaces due to temperature gradients is known as thermocapillary migration [36,37]. Another possible reason for the migration of lubricant out of the contact zone are centrifugal forces which can occur in rotating machine elements [38]. In order to prevent the migration of the lubricant out of the contact zone, chemical anti-creep agents might be employed [39,40]. However, these are potentially harmful to the environment since hazardous chemicals like fluororganic compounds are used. Another possibility to obstruct the thermocapillary migration is to apply surface patterns in the near vicinity of the contact zone as a mechanical barrier to lubricant flow [35,39]. By avoiding the loss of lubricant out of the tribologically loaded contact, starved lubrication and thus drastically increased friction and wear can be prevented, additionally leading to a longer lifetime of the surface patterns situated within the contact zone. Furthermore, surface patterns, which are not directly located inside the contact zone, have the additional benefit of not being subject to wear and thus can outlive the component.

For proper performance of the patterns regarding their tribological and wetting performance, the design of the patterns is crucial [22]. In this context surfaces with outstanding properties, like wetting or adhesive properties, have evolved in nature over millions of years. The origin of those remarkable effects can often be found in sophisticated topographical designs. It is interesting to note that in nature many functional surfaces show hierarchical surface roughness with surface features on multiple scales. The reason for this might lie in the multi-scale nature of friction itself, whereby friction acts on and is affected by multiple scales, from large to small. Depending on the complexity of the system and the level of detail of the investigation, friction has to be considered on various scales. This might be macroscopic friction inside a device or a component, or even the interaction between two surfaces, single asperities or molecules [41].

The most discussed surface, showing a multi-scale surface pattern, is the lotus leaf surface, which exhibits superhydrophobicity and low adhesion and friction [4,41]. Other examples of naturally occurring multi-scale surface patterns comprise the scales of sharks, which reduce drag and thus allow for the high speeds with which sharks swim [42–44], or the scale-like skin of snakes or sandfish lizards, which shows low friction and wear depending on the sliding direction (see **Fig. 2**) [45–47]. In this context, surface topographies as they occur in nature might be an exciting model for tribological beneficial

surface patterns which induce reduced friction and/or wear. First tribological studies with multi-scale surfaces, directly mimicking the natural surface pattern or inspired by natural surface patterns, show auspicious results regarding the tribological behavior^[48–50].

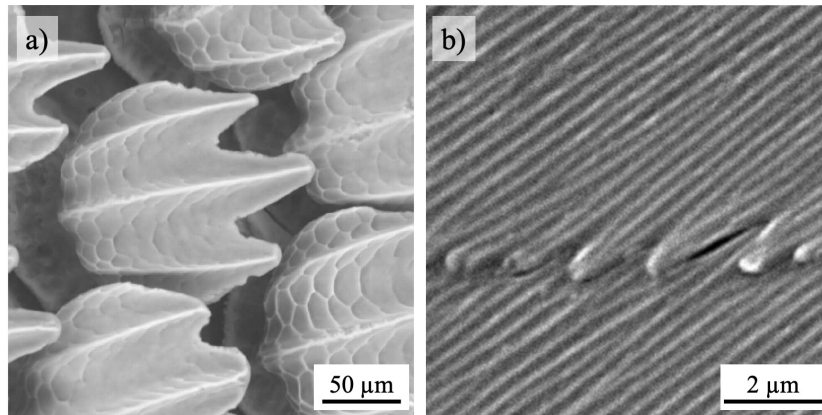


Figure 2: Scale-like surface topographies of a) shark skin^[43] and b) snakeskin^[47].

In the present dissertation, a combination of laser patterning and micro-coining is used to improve the tribological properties of steel surfaces by introducing bio-inspired **multi-scale** surface patterns **inside** and **outside** of the contact zone. Both methods are versatile regarding possible pattern geometries and offer the possibility to transfer laboratory processes to an industrial scale through their simple implementation in existing production lines. Laser patterning is especially effective in creating small patterns on a scale of less than 20 μm, whereas micro-coining is used to fabricate patterns on a larger scale, greater than 100 μm in spatial dimensions. Depending on the size of the patterns they can have different functions, whereby a distinction in terms of the patterns' size can be made with regard to the Hertzian contact width. Patterns which are larger or smaller than the contact width can result in significant differences in load-carrying capacity^[51]. It has been shown that especially surface features being smaller than the Hertzian contact width can induce hydrodynamic pressure^[52,53], whereas larger surface features can entrap more wear particles and store more lubricant as a result of their greater volume^[52]. Patterns inside the contact zone are designed to **improve the tribological behavior** directly by decreasing the real area of contact, entrapping wear particles, creating reservoirs for lubricant and generating additional hydrodynamic pressure, thus increasing load carrying capacity. Patterns outside the contact zone can **prevent migration of lubricant** out of the contact zone and thus indirectly improve the tribological behavior. In a subsequent step, surface patterns that have shown beneficial effects in laboratory experiments are **transferred to a machine element** to verify the patterns' effectiveness under realistic working conditions. Since bearings were identified as one of the main components being responsible for friction losses in the engine and transmission system of cars, a journal bearing is chosen as the machine element^[6]. The main objectives of the dissertation can be defined as follows:

OBJECTIVE 1

The first objective is to investigate the efficiency of surface patterns outside the contact zone. In the first step, causes for lubricant migration on steel surfaces are to be identified. In particular, centrifugal forces and thermocapillary migration shall be examined concerning their influence on the tribological behavior or lubricant migration, respectively. Subsequently, strategies to either prevent lubricant migration or guide lubricants over surfaces are to be developed. In this regard, the effect of single-scale laser and micro-coined patterns, as well as multi-scale patterns, on lubricant migration is investigated. Especially, the influence of orientation and topographical parameters like depth, width, and periodicity on lubricant migration is to be investigated.

OBJECTIVE 2

The second objective is to develop tribologically effective surface patterns for the application inside the contact zone. Therefore, multi-scale surface patterns shall be precisely fabricated by a combination of laser patterning and micro-coining. For this purpose, single-scale laser and micro-coined patterns, which have shown a beneficial tribological behavior in initial laboratory experiments are to be selected and combined suitably. The characteristic surface features of both single-scale patterns should be left intact. After successful fabrication, the tribological behavior of these designed multi-scale patterns under lubricated conditions is evaluated in detail. Special attention is to be paid to the mechanisms of friction reduction and the correlation of the modified tribological behavior with the topographical surface parameters of the designed patterns.

OBJECTIVE 3

The final objective is to transfer tribologically effective single- and multi-scale patterns onto the curved surface of shafts of journal bearings. The manufacturing techniques must be further developed and modified to accurately reproduce the relevant patterns onto the bearing. Particular emphasis should be placed on the precise fabrication of the patterns on the curved surface of the shaft. Furthermore, the comparability between the preliminary laboratory investigations and the results from the journal bearing tests are to be examined. This is a particularly important task as the friction force is not a material property but highly dependent on the tribosystem and thus on the contact conditions [54,55]. In this context, real machine elements operate under very different conditions from laboratory conditions, such as different kinematics, atmospheres, and other prevailing pressures.

2. STATE OF THE ART

2.1 Techniques for designing surface patterns

Various techniques can be used to manufacture surface patterns. These can be classified into several categories: removal of material (mechanical, thermal, and chemical), addition of material, moving material and self-forming methods^[56]. Thereby, each method has its limitations and benefits regarding productivity, efficiency, geometric flexibility and accuracy, material flexibility, possible feature sizes, etc. Naturally, the choice of the technique depends on the application and its requirements. However, as key criteria, productivity (patterning speed), efficiency and geometric accuracy can be named. In this regard, laser surface patterning and micro-coining seem to be suitable methods since both offer the possibility of mass production and are versatile fabrication methods. Related to laser surface patterning, especially direct laser interference patterning (DLIP) allows to reach very high process speeds (close to 1 m²/min) in combination with feature sizes down to the nanometer scale (<100 nm)^[57]. Furthermore, the two methods are capable of producing multi-scale patterns as they produce patterns on two different scales. In this context, laser surface patterning is particularly effective in producing small patterns with lateral extensions of less than 20 μm and a depth of around 1 - 2 μm, while micro-coining can accurately manufacture larger surface features, having a diameter of more than 30 μm and variable depth. Another technique frequently employed in manufacturing surface patterns for tribological applications is photochemical patterning^[56]. Due to the great variety of patterning techniques and new techniques emerging every day, the state of the art will subsequently merely focus on these three techniques which belong to the family of ‘material removal’.

2.1.1 Laser surface patterning

Laser surface patterning is nowadays the most used technique to pattern surfaces in engineering applications^[56]. This is reflected in increased sales of laser systems, leading to a growth of the total market from 8.6 to 12.5 billion \$ in between 2007 and 2017 alone^[58,59]. Material processing accounts for roughly 20 % of this market and micro- and nanofabrication for about 10 %. Additionally, the number of publications dealing with laser material processing continuously grows reflecting the continuous development of laser systems and laser processing. The great popularity of laser processing can be attributed to the possibility to permanently alter the surface’s material properties through the unique interaction with laser light. In the course of the process, the crystal structure, the topography, and the surface chemistry can be locally modified, which results in drastic changes in the material’s behavior. Taking advantage of this, the material properties can be designed and optimized to obtain the best functionality for the desired application^[58]. Laser processing is a contactless method that uses the energy of electromagnetic radiation to remove material from the surface or move material on the

surface^[58]. Usually, pulsed laser systems with pulse durations shorter than μs are used for surface engineering applications to reduce the thermal impact on the material^[58]. For pulsed laser systems, the energy of the electromagnetic radiation is precisely delivered to a very confined region near the surface over a short period, resulting in the desired laser-material interaction and hence control of the local material properties. The initial interaction between laser light and material always occurs by excitation of electrons. Since the electron-electron interaction time is very short, it can be assumed that the thermalization of the electrons happens instantaneously^[60]. By electron-phonon coupling, the system reaches an equilibrium, which results in local heating^[58,60]. In order to control the laser process several laser parameters can be adjusted, being the wavelength λ' , the laser fluence (J/m^2), the number of applied pulses, the beam characteristics, the pulse duration, and the approach to generate surface patterns^[58]. Regarding the wavelength, the spectral absorptivity has to be considered. Taking copper as an example, the absorption at 532 nm is 40 % whereas at 1064 nm most of the radiation is reflected resulting in absorptivity of only 2 %. Hence, an increase in absorptivity by a factor of 20 is achieved when changing the wavelength from 1064 to 532 nm^[58]. One possibility to tune the wavelength in neodymium lasers is frequency doubling by second harmonic generation. Regarding the laser fluence, it must be high enough to exceed the ablation threshold and thus to initiate moving or removing of material^[61]. Typical ablation thresholds for metals lie between 1 and 10 J/cm^2 , which can be reached easily with laser systems^[58]. After exceeding the ablation threshold, the ablation diameter and depth (i.e., the ablation volume) as well as the thermal impact increase with increasing laser fluence^[58]. The Lambert-Beer law describes the penetration depth z of the laser intensity:

$$I(z) = I_0 \cdot e^{-\alpha \cdot z} \quad (1)$$

The intensity I at a certain depth z is a function of the material's absorption coefficient α and the intensity I_0 just beneath the surface after considering losses due to reflection^[58]. Therefore, increasing the laser fluence results in faster processing speeds but also increases the size of the heat affected zones^[58,62]. The laser fluence can be affected by focusing of the laser beam and the power or energy of the laser beam. Since the output power is a function of the pumping source's power and the active medium's volume that the laser beam traverses during amplification, it can be controlled by controlling either one of these parameters. One important parameter, which is frequently used to manipulate the laser-material interaction, is the pulse duration of the laser beam. Usually, a distinction is made between short and ultra-short laser pulses since the laser-material interaction is fairly different in these two regimes. The duration of laser pulses is considered to be ultra-short if it is equal to or smaller than 10 ps^[58,63]. At pulse durations below 10 ps, the classical heat conduction theory, which describes the material with one temperature, loses its validity and the time scales of the different excitation mechanisms have to be considered^[63]. In metals, the laser light is absorbed by the electrons within a period of approximately 10 fs. The transformation of the absorbed energy into thermal energy by electron-electron relaxation within the electron system takes roughly 100 fs. The transfer of heat from the electron system to the lattice by electron-phonon relaxation starts after 1 - 10 ps^[58]. For pulse durations

shorter than the electron-phonon relaxation time, the laser energy introduced into the material during the pulse duration cannot be transferred to the lattice^[63]. About 1 - 10 ps after the initial laser-material interaction (i.e., the ultrashort laser pulse has already ceased), the energy stored in the electron system is transferred to the lattice. For ultrashort laser pulses, the energy is usually high enough to break the bonds of the lattice structure leading to direct ablation and negligible energy transfer to neighboring lattice ions^[64]. As a consequence of the different interaction mechanisms of short and ultrashort laser pulses, the material response also differs significantly. The material interaction of short pulses (micro- and nanosecond regime) is characterized by heat conduction, melt formation and evaporation, depending on the temperature achieved. In contrast, for ultra-short pulses a direct transition from solid to vapor dominates, where the overheated liquid is ejected out of the process zone as liquid droplets and vapor (Fig. 3)^[65].

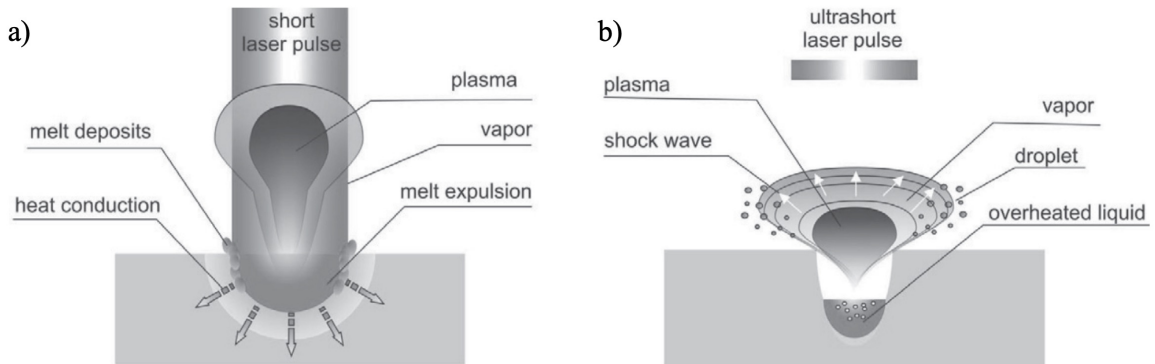


Figure 3: Schematic of the laser-material interaction in the case of a) short and b) ultrashort laser pulses^[65].

Since the mechanism for ultra-short laser pulses is not based upon heat conduction, the thermal impact is greatly reduced, and material can be removed without thermally affecting the surrounding material^[58]. The thermal penetration depth l_d can be estimated with the laser pulse duration τ_p and the material's thermal diffusivity κ ^[63,66]:

$$l_d = 2\sqrt{\kappa \cdot \tau} \quad (2)$$

The result of reducing the laser pulse duration from the nanosecond regime (short pulses) down to femtoseconds (ultrashort pulses) on the depth of thermal penetration is represented in Fig. 4. As can be seen from this figure, especially for ultrashort pulses the heat is concentrated in areas very close to the surface. However, as described above, for ultrashort pulses the classical heat conduction theory is no longer valid. Therefore, the thermal penetration depth does not reach zero but rather approaches a minimum^[63].

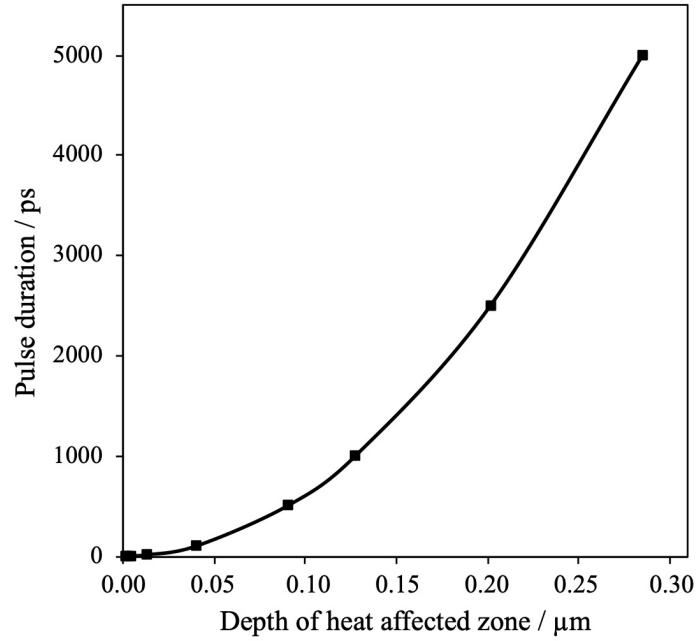


Figure 4: Representation of the effect of pulse duration on the thermal penetration depth in steel according to equation (2). The pulse duration is varied from 5 ns down to 100 fs resulting in a significant reduction in the depth of thermal penetration.

Furthermore, higher surface aspect ratios (ratio between depth and width of the surface pattern) can be achieved using ultra-short laser pulses since the material is evaporated with each individual pulse even from greater depths. In contrast, the ejection of melt becomes less efficient with increasing depth, and the produced surface features might be partially reclosed by the ejected melt ^[65].

It is also worth mentioning that the ablation threshold for a material is reduced for shorter pulse durations due to non-linear multi-phonon absorption processes leading to a reduction of laser fluence, which is necessary for material ablation ^[58,65]. Another effect of the non-linear absorption of ultra-short laser pulses is the possibility to process materials, which are usually optically transparent for the applied wavelength, like glasses ^[58].

An elegant solution to obtain ultra-short pulses is mode locking. Since the pulse duration is inversely proportional to the spectral width of the active medium, systems with a broad bandwidth, like Ti:Sapphire, are employed. Either active or passive mode locking can be used, which causes the oscillating modes in the laser cavity to maintain a fixed phase in relation to each other. Thereby, active mode locking uses intracavity optical modulators like acousto-optic modulators, whereas in passive mode locking non-linear materials like saturable absorbers or a Kerr lens are used. The result is a laser output, which varies in a very well defined manner as a function of time, hence ultra-short pulses ^[58].

Finally, the approach to generate surface patterns largely influences the process. The most straightforward technique, called direct laser writing (DLW), focuses the laser beam onto the sample and irradiates desired sample areas by either moving the sample via a translation stage or scanning the beam over the sample's surface ^[58,60,67]. In both cases, the laser beam is delivered onto the sample

surface in a continuous or quasi-continuous way^[58,67]. In the case of pulsed lasers, single spots can be overlapped to create line-like or various other pattern geometries^[60,67,68]. The advantage of DLW is the high flexibility of the process in terms of possible geometries^[58]. However, the process is time-consuming, and the minimum feature size depends on the capability of the focusing system^[57]. A possible approach to decrease the minimum feature size to the nanometer scale and increase the processing speed at the same time is DLIP^[57]. The method makes use of interference, which generates periodic intensity distributions upon interference of two or more laser beams due to constructive and destructive interference. By varying the number of interfering beams, the intensity distribution on the surface and therefore the pattern geometry can be designed. Two beams, for example, result in line-like intensity distribution, whereas three beams generate dot-like patterns. Furthermore, the angle between the beams defines the distance between the intensity maxima^[69-71]. A distinctive characteristic of the method is that the configuration of the laser beams creating the desired pattern can be calculated, which makes the design of the patterns very convenient^[69,72]. Therefore, the discrete Fourier transformation is applied to the desired pattern and the most significant points are determined in Fourier space^[69]. All information needed to reproduce the patterns is included in these points, which are vectors and can be extracted by constructing an Ewald-sphere^[69]. By a clever combination of the resulting intensity distribution, manifold and complicated patterns can be generated, such as Penrose patterns^[72].

Overlapping of the laser beams on the sample surface results in the typical laser-material interactions at positions of high laser intensity whereas those positions irradiated with low intensity remain virtually unchanged^[73]. Thereby, the material is molten or directly ablated at the positions of maximum laser intensity, depending on the laser's pulse duration. In case of thermal processes with melt generation (i.e., for greater pulse durations) a temperature gradient develops on the sample surface, which can be up to 3500 K/ μm ^[73]. As a result, a surface tension gradient is produced in the molten material leading to Marangoni convection and hence a material flow from the hot intensity maxima positions to colder intensity minima positions^[73]. The distance between individual features, also called periodicity, can be controlled by the wavelength and the angle between the interfering beams, making DLIP a versatile tool to create defined and periodic surface topographies^[69]. **Fig. 5** schematically illustrates the DLIP process for a nanosecond laser system.

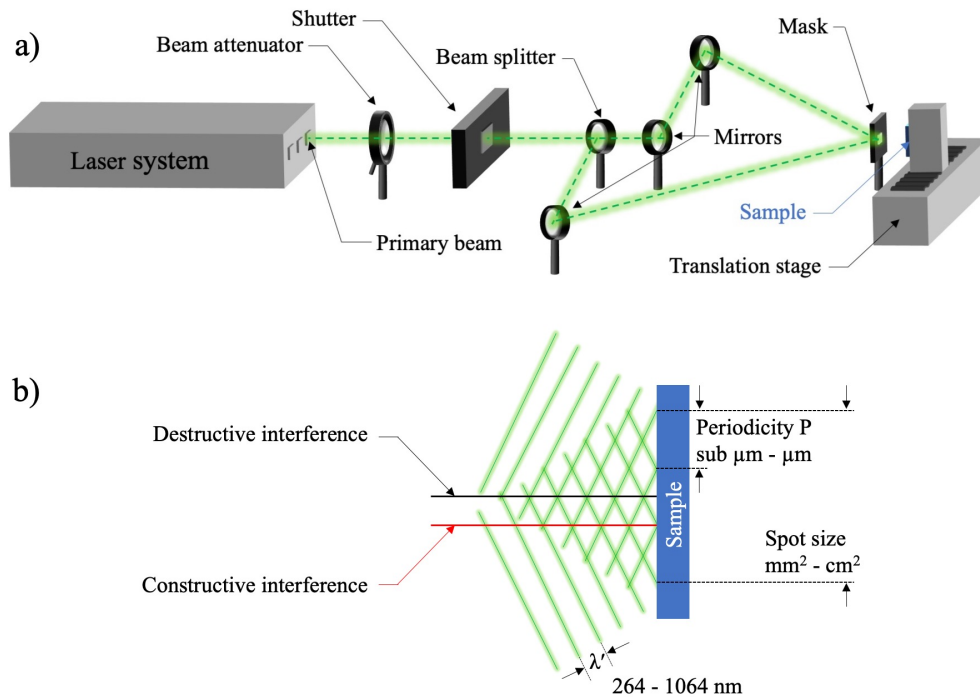


Figure 5: a) Schematic of the DLIP process set-up with the necessary equipment to guide the beam and scan the sample: beam attenuator, shutter, beam splitter, mirrors, mask and translation stage. Here, the beam is split into two beams to create a line-like intensity distribution. b) Generation of a periodic intensity distribution due to constructive (high intensity) and destructive (low intensity) interference of two beams. The periodicity indicates the distance from one intensity maximum to the next and depends on the angle of the two beams as well as the laser wavelength λ .

2.1.2 Micro- and roller-coining

The process of coining has been used throughout the last thousand years to produce coins^[74]. In the context of surface patterning, it is a suitable technique to precisely and efficiently manufacture larger surface features onto metals in the micrometer range (periodicity of roughly 20 - 200 μm)^[18,75,76]. The depth of the coined patterns can be varied by controlling the coining force^[76]. Typically, coined patterns are used for microfluidic applications in components like micro heat exchangers or micro fuel cells^[77,78]. The patterns are created by using a pre-structured tool to transfer the patterns onto the sample under high coining pressures. A schematic of the process is shown in **Fig. 6**. The die of the tool-set is often made out of hardened steel to increase the maximum stress, which it can resist, and the surface patterns can be applied onto the die by grinding or laser ablation^[18,79]. For the micro-coining process, a closed die set-up is used to prevent material from flowing outwards and to increase the form filling, which is the ratio of pattern depth to tool structure height^[80]. Early studies mainly discussed cold coining of relatively soft metals, like copper or aluminum alloys^[77,78,81]. However, to achieve complete form filling, high pressures are needed for cold coining as a result of high initial flow stresses. Especially for higher strength materials, like stainless steels, this could result in damaging of the die^[79]. To overcome this limitation, the die material or the process itself can be modified.

Regarding the process, heating methods have been proposed, which reduce the flow stress of the material to be coined ^[79]. Out of these, conductively heating the sample seems to be the most promising method ^[78–80]. The electric conductive heating method can be integrated directly into the coining tool-set and allows for rapid heating to a defined and homogenous temperature ^[79,80]. By using this technique, it has been shown that during micro-coining of hemispherical and ellipsoidal lubrication pockets no wear occurs on the die after 230 cycles ^[18].

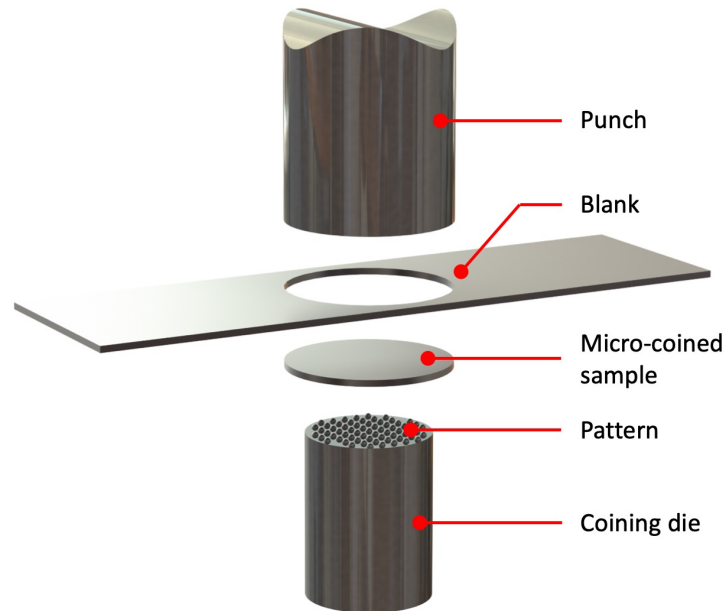


Figure 6: Schematic of the micro-coining process showing the different components used for manufacturing micro-patterns.

Since micro-coining is limited to flat substrates, another process is necessary to accurately and efficiently apply surface patterns to curved surfaces, such as occurring for example in journal bearings ^[75]. Szurdak et al. developed a new roller-coining set-up, which can fulfill this task ^[75]. The protruding surface features on the coining tool can be fabricated by another coining process or by laser ablation ^[75,82]. In the case of fabrication by coining, the tool is first coined and then hardened to increase the tool strength ^[75]. To produce the surface patterns on the counter-part, the coining tool is attached to a pneumatic system, which is integrated into a conventional turning machine. The advantages of using a pneumatic system are the possibility to continuously adjust the forming force by modifying the pneumatic pressure and the self-adjustment of the tool position, which results in a constant forming force and thus pocket depth despite surface irregularities. Thus, it is possible to improve the accuracy of the formed pockets compared to an experimental set-up without a pneumatic actor. By using the method of roller-coining with a pneumatic system, lubrication pockets have been fabricated accurately onto flat and curved surfaces ^[75,82].

2.1.3 Photochemical patterning

Photochemical patterning is a two-step process consisting of applying a mask on the substrate by photolithography and a subsequent chemical etching process [14,56]. The technique is used to create patterns from the sub- μm regime up to several mm [14,16,56,83,84]. A schematic of the photochemical patterning process is depicted in **Fig. 7**.

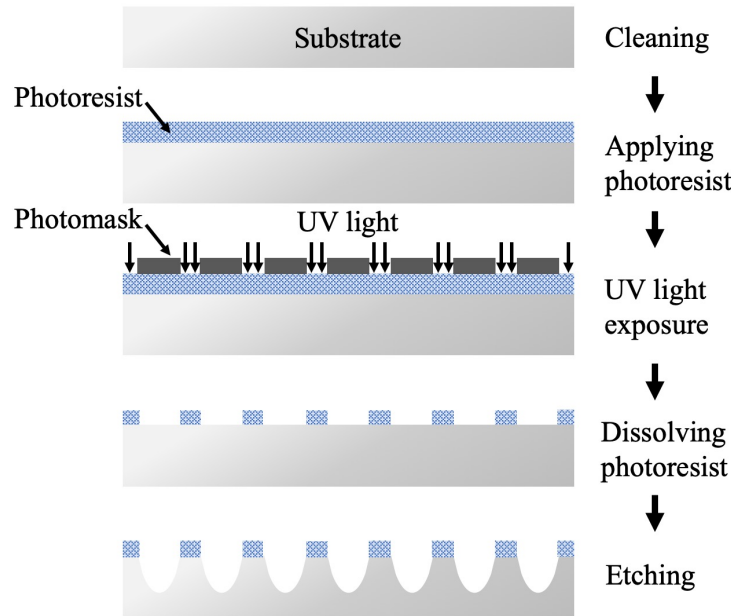


Figure 7: Schematic of the photochemical patterning process. Before the process, the substrate is cleaned. Subsequently, a photoresist is applied, which is then exposed to UV light at the positions not covered with the photomask to increase the resistance against the developing solution (negative photoresist). Finally, the photoresist is dissolved, and the substrate is chemically etched, resulting in surface patterns.

In a first step, the photoresist is applied onto the substrate, typically by a spin coating process to create a thin and even film [56,85]. By using a mask, the photoresist can be exposed to UV light at specific areas. The photoresist can be either positive or negative. Positive photoresists are weakened by the exposure to UV light, making them more soluble in the developing solution, whereas negative photoresists strengthen the polymer chains of the photoresist by promoting cross-linking [56]. After dissolving the photoresist at specific positions, the substrate's surface is etched with a chemical agent at the positions which are not covered with the photoresist. The depth of the patterns can be controlled by the etching time [14,56]. Advantages of the process are that merely the topography of the substrate is modified, rather than the material properties, there is no stress introduced, no burrs or edges are created on the surface, the resolution is high, and it is a versatile technique in terms of shapes and materials [14,16,56,85]. However, the two-step process is rather time-consuming and demands high standards in terms of environmental conditions [14,56].

Due to their advantages in terms of flexibility, cost, applicability, and processing speed, laser surface patterning and micro-coining were chosen as patterning techniques in this dissertation. Single-scale patterns are created by these techniques individually, whereas the combination of the two techniques allows for the generation of multi-scale patterns.

2.2 Surface patterning to control friction and wear in lubricated systems

Usually, lubricants such as oils or greases are applied to reduce friction and wear in machine elements. However, due to higher efficiency requirements, low viscosity oils, which minimize viscous drag losses get more popular rendering the system more susceptible to drop below the optimum film thickness^[86]. Besides, machine elements are often operated under harsher conditions, like higher loads or frequent start-stop cycles^[87,88]. This results in contact of the rubbing surfaces and tends to increase friction and wear.

A possibility to correlate the operating conditions in lubricated systems with the COF is the Stribeck curve, which relates the COF with the Sommerfeld parameter, being the product of viscosity and velocity, divided by the applied load (see **Fig. 8**). Furthermore, the Stribeck curve can be divided into three main lubrication regimes, namely boundary, mixed and hydrodynamic lubrication. In combination with the lambda (λ) parameter, which is the relation of lubricant film thickness h_0 to the combined surface roughness of substrate and counter body σ , a classification between the three lubrication regimes can be done. For thin lubrication films, with λ values smaller than 1, boundary lubrication prevails, which is characterized by the surface asperities bearing the load. For higher velocities, viscosities or lower loads (F_N), the lubricant film thickness increases resulting in an increase of the lambda parameter to 1 - 3. This regime is called mixed lubrication, and the film thickness is high enough to carry the applied load partially, but the friction partners still are not entirely separated, and the asperities still touch each other. Since in this regime the roughness is in the same range as the film thickness, it has a significant influence on the build-up of hydrodynamic pressure and thus the film formation^[89]. For λ values larger than 3, both surfaces are completely separated from each other, the lubricant film entirely carries the applied load and hence the properties of the lubricant mainly influence the frictional behavior. Additionally, under hydrodynamic lubrication, no wear is to be expected^[90].

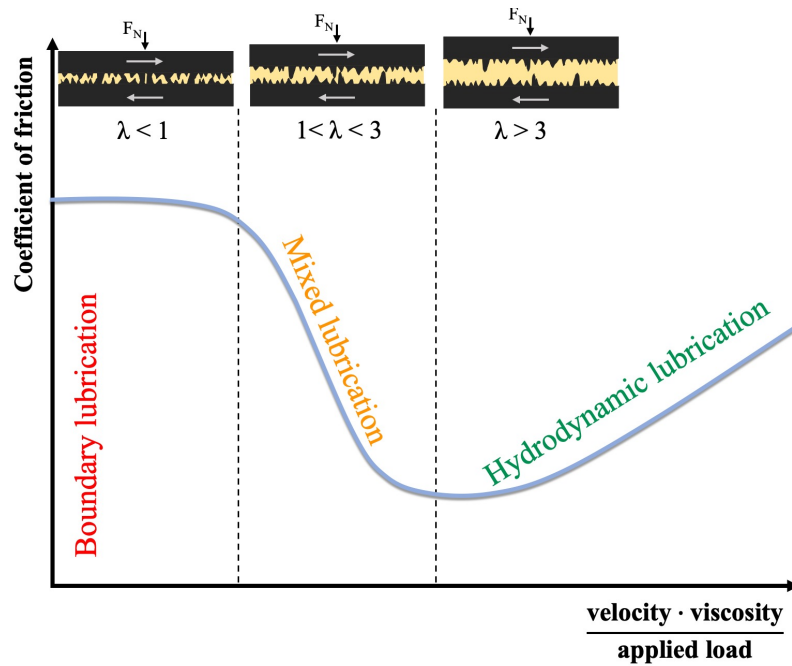


Figure 8: Stribeck curve showing the different lubrication regimes, boundary, mixed and hydrodynamic lubrication.

As can be seen from the Stribeck curve, the COF usually increases with decreasing film thickness^[9]. Therefore, the frictional behavior can be improved by strategies, which extend the hydrodynamic friction regime, or which reduce friction in the mixed or boundary lubrication regimes^[24,91]. Several strategies have been proposed to enhance the tribological behavior of surfaces under lubricated conditions, such as lubricant engineering, new materials, and coatings as well as surface patterning^[5].

Surface patterning is a viable method to increase the film thickness permanently and thus shift the onset of contact between the surfaces to higher loads, lower speeds or viscosities^[92]. Additionally, the surface patterns improve the tribological properties during boundary or mixed lubrication and thus increase the components' lifetime when operating conditions are more severe. However, the patterns have to be designed very carefully since also detrimental effects (i.e., increased friction and/or wear) have been observed if the pattern design is inappropriate with respect to the tribosystem and its contact conditions^[18,22].

2.2.1 Single-scale surface patterns

Surface patterns can influence the tribological behavior in various ways. The main influencing factors are:

- Reduction of the real area of contact,
- Trapping of wear debris,
- Create reservoirs for lubricant, and
- Generation of additional hydrodynamic pressure.

Reduction of the real area of contact

Despite the fact that according to Amontons' second law of friction, the friction force is independent of the apparent area of contact, the friction force depends greatly on the real area of contact^[4,93]. This correlates directly with Amontons' first rule, stating that friction during sliding is directly proportional to the normal load since the real area of contact is also directly proportional to the normal load^[4,23,94,95]. As can be seen in **Fig. 9**, the apparent contact area is merely the projected area of the surfaces, whereas the real area of contact is much smaller since it is the sum of discrete contact spots (junctions). Furthermore, it is demonstrated how roughness or a deterministic surface pattern influences the real area of contact.

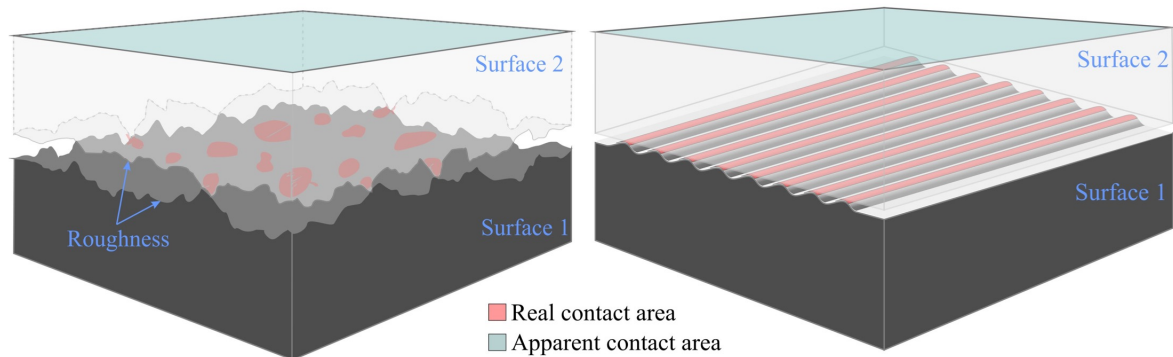


Figure 9: Schematic illustration of the real area of contact and the apparent contact area of contact between two rough surfaces or a surface with deterministic surface topography and a flat surface^[96].

The correlation of the real contact area and the friction force is a direct indication that the frictional behavior can be strongly influenced by surface patterning and thus by influencing the real contact area. Bettscheider et al. developed an approach to measure the real area of contact for laser-patterned surfaces during static loading, using a marker technique^[97]. They deposited thin Au₈₀Pd₂₀ films of 10 nm thickness on top of the surfaces to increase the contrast in the secondary electron images acquired with a scanning electron microscope (SEM). Subsequently, the samples were indented with a steel ball using different normal loads of 1 and 5 N. As can be seen from **Fig. 10**, the results show a significantly

decreased real area of contact for the laser-patterned samples. Furthermore, the real area of contact increases for all samples with higher loads.

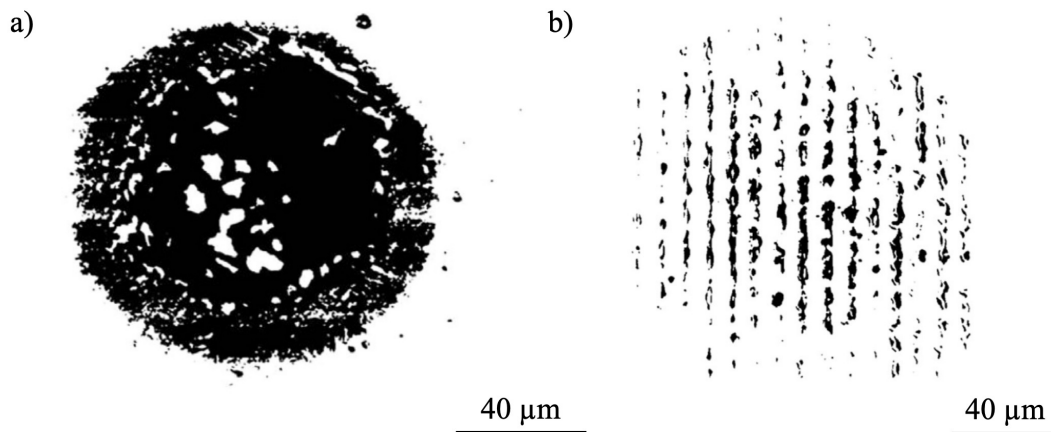


Figure 10: Reduction of the real area of contact as a result of laser patterning. The images show the real area of contact upon contact of a steel ball (diameter 6 mm) with a polished steel sample (a) and with a laser-patterned sample having a periodicity of 9 μm (b). The ball was loaded onto the sample with 1 N. Modified from [97].

There are several studies in the literature, which connect a reduced COF of patterned samples with a reduction of the real area of contact [50,72,98–103]. All of these studies work under mixed or boundary lubrication, or even dry sliding conditions. Since the contact area increases with decreasing lubricant film thickness, it is not surprising that the influence of the real area of contact in these lubrication regimes is particularly pronounced. However, with decreasing real area of contact also contact stresses, especially at the edges of the surface features, increase. This cannot only limit the friction reducing effect induced by the surface patterns but also lead to an increase in friction compared to a flat surface [102,104,105]. In this context, higher surface coverage with surface patterns (i.e., high area density) tends to weaken the surface integrity by decreasing the real area of contact. In combination with high contact pressures at the asperity tips, this leads to plastic deformation and thus to high wear rates [93,102,106–109]. This holds especially true for protruding surface features in comparison with dimpled surface patterns since the load bearing capacity of the protruding surface features is much lower resulting in higher local contact pressures [106,110]. Therefore, the optimization of the surface patterns has to be carried out carefully with regard to the area density and thus the real area of contact.

Trapping of wear debris

The entrapment of wear particles in depressions formed by surface patterns is a well-known mechanism contributing to friction and wear reduction of patterned surfaces under dry and lubricated conditions [14,21,99,111–114]. **Fig. 11** shows a schematic of the process.

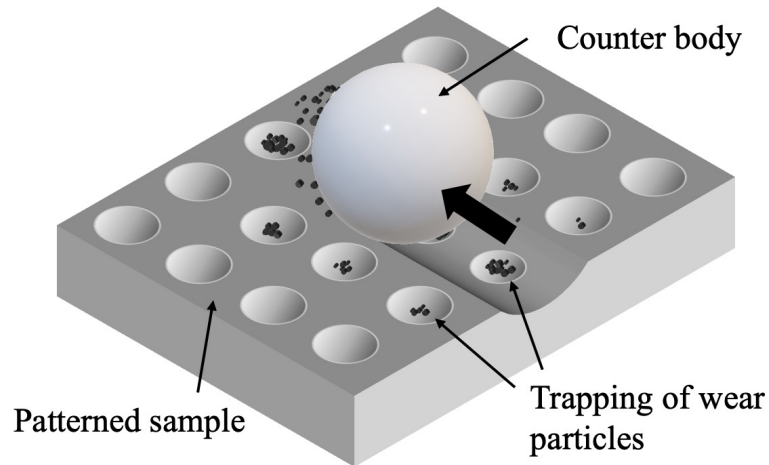


Figure 11: Schematic of the entrapment of wear particles in the topographic minima of a patterned surface. During sliding, plastic deformation of the substrate occurs resulting in the generation of wear particles. These particles are entrapped in the surface depressions and hence cannot contribute to further abrasion of the surface.

The mechanism of trapping wear debris can be regarded to be particularly important for unlubricated systems (e.g., for high temperature or vacuum applications) or those working under boundary lubrication due to high friction, severe wear, and even possible seizure under these contact conditions^[114]. The entrapment of the generated wear particles in the depressions helps to reduce abrasion which otherwise would enhance friction and wear^[14]. The generation of wear particles during sliding motion of metals is normally preceded by oxidation of the surface^[115]. Beyond a critical thickness, this oxide layer breaks up, and oxidic wear debris is formed^[115–117]. Since these oxidic particles are often harder than the substrates, substantial abrasive third-body wear can take place^[112,117]. To efficiently remove wear particles from the sliding surfaces by trapping them in the surface patterns, it is vital to design the surface patterns accordingly. Thereby, the size of the surface patterns must be sufficient to trap the largest wear particles in the depressions^[21,114].

Creating lubricant reservoirs

Another effect frequently reported in the literature is the replenishment of lubricant onto the sliding surfaces from lubricant reservoirs created by the surface patterns^[16,17,118–121]. By increasing the surface area and creating reservoirs for a lubricant, the quantity of lubricant in the contact zone is increased, thus contributing to better lubrication, which decreases friction and wear^[27,119,122]. A well-known application that makes use of this effect are honed cylinder liners in combustion engines, where the pattern stores oil and supplies it back to the contact zone^[123]. The effect, also called secondary lubrication effect, seems to be the dominant mechanism when the friction pair experiences lubricant starvation^[16,124]. Upon contact of the counter body with the pattern, the retained lubricant is squeezed out of the reservoirs, and as a result, the lubricant spreads in the contact zone, which is replenished with lubricant^[124]. Hence, the continuity of a lubricant film can be ensured as long as the patterns are not

destroyed due to excessive wear. Therefore, the secondary lubrication effect aids at prolonging the lifetime of machine elements by preventing lubricant starvation ^[21,125,126].

Regarding the pattern's geometry, it has been shown that a higher area density and thus more surface features aid at reducing friction and wear ^[121,124]. Also, a higher structural depth of the patterns can lead to a larger volume of the lubricant reservoirs, which results in improved tribological performance in the form of a greater lifetime ^[127]. However, if the depth of the patterns is too large, the lubricant may be trapped within the deep depressions in the surface and can therefore not be supplied as easily into the contact zone compared to patterns with a smaller aspect ratio ^[123,128,129]. Finally, lubricant reservoirs can also contain lubricant within them and thus prevent migration of lubricant out of the contact due to centrifugal forces or temperature gradients ^[127,130].

Generating additional hydrodynamic pressure

Finally, surface patterns can build-up an additional hydrodynamic pressure, which creates a force acting on the surfaces, pushing them apart from each other to further separate the surfaces ^[19,22,91,92,131]. The mechanism of increasing the hydrodynamic pressure by surface patterns can be seen from **Fig. 12**. Upon contact between the surface pattern and the tribological counter body, there is a pressure drop at positions where the lubricant gap height increases (diverging region), whereas at positions where the lubricant gap height decreases again (converging regions) the pressure is enhanced. Usually, this results in anti-symmetric pressure distribution and the pressure increase and pressure decrease cancel each other out, as can be seen in **Fig. 12 (a)**. For low velocities the maximum pressure is smaller than the absolute value of the cavitation pressure and the pressure distribution is anti-symmetric. Therefore, the net pressure is zero, and no hydrodynamic pressure or load carrying capacity is generated ^[132]. This also underlines the importance of the mechanisms described above, especially at low velocities. However, for higher velocities, the minimum pressure approaches the cavitation pressure, and gas bubbles (cavitation) begin to form in the diverging region (**Fig. 12 (b)**). This results in the development of an asymmetrical pressure distribution since the pressure drop is limited from below by the cavitation pressure, whereas the maximum pressure is not limited ^[24,132]. Hence, the net pressure is positive and hydrodynamic pressure and load carrying capacity is generated. The sum of the contributions of the hydrodynamic pressure generated by each individual surface feature totals the additional hydrodynamic pressure build-up of a patterned surface.

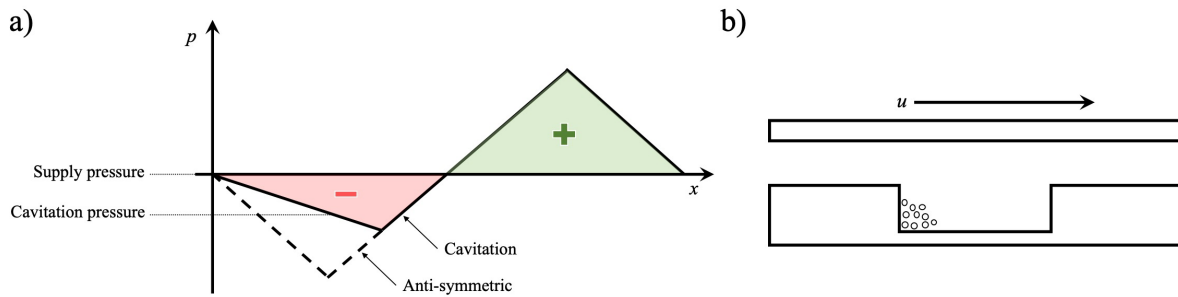


Figure 12: Asymmetric pressure distribution due to local cavitation at the patterns' sites. The net pressure is positive since the cavitation pressure of the lubricant limits the negative pressure. Note that additional hydrodynamic pressure can only be generated when the cavitation pressure is inferior to the supply pressure [22].

Since a certain film thickness in relation to the surface roughness is necessary to induce hydrodynamic pressure, the mechanism of generating additional pressure is relevant under mixed and hydrodynamic lubrication [22]. As a result of the additional hydrodynamic pressure induced by the surface patterns, friction in these regimes can be decreased [91]. Furthermore, hydrodynamic or mixed regimes can be extended to higher loads or lower velocities [24,91,92].

Several mechanisms have been proposed on how surface patterns can decrease friction and wear. In this context, high area densities of the surface patterns are beneficial for decreasing the real area of contact, creating lubricant reservoirs and trapping wear debris. Additionally, the surface patterns can create an additional hydrodynamic pressure, which helps to increase the surface separation. However, surface patterns may also weaken the surface integrity and increase contact stresses when there is solid-solid contact, thus possibly overcompensating positive effects of the surface patterns. Therefore, the design of the surface patterns regarding shape, area density, width, and depth has to be carefully optimized.

Surface patterns were first extensively used in the 1940s, where they were applied to bearings and engine cylinders [10,133]. In this context, surface patterning of cylinder liners of combustion engines was also the first successful commercial application [22,134]. In 1966 Hamilton et al. were the first to relate the positive effects of surface patterns to the generation of additional hydrodynamic pressure and hence increased load-carrying capacity when they investigated surface irregularities on rotary-shaft seals [11,22]. Since then a lot of different methods have been used to produce a variety of single-scale surface patterns. Especially the pioneering work of Etsion et al. is to be mentioned here, which started in 1996 [20,135]. Etsion et al. used laser surface patterning to produce hemispherical, dimple-like shapes [20,136]. In later years among the proposed geometries were triangular [137], diamond-like [138], elliptical [139], chevron-like [140], cross-like [21], and many more shapes. Thereby, the patterns have to be optimized with respect to the application and thus contact conditions, which is a difficult task due to the variable and complicated lubricated conditions. Machine elements to which surface patterns have been successfully applied over the years to improve their tribological properties are among others the piston-

cylinder contact ^[141,142], mechanical seals ^[143,144], cutting tools ^[14,145], the cam/tappet contact ^[146], and journal bearings ^[82,121,147,148]. Even though hierarchical or multi-scale surface patterns frequently occur in nature where they show fascinating properties, they have been very seldomly manufactured to manipulate the tribological behavior of machine elements.

2.2.2 Multi-scale surface patterns

Biological materials offer outstanding adhesion, frictional, wetting properties, and can be self-healing or self-cleaning. The secret for these outstanding properties seems to lay in hierarchical or multi-scale surface topography. The extensively studied structure of the bone, for example, shows seven levels of structural hierarchy, resulting in strength and toughness orders of magnitude greater than those of the constituent phases ^[149]. This multi-scale design of materials in nature is especially interesting for tribological applications since friction itself is intrinsically a multi-scale problem, as pointed out by Nosonovsky and Bhushan ^[41,150]. In this context, the gecko paw, which shows a three-level surface hierarchy, is a widely considered example as it exhibits either high adhesion (attachment to surfaces/walls) or low adhesion (detachment from surfaces) ^[41,149,151]. Other examples of multi-scale surfaces in nature, which show low friction or adhesion, are the patterned skins of snakes or sharks and the lotus leaf ^[46,50,152,153]. Due to the interesting frictional properties of these multi-scale surfaces, there have been efforts mimicking these surfaces. Usually, an improvement of material properties is achieved by mimicking the topographical features of the surface rather than its physical or chemical properties ^[150].

This way Shafiei and Alpas replicated the surface morphology of a lotus leaf in nanocrystalline nickel by imprinting surface patterns of the natural sample on an acetate film and subsequently depositing nanocrystalline nickel on the negative imprint ^[50]. The samples with the lotus-like surface patterns exhibited smaller COFs and especially less pronounced peak values of the COF due to a smaller real area of contact as well as wear particle trapping ^[50,98]. However, introducing nanoscale surface features on the microscale protuberances did not contribute to a further reduction of the COF ^[50]. Similarly, Baum et al. investigated snake inspired surface patterns on polymer samples and found a substantial reduction in friction as well as a reduction in stick-slip vibrations ^[46,154]. Apart from directly mimicking biological surfaces, there have been some attempts to manufacture multi-scale surfaces, which are bioinspired but rather based upon conventional manufacturing methods. Resendiz et al. used a combination of diamond cutting and shot blasting to create multi-scale surface patterns on aluminum. In comparison to a flat surface and the single-scale patterns, the multi-scale surface showed synergetic effects on the frictional behavior, resulting in the lowest COF under lubricated conditions. The authors attributed the reduced COF mainly to the generation of an additional hydrodynamic pressure, which was greatest for the multi-scale surface ^[48]. Wang et al. combined large dimples with a diameter of 350 μm with small dimples having a diameter of 40 μm , both fabricated by lithography and reactive

ion etching, to improve the frictional behavior of silicon carbide surfaces sliding in water. The authors assumed that large dimples increase the hydrodynamic pressure, whereas smaller but densely distributed dimples act as lubricant reservoirs providing lubricant to the contact zone. Indeed, the patterned surfaces with multi-scale dimples showed the highest critical load for the transition from hydrodynamic to mixed lubrication and thus the widest range of hydrodynamic lubrication regarding the operating conditions ^[155]. Segu et al. fabricated dimples on steel samples by laser patterning, combining different shapes (circular, square, triangular) and sizes. Under lubricated, conformal contact conditions, the authors showed an overall lower COF and a transition to hydrodynamic lubrication at smaller sliding speeds for the multi-shaped patterned surface compared to the non-patterned surfaces. The improved behavior was attributed to the generation of a hydrodynamic pressure induced by the patterns and additional oil supply from the patterns into the contact zone ^[156,157]. Additionally, they showed an improvement in the frictional behavior of patterned steel surfaces with multi-shaped dimples under lubricated, non-conformal conditions (ball-on-disk experiments) compared to non-patterned or surfaces patterned with only one kind of dimples ^[49]. Again, this improvement was associated with an additional hydrodynamic pressure and lubricant reservoirs. Some examples of artificial multi-scale patterns are depicted in **Fig. 13**.

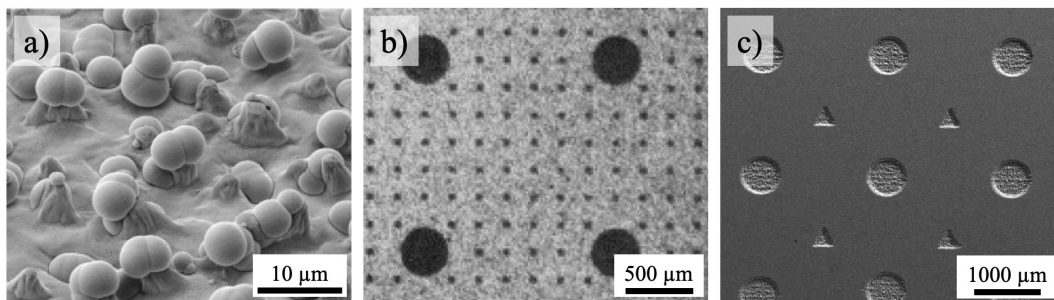


Figure 13: Examples of artificially manufactured multi-scale patterns. Shown are electrodeposited lotus leaf patterns in nickel (a) ^[50], a combination of large and small dimples in silicon carbide (b) ^[155] and multi-shaped patterns manufactured by laser patterning on steel (c) ^[157].

Despite numerous investigations of hierarchical surfaces dealing with their influence on adhesion and wetting (superhydrophobicity), such surfaces have seldomly applied to achieve low friction solid surfaces. Additionally, the exact mechanisms by which these multi-scale surface patterns improve the tribological behavior is still unclear.

Plausible explanations for the improvement of the tribological behavior induced by multi-scale patterns are that surface patterns on different sizes can influence the tribological behavior on different scales. Thus, adhesion could be decreased on the nanoscale and interlocking on the microscale both contributing to an overall reduced friction force ^[154]. Similarly, small-scale patterns may reduce the real area of contact while large surface features can entrap wear particles. Furthermore, under lubricated conditions surface patterns on different size scales could be effective at different lubricant film thicknesses and thus lubrication regimes since maximum hydrodynamic pressure is generated when

the structural depth is approximately equal to the lubricant film thickness^[21,22,89,158]. This would result in a synergetic effect of the multi-scale surface patterns by improving the tribological properties under various lubrication conditions simultaneously. Additionally, smaller-scale patterns on top of larger patterns might contribute to a better distribution of lubricant in the contact zone resulting in a reduction of cavitation phenomena, which otherwise might overcompensate positive effects induced by the build-up of a hydrodynamic pressure^[159].

2.3 Lubricant migration

Guiding of liquids on surfaces can be beneficial in various fields such as lab-on-chip systems, microfluidics, inkjet printing, micropump needles and thin-film lubrication^[160–162]. In nature, several animals exploit the phenomenon of guiding liquids through superficial channels or the anisotropic wetting of surfaces. The wings of butterflies exhibit anisotropic wetting properties, whereby a water droplet can easily roll away from the butterfly's body but is pinned on the wing in the opposite direction^[163]. This behavior can be explained by a directional arrangement of nano-tips on the wings^[162,163]. The rice leaf shows channel-like multi-scale patterns on its surface parallel to the leaf edge also leading to an anisotropic roll-off behavior of water droplets. Thereby, the droplets roll off more easily along the channel-like patterns^[164]. Furthermore, some lizards have adapted to arid environments by creating a capillary system on their bodies. Channels between their scales help them to collect and direct water towards their mouth using capillary forces and thus without external energy^[165–167].

Inspired by these functional surface topographies found in nature, tailored surface patterns, which exhibit a directionality, can be put to use to modify the wetting behavior of surfaces and guide liquids over surfaces. Such surface patterns might also be interesting for tribological applications, in which they can be applied to guide lubricants to the contact zone where they are required to reduce friction and wear. Especially in cases where lubricant migration out of the contact might occur, preventing lubricant migration or guiding lubricant back to the contact zone is of utmost importance. Lubricant migration out of the contact can lead to starved lubrication conditions (i.e., insufficient lubrication) in the tribological contact, which can significantly increase friction and accelerate wear thus causing severe damages and ultimately resulting in the failure of the entire component^[12,35]. As a result of starved lubrication conditions, energy consumption is drastically increased, which in turn decreases the energy efficiency. The migration of lubricants is of great importance in applications like miniature ball bearings or hard disks^[33]. Moreover, lubricant migration is a serious problem for space applications in which temperature changes from -100 to 200 °C, causing a decrease in the device's performance and components' lifetime^[35]. To prevent starved lubrication, the lubricant migration out of the contact should be inhibited. In this context, Ke et al. could prevent thermocapillary lubricant migration of ferrofluids out of the contact zone using a magnetic field. As a result, an increase in friction can be prevented resulting in a constant and low COF^[168].

2.3.1 Reasons for lubricant migration

Two main causes are resulting in the migration of lubricant out of the contact zone, namely: thermocapillary migration and centrifugal forces. Thermocapillary migration can occur wherever there is a temperature gradient whereas lubricant migration due to centrifugal forces only occurs in rotating machine elements, such as ball- or roller-bearings.

Thermocapillary migration

The theoretical background related to the movement of droplets on surfaces is described by the Marangoni effect, which is also known as the “tears of wine” phenomenon. In a glass of wine, the alcohol at the side of the wine glass, which has a lower surface tension and higher volatility than the water, evaporates more rapidly resulting in an inhomogeneous alcohol concentration and thus a gradient in surface tension [32,169]. As a result of this surface tension gradient, wine is pulled up towards the regions with higher surface tension where a thin film is formed. As more liquid is pulled upwards, droplets are formed, which, under the force of gravity, fall back into the wine like tears [32,170]. A change in the surface tension as a function of the location can be induced by various mechanisms, such as electric and magnetic fields, or chemical and thermal gradients on the surface [33,171]. Thereby, the movement of a liquid, which is induced by a temperature gradient, is referred to as thermocapillary migration [31,34,35,171–173]. The movement of a droplet on a surface with a temperature gradient and the forces acting on the droplet are shown in **Fig. 14**.

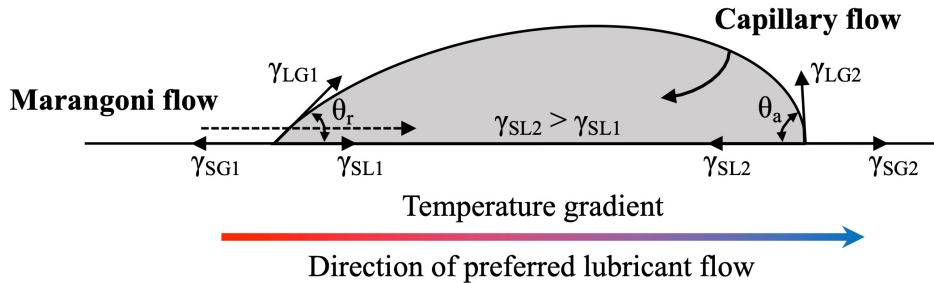


Figure 14: Schematic illustration of the flow patterns on the solid-liquid interface and inside a liquid droplet sitting on a surface with a temperature gradient. The advancing (θ_a) and receding (θ_r) contact angles, which are related by Young’s equation with the interfacial tensions existing at the solid-liquid (γ_{SL}), solid-gas (γ_{SG}) and liquid-gas (γ_{LG}) interfaces [174], differ as a result of the applied temperature gradient. The droplet moves toward cold regions of the surface. Modified from [175].

The spatial variation in surface tension at the solid-liquid interface creates tangential stress at that surface pointing toward higher surface tension, namely colder regions. This stress acts on the adjacent fluid, and, if it is greater than the viscous resistant force, the interfacial fluid is set into motion, which is then transferred to the fluid inside the lubricant droplet [175–177]. As shown in **Fig. 14**, the Marangoni flow propels the droplet towards cooler regions, leading to an asymmetric droplet shape, also known

as contact angle hysteresis, where the contact angle at the front (advancing contact angle) is greater than at the back (receding contact angle). Since the curvature of the droplet's advancing side is smaller than that of the receding side, a pressure difference across the drop is generated, which produces a capillary flow in the opposite direction to the Marangoni flow^[33,175]. Therefore, the droplet can only move if the Marangoni flow overcompensates the capillary flow^[175,178]. In this context, Fote et al. have shown that a small temperature gradient of 0.2 °C/mm is sufficient to cause lubricant migration^[36,39,179]. Thereby, the migration velocity can be increased by increasing the temperature gradient or the oil volume as well as by decreasing the lubricant viscosity^[33,34,172,180]. The dependency of the migration velocity v on the lubricant viscosity and temperature gradient can also be seen from the following formula^[175,181]:

$$v = \frac{h_0}{2\mu} \cdot \frac{d\gamma}{dT} \cdot \frac{dT}{dx} \quad (3)$$

where h_0 is the lubricant film thickness, μ is the dynamic viscosity of the lubricant, $d\gamma$ is the change in surface tension with temperature dT , and dT/dx is the temperature gradient parallel to the surface.

The idea to deliberately use a temperature gradient as the driving force to move a liquid droplet over a surface was recognized at the beginning of the 20th century by Bouasse, who moved drops against the force of gravity on an upwards tilted metal wire by heating the lower end^[172,182]. Such a temperature gradient can also develop in a frictional contact where it may lead to lubricant migration out of the contact zone, and thus to starved lubrication conditions and ultimately a downgraded tribological behavior. Zooming into the contact zone between rubbing surfaces under mixed lubrication reveals that both rough surfaces meet at single small spots, the contacting asperities^[23,94,95]. Due to the high contact pressure at these contact spots, frictional heat is locally generated upon relative movement (i.e., sliding) of the two surfaces^[29,32,35]. As a result, the interfacial temperature close to the contact zone is increased, whereas the temperature in adjacent regions without asperity contact remains considerably low^[28,32,35]. Hence, a temperature gradient is generated, where the surface tension in the colder regions is higher than in the warmer regions, leading to a surface tension gradient. As a result, the lubricant is pulled from the hotter contact zone toward the colder regions surrounding the tribological contact to reduce its free surface energy, which yields in a lack of lubricant at the contacting asperities, where it is most urgently needed^[32,172,175,183]. The problem of lubricant migration possibly leading to lubricant starvation in a tribologically loaded contact is schematically depicted in **Fig. 15**.

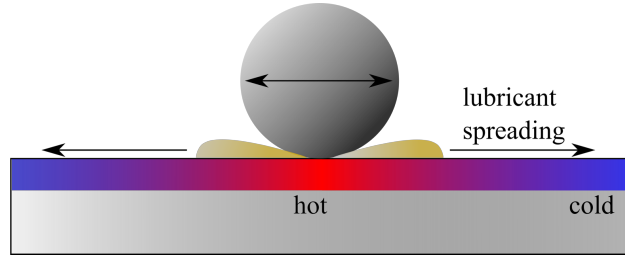


Figure 15: Schematic illustration of the lubricant's migration out of the hot contact zone toward the colder surrounding areas. The contact zone is heated by frictional heating resulting in a reduction of the interfacial tension and ultimately in the loss of lubricant out of the contact zone.

Temperature gradients on surfaces are in the range of several °C/mm, whereby typical temperature gradients account for 1 - 10 °C/mm depending on speed and load ^[184–187]. In tribological contacts, the Marangoni flow typically is the dominating effect over capillary effects and lubricant migration out of the contact zone can occur. In this context, Ke et al. have shown that an increase in the temperature gradient from 1.0 to 4.33 °C/mm leads to a faster lubricant migration out of the contact zone and thus to higher COFs ^[180].

Centrifugal forces

Besides, centrifugal forces can cause the loss of lubricant in the contact zone leading to increased friction and/or wear ^[38,188]. Roller bearings in high-speed spindles and aircraft engines, for instance, often operate under high speeds, where centrifugal forces can affect the lubrication conditions ^[189]. This can be explained by a rapid increase of the centrifugal forces with increasing rotational speed. Thereby, the relation of the centrifugal force F_c with the mass of the lubricant m (can be calculated from the lubricant's density and volume), the rotational speed v_r and the radius of the point at which the centrifugal force is determined in relation to the axis of rotation R is given by following formula ^[190]:

$$F_c = \frac{m \cdot v_r^2}{R}, \quad (4)$$

Liang et al. performed ball-on-disk experiments varying the rotational speed from 3 to 30 m/s and found that lower speeds can enhance the lubricant replenishment to the contact zone, which is beneficial for the tribological behavior, whereas higher speeds weaken the lubricant replenishment. Hence, at higher speeds centrifugal forces govern the lubrication conditions, leading to a loss of lubricant, a decrease in lubricant film thickness, and ultimately starved lubrication conditions ^[189,190]. Therefore, speed limits have to be defined for roller- and ball-bearings to restrict the loss of lubricant from centrifugal throw-off of lubricant ^[191]. The reduction of lubricant in the contact zone is schematically shown in **Fig. 16**.

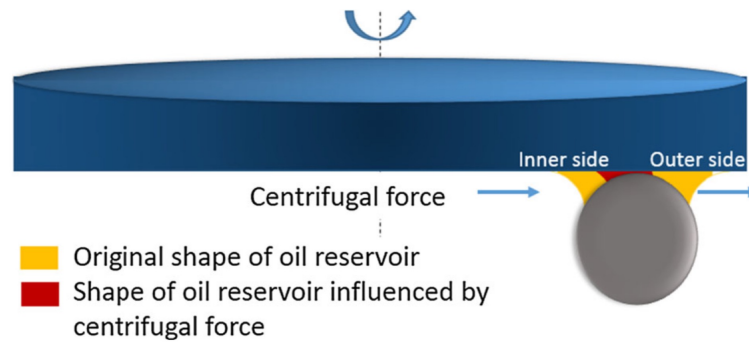


Figure 16: Schematic illustration of the lubricant loss from the contact zone due to centrifugal forces in a ball-on-disk experimental set-up. The oil reservoir represents the lubricant film, which is present in excess in the contact zone. Due to the acting centrifugal forces, the surface area of the lubricant film significantly decreases possibly leading to a reduction in lubricant film thickness. Reproduced from ^[189].

It has been shown that both temperature gradients and centrifugal forces affect lubricant migration out of the contact zone leading to a loss of lubricant and therefore an increase in friction and/or wear. To improve lubricant migration by preventing lubricant movement or by guiding lubricant several parameters can be controlled, namely the surface roughness, the surface chemistry, and the lubricant's physical properties.

2.3.2 Chemical modification to improve lubricant migration

One way to improve the lubricant migration on surfaces is to chemically modify the surface or the lubricant, which alters the wettability and thus the adhesion of the lubricant on the surface ^[192–194]. Dai et al. showed that by changing the surface material, the ability of diester droplets to migrate over surfaces under the influence of a temperature gradient (2.2 °C/mm) is strongly affected. Thereby, the migration velocity accounted for 0.5 - 0.6 mm/s in case of Au, Ti or Si surfaces, while the droplets did not migrate at all on polytetrafluoroethylene surfaces ^[195]. Additionally, low surface energy coatings can be applied as anti-migration barriers in order to prevent lubricant migration ^[196–198]. These coatings, which are mostly fluorocarbon compounds, are usually not directly applied within the machine elements but only to escape gaps such as bearing lands ^[196,197]. As a result of the low surface energy of the coating, most lubricants do not migrate across the coating, and thus the lubricant can be contained within the contact zone ^[196]. Hence, the tribological properties of machine elements and their lifetime can be improved ^[199]. By applying an anti-migration coating, Fitzsimmons et al. increased the lifetime of miniature ball bearings from 300 to nearly 4000 h ^[200]. Apart from that, watches are treated with anti-migration coatings for lifetime lubrication ^[193]. However, several problems are encountered when using coatings to decrease lubricant migration and have to be taken into consideration. First, the coatings can be easily removed during wear or as a result of chemical reactions between lubricant and coating ^[197,199]. Secondly, the use of coatings at very low or high temperatures is often restricted ^[199].

Finally, the chemicals used for the anti-migration coatings are often hazardous for the environment [40,201].

Additionally, the chemical composition of the lubricant can be modified to decrease the tendency for lubricant migration. Thereby, either a lubricant with higher surface tension or viscosity, which tends to show less lubricant migration, can be employed (see also equation 3) or additives can be added to the lubricants [181,193,197,199,202]. In this context, Huang et al. investigated the migration behavior of an ionic liquid in comparison to various other lubricants under a temperature gradient on steel surfaces. They showed that the ionic liquid do not migrate at a temperature gradient of 2.33 °C/mm whereas a polyalphaolefin oil (PAO) migrated with a maximum velocity of 2.5 mm/s [198]. Moreover, Dai et al. investigated the effect of lubricant additives on the migration behavior and found that by adding oleic acid or polydimethylsiloxane the migration of lubricants can be slowed down [181]. This was attributed to a lower dependency of the surface tension on temperature as well as enhanced adsorption for polydimethylsiloxane and oleic acid, respectively.

Finally, chemical patterns of alternating hydrophobic and hydrophilic stripes have been shown to exhibit an anisotropic liquid spreading behavior [162,203–205]. Such surfaces could be highly attractive to control lubricant migration under the effect of an applied temperature gradient. Bliznyuk et al. created chemically defined patterns of hydrophobic stripes of fluorinated self-assembled monolayers on a hydrophilic SiO₂ substrate by optical lithography [203]. The striped pattern resulted in a preferential spreading of water droplets parallel to the line-like pattern but obstructed fluid movement in the perpendicular direction. Furthermore, by varying the relative widths of hydrophobic and hydrophilic regions on the sample a surface energy gradient was generated, resulting in a preferential direction of liquid spreading to the more hydrophilic side.

2.3.3 Topographical modification to improve lubricant migration

Another possibility to improve lubricant migration on surfaces is to modify their topography, thereby creating mechanical barriers or edge effects [193]. The simplest method is to create depressions on the surface, which act as a sink and are filled with the migrating liquid, therefore hindering spreading [33,193]. However, this method has the disadvantage that, even though the liquid cannot spread further, it is still removed from the contact zone. Another approach to obstructing liquid motion on a surface by topographical features is based upon edge effects. The effect of a single topographical defect on the liquid's contact line was discussed by Quéré and is schematically shown in **Fig. 17** [206]. Upon contact with a depression on the surface, the front of a liquid droplet can be stopped as if the defect on the surface was nonwetting, which is called contact line pinning.

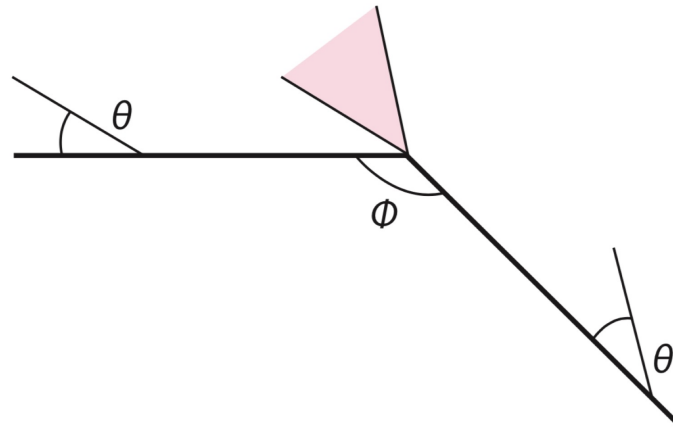


Figure 17: A droplet's contact line with the contact angle θ is pinned on an edge as the liquid migrates from left to right. Upon contact with the edge, the contact angle can take any value with respect to the horizontal reference value between θ and $\pi - \phi + \theta$, which is represented by the colored region. Only after exceeding a contact angle of $\pi - \phi + \theta$ the droplet can migrate further to the right. Reproduced from [206].

Since technical surfaces are not perfectly flat but exhibit roughness, often on a micrometric scale, Dai et al. investigated the thermocapillary migration behavior of lubricants on rough surfaces having a surface roughness in the range of $0.2 - 1.2 \mu\text{m}$ [32,34,206]. Interestingly, statistically rough surfaces without preferential direction showed an increase in migration velocity with higher surface roughness [34]. This was explained by the Wenzel model, which predicts smaller contact angles for hydrophilic surfaces and hence a higher tendency to spread over the surface with increasing surface roughness. Therefore, the pinning effect of surface asperities can be overcompensated by the greater tendency of the lubricant to spread on rougher surfaces. However, if the surface roughness showed a preferential orientation, such as after grinding, the migration velocity strongly depended on the orientation of the grinding scars with respect to the temperature gradient [32]. In the case of perpendicular orientation of the grinding scars with respect to the temperature gradient, the lubricant migration towards the cold side was effectively hindered by acting as a barrier to the lubricant motion. In contrast, parallel orientation of the grinding scars led to an increase in migration velocity which could be attributed to an additional force from capillary forces.

Various studies can be found in the literature using deterministic line- or channel-like surface topographies, fabricated by mechanical grinding, optical lithography, imprinting/coining, or laser surface patterning to create anisotropic wetting properties [204,207–209]. According to Xia et al. anisotropic wetting is defined as “the inhomogeneous distribution of liquid and accompanying wetting properties upon a surface” [209] and can result in either different contact angles parallel and perpendicular to the channels or different sliding angles off the surface for different directions [209]. Besides, some studies define an anisotropic droplet spreading on the surface, which measures the relative propagation of the droplet in x- and y-directions from above also called droplet distortion [207,208]. The anisotropic wetting properties, which result in different contact angles for different directions or a droplet distortion can

be explained by pinning of the contact line perpendicular to the channel-like surface patterns and capillary forces acting parallel to the patterns, thus stretching the droplet in this direction ^[35,204,207,208,210].

In this context, the spreading characteristics of liquids through open micro-channels have been thoroughly investigated in the literature ^[211–216]. It has been shown that the velocity of the liquid inside open surface channels can be described by balancing the capillary force with the viscous friction force ^[211,213,214,216]. This leads to the well-known Lucas-Washburn equation ^[217,218], which Rye et al. brought into a more general form ^[216]:

$$l^2 = K(\beta, \theta) \cdot \frac{\gamma \cdot d}{\mu} \cdot t \quad (5)$$

where l is the length of the wetted portion of the channel, $K(\beta, \theta)$ is a geometric term depending on the channel angle β and the contact angle, d is the structural depth and t is the time. It can be concluded that the spreading velocity of the liquid inside a channel is increased with increasing channel depth but decreased with increasing viscosity. Besides, the velocity of the liquid is decreased proportionally to $1/\sqrt{t}$, which can be explained with an increasing viscous friction force or wall friction as the liquid propagates through the channel ^[211].

The combination of pinning effects and capillary forces induced by deterministic channel-like surface patterns opens the possibility to manipulate the migration behavior of lubricants on such patterned surfaces. Thereby, obstructing lubricant migration out of the contact, or guiding lubricant back into the contact can prevent lubricant loss by thermocapillary migration or capillary forces and thus a dramatic increase in friction and or/wear ^[168,180]. In early studies, Fote et al. showed that geometrical barriers with different shapes (channels, steps, corners) on steel surfaces could prevent the thermocapillary migration of hydrocarbon oil ($\Delta T = 0.5 \text{ }^\circ\text{C/mm}$) ^[39]. More recently, Dai et al. investigated the thermocapillary migration behavior on steel surfaces, which were patterned with a line-like geometry by a combination of photolithography and electrolytic etching ($\Delta T = 0.6 - 3 \text{ }^\circ\text{C/mm}$) ^[35,210]. They found that the migration velocity of a paraffin oil can be slowed down or even completely stopped when orienting the channels perpendicular to the temperature gradient, whereas the migration velocity is increased for a parallel orientation with respect to the temperature gradient. Furthermore, deeper grooves showed a more significant effect in hindering lubricant migration and increasing the depth or width both resulted in faster lubricant migration.

Finally, multi-scale or hierarchical surface patterns, like that of the lotus leaf, have shown fascinating wetting properties as well as high anisotropy ^[209,219,220]. Therefore, such surface patterns are especially attractive to manipulate lubricant migration behavior.

Both chemical and topographical modifications of the surface are viable methods to modify the spreading behavior of lubricants. However, modifying the topography of the surface has various advantages over chemical modifications, such as greater robustness and environmental compatibility. Therefore, topographical modifications, and, in particular, multi-scale surface patterns are chosen in the present dissertation to manipulate the lubricant migration on surfaces.

3. OVERVIEW

As already stated in the motivation and objectives chapter, the present dissertation aims at investigating the effect of tailored multi-scale surface patterns **inside and outside** the tribological contact zone. Moreover, effective surface patterns, selected in preliminary laboratory experiments, are to be transferred to the shafts of journal bearings to improve the friction and wear behavior of this machine element, ultimately resulting in a greater lifetime and efficiency. Therefore, three main objectives have been defined, being: (1) the investigation of the underlying **reasons for lubricant migration**, which lead to starved lubrication as well as the application of topographical patterns **outside the contact zone** to obstruct lubricant migration, (2) the design, fabrication and tribological testing of suitable **multi-scale** surface patterns **inside the contact zone**, and (3) the transfer of tribologically effective single- and multi-scale patterns onto curved surfaces of **journal bearings' shafts** and their tribological testing.

This chapter intends to relate these objectives to the results achieved in the present dissertation as well as to give a complete overview of the presented results. The key results are presented subsequently in chapter 4, in the form of seven papers, published in internationally recognized, peer-reviewed journals. These papers give detailed information about the used methods, all results as well as a thorough discussion of the observed effects.

OBJECTIVE 1

Chapter 2.3 of the state of the art deals with the reasons for lubricant migration as well as with means to modify it. On the basis of the findings in the literature, it can be stated that lubricant migration is a serious problem, which has to be addressed to avoid starved lubrication thus leading to significantly increased friction and/or wear. Lubricant migration due to centrifugal forces is particularly relevant in high-speed elements, which can be found for example in aircraft engines, whereas thermocapillary lubricant migration is especially relevant in highly loaded miniature ball bearings or spacecraft machinery where large temperature gradients prevail. In the first step, causes for lubricant migration and their effect on the frictional properties are investigated. Subsequently, suitable surface patterns placed **outside the contact zone** are designed to guide lubricants over surfaces or obstruct the lubricant migration. An overview of the conducted research, as well as the respective journal publications, is given in **Fig. 18**.

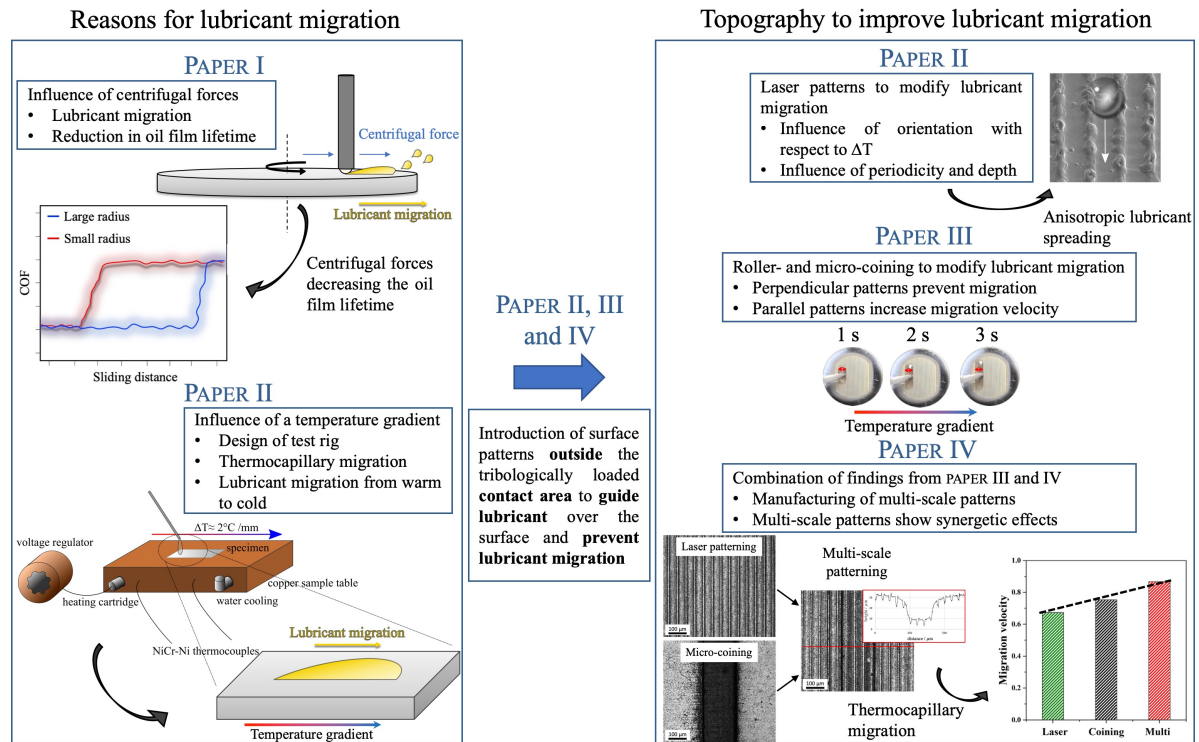


Figure 18: Overview of the respective papers regarding objective 1. Reasons for lubricant migration, the effects of lubricant migration on the tribological behavior, as well as topographical designs to modify it are investigated.

PAPER I deals with the influence of centrifugal forces on lubricant migration and friction of polished steel samples. Therefore, ball-on-disk experiments were performed in rotational sliding mode with different sliding radii under fully-flooded conditions (i.e., with an excess of oil). The rotation of the sample causes centrifugal forces to act on the oil driving it outwards. By keeping the linear velocity constant and decreasing the sliding radius, the angular velocity and thus the capillary forces increase. When normalizing the centrifugal forces to the mass of the oil, which is constant for both radii, the centrifugal forces are increased by a factor of roughly 4 for the smaller radius. The ball-on-disk experiments are accompanied by measurements of the solid-solid contact ratio with an electrical resistivity circuit, which allows for a systematic analysis of the dominant lubrication regime. Since the lubricant functions as an isolator, the electric current cannot flow when a lubricant film separates the surfaces. Upon contact of the surfaces, the electric current flows and an electric output signal can be measured. By relating the output signal with the input signal, the solid-solid contact ratio can be calculated, whereby the output signal is roughly zero for hydrodynamic lubrication and one for boundary lubrication. Hence, the breakdown of the oil film and the prevailing lubrication regime can be precisely determined.

When starting the tribological experiments, the COF is about 0.1 independent of the sliding radius, and the solid-solid contact ratio shows for both sliding radii that the tribological experiment is running under mixed lubrication, which is typical for many machine elements. Hence, the tribological proper-

ties at the beginning of the measurements are independent of the sliding radius and therefore the centrifugal forces, but rather depend on the experimental conditions, such as normal force and linear velocity. For a short time, irrespective of the sliding radius, the measurements are characterized by a stable and constant evolution of the COF. However, after a certain sliding distance, a pronounced increase in the COF can be observed, which can be traced back to a transition from mixed to boundary lubrication. This finding is confirmed by the measurements of the solid-solid contact ratio, which similarly show an increase to almost 100 % solid-solid contact ratio, representing boundary lubrication. This transition to boundary lubrication happens at smaller sliding distances for smaller sliding radii, which can be explained by a faster lubricant migration out of the contact, induced by centrifugal forces.

Additionally, the viscosity of the PAO oil is varied to further examine the effect of centrifugal forces on the lubricant migration. Therefore, oils with three different viscosities – PAO 8, 20 and 30 – were used. For the smaller viscosity of 8 cSt, all measurements result in an instantaneous increase of the COF and the solid-solid contact ratio and hence no significant differences between the sliding radii can be observed. However, when comparing the measurements with PAO 20 and 30, it can be seen that while the evolution of the COF is qualitatively similar, an increase in viscosity leads to a substantial increase in the sliding distance until the COF is significantly increased, called oil film lifetime. Thereby, the measurements with PAO 30 show an increase in oil film lifetime by a factor of roughly 20 for the smaller sliding radius, whereas the measurements with the larger sliding radius do not show a breakdown of the oil film at all over the sliding distance of 300 m. Two factors have to be taken into consideration when changing the oil viscosity. First, increasing the viscosity results in a greater oil film thickness in the tribological contact zone resulting in less asperity contact, which is also confirmed by the electrical resistivity measurement. Secondly, and more importantly, the viscous resistance force is proportional to the viscosity, resulting in higher friction and a less-pronounced influence of the centrifugal forces on the oil in the contact zone. Therefore, increasing the viscosity leads to reduced migration of oil out of the contact zone and thus favors an extended oil film lifetime. It is worth mentioning that the results of the COF measurements and the solid-solid contact ratio are in accordance with the wear measurements since the samples measured with greater sliding radii or higher lubricant viscosities show less pronounced wear marks.

PAPER II investigates the lubricant migration on steel surfaces induced by temperature gradients. Therefore, a special test-rig is designed, consisting of a copper table which is heated on one side by a heating cartridge and cooled on the other side by water cooling. The hotter regions simulate the tribological contact zone, which is heated by frictional heating, whereas the colder regions represent the cooler areas surrounding the tribological contact zone. The temperature gradient, which is measured by two thermocouples, accounts for roughly 2.0 °C/mm. At the beginning of the measurement, a droplet of PAO 4 oil having a viscosity of 3.9 cSt and a volume of 1.5 µl is applied onto the warmer side of the sample. As a result of Marangoni flow, the lubricant starts to migrate towards the colder regions of the sample, showing a preferential droplet spreading. This behavior is also confirmed in **PAPER III**.

As the droplet approaches the colder side of the sample, a decline in migration velocity is observed, which can be traced back to an increase in viscosity associated with the movement to cooler areas on the surface. Additionally, some of the oil is firmly adsorbed on the surface and does not migrate, leading to a depletion of the droplet volume as the droplet moves towards the cold side. The reduction of the droplet size results in pinning of the droplet front due to contact angle hysteresis.

After having identified possible causes for lubricant migration and the consequences, **PAPER II, III** and **IV** show the possibilities to improve lubricant migration by preventing lubricant migration or guide lubricant over the surface, with an emphasis on thermocapillary migration. Thereby, **PAPER II** investigates laser-patterned surface topographies, **PAPER III** roller- and micro-coined patterns, and **PAPER IV** bio-inspired multi-scale surfaces, which are manufactured by a combination of micro-coining and laser patterning.

The laser patterns fabricated by DLIP and DLW in **PAPER II** show a strong dependency on their orientation. Thereby, the velocity of lubricant migration changes significantly depending on the orientation of the patterns with respect to the temperature gradient. A parallel orientation of the surface patterns to the temperature gradient increases the migration velocity, while a perpendicular orientation hinders the migration. This can be traced back to lubricant spreading inside the channel-like surface topography due to capillary forces, pulling the droplet in a direction parallel to the patterns, as well as the channels acting as pinning sites for the droplet's contact line, thus obstructing movement perpendicular to the patterns. An analysis of the migration behavior concerning the structural parameters shows that the pinning effect of lubricant as well as the migration velocity is increased with decreasing periodicity of the patterns and increasing structural depth. Decreasing the periodicity and hence the distance between the topographical features results in a higher number of pinning sites, whereas increasing the structural depth leads to greater capillary forces. Additionally, the substantial decrease in lubricant migration velocity over time for the parallel orientation of the patterns can be well described by the Lucas-Washburn equation, which predicts a decrease proportional to $1/\sqrt{t}$ as a result of a greater viscous resistance force as a greater portion of the capillaries are wetted.

PAPER III demonstrates the capabilities of roller-coined single channels and micro-coined multi-channel samples to improve lubricant migration of a PAO 4 oil on steel surfaces. The measurements of the lubricant migration in single channels can further illuminate the effects of multi-channel samples since the lubricant is spreading faster inside the channel-like patterns pulling the droplet over the surface by creating free space inside channels during migration. The migration velocity of the lubricant inside the single channels, which are oriented parallel to the applied temperature gradient is significantly affected by their structural depth. Following the results presented in **PAPER II**, the migration velocity increases with the structural depth due to greater capillary forces. In addition, another effect has to be taken into consideration for coined patterns, since their volume to area ratio is higher than that of the laser patterns. Deeper channels with a larger volume to area ratio show less wall friction resulting in a smaller resistance to thermocapillary migration. Furthermore, a decrease in migration

velocity over time due to an increase in viscosity and wall friction (Lucas-Washburn) can be again observed. Regarding the lubricant migration of the multi-channel samples a strong dependency of the patterns with respect to the temperature gradient is demonstrated. If the patterns are oriented perpendicularly, the lubricant migration towards the cold side can be completely prevented as a result of pinning effects of the droplet's contact line. Compared to the laser patterns in **PAPER II**, the depth of the micro-coined patterns is increased by a factor between 5 (DLW) and 30 (DLIP), leading to much stronger pinning. Therefore, such deep patterns with sharp edges are a viable method to overcome the Marangoni forces induced by a temperature gradient and thus represent a viable method to obstruct lubricant migration out of the tribological contact. For the parallel orientation of the patterns with respect to the temperature gradient the migration velocity is substantially increased. Thereby, the structural depth of the micro-coined patterns only shows a minor influence, whereas a smaller periodicity and therefore a greater number of channels in contact with the lubricant leads to faster lubricant spreading. Summarizing, a perpendicular orientation of the patterns can prevent lubricant migration, while a parallel orientation of the patterns opens up the possibility of guiding lubricant over the surface.

The insights from **PAPER II** and **PAPER III** are combined in **PAPER IV** to create bio-inspired multi-scale patterns on steel surfaces. To fabricate such multi-scale surface patterns, micro-coining is combined with laser patterning. Particular emphasis is put on a precise fabrication and a homogenous distribution of the patterns on the surface. Therefore, micro-coining is the first step followed by a superposition of the micro-coined patterns with the laser patterns, which ensures the presence of the secondary laser pattern both in and between the micro-coined channels. Considering the inverted fabrication route, the laser patterns could be easily destroyed by a subsequent coining process due to the high coining pressures. The investigation of the migration behavior of lubricant droplets (PAO 4) on the laser-patterned (DLIP and DLW), micro-coined and multi-scale surfaces with and without temperature gradient demonstrates a preferential droplet migration parallel to the patterns. This behavior can be, in agreement with the findings from **PAPER II** and **PAPER III**, traced back to pinning effects perpendicular to the patterns and capillary forces along the channel-like patterns. The analysis of the lubricant migration with respect to the geometrical parameters of the patterns highlights the interplay between structural period and depth, whereby both greater depth and smaller periodicity lead to faster lubricant migration. The multi-scale samples show the highest migration velocity for the measurements with and without temperature gradient, which is a result of stronger pinning and stronger capillary forces due to the additional laser pattern, as well as a higher surface roughness for the multi-scale samples leading to a greater tendency to lubricant spreading. Therefore, multi-scale patterns show the most significant potential to guide lubricants over the surface.

The findings in *PAPER I* through *IV* demonstrate centrifugal forces and thermocapillary migration as causes for lubricant migration, which ultimately can result in a downgraded tribological behavior. Topographical surface patterns **outside the contact zone** fabricated from laser patterning, micro-coining and a combination of both creating multi-scale surfaces are a viable method to improve lubricant migration by either preventing it or guiding lubricant over the surface.

OBJECTIVES 2 AND 3

Chapter 2.2 of the state of the art section demonstrated that friction and wear can be effectively reduced by surface patterning **inside the contact zone**, which results in more efficient processes and longer lifetimes. In this context, especially multi-scale patterns seem to be suitable to improve the tribological behavior. In the first step, multi-scale patterns are topographically designed in laboratory experiments (objective 2). Effective patterns are then transferred to the shaft of a journal bearing and examined with respect to their frictional behavior in different lubrication regimes (objective 3). **Fig. 19** schematically addresses the method by which surface patterns are designed and transferred to the shaft of a journal bearing.

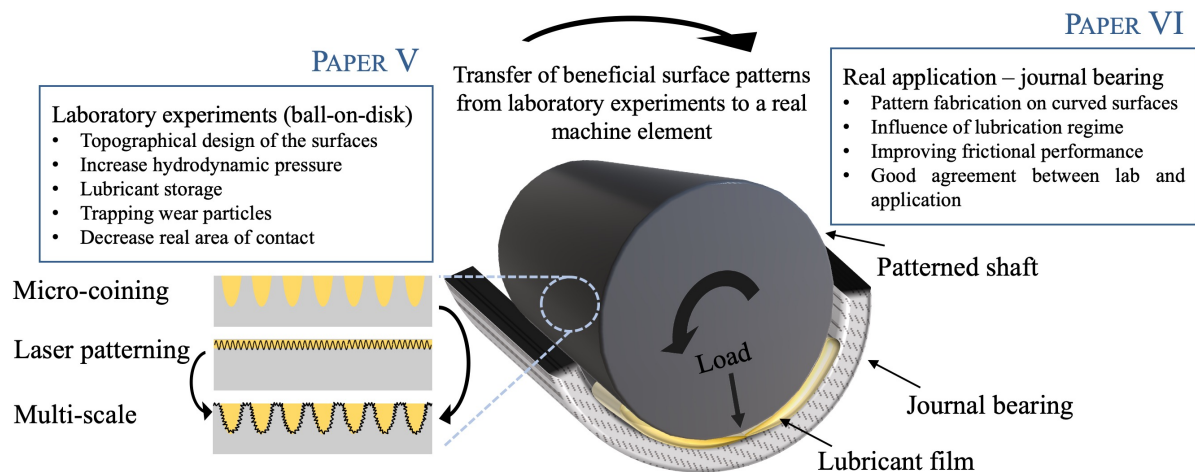


Figure 19: Overview of the respective papers regarding objective 2 and 3. First, multi-scale patterns are designed and tested for their tribological behavior. Effective patterns are then transferred to the shaft of a journal bearing, and the comparability with the preliminary results is demonstrated.

In *PAPER V*, suitable single-scale patterns fabricated by micro-coining or laser-patterning are selected and combined to create multi-scale surfaces inside the contact zone, aiming at improved friction and wear behavior of steel samples under lubricated conditions. The selection of the patterns is based upon experiments by Rosenkranz et al. who systematically investigated the tribological behavior of topographies fabricated by DLIP and micro-coining^[19,21]. Thereby, hemispherical micro-coined patterns could significantly reduce the COF under mixed elastohydrodynamic lubrication (EHL) and EHL, while the cross-like laser patterns increased the oil film lifetime (i.e., the time until the onset of severe wear) by a factor of 130 under mixed lubrication.

The multi-scale surface patterns can be precisely fabricated, whereby the hemispherical micro-coined dimples and the superimposed cross-like laser patterns are homogeneously distributed on the sample's surface. The smaller laser pattern is present inside the dimples as well as on the free spaces in between. Regarding their frictional performance, the multi-scale samples show an improved behavior with a reduced COF compared to the polished reference sample and the purely laser-patterned sample. This improvement can be traced back to the secondary lubrication effect, whereby especially the larger micro-coined dimples act as lubricant reservoirs. Furthermore, additional hydrodynamic pressure is created by both patterns. However, compared to purely micro-coined patterns, the multi-scale samples can either improve or downgrade the frictional performance depending on the depth of the primary micro-coined pattern. For lower coining depths, the multi-scale surface patterning approach results in higher COF values. This can be attributed to the greater surface roughness induced by the additional laser pattern, leading to higher contact pressures, undesired edge effects, and a reduced load carrying capacity. For deeper coining depths, which are more prone to cavitation, the additional laser pattern can reduce cavitation effects due to a better wetting and thus distribution of lubricant in the contact zone. Therefore, for the deeper micro-coined dimples superimposed with the laser pattern, the additional pressure build-up may be greater leading to an increased load carrying capacity, a larger local oil film thickness, and ultimately a reduced COF.

After having identified tribologically beneficial single-scale and multi-scale surface patterns as well as having understood the underlying mechanisms regarding the tribological properties of the surface patterns in **PAPER V**, these patterns are transferred onto the shafts of journal bearings made from steel in **PAPER VI**. To produce patterns precisely on shafts despite their curved surfaces, the fabrication techniques are modified. In this context, a rotation motor is incorporated into the experimental setup for DLIP described in chapter 2.1.1. Additionally, the larger hemispherical coined patterns are fabricated by roller-coining, which allows for the processing of curved parts. The roller-coining tool is equipped with a pneumatic system, which significantly increases the accuracy of the forming process by continuous control of the forming force and the tool-position, thus keeping the forming force and, as a result, the pocket depth constant. Both the single-scale and multi-scale patterns can be fabricated with high accuracy and reproducibility onto the shafts. Furthermore, the patterns resemble those used in the preliminary laboratory experiments ^[19,21,221] and therefore enable a direct comparison between laboratory experiments and the measurements of the bearings' shafts under more realistic conditions.

The frictional behavior under mixed and hydrodynamic lubrication of the single-scale and multi-scale patterned shafts in comparison to a non-patterned reference shaft is investigated on a special journal bearing test rig. The counter bodies are turned journal bearings made from CuSn12NiC-GCB. In accordance with the preliminary laboratory experiments, all patterned shafts show reduced COFs over the entire range of rotational speeds. Similar to the preliminary experiments with micro-coined samples, friction is reduced by a factor of 2 - 3 under mixed lubrication and up to a factor of 4.6 under hydrodynamic lubrication. Additionally, the transition from mixed to hydrodynamic lubrication is

shifted to smaller rotational speeds for the patterned shafts, increasing the range under which the journal bearings can operate with minimal friction and wear. These positive effects regarding the tribological behavior can be traced back to the build-up of an additional hydrodynamic pressure leading to a greater separation of the surfaces and an increased load carrying capacity. If there is contact between the rubbing surfaces' asperities (mixed lubrication), the patterns additionally act as reservoirs for lubricant and trap wear particles.

When comparing the frictional performance of the individual patterns, great similarities can be noted between the preliminary laboratory experiments and the tribological measurements of the patterned shafts, despite different contact conditions. Thereby, the coined patterns show a more significant improvement of the frictional behavior with smaller coined depth. Besides, the frictional performance of the multi-scale patterns likewise depends on the depth of the primary coined pattern. For shallower coined dimples the frictional performance of the multi-scale pattern is downgraded compared to the purely micro-coined shaft, whereas for deeper coined dimples the multi-scale patterning approach shows beneficial effects, leading to the greatest measured friction reduction by a factor of 4.6 compared to the reference shaft. In conclusion, the experimental trends obtained in the preliminary laboratory experiments can be verified in the journal bearing measurements. The obtained findings from **PAPER VI** underline the unique possibility to transfer tribological results of surface patterns in laboratory experiments to real machine elements. Therefore, surface patterns can be classified and selected in simplified laboratory experiments, such as ball-on-disk set-ups, which are far less time-consuming and complex. After classification, suitable and effective patterns can be transferred to the real machine element to improve its tribological properties.

*Paper V and Paper VI investigate the fabrication and the tribological mechanisms of **multi-scale** surfaces applied **inside the contact zone**. First, the patterns are tested in preliminary laboratory experiments to select suitable patterns and to investigate the underlying mechanisms of friction reduction. Subsequently, tribologically effective patterns are transferred to the curved surfaces of the shafts of **journal bearings**. The results show high comparability between preliminary laboratory experiments and the tested journal bearings with substantially reduced friction for the multi-scale patterns. This represents the unique possibility to **transfer the results** and insights from the laboratory into the application.*

PAPER VII, which is an invited review article, critically summarizes the state of the art of surface patterning in machine elements under different operating and contact conditions. Particular emphasis is put on piston rings, seals, roller bearings and gears, whereby piston rings and seals are sliding components (conformal contacts), and roller bearings and gears represent rolling components (non-conformal contacts). It is essential to make a distinction between these two contact conditions, as the effect of the patterns depends strongly on them. For all elements, optimal pattern designs are summarized,

and positive as well as negative effects of surface patterns in the respective machine element are presented.

Regarding conformal contacts, contact pressures are relatively low, which often leads to hydrodynamic lubrication with a full film separating the surfaces. Piston rings are especially sophisticated because the lubrication conditions and kinematics change during one cycle as a result of the reciprocating movement of the piston in the cylinder. Therefore, patterns should be tailored with respect to the position of the piston ring in the cylinder and hence to the lubrication conditions. At the reversal points, where speed is minimal, high area densities are beneficial, whereas at positions where full film lubrication prevails lower area densities are preferable. For seals, a compromise has to be found regarding the effect of surface patterns to reduce both friction and leakage. As optimal pattern geometries, an area density of 10 - 20 % and low aspect ratio in the range between 0.05 and 0.1 are identified. For both machine elements, laser surface patterning is most frequently used. In the case of non-conformal contact conditions, the applicability of surface patterns is limited primarily due to the high prevailing contact pressures. Furthermore, introducing surface patterns might be detrimental, as they can increase rolling contact fatigue in rolling elements. However, surface patterns, if designed correctly, might still improve the frictional performance of rolling machine elements as well as reduce rolling contact fatigue. In this context, closed patterns with smaller depths and diameters (i.e., lower micrometer range) as for sliding elements should be used. In gears, surface patterns should be applied to the face and flank region of the gear teeth, since the loads at these positions are lower than around the pitch point, leading to a greater lifetime of the patterns.

Finally, general design guidelines for surface patterning in machine elements are derived. These guidelines are essential as a starting point when designing surface patterns for machine elements since the patterns' effectiveness depends strongly on the contact conditions and lubrication regime. Therefore, the selection of beneficial patterns is difficult and must be done concerning the load and speed collective. This can be a particularly difficult task as machine elements often do not operate under constant tribological conditions but under different lubrication regimes with varying velocities, normal forces, lubricant supply conditions or slide-to-roll ratios. In this context, the transferability of results from laboratory to machine element, as demonstrated in **PAPER VI**, is advantageous since it is faster and easier to study the underlying effects in simplified laboratory experiments. In addition, the multi-scale patterning approach might be beneficial for applications with varying operating conditions since patterns on different scales are effective under different lubrication regimes, leading to an extension of the operating regime under which the surface patterns lead to improved frictional behavior.

4. INCLUDED PAPERS

4.0 Outline

THE INFLUENCE OF CENTRIFUGAL FORCES ON FRICTION AND WEAR IN ROTATIONAL SLIDING

I

Centrifugal forces are found to greatly influence the lubricant migration on mirror polished steel surfaces and thus the oil film stability and the lubrication regime under rotational sliding. By keeping the linear velocity constant and changing the sliding radius, the angular velocity can be manipulated resulting in greater centrifugal forces for smaller radii or greater angular velocities. It could be shown that the lubricant migration out of the contact zone is more severe for greater centrifugal forces leading to a faster transition from mixed to boundary lubrication and hence to a shorter oil film lifetime.

HOW TO GUIDE LUBRICANTS – TAILORED LASER SURFACE PATTERNS ON STAINLESS STEEL

II

Temperature gradients are identified to cause thermocapillary migration of an additive-free synthetic polyalphaolefin base oil on steel surfaces. Furthermore, the possibility to manipulate the lubricant migration behavior under a temperature gradient by applying channel-like laser surface patterns onto the surface by laser patterning is investigated. It is found that laser surface patterns can strongly influence the migration behavior, whereby the migration velocity is significantly affected by the topographical parameters, depth and periodicity, as well as the orientation of the patterns with respect to the temperature gradient.

GUIDING LUBRICANT ON STAINLESS STEEL SURFACES BY CHANNEL-LIKE STRUCTURES FABRICATED BY ROLLER- AND MICRO-COINING

III

The influence of geometrical parameters of roller- and micro-coined single channel and multi-channel samples on the resulting thermocapillary migration of an additive-free synthetic polyalphaolefin base oil is systematically analyzed. For single channels, a strong dependency between structural depth and migration velocity is observed. For multi-channel samples, a pronounced anisotropic spreading behavior is demonstrated. Thereby, thermocapillary migration can be prevented if the patterns are oriented perpendicular to the temperature gradient, whereas the migration velocity is enhanced if the patterns are oriented parallel with respect to the temperature gradient.

LUBRICANT MIGRATION ON STAINLESS STEEL INDUCED BY BIO-INSPIRED MULTI-SCALE SURFACE PATTERNS

IV

On the basis of the findings in **PAPER II and III**, multi-scale surface patterns are realized on steel by a combination of micro-coining and laser patterning. The lubricant spreading without an applied temperature gradient as well as the thermocapillary migration are investigated on the produced surface patterns. It is found that the combination of both patterns results in synergetic effects leading to a greater droplet distortion and faster migration velocity for the multi-scale surfaces, making them ideal to guide lubricant over surfaces.

EFFECTS OF MULTI-SCALE PATTERNING ON THE RUN-IN BEHAVIOR OF STEEL–ALUMINA PAIRINGS UNDER LUBRICATED CONDITIONS

V

Tribologically beneficial single-scale micro-coined and laser surface patterns are combined to realize multi-scale surface patterns on steel. Their tribological effectiveness is investigated in preliminary laboratory tests and compared to the single-scale patterns. It is found that the structural depth of the primary micro-coined pattern strongly affects the frictional behavior of the multi-scale samples. Multi-scale samples that contain dimples with a lower coining depth increase the COF, whereas for deeper coining depths, the multi-scale patterning approach results in stable and lower friction values.

FROM LAB TO APPLICATION - IMPROVED FRICTIONAL PERFORMANCE OF JOURNAL BEARINGS INDUCED BY SINGLE- AND MULTI-SCALE SURFACE PATTERNS

VI

On the basis of preliminary laboratory tests, especially from **PAPER V**, single-scale and multi-scale surface patterns, showing beneficial tribological effects are selected and transferred onto the shafts of journal bearings made of steel. The frictional performance under different lubrication regimes is evaluated on a special test rig for journal bearings by varying the rotational speed. It is found that all patterns can significantly reduce the COF as well as shift the transition from mixed to hydrodynamic lubrication to smaller rotational speeds compared to the non-patterned reference sample. The observed effects are in good agreement with the preliminary laboratory tests.

SURFACE TEXTURING IN MACHINE ELEMENTS - A CRITICAL DISCUSSION FOR ROLLING AND SLIDING CONTACTS

VII

The comprehensive review shows the possibility to introduce surface patterning to different machine elements, with a special emphasis on piston rings, seals, roller bearings and gears. The effect of surface patterns under different lubrication conditions is examined, positive and negative aspects of surface patterning are illuminated, and different manufacturing techniques are introduced. Based upon the main evidence from the literature, general design guidelines for surface texturing in machine elements are discussed.

I The influence of centrifugal forces on friction and wear in rotational sliding

Philipp G. Grützmacher¹, Andreas Rosenkranz², Sebastian Rammacher¹, Carsten Gachot³, Frank Mücklich¹

¹ Chair of Functional Materials, Saarland University, 66123 Saarbrücken, Germany

² Department of Mechanical and Aerospace Engineering, Center for Magnetic Memory and Recording, University of California, 92093, La Jolla, United States

³ Institute for Engineering Design and Technical Logistics, Tribology Division, Vienna University of Technology, 1060, Vienna, Austria

Published in “*Tribology International*” (Impact factor (2017): 3.246)

Accessible online at: <http://dx.doi.org/10.1016/j.triboint.2017.07.021>

Own contribution:

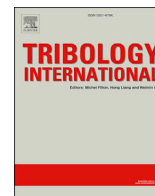
Project management; scientific discussion; paper writing; data analysis; measurements: laser scanning microscopy, tribological testing

Abstract:

To investigate the influence of centrifugal forces on the oil film stability and the lubrication regime, mirror polished steel surfaces (AISI 304) were tested using a ball-on-disc tribometer in rotational sliding mode with a steel counter body (AISI 52100). Different sliding radii (1.5 and 6 mm) were used to vary the angular velocity. The tests were conducted under fully-flooded conditions using Poly-alpha-olefin oils. The measured coefficients of friction were complemented by the measurement of solid-solid contact ratios and the analysis of the respective wear tracks. It could be shown that the centrifugal forces have a great influence on the oil film lifetime. Thereby, the oil film lifetime is longer for larger sliding radii and higher viscosities.

Cite this as:

P.G. Grützmacher, A. Rosenkranz, S. Rammacher, C. Gachot, F. Mücklich, The influence of centrifugal forces on friction and wear in rotational sliding, *Tribol. Int.* **2017**, 116, 256–263. (<https://doi:10.1016/j.triboint.2017.07.021>)



The influence of centrifugal forces on friction and wear in rotational sliding



Philipp G. Grützmacher^{a,*}, Andreas Rosenkranz^b, Sebastian Rammacher^a, Carsten Gachot^c, Frank Mücklich^a

^a Department of Functional Materials, Saarland University, 66123, Saarbrücken, Germany

^b Department of Mechanical and Aerospace Engineering, Center for Magnetic Memory and Recording, University of California, 92093, La Jolla, United States

^c Institute for Engineering Design and Technical Logistics, Tribology Division, Vienna University of Technology, 1060, Vienna, Austria

ARTICLE INFO

Keywords:

Lubrication regimes
Centrifugal force
Coefficient of friction
Solid-solid contact ratio

ABSTRACT

To investigate the influence of centrifugal forces on the oil film stability and the lubrication regime, mirror polished steel surfaces (AISI 304) were tested using a ball-on-disc tribometer in rotational sliding mode with a steel counter body (AISI 52100). Different sliding radii (1.5 and 6 mm) were used to vary the angular velocity. The tests were conducted under fully-flooded conditions using Poly-alpha-olefin oils. The measured coefficients of friction were complemented by the measurement of solid-solid contact ratios and the analysis of the respective wear tracks. It could be shown that the centrifugal forces have a great influence on the oil film lifetime. Thereby, the oil film lifetime is longer for larger sliding radii and higher viscosities.

1. Introduction

Friction, wear and lubrication play a significant role in lots of daily applications such as cars or engines as well as manufacturing processes. In some applications like brakes or clutches, friction is highly welcome since the involved energy dissipation mechanisms can be used to tremendously decelerate movements. In contrast to that, a lot of researchers around the globe try to reduce friction and wear because these processes significantly downgrade the energy efficiency of plenty of applications and processes [1–5]. There are several techniques and possibilities available in order to improve the tribological properties of bodies in relative motion. Probably, the easiest way to efficiently reduce friction and wear is the use of a lubricant. Depending on the relative velocity and the applied load, lubrication makes the separation of both rubbing surfaces from each other possible which results in a significant reduction in friction and wear. In this context, the correct choice of the lubricant and the lubricant's properties is of utmost importance. Together with the kinematics and loading conditions, the lubricant's properties and the surface conditions (surface roughness and surface chemistry) define the acting lubrication regime [6]. Considering the ratio of the oil film thickness to the combined surface roughness of both rubbing surfaces (λ -parameter) as well as the well-known Stribeck-curve, it is in theory rather straight forward to distinguish between different lubrication regimes. For small λ values ($\lambda < 1$), the oil film is not very effective and almost the complete normal load will be supported by the surface

asperities [7]. The respective lubrication regime can be assigned to boundary lubrication. For intermediate values ($1 < \lambda < 3$), the load is partly carried by the surface asperities and the oil film. This regime is called mixed lubrication [8,9]. For λ values larger than 3, the oil film is much thicker than the combined surface roughness. Consequently, it is possible to form a thick oil film that completely separates both rubbing surfaces from each other which represents the regime of hydrodynamic (full film) lubrication. The transition from mixed to hydrodynamic lubrication is rather smooth and typically associated with elastohydrodynamic lubrication (EHL) [10]. In this lubrication regime, the elastic properties of the substrate and the counter body as well as a pronounced viscosity increase due to high contact pressures become important [10]. Since the surface roughness is sometimes determined by the manufacturing or finishing process of the involved surfaces, it can be clearly seen that the amount of oil in the tribological contact or the oil film thickness is highly important. In case of an insufficient oil film thickness or oil supply, changes in the lubrication regime can be induced thus leading to downgraded tribological properties or performance.

For polished reference samples there are changes in the lubrication regime from mixed to dry friction during tribological testing possible as could be shown in Ref. [11]. The transition from mixed to boundary lubrication or even solid-state friction could be attributed to a collapse of the oil film which is accompanied with a higher coefficient of friction (COF). This collapse can be explained with the wearing off of surface asperities which could act as a secondary oil source by storing a small

* Corresponding author.

E-mail address: philipp.gruetzmacher@uni-saarland.de (P.G. Grützmacher).

amount of lubricant. Once the surface asperities are worn off, this effect is lost. Furthermore, wear particles can be formed which account for another increase of the friction forces.

The amount of oil which is available in the contact zone is not only dependent on the surface itself but also on the motion and the velocity of the surfaces. The different velocities become important for instance during start-stop cycles in machine components. Therefore, Greiner et al. investigated the effect of velocity gradients on the tribological behavior by performing experiments with dimpled brass surfaces for two different sliding radii while keeping the average sliding velocity constant [12]. The authors could verify that larger velocities favor smaller dimples and vice versa. But not only velocity gradients are decisive when measuring with different sliding radii. Also, the effects coming from centrifugal forces on the oil have to be taken into consideration. Therefore, in this work the effect of a variation in the centrifugal forces on the friction and wear behavior under mixed lubrication is investigated. Plain steel (AISI 304) specimens are tested using a ball-on-disc tribometer in rotational sliding mode. Thereby, the ball is guided over the surfaces in a circular motion with two different radii. The sliding velocity for both radii is kept constant. Additive-free Poly-alpha-olefin (PAO) oils with different viscosities (8, 20 and 30 cSt at 100 °C) is used as lubricant to further examine the effect of the centrifugal forces. An electrical resistivity circuit was used to measure the contact ratio and to define the oil film lifetime for different sliding radii and oil viscosities. The oil film lifetime is defined as the cycle number after which the COF shows a significant increase.

2. Experimental procedure

2.1. Tribological characterization

The tribological tests were conducted on a ball-on-disc tribometer (CSM) in rotational sliding mode. As disc material, stainless steel (AISI 304) with a mirror-polished surface ($R_q \approx 20$ nm) was used, while the balls with a diameter of 6 mm which serve as the tribological counter body are made of 100Cr6 bearing steel (AISI 52100) ($R_q \approx 51$ nm). During the experiments, the normal load (applied by dead weights) was kept constant at 1 N. In order to investigate the effect of the sliding radius, the radius of the ball on the steel disc was varied between 1.5 and 6 mm. The experiments were performed under fully-flooded conditions with 7 ml Poly-alpha-olefin oil. Oils with three different viscosities – PAO 8, 20 and 30 (provided by Castrol) – were used as lubricant allowing for the analysis of the mutual influence of the lubricant viscosity and the sliding radius on the resulting frictional performance. Furthermore, comparability was ensured by a constant sliding speed of 80 mm/s. To guarantee a constant temperature of 25 ± 1 °C and a relative humidity of $45 \pm 1\%$ for all experiments, the tribometer is embedded in a climatic chamber. The stop condition was set at a sliding distance of 300 m to ensure that even late changes in lubrication regime can be detected. For each pair of sliding radius and lubricant the respective test was repeated two times. A summary of all experimental conditions is given in Table 1.

Table 1
Summarized testing parameters used for the tribological experiments.

Testing parameter	Value
Ball diameter (mm)	6
Normal load (N)	1
Sliding radius (mm)	1.5 and 6
Linear velocity (mm/s)	80
Kinematic viscosity of PAO at 100 °C (cSt)	8, 20 and 30
Lubricant volume (ml)	7
Lubricant density (g/cm ³)	0.831 (PAO 8), 0.843 (PAO 20), 0.850 (PAO 30)
Temperature (°C)	25 ± 1
Relative humidity (%)	45 ± 1

2.2. Topographical analysis

Prior to and after the tribological experiments, the surfaces were analyzed by Laser Scanning Microscopy (LSM: LEXT OLS 4100, Olympus).

2.3. Measurement of the solid-solid contact ratio

The solid-solid contact ratios were determined during the experiments to be able to precisely define the breakdown of the oil film and the acting lubrication regime. Those contact ratios were measured using an experimental setup by Rosenkranz et al. [13]. According to [13], the electric conductivity of the lubricant PAO 40 is negligible (measured value $\sigma_{\text{PAO40}} = 2.3 \times 10^{-13} (\Omega\text{m})^{-1}$). The isolating properties of the lubricant are essential to prevent the flow of electric current when a sufficient oil film separates the friction partners. Using a ball-on-disc setup combined with the electrical test rig (see Fig. 1), the solid-solid contact ratios during the tribological experiments were measured for different sliding radii ranging from 1.5 to 6 mm. By applying an alternating voltage V_0 (rectangular) with amplitude of 5 V, the voltage V_{meas} between the ball and the specimen can be measured using a sliding contact. The mentioned solid-solid contact ratio $r_{\text{solid-solid}}$, as an indicator for the different lubrication regimes, can be directly calculated from the measured voltage-time-signals as

$$r_{\text{solid-solid}} = \frac{I_{\text{Output}}}{I_{\text{Input}}} = \frac{\int_{t_0}^t |V_{\text{meas}}| dt}{\int_{t_0}^t |V_0| dt}, \quad (1)$$

where I_{Output} is the output signal and the I_{Input} input signal. Caused by the isolating properties of the lubricant, V_{meas} will approach approximately zero when an oil film completely separates the disc and the ball. When there is no oil film separating the friction partners (boundary lubrication) there will be metallic contact resulting in an electrical signal. In this case the measured voltage V_{meas} will be equal to the input voltage V_0 . Summarized the solid-solid contact ratio $r_{\text{solid-solid}}$ will be roughly zero for hydrodynamic lubrication and roughly one for boundary lubrication. The measuring time for one voltage-time-signal was set at 10 ms while the stop condition is at 30 m sliding distance. The solid-solid contact ratios were calculated 10 times (equidistant time step) for both sliding radii to study the temporal evolution of the ratio during the experiments.

3. Results and discussion

3.1. The effect of different sliding radii on friction

In order to determine the influence of the sliding radius on the resulting frictional performance, tribological experiments were performed with two different sliding radii of 1.5 and 6 mm and three viscosities (8, 20 and 30 cSt at 100 °C) while keeping the relative velocity between the friction partners (linear velocity) constant. Fig. 2 depicts the temporal evolution of the COF for all sliding radii and viscosities tested.

For the lowest oil viscosity (Fig. 2 a), both frictional curves start at

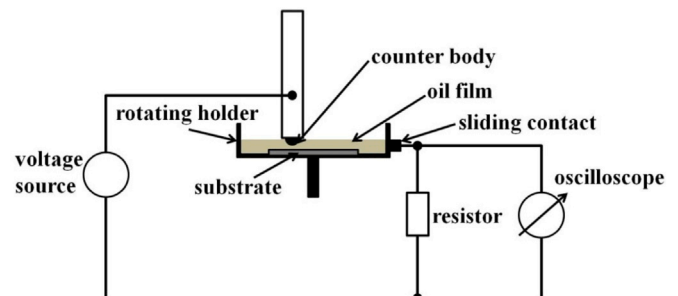


Fig. 1. Setup of electrical circuit combined with a ball-on-disc tribometer to measure the solid-solid contact ratio, modified according to [13].

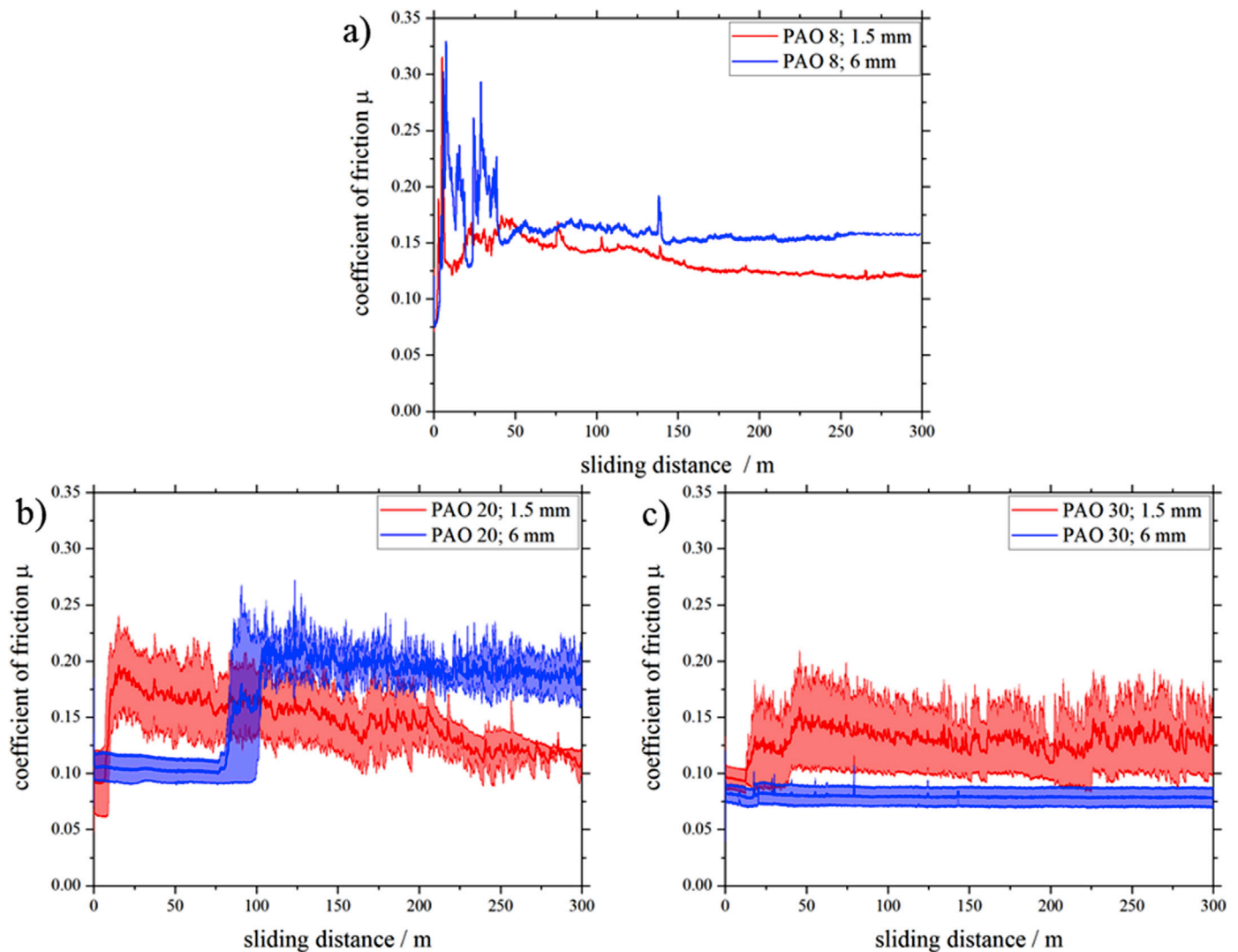


Fig. 2. Temporal evolution of the COF over 300 m sliding distance for three different viscosities of Poly-alpha-olefin oil (a) PAO 8, b) PAO 20, c) PAO 30) and two different sliding radii of 1.5 and 6 mm.

around $\mu = 0.075$. Irrespective of the sliding radius, the μ curves are characterized by a sharp, instantaneous increase in the COF up to values of roughly 0.35 after a sliding distance of 5 m. This implies that no stable oil film can be formed and pronounced solid-solid contact happens after short sliding distances thus leading to more severe tribological conditions. As can be seen from Table 2 which shows the estimation of the minimum oil film thickness as a function of the oil viscosities based upon to the Dowson-Hamrock approach for point contacts, the estimated oil film thickness of 16.85 nm (PAO 8) is smaller than the surface roughness ($R_q \approx 20$ nm) of the specimen [14–16]. Therefore, no stable oil film can be established and mixed EHL is prevailing from the start of the experiment. In the following 30 m sliding distance, the frictional curves show some fluctuations (more pronounced for a sliding radius of 6 mm) being typical for tribological contacts with high contact ratios due to the

presence of wear particles and the interaction of contacting asperities [17–22]. The formation of those particles and the interaction of them with the rubbing surfaces can result in rather high friction peaks [17,18]. In an earlier study by Rosenkranz et al. which investigated the formation of wear particles by collecting and analyzing them after the experiment, particle sizes up to 11.5 μm could be detected [11]. The existence of those particles combined with the small oil film thickness makes it likely that those particles are responsible for the strong fluctuation of the COF. After a certain sliding distance (here roughly 50 m), equilibrium-like conditions (including the processes of formation, agglomeration, break down and re-agglomeration of particles as well as the flattening of the contacting asperities) can be found which results in a more stable evolution of the COF [17,18]. Consequently, the COF reaches stable values of around 0.125 and 0.15 for sliding radii of 1.5 and 6 mm, respectively. Finally, it can be concluded that no significant influence of the sliding radius on the resulting frictional response was found for the lowest oil viscosity. It is worth to mention that the experiments were repeated three times. All experiments showed the same experimental trend. Due to the instantaneous increase and the fluctuating behavior of the COF, no mean values and error bars are depicted in order to improve the visibility of the presented data.

In contrast to that, the frictional curves recorded for oil with a viscosity of 20 cSt (Fig. 2 b) show a completely different behavior and

Table 2
 Calculated minimum oil film thickness for the different oil viscosities according to the Dowson-Hamrock equation for point-contacts [14–16].

Used lubricant	h_{min} (nm)
PAO 8	16.85
PAO 20	41.82
PAO 30	58.67

evolution of the COF over time. Taking the standard deviation into consideration, both curves start at roughly the same COF of around 0.09 irrespective of the sliding radius. For a short period of time the COF remains constant and stable which can be related to a thicker oil film (41.82 nm) and therefore no asperity contact or formation of wear particles as could be seen in the experiments performed with PAO 8 (see Table 2). Then, the COF shows a pronounced increase. For a sliding radius of 1.5 mm, this transition takes place at roughly 10 m sliding distance, while the COF measured for a sliding radius of 6 mm remains much longer constant and shows a significant increase at about 85 m. The observed transition from a low and stable to a high COF can be well correlated to a break-down of the oil film and the formation of wear particles due to increasing contact between the rubbing surfaces [23]. The subsequent fluctuations observed in the COF can be traced back to the interaction of wear particles with the contacting surfaces and contacting asperities. The decrease of the COF afterwards can be again associated with the formation of equilibrium-like conditions regarding the formation and break down of wear particles (including agglomeration and re-agglomeration) and a smoothing of the contacting surfaces. Furthermore, wear particles are carried out of the contact zone due to the centrifugal forces acting on the oil which can result in a reduced COF. As can be seen in this figure, the transition is delayed by a factor of 8 for tribological experiments with larger sliding radii of 6 mm implying a strong influence of the tribological testing conditions, especially the sliding radius and the oil viscosity. For the smaller sliding radius, the angular velocity ω is increased from approximately 13 to 53 s⁻¹. Assuming that the oil mass can be considered as constant, this leads to an increase of the centrifugal forces by a factor of 4. The centrifugal force F_c can be determined by the angular velocity ω , the mean molecule mass m of the oil and the sliding radius r [24]:

$$F_c = \omega^2 \cdot r \cdot m. \quad (2)$$

The centrifugal force which is normalized with respect to the mass of the oil is summarized in Table 3 for each radius and angular velocity. The centrifugal forces cause an oil transfer out of the contact zone. This leads to a depletion of lubricant in the contact zone and therefore to an oil film breakdown. Consequently, an earlier oil film breakdown is induced by higher centrifugal forces for a sliding radius of 1.5 mm.

For the highest oil viscosity, the frictional curves show a rather similar behavior. Both curves start at roughly the same value of 0.09 and show initially stable friction values. The similar behavior compared to the experiments performed with PAO 20 can be ascribed to similar estimated oil film thicknesses which exceed the surface roughness of the specimen in both cases (see Table 2). After the initial low and stable friction values, the COF measured for a sliding radius of 1.5 mm shows a pronounced increase after a sliding distance of 15 m while the COF measured for 6 mm remains rather constant over the entire sliding time. This demonstrates a shift in the oil film breakdown towards greater sliding distances compared to the measurements performed with lower viscosity oils. Due to the higher viscosity of PAO 30 the centrifugal forces have a less-pronounced influence on the oil in the contact zone which leads to a reduced oil transfer. Finally, this favors an enlarged oil film lifetime. In comparable spin coating processes the spin-off rate q , representing a volume loss per unit time and unit circumference at a specific sliding radius r , is proportional to the square of the angular velocity ω and inversely proportional to the dynamic oil viscosity η . Furthermore, q is a

function of the density of the oil ρ and the fluid level in the containment h [25]:

$$q = \frac{\rho \cdot \omega^2 \cdot r}{3 \cdot \eta} h^3. \quad (3)$$

As Eq. (3) shows, for equal radii and therefore equal angular velocities, the spin-off rate mainly depends on the viscosity since the initial fluid level in the containment can be assumed to be the same for identical oil volumes and the differences in oil density are negligible. This leads to a decreased lubricant loss in the tribological contact zone for higher viscosities and thus a less-pronounced influence of the centrifugal forces for equal angular velocities. The lubricants used in this study were only not-additivated, synthetic polyalphaolefins which are by nature characterized by mostly saturated bonds and lower surface energies as other lubricants. Furthermore, the difference in viscosity between the PAOs is just based upon longer and/or more branched hydrocarbons and the position at which the next branch is located within the chain. Therefore, we believe an effect of varying adhesive properties on retaining the lubricant in the contact can be neglected.

Summarizing, it can be stated that there is a clear correlation between the sliding radius and the frictional behavior of the tested samples. For experiments with PAO 20 or 30, the oil film lifetime increases with an increasing sliding radius due to smaller centrifugal forces acting on the oil. Additionally, the influence of the centrifugal forces on the oil film lifetime is noticeable when performing tests with varying viscosity since a higher viscosity results in a less pronounced influence of the centrifugal forces and therefore a longer oil film lifetime. It is worth mentioning that the COF is nearly the same at the beginning of each experiment irrespective of the viscosity used which ensures similar initial frictional testing conditions.

The observed differences in frictional behavior regarding the two sliding radii can be further investigated using an advanced electrical resistivity circuit which allows for the measurement of the solid-solid contact ratio. Fig. 3 exemplarily correlates the observed frictional curves (measured for sliding radii of 1.5 and 6 mm as well as PAO 20) with the measurement of the electrical test-rig depicted at selected points along the frictional curve.

For both sliding radii, the first measuring point is located in the region in which the COF is stable and low. The electrical output signal reveals strong fluctuations being an indicator for mixed lubrication [13]. Afterwards, the electrical signals of two additional points, one in the sharp increase and another one after the increase, are displayed. Irrespective of the used sliding radii, it can be seen that the increase in the COF goes hand in hand with a significant change in the electrical output signal. For the measuring point located in the sharp increase, some less-pronounced fluctuations (especially for a sliding radius of 1.5 mm) and little differences between the electrical input and output signal can be noticed. For the third measuring point, the electrical input and output signal are basically identical. The observed behavior can be explained with a transition from mixed lubrication to almost dry conditions going hand in hand with a significant increase in the solid-solid contact ratio.

Table 4 summarizes the mean values as well as standard deviations of the measured solid-solid contact ratios after a respective sliding distance as function of the oil viscosity and sliding radius. For PAO8, it is noticeable that the solid-solid contact ratios start well above 80 (1.5 mm) and 90% (6 mm), respectively. Afterwards, the contact ratio slightly increases for a sliding radius of 1.5 mm while, for 6 mm, it remains more or less constant having a high level. The high values of the contact ratios correlate well with the instantaneous increase of the COF observed in Fig. 2 a. Due to the low oil viscosity and the acting centrifugal forces, no stable oil film can be established. In the case of PAO20, the initial values of the solid-solid contact ratio are lower for both sliding radii (compared to PAO 8) thus implying a slightly increased initial oil film thickness. Over the course of the experiment mean contact ratios of about 99% are

Table 3

Resulting angular velocity and centrifugal force normalized with respect to the mass of the oil for the sliding radii 1.5 and 6 mm.

sliding radius (mm)	angular velocity (s ⁻¹)	normalized centrifugal force ($\frac{m}{s^2}$)
1.5	53.33	4.27
6	13.33	1.07

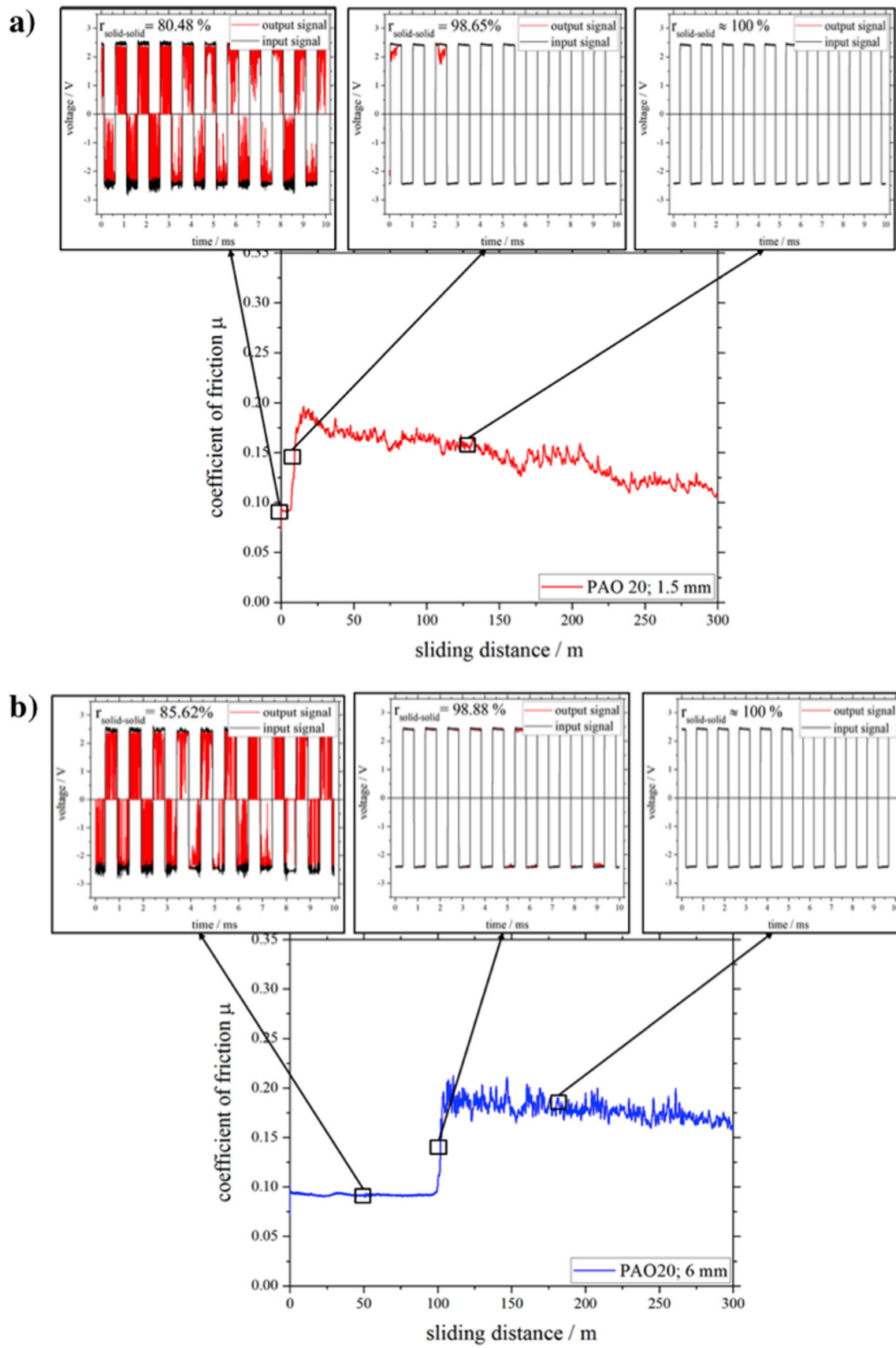


Fig. 3. Temporal evolution of the COF for PAO 20 and a sliding radius of 1.5 mm (a) and 6 mm (b). The frictional behavior is correlated with the measurement of the solid-solid contact ratio at selected sliding distances.

Table 4
Summary of the measured solid-solid contact ratios for PAO 8, 20 and 30 as well as the two sliding radii of 1.5 and 6 mm.

Sliding distance (m)	PAO8		PAO20		PAO30	
	Sliding radius (mm)					
	1.5	6	1.5	6	1.5	6
1	82.0 ± 2.3	92.2 ± 7.8	70.2 ± 14.0	58.4 ± 13.1	16.0 ± 2.8	41.1 ± 38.4
5	73.2 ± 0.9	89.0 ± 11.0	93.2 ± 6.8	80.6 ± 0.5	74.8 ± 10.6	50.8 ± 14.8
20	78.0 ± 12.0	93.0 ± 5.6	97.2 ± 1.9	86.3 ± 1.3	81.7 ± 2.8	56.9 ± 19.2
50	74.9 ± 19.8	75.7 ± 17.9	98.5 ± 1.6	86.7 ± 1.7	79.0 ± 1.0	53.6 ± 4.0
100	93.2 ± 0.1	84.1 ± 15.9	99.7 ± 0.3	99.6 ± 0.5	99.9 ± 0.1	44.3 ± 17.7
200	61.5 ± 3.5	78.8 ± 17.5	99.7 ± 0.2	99.8 ± 0.2	97.1 ± 2.9	53.0 ± 22.1
300	70.8 ± 12.6	85.3 ± 11.4	99.1 ± 0.9	100.0 ± 0.1	100.0 ± 0.0	46.1 ± 29.0

reached for both radii. It is worth to mention that for a sliding radius of 6 mm those values are detected for significantly higher sliding distances which correlates well with the delayed oil film breakdown for this sliding radius (Fig. 2 b). Consequently, the influence of the centrifugal forces can be also seen in the measured solid-solid contact ratios. Similar to the presented temporal evolution of the COF in Fig. 2 c for the highest tested oil viscosity (PAO 30), the solid-solid contact ratios also show distinct differences depending on the sliding radius. While the contact ratios steadily increase and finally reach roughly 100% for a sliding radius of 1.5 mm, the values for a sliding radius of 6 mm remain significantly lower with mean values around 50%. This observation correlates quite well with the observed frictional behavior since no oil film breakdown could be detected for a sliding radius of 6 mm. Finally, it can be concluded that the measurements of the solid-solid contact ratio confirm the frictional results and show the influence of the centrifugal forces on the frictional behavior.

Fig. 4 and Table 5 summarize the measured maximum oil film lifetime for all viscosities and sliding radii. As already discussed, no significant differences in the maximum oil film lifetime can be seen for the lowest oil viscosity. However, for an oil viscosity of 20 and 30 cSt, this situation changes significantly. The breakdown of the oil film is significantly delayed for experiments performed with a larger sliding radius. In the case of PAO 30 and a sliding radius of 6 mm, no breakdown of the oil film or a transition in the lubrication regime can be observed.

In addition to that, the wear behavior of the samples was investigated for all samples after the tribological tests.

The observed wear behavior for all samples correlates well with the temporal evolution of the COF and the measurements of the solid-solid contact ratio. For the samples with a lower oil viscosity (PAO 8 and 20), an oil film breakdown and a transition from mixed to almost dry was observed during the measurements. The observed wear behavior fits well into that picture since pronounced wear marks can be seen after the

Table 5
Sliding distances at which oil film breakdown occurred for PAO 8, 20 and 30 as well as the two sliding radii 1.5 and 6 mm.

	PAO 8		PAO 20		PAO 30	
	1.5 mm	6 mm	1.5 mm	6 mm	1.5 mm	6 mm
breakdown at	1.75 m	5.50	2.75	89.50	50.00	–

entire sliding distance of 300 m (Fig. 5 a–e). For PAO 30 the situation changes. The sample measured with a sliding radius of 1.5 mm also shows pronounced wear marks whereas the sample measured with a sliding radius of 6 mm barely shows any wear (Fig. 5 e and f). This goes hand in hand with the measurements of the solid-solid contact ratio and the temporal evolution of the COF since no breakdown in the oil film could be detected for the sliding radius of 6 mm but for the sliding radius of 1.5 mm at the end of the experiment, after 300 m sliding distance. The presence of tiny wear marks for said sample (PAO 30, 6 mm sliding radius) also demonstrates the initial state of mixed lubrication.

To further investigate the different wear behavior for varying sliding radii the tribological experiments with PAO 20 were stopped after a sliding distance of 50 m. As can be seen in the LSM images in Fig. 5 g and h, the sample which was measured with a sliding radius of 1.5 mm shows a pronounced wear track whereas the sample with a sliding radius of 6 mm only reveals tiny wear marks. Those differences in wear behavior prove again the influence of the centrifugal forces on the oil film lifetime. In this regard, also these experiments support the fact that higher centrifugal forces result in an earlier oil film breakdown.

4. Conclusions

The aim of this experimental study was to investigate the influence of the centrifugal forces on friction and wear of polished stainless steel samples (AISI 304). Therefore, tribological experiments were performed with two different sliding radii of 1.5 and 6 mm leading to a difference in centrifugal forces by a factor of 4 assuming constant viscosity. Additionally, the viscosity of the used oils was varied (PAO 8, 20, 30) since the spin-off rate has a threefold dependency on the viscosity. The following conclusions could be obtained:

- The sliding distance until oil film breakdown strongly depends on the sliding radius and accordingly on the angular velocity. Thereby, greater sliding radii favor a longer oil film lifetime, which can be explained with decreasing centrifugal forces for greater sliding radii.
- The oil film lifetime highly depends on the used oil viscosity. A higher oil viscosity results in longer oil film lifetimes since the influence of the centrifugal forces on the oil in the contact zone decreases for higher viscosities.
- The results of the COF could be confirmed by measurements of the solid-solid contact ratio which also demonstrate a remarkable increase of solid-solid contact at shorter sliding distances for smaller radii and lower oil viscosities.

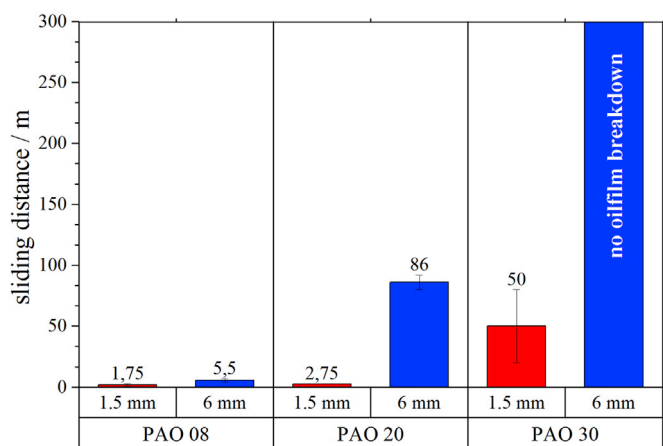


Fig. 4. Summary of the sliding distance at oil film breakdown for different viscosities and sliding radii.

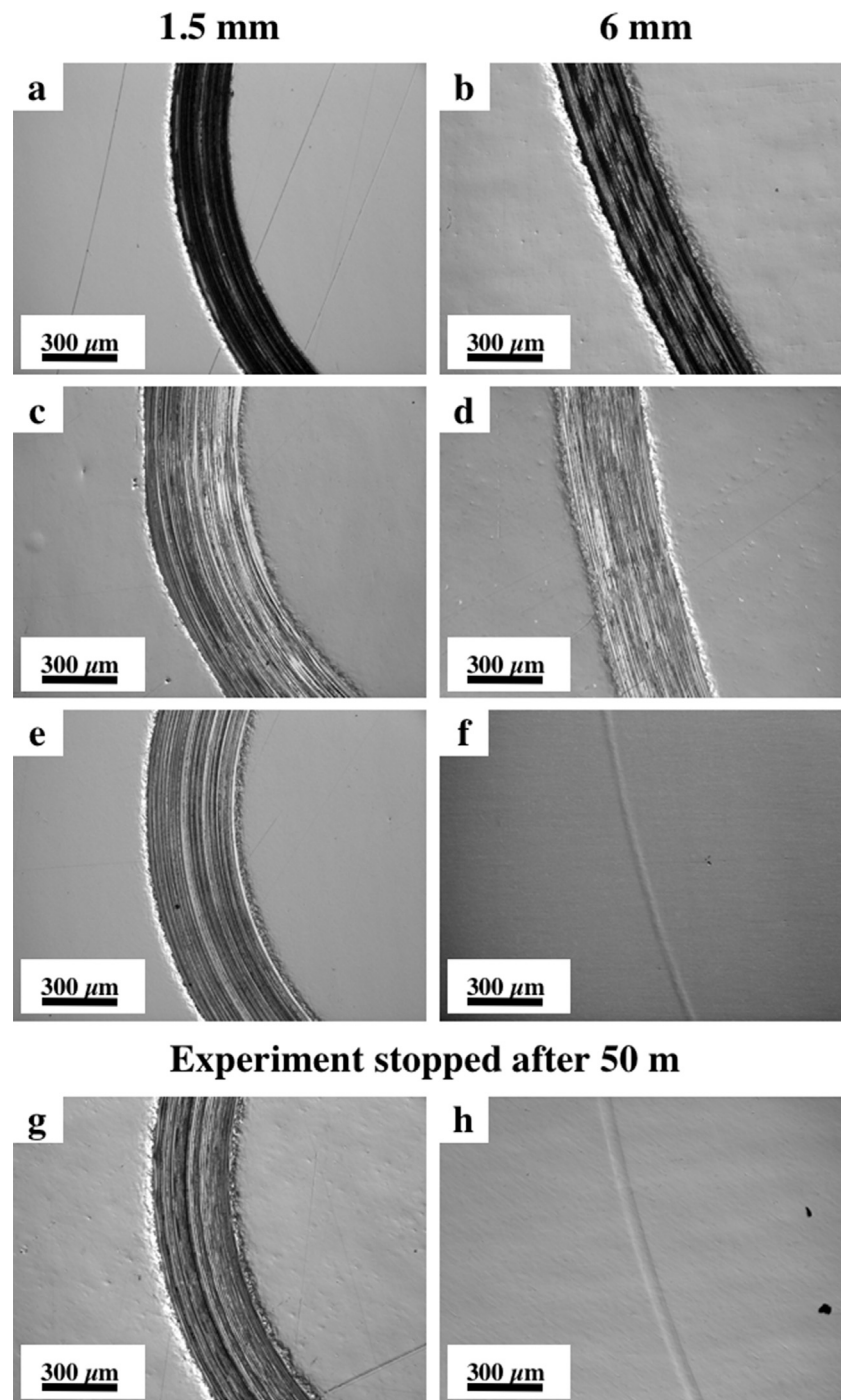


Fig. 5. LSM images of the wear behavior of all samples after 300 m sliding distance with PAO 8 (a) and (b) PAO 20 (c) and (d) and PAO 30 (e) and (f) as lubricant. Additionally, the wear behavior for the sample measured with PAO 20 is shown after 50 m sliding distance for 1.5 and 6 mm sliding radius, respectively.

- The investigation of the wear behavior also affirms these results since the samples tested with higher oil viscosities or greater sliding radii show less pronounced wear marks.
- Based on the Dowson-Hamrock approach for point contacts the minimum film thickness was estimated. For the lowest oil viscosity (PAO 8), the small minimum oil film thickness does not allow to establish a stable oil film since the minimum oil film thickness is smaller than the surface roughness. Therefore, no differences for varying sliding radii can be seen. However, for the oils with a larger oil viscosity (PAO 20 and 30), the estimated oil film thickness is comparable and greater than the surface roughness of the specimens.

Finally, this leads to a detectable difference in oil film lifetime in dependence on the radius as well as the oil viscosity.

Acknowledgements

The present work is supported by funding from the Deutsche Forschungsgemeinschaft (DFG, projects: MU 959/27-2 and HI 790/33-2 within the SPP 1551). A.R. gratefully acknowledges the Alexander von Humboldt Foundation for the financial support of his postdoctoral fellowship (Feodor Lynen research fellowship).

References

- [1] Holmberg K, Andersson P, Erdemir A. Global energy consumption due to friction in passenger cars. *Tribol Int* 2012;47:221–34. <http://dx.doi.org/10.1016/j.triboint.2011.11.022>.
- [2] Priest M, Taylor CM. Automobile engine tribology—approaching the surface. *Wear* 2000;241:193–203. [http://dx.doi.org/10.1016/S0043-1648\(00\)00375-6](http://dx.doi.org/10.1016/S0043-1648(00)00375-6).
- [3] Tung SC, McMillan ML. Automotive tribology overview of current advances and challenges for the future. *Tribol Int* 2004;37:517–36. <http://dx.doi.org/10.1016/j.triboint.2004.01.013>.
- [4] Holmberg K, Kivikytö-Reponen P, Härkisaari P, Valtonen K, Erdemir A. Global energy consumption due to friction and wear in the mining industry. *Tribol Int* 2017;115:116–39. <http://dx.doi.org/10.1016/j.triboint.2017.05.010>.
- [5] Gachot C, Rosenkranz A, Hsu SM, Costa HL. A critical assessment of surface texturing for friction and wear improvement. *Wear* 2017;372–373:21–41. <http://dx.doi.org/10.1016/j.wear.2016.11.020>.
- [6] Stribeck R. Die wesentlichen Eigenschaften der Gleit- und Rollenlager. *Z VDI* 1902;46:1341–8.
- [7] Hsu SM, Gates RS. Boundary lubricating films: formation and lubrication mechanism. *Tribol Int* 2005;38:305–12. <http://dx.doi.org/10.1016/j.triboint.2004.08.021>.
- [8] Spikes HA. Mixed lubrication — an overview. *Lubr Sci* 1997;9:221–53. <http://dx.doi.org/10.1002/ls.3010090302>.
- [9] Spikes HA, Olver AV. Basics of mixed lubrication. *Lubr Sci* 2003;16:1–28. <http://dx.doi.org/10.1002/ls.3010160102>.
- [10] Spikes HA. Sixty years of EHL. *Lubr Sci* 2006;18:265–91. <http://dx.doi.org/10.1002/ls.23>.
- [11] Rosenkranz A, Heib T, Gachot C, Mücklich F. Oil film lifetime and wear particle analysis of laser-patterned stainless steel surfaces. *Wear* 2015;334–335:1–12. <http://dx.doi.org/10.1016/j.wear.2015.04.006>.
- [12] Greiner C, Merz T, Braun D, Codrignani A, Magagnato F. Optimum dimple diameter for friction reduction with laser surface texturing: the effect of velocity gradient. *Surf Topogr Metrol Prop* 2015;3:44001. <http://dx.doi.org/10.1088/2051-672X/3/4/044001>.
- [13] Rosenkranz A, Martin B, Bettscheider S, Gachot C, Kliem H, Mücklich F. Correlation between solid-solid contact ratios and lubrication regimes measured by a refined electrical resistivity circuit. *Wear* 2014;320:51–61. <http://dx.doi.org/10.1016/j.wear.2014.08.018>.
- [14] Lubrecht AA, Venner CH, Colin F. Film thickness calculation in elasto-hydrodynamic lubricated line and elliptical contacts: the Dowson, Higginson, Hamrock contribution. *Proc Inst Mech Eng Part J J Eng Tribol* 2009;223:511–5. <http://dx.doi.org/10.1243/13506501JET508>.
- [15] Hamrock BJ, Dowson D. Isothermal elasto-hydrodynamic lubrication of point contacts: Part 1—theoretical formulation. *J Lubr Technol* 1976;98:223. <http://dx.doi.org/10.1115/1.3452801>.
- [16] Hamrock BJ, Dowson D. Isothermal elasto-hydrodynamic lubrication of point contacts: Part III—fully flooded results. *J Lubr Technol* 1977;99:264. <http://dx.doi.org/10.1115/1.3453074>.
- [17] Hwang D, Kim D, Lee S. Influence of wear particle interaction in the sliding interface on friction of metals. *Wear* 1999;225–229:427–39. [http://dx.doi.org/10.1016/S0043-1648\(98\)00371-8](http://dx.doi.org/10.1016/S0043-1648(98)00371-8).
- [18] Suh NP, Mosleh M, Howard PS. Control of friction. *Wear* 1994;175:151–8. [http://dx.doi.org/10.1016/0043-1648\(94\)90178-3](http://dx.doi.org/10.1016/0043-1648(94)90178-3).
- [19] Denape J, Lamon J. Sliding friction of ceramics: mechanical action of the wear debris. *J Mater. Sci* 1990;25:3592–604. <http://dx.doi.org/10.1007/BF00575394>.
- [20] Lee L, Behera P, Sriraman KR, Chromik RR. Effects of humidity on the sliding wear properties of Zn–Ni alloy coatings. *RSC Adv* 2017;7:22662–71. <http://dx.doi.org/10.1039/C6RA27352A>.
- [21] Zhai H, Huang Z. Instabilities of sliding friction governed by asperity interference mechanisms. *Wear* 2004;257:414–22. <http://dx.doi.org/10.1016/j.wear.2004.01.018>.
- [22] Reinert L, Lasserre F, Gachot C, Grützmacher P, MacLucas T, Souza N, et al. Long-lasting solid lubrication by CNT-coated patterned surfaces. *Sci Rep* 2017;7:42873. <http://dx.doi.org/10.1038/srep42873>.
- [23] Blau PJ. On the nature of running-in. *Tribol Int* 2005;38:1007–12. <http://dx.doi.org/10.1016/j.triboint.2005.07.020>.
- [24] Koeneke CE, Tanaka M, Motoi H. Axial oil film rupture in high speed bearings due to the effect of the centrifugal force. *J Tribol* 1995;117:394. <http://dx.doi.org/10.1115/1.2831264>.
- [25] Scriven LE. Physics and applications of DIP coating and spin coating. *MRS Proc* 1988;121:717. <http://dx.doi.org/10.1557/PROC-121-717>.

II How to guide lubricants – Tailored laser surface patterns on stainless steel

Philipp G. Grützmacher¹, Andreas Rosenkranz¹, Carsten Gachot¹

¹ Chair of Functional Materials, Saarland University, 66123 Saarbrücken, Germany

Published in “*Applied Surface Science*” (Impact factor (2017): 4.439)

Accessible online at: <http://dx.doi.org/10.1016/j.apsusc.2016.02.115>

Own contribution:

Project management; scientific discussion; paper writing; data analysis; design of test rig; sample preparation: laser surface patterning; measurements: white light interferometry, lubricant spreading

Abstract:

In this experimental study, periodic line-like structures with different periodicities (5, 10, 19, and 300 μm) and structural depths (approximately 1 and 4 μm) were fabricated on stainless steel samples (AISI-304) by short-pulse laser interference and ultrashort-pulse laser patterning. A detailed characterization of the resulting surface topography was performed by white light interferometry and scanning electron microscopy. The spreading dynamics of additive-free synthetic polyalphaolefine oil on a polished reference sample are compared to laser patterned surfaces. These studies are conducted using a newly developed test rig, which allowed for controlled temperature gradients and a precise recording of the spreading dynamics of lubricants on sample surfaces. It could be demonstrated that the spreading velocity parallel to the surface pattern is higher for all samples which can be explained by increased capillary forces and liquid pinning induced by the surface patterning. Furthermore, a decline of the spreading velocity over time for all samples and orientations is clearly visible which can be traced back to a viscosity increase induced by the temperature gradient and a reduced droplet volume. For parallel orientation, the experimental findings are in good agreement with the Lucas–Washburn equation and established models.

Cite this as:

P.G. Grützmacher, A. Rosenkranz, C. Gachot, How to guide lubricants – Tailored laser surface patterns on stainless steel, *Appl. Surf. Sci.* **2016**, 370, 59–66. (<http://doi:10.1016/j.apsusc.2016.02.115>)



How to guide lubricants – Tailored laser surface patterns on stainless steel



Philipp G. Grützmacher*, Andreas Rosenkranz, Carsten Gachot

Department of Functional Materials, Saarland University, 66123 Saarbruecken, Germany

ARTICLE INFO

Article history:

Received 18 November 2015
Received in revised form 27 January 2016
Accepted 11 February 2016
Available online 15 February 2016

Keywords:

Laser surface texturing
Stainless steel
Wetting
Anisotropic spreading
Lucas–Washburn

ABSTRACT

In this experimental study, periodic line-like structures with different periodicities (5, 10, 19, and 300 μm) and structural depths (approximately 1 and 4 μm) were fabricated on stainless steel samples (AISI-304) by short-pulse laser interference and ultrashort-pulse laser patterning. A detailed characterization of the resulting surface topography was performed by white light interferometry and scanning electron microscopy. The spreading dynamics of additive-free synthetic polyalphaolefine oil on a polished reference sample are compared to laser patterned surfaces. These studies are conducted using a newly developed test rig, which allowed for controlled temperature gradients and a precise recording of the spreading dynamics of lubricants on sample surfaces. It could be demonstrated that the spreading velocity parallel to the surface pattern is higher for all samples which can be explained by increased capillary forces and liquid pinning induced by the surface patterning. Furthermore, a decline of the spreading velocity over time for all samples and orientations is clearly visible which can be traced back to a viscosity increase induced by the temperature gradient and a reduced droplet volume. For parallel orientation, the experimental findings are in good agreement with the Lucas–Washburn equation and established models.

© 2016 Elsevier B.V. All rights reserved.

1. Introduction

Insufficient lubrication in loaded tribological contacts such as bearings and gears is a generalized problem that causes severe damage [1]. Due to frictional heating within the contact zone, a temperature gradient develops between the loaded contact (higher temperature) and the unloaded regions (lower temperature). This typically leads to a surface tension gradient within the lubricant and consequently migration from hotter to cooler regions by Marangoni-forces, finally yielding in a lack of lubricant in the zones where it is most urgently needed [2]. In contrast to that, there are stabilizing factors, such as capillary forces and the viscosity of the lubricant, which hold the liquid in the zone of higher temperature. All these factors are highly depending on temperature.

The possibly resulting inadequate lubrication conditions may produce changes in the lubrication regime leading to increased contact between the sliding surfaces, increased wear and component failure.

To counter this, identifying and controlling the governing forces involved in promoting or impeding lubricant migration becomes

decisive. Temperature gradients, surface chemistry and topography effects play an important role in this context [3–5]. One approach could be to overcome the acting Marangoni forces by removing heat from the contact zone and thus compensating the temperature gradient. Another solution, used in precision mechanics for the lifetime lubrication of watches, may be the use of very thin fluororganic epilame films as antispread barriers [6]. Furthermore, Morita et al. reported about chemical patterns consisting of alternating hydrophobic and hydrophilic stripes which can be tailored to influence the lubrication migration [7]. However, a problem often encountered with thin organic layers, or chemical surface treatments in general, is the use of environmentally hazardous chemicals and their reduced resistance against abrasion [6].

Apart from chemical treatments, there are numerous techniques to create well-defined topographies and thereby manipulate wetting and lubricant spreading [3,8,9]. Introducing channel-like structures in material surfaces have the benefit of using capillary forces by guiding the lubricant to the tribologically stressed areas. Lithography-based methods such as UV, electron beam or interference lithography are quite common in this context [8]. Some mechanical approaches like micro-coining or roller burnishing are also used to create different pattern geometries on metal surfaces [10].

* Corresponding author.

E-mail address: philipp.gruetzmacher@uni-saarland.de (P.G. Grützmacher).

Major drawbacks of most of the abovementioned methods include their multiple processing steps and their limitations in geometry and feature sizes. In this context, laser-patterning techniques are very efficient because they allow for fast and precise surface treatment of various materials [11]. In particular, ultrashort-pulsed lasers which are scanned over the substrate surface have some benefits in creating well-defined surface topographies due to their minimized heat input [12]. Another promising approach is the use of interfering laser beams and the resulting intensity distribution. This technique makes it possible to fabricate well defined, periodic surface patterns on metals with a great variability in lateral feature sizes in one single laser shot [13]. However, it should be mentioned that the maximum achievable structural depths using laser interference patterning are roughly between 1.5 and 2.5 μm [13]. In order to investigate larger structural depths, femtosecond laser processing was used in this study as well. The work by Rosenkranz et al. already clearly revealed the impact of laser-induced surface patterns by direct laser interference patterning (DLIP) on the spreading behavior of an additive-free polyalphaolefin (PAO) oil, yet without taking into account temperature gradients [14].

In the work presented here, the spreading dynamics of additive-free, synthetic PAO 4 oil on polished stainless steel samples is compared to that of laser-patterned steel surfaces, studied by a newly developed test rig, which allows for controlled temperature gradients and a precise recording of the spreading dynamics of lubricants on sample surfaces. Four different line-like patterns were produced: periodicities of 5, 10 and 19 μm with a structural depth of approximately 1 μm were fabricated by DLIP; finally, sharper and deeper patterns with a line-spacing of 300 μm and depth of 4 μm were created by scanned, ultrashort femtosecond pulses. Apart from larger structural depths for the femtosecond laser processing, also the shape of the topography profiles differs from the ones produced by nanosecond interference patterning. Therefore, both techniques were applied in this study in order to reveal the effects of said differences on the lubricant spreading behavior.

2. Materials and methods

2.1. Materials

Commercially available austenitic stainless steel samples (AISI 304: 20 mm \times 20 mm \times 0.75 mm) with a mirror-like surface finish (root mean square roughness (R_q) of 30 nm) were used for the spreading experiments. The chemical composition of the used steel is given in Table 1 as specified by the supplier and confirmed by energy-dispersive X-ray spectroscopy (EDS). Prior to the spreading experiments, the samples were cleaned with a multi-step cleaning procedure in an ultrasonic bath employing cyclohexane, acetone and isopropanol 10 min each in the given order to remove polar and non-polar contamination.

2.2. Laser interference patterning

A well-defined, line-like surface topography with a periodicity of 5, 10 and 19 μm , which is defined by the laser wavelength λ and the angle between two interfering beams, was created by DLIP on the stainless steel substrates [13,15,16]. For this purpose,

Table 1
Chemical composition of the used steel samples in wt.% as specified by the supplier and confirmed by EDS.

Used steel specimens	Fe	Cr	Ni	Mn	Si	C	Mo
Stainless steel (AISI 304)	68.9	18	10	2	1	0.1	/

a high-power pulsed solid-state Nd:YAG laser (*Quanta Ray Pro 290*, Newport Spectra Physics) with a pulse duration of 10 ns, a wavelength of 355 nm and a repetition rate of 10 Hz was used. In order to obtain interference, the primary beam travels through an optical set-up which is described in a previous publication by Rosenkranz et al. [14]. Finally, the line-like pattern with the characteristic periodicity is produced on the substrate surface. The laser fluence was kept constant at 29 J/cm² for all sample types in order to produce a well-defined and homogeneous surface pattern. The DLIP was done under ambient conditions using a single laser pulse. Further details about the DLIP have been already published elsewhere [13,15,16].

2.3. Laser patterning using a femtosecond laser

One sample was patterned using ultrashort-pulse laser patterning (UPLP). To this end, a passively mode-locked ultrashort-pulsed Ti: Sapphire laser (*Spitfire*, Newport Spectra Physics) was used with a repetition rate of 1 kHz and a wavelength of 800 nm. The underlying physical principle of this laser system is chirped pulse amplification which allows for the production of ultrashort laser pulses (tunable pulse duration ranging from \approx 100 fs up to approximately 4 ps). The pulse duration (full width at half maximum) used in this study was 130 fs and was measured by autocorrelation. The primary laser beam was focused on top of the steel sample with a lens (focal length: 200 mm), which resulted in a beam diameter of 70 μm . The laser spot was scanned across the sample with a synchronized, automatic (sample) translation table, placing each pulse 35 μm apart within each line in order to produce a homogeneous line-like pattern. The lines were given a separation (periodicity) of 300 μm . To achieve a higher structural depth and sufficient homogeneity, each pattern line was scanned four times. The UPLP was performed under ambient conditions.

2.4. Topographical analysis

The topography of the samples was characterized by white light interferometry (WLI: *New View 7300*, Zygo) prior to and after the laser patterning (DLIP and UPLP) in order to study the surface roughness and the quality of the patterns. Typical roughness parameters such as the root-mean-square roughness R_q as well as structure-dependent parameters such as periodicity and structural depth were chosen to describe the surface topography of the laser-patterned surfaces. In addition to that, the resulting topography was imaged by scanning electron microscopy (SEM: *Helios 600*, FEI) in secondary electron contrast after patterning.

2.5. Surface temperature analysis

The linearity of the temperature gradient on the sample and the comparability of the temperature between sample table and specimen was determined by a thermal imaging camera (*FLIR i7*). The sample table was painted black in order to minimize the reflection of the copper sample table.

2.6. Spreading velocity measurements

For the spreading experiments, a new experimental setup with a copper table was designed which is illustrated in Fig. 1a. The sample table is heated on one side by a heating cartridge (*RS Components*) and cooled on the other side by water cooling in order to achieve a temperature gradient of approximately 2 °C/mm. In order to adjust the temperature gradient, the heating cartridge is controlled by a voltage regulator. The temperature gradient at the surface of the sample table is measured with NiCr-Ni thermocouples. In order to affirm a negligible temperature difference between the table surface and sample, thermal image measurements and a

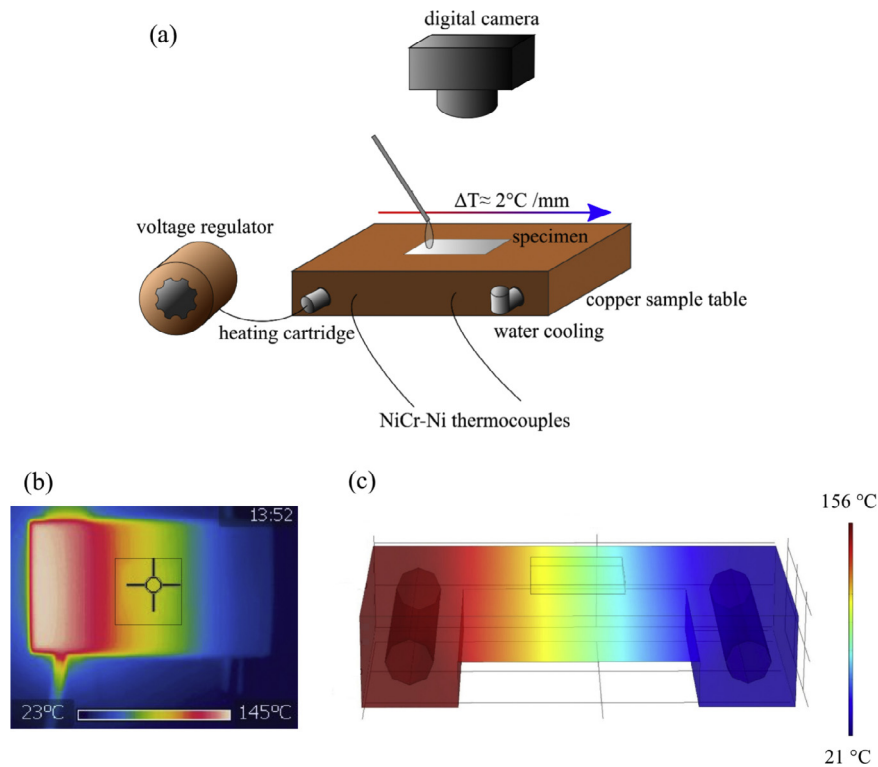


Fig. 1. (a) Schematic drawing of the experimental set-up with a temperature gradient. (b) Thermal image of the sample table with a steel sample on top, as indicated by the dotted line. The sample is nearly not recognizable on the sample demonstrating a negligible temperature difference between sample and table. (c) Temperature gradient as simulated by COMSOL Multiphysics.

thermal simulation were conducted. This is demonstrated in Fig. 1b since the sample is almost not visible in the thermal image and the simulation. A droplet volume of $1.5 \mu\text{l}$ was chosen in order to avoid gravity effects on the droplet shape [3]. Additionally, this droplet volume results in a drop size which allows for a good handling on the patterned area and a sufficient wetting of multiple adjacent surface patterns at the same time. For the experiment, the oil was applied on top of the surfaces close to the hot side of the samples by a pipette (Eppendorf). Since low viscosity oils lead to a significant friction reduction and increase the energy efficiency in tribological systems [17], a synthetic, non-polar and additive free PAO oil with a low kinematic viscosity of 3.9 cSt at 100°C was used. The properties of the oil are summarized in Table 2. A digital camera (EOS 500 D, Canon) recorded the motion of the droplet. To evaluate the spreading velocity, the pictures were analyzed with an image editing software (a4i Analysis, Aquinto AG). The distance from the hot substrate edge to the droplet front, which advances toward the cold substrate edge, was measured until the droplet reached the cold side of the patterned surface. Finally, the spreading velocity of the droplet (v) was calculated.

2.7. Finite element method

The dispersion of the temperature gradient on the table and sample surface was simulated by FEM (COMSOL Multiphysics,

version 4.3b) using a model of heat transfer in solids based upon the thermal conductivity equation. Hence, it is determined by the density ρ , the specific heat capacity at constant pressure C_p , the absolute temperature T , the thermal conductivity k and Q , which contains heat sources:

$$\rho C_p \cdot \nabla T = \nabla \cdot (k \nabla T) + Q \quad (2.1)$$

In the stationary case, the first term ρC_p is 0. Since the transition coefficients from the heating cartridge and the water-cooling to the copper table are unknown, the temperatures on each side are simply measured by thermocouples and Q can be set to zero. This can be done, because of reasons of simplification, it is assumed that there are no heat sources and instead two constant temperatures are used. Therefore, the equation is merely dependent on the thermal conductivity of the material and the temperatures on each side of the sample table:

$$0 = k \cdot \nabla^2 T \quad (2.2)$$

where k is the thermal conductivity of copper ($400 \text{ W}/(\text{m K})$) and T the respective temperature (hot side 429 K , cold side 294 K). As can be seen in Fig. 1c this results in a linear temperature gradient along the table axis.

The value for the thermal conductivity is selected from the material browser of the used Multiphysics software.

3. Results and discussion

3.1. Topographical characterization

The cross-section plots for the line-like surface patterns produced by DLIP and UPLP with periodicities of 5, 10, 19 and $300 \mu\text{m}$ are summarized in Fig. 2a–d. Those in Fig. 2a, b and d show a rather homogeneous height distribution. In the case of DLIP, the metal surface is mostly molten at the interference maximum positions. This

Table 2
Properties of the used PAO oil as specified by the supplier.

Property	PAO 4
Kinematic viscosity at 100°C in cSt	3.9
Kinematic viscosity at 40°C in cSt	16.8
Viscosity index	124
Specific gravity	0.82

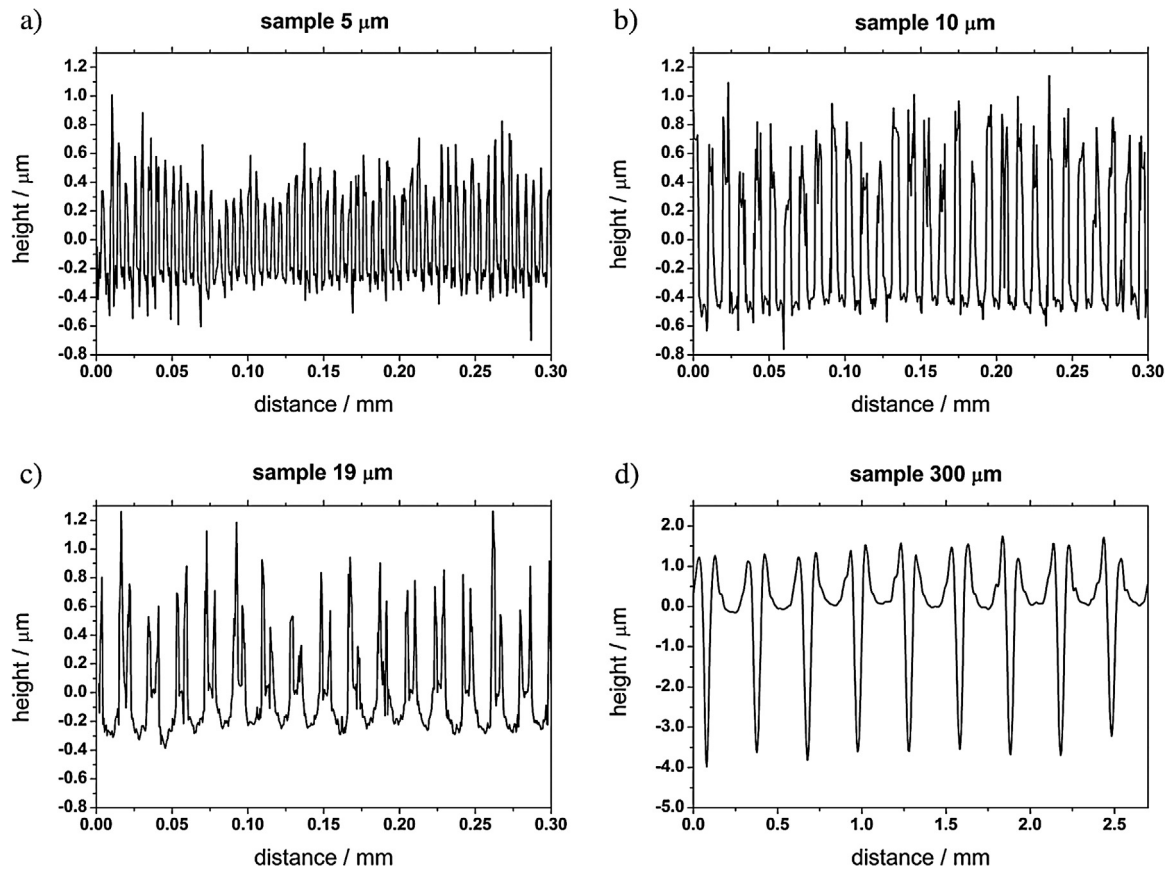


Fig. 2. Cross-section profiles of line-like surface patterns produced by DLIP (a–c) and UPLP (d) with periodicities P of 5, 10, 19 and 300 μm measured by WLI.

produces a movement of molten metal from the hot regions (interference maxima) to the cold regions (interference minima) which is driven by the surface tension gradient of the molten metal, also called Marangoni effect [16,18,19]. For a periodicity of 19 μm , this was too large for the molten metal to bridge the gap. Consequently, a double-peak pattern is formed (Fig. 2c). UPLP is a very precise process with a small heat-affected zone, compared to DLIP, and thus more homogeneous (Fig. 2d). As can be seen in Fig. d the double-peak pattern also occurs in UPLP, however to a lesser extent, with these shallower gaps reaching 25% of the entire structural depth, versus 80% in the 19 μm DLIP sample.

Fig. 3 shows the SEM images of all produced patterns. The double-peak pattern of the 19 μm sample is clearly visible (Fig. 3d) as well as the morphological differences between the samples patterned by DLIP, which show melt residues, and the sample patterned by UPLP. In order to describe the patterned surfaces, the root-mean-square roughness R_q , the periodicity and the structural depth are summarized in Table 3. As can be seen from this table, the roughness of the samples with a periodicity of 5 and 19 μm is almost the same, whereas that of the sample with a periodicity of 10 μm is two times higher. R_q correlates well with the variation of

the structural depth. Hence, the samples with a higher structural depth have a higher R_q . In order to explain the larger structural depth for the 10 μm periodicity, one must distinguish between nominal and real laser fluence. The nominal laser fluence was kept constant for all samples but the real fluence differs because, with larger periodicity, it is distributed over fewer intensity maxima. Therefore, the real laser fluence per maximum is higher which leads to an increase in structural depth [20]. The deviation of the 19 μm sample from this trend can be explained by the smaller structural depth between the double peaks [20]. Worth mentioning are also the small standard deviations of R_q and the structural depth which are less than 10%, demonstrating a well-defined topography. The only exception is the sample with a periodicity of 19 μm showing slightly higher standard deviations which can be traced back to a more irregular surface pattern due to the double peaks.

3.2. Anisotropic spreading behavior

Fig. 1b and c shows the thermographic measurement and thermal simulation of the experimental setup including the sample. As can be seen, the temperature gradient on the sample table is homogenous and linear. Therefore, a driving force transverse to the spreading direction as well as a variation of the temperature gradient with progressive lubricant spreading can be neglected. Furthermore, the temperature gradient on the sample is almost identical to that on the table thus allowing for a correct measurement of the temperature gradient.

Fig. 4 shows the temporal evolution of the droplet spreading over the samples imaged by the digital camera. A significant difference in droplet geometry is evident, which can be ascribed to an anisotropic spreading behavior due to the surface patterns [14]. The spreading velocity over time for all samples is shown in Fig. 5.

Table 3
Summary of the periodicity P , structural depth T and root-mean-square roughness R_q measured by WLI.

Sample	P (μm)	T (μm)	R_q (nm)
Reference	/	/	9 ± 3
5 μm	5	0.70 ± 0.05	140 ± 10
10 μm	10	1.21 ± 0.09	319 ± 6
19 μm	19	0.94 ± 0.10	154 ± 20
300 μm	300	4.21 ± 0.20	1296 ± 37

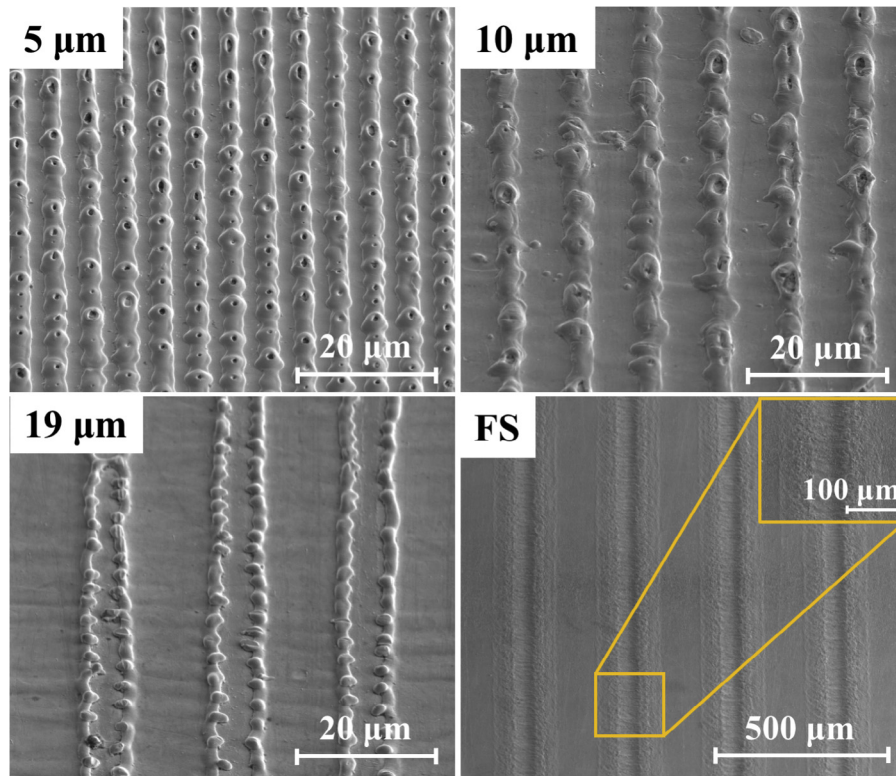


Fig. 3. SEM micrographs of periodic line-like surface patterns with a pattern periodicity P of 5, 10, 19 and 300 μm (femtosecond FS). The zoomed part in the bottom right image represents a single groove of the sample patterned by UPLP.

Evidently, the spreading velocity parallel to the surface pattern is higher compared to the perpendicular case, for all samples. This can be explained by capillary forces, which are intensified by the line-like surface pattern and act along the lines thus favoring propagation in this direction [3]. Additionally, the grooves, which are in the micrometer range, act as pinning centers which impede the propagation perpendicular to the surface pattern [14]. For this reason, the spreading velocity perpendicular to the structures is slower for smaller periodicities.

Besides the anisotropic spreading behavior, a decline in the spreading velocity over time for all samples and orientations can be observed. In order to explain this effect, several contributions have to be taken into consideration. At first, the viscosity increases as the drop moves toward the cold side of the sample. Secondly, the drop volume is depleted over time which leads to a pinning of the droplet front as a consequence of contact angle hysteresis [21]. The decrease in spreading velocity holds especially true for the parallel orientation. As the liquid propagates along the line-like surface grooves, the capillary length is reduced which leads to a decrease in capillary forces and therefore penetration velocity, following the Lucas–Washburn-equation [22,23]:

$$l^2 = \frac{\gamma r \cos \theta}{2\eta} t \quad (3.1)$$

where l is the position of the traveling meniscus along the channel, γ is the surface tension of the liquid, r is the channel radius, θ is the static contact angle of the liquid on the channel wall and η is the dynamic viscosity of the liquid phase. This relationship has been verified experimentally [24]. Furthermore, numerous researchers showed theoretically and experimentally that the linear behavior, $l^2 \sim t$, holds also true for open micro channels with different

geometries [25–29]. Rye et al. found a general expression to describe the liquid penetration in open micro channels [25]:

$$l^2 = K(\alpha, \theta) \frac{\gamma T}{\eta} t \quad (3.2)$$

where $K(\alpha, \theta)$ is a geometric term which depends on the groove angle α and the contact angle and T is the structural depth. The spreading velocity of the droplet on the surface is strongly connected to the liquid penetration into the surface grooves. Therefore, a higher penetration velocity into the surface grooves will result in a higher spreading velocity of the droplet on the surface. Since a greater structural depth leads to a higher liquid penetration into the grooves, due to higher capillary forces, those samples also show a higher spreading velocity on the surface. Interestingly, the spreading velocity in the perpendicular orientation is comparable or even slightly above the spreading velocity on the reference sample. Conceivably the increased roughness of the patterned samples compared to the reference (see Table 3) is the reason for this.

According to the wetting theory of Wenzel, the contact angle on a rough surface decreases for a contact angle smaller than 90° on a perfectly plane surface [30]. A smaller contact angle enhances the spreading behavior and hence the propagation velocity. Despite this, a slight tendency for a reduced spreading velocity of the sample with a periodicity of 5 μm compared to the reference can be noticed looking at Fig. 5a and Table 4. This can be explained by a more pronounced pinning as the periodicity is reduced which might overcompensate the roughness effect. Being aware of the influence of the periodicity, the values for the spreading velocities for the sample patterned by UPLP compared to the samples patterned by DLIP in Table 4 give finally rise to the question for the governing surface parameter. Despite a much larger periodicity of 300 μm , the spreading velocities of the UPLP samples for parallel orientation as well as perpendicular orientation are comparable or even slightly higher than those of the DLIP samples. This can be

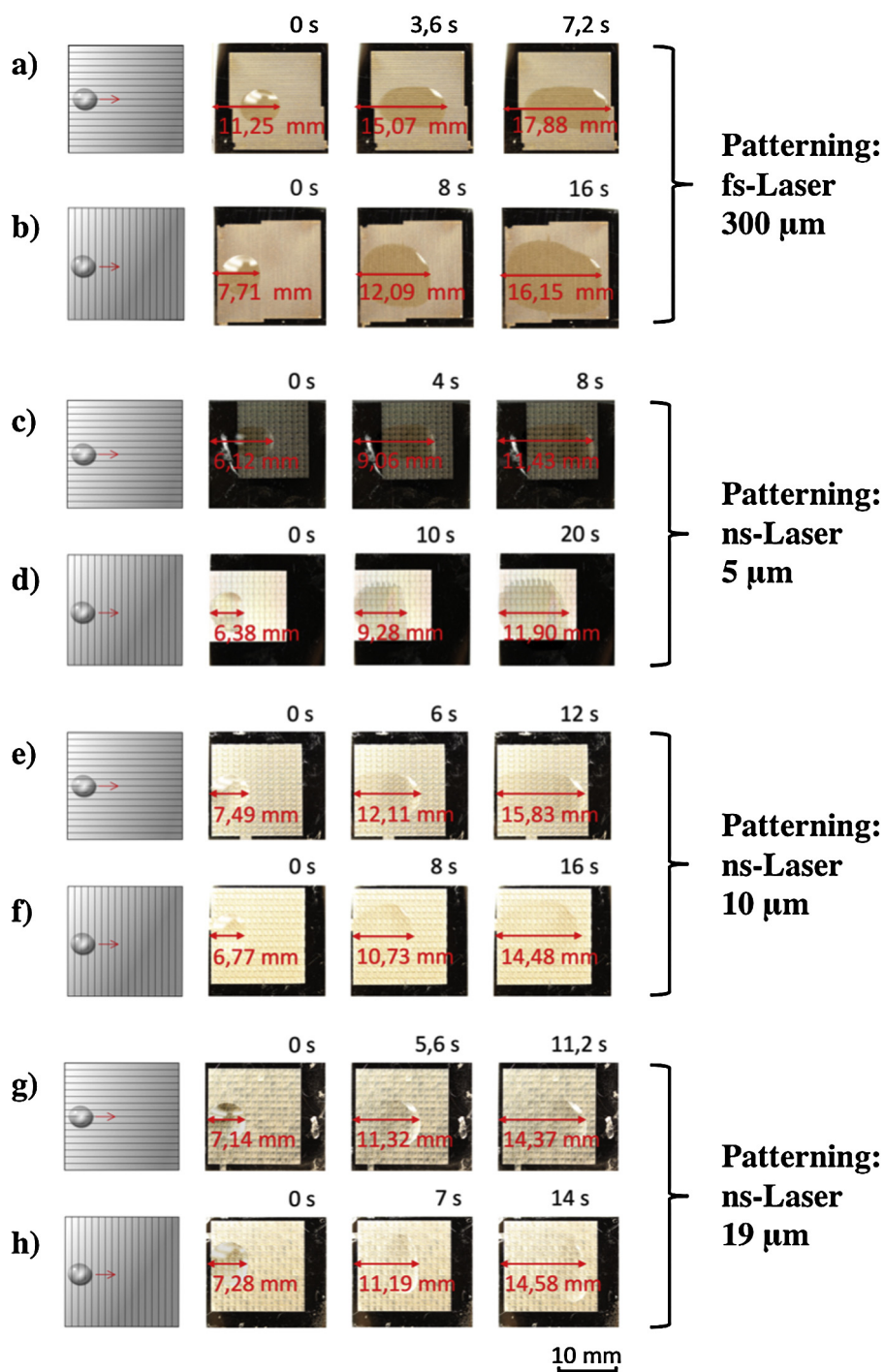


Fig. 4. Temporal evolution of the droplet propagation parallel and perpendicular to the surface patterns for several samples with different periodicities imaged by a digital camera.

Table 4
Summary of the measured temperature gradient and spreading velocity.

Sample	$\Delta T (^{\circ}\text{C})$	$\nu (\text{mm s}^{-1})$
Reference	2.03	0.367 ± 0.077
5 μm parallel	2.02	0.607 ± 0.155
5 μm perpendicular	2.02	0.322 ± 0.056
10 μm parallel	2.05	0.744 ± 0.090
10 μm perpendicular	2.05	0.455 ± 0.043
19 μm parallel	2.04	0.685 ± 0.110
19 μm perpendicular	2.05	0.501 ± 0.092
300 μm parallel	2.06	0.841 ± 0.140
300 μm perpendicular	2.06	0.464 ± 0.073

explained by looking at the structural depths of the samples listed in Table 3. There seems to be a tendency for a higher spreading velocity in the parallel orientation along with a stronger pinning in the perpendicular orientation with an increasing structural depth. These findings are consistent with the theoretical model proposed by Rye et al. (see Eq. (3.2)). The same spreading velocity/structural depth dependency was found by Chen who investigated the penetration of a wetting liquid in open metallic grooves [29].

Apart from topographical effects, it is well known that the surface chemistry can significantly influence the spreading and wetting properties as already stated in the introduction. As a

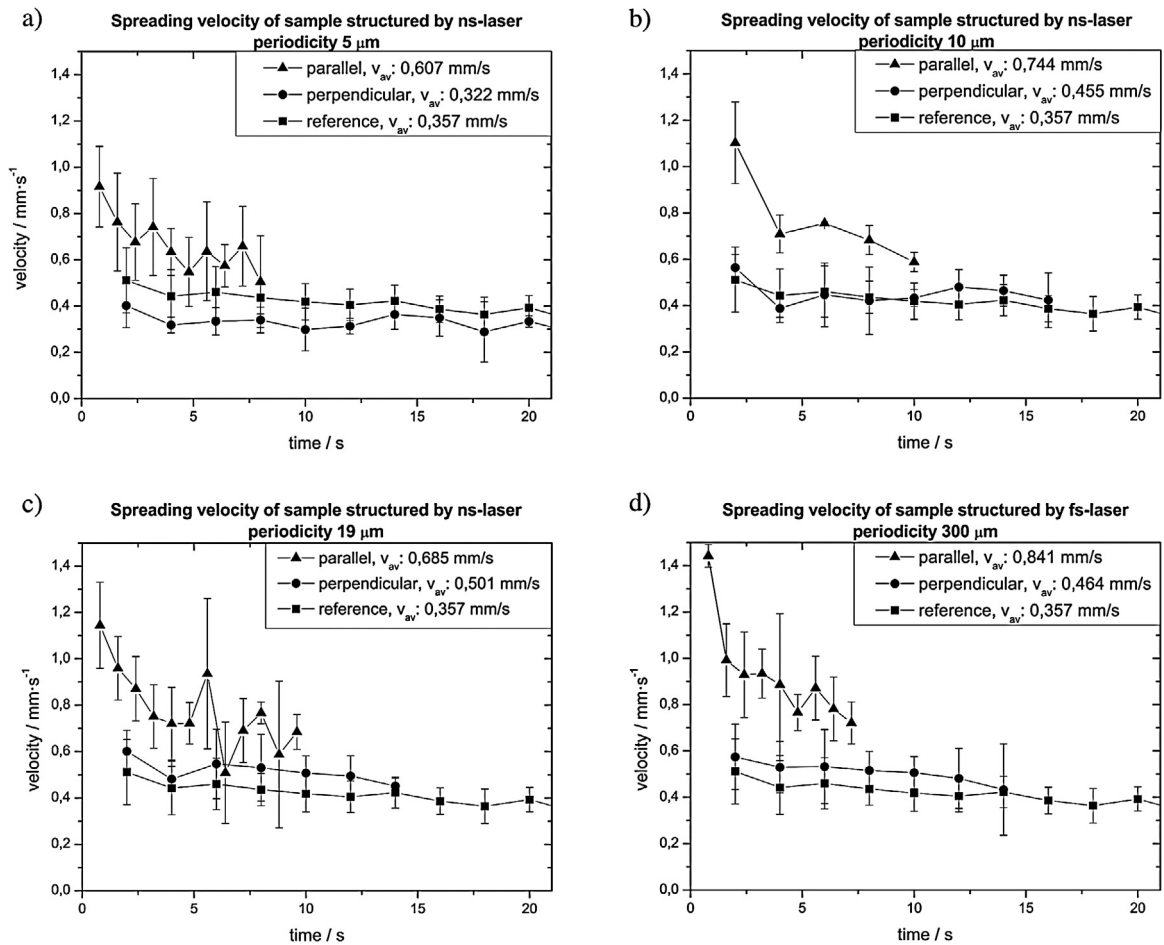


Fig. 5. Spreading velocities of samples patterned by DLIP and UPLP with periodicities P of 5, 10, 19 and 300 μm . For each periodicity the spreading velocity parallel and perpendicular to the pattern is shown compared to the spreading velocity of the unpatterned reference sample.

consequence, in previous studies, the surface chemistry and the anisotropic spreading behavior of laser-interference-patterned steel samples (1.4301) were investigated [14,31]. As could be shown, the surface topography is the governing factor with regard to the spreading behavior whereas the surface chemistry plays only a minor role because both the polished and laser-patterned surfaces are covered with an oxide layer consisting of iron and chromium oxides.

4. Conclusions

In this experimental study, a new test rig was designed which allows for the recording of the spreading dynamics of liquids on metallic surfaces under a controlled temperature gradient.

Here, periodic line-like patterns with different periodicities (5, 10, 19 and 300 μm) and structural depths (approximately 1 and 4 μm) were fabricated by laser interference (DLIP) and ultrashort pulse laser patterning (UPLP) on stainless steel samples.

The temporal evolution of the oil spreading (additive-free PAO oil) as well as the spreading velocity under the influence of a temperature gradient of 2 °C/mm were studied for the patterned surfaces and compared to a polished reference. The main findings are the following:

- The spreading velocity parallel to the surface patterns is higher compared to perpendicular to them for all samples, which can

be explained by increased capillary forces parallel to the surface patterning and liquid pinning perpendicular to the patterns.

- Besides the anisotropic spreading behavior, a decline in the spreading velocity over time for all samples and orientations can be observed. This behavior can be attributed to the increase in oil viscosity, depletion of drop volume and a decrease in capillary forces in the parallel direction.
- The experimental findings for the spreading dynamics in the parallel orientation can be well described by the Lucas–Washburn equation and the empirical equation of Rye et al.

Acknowledgements

The present work is supported by funding from the Deutsche Forschungsgemeinschaft (DFG, project: MU 959/27-2 within the SPP 1551). The authors kindly acknowledge Dr. M. Jung for helpful advice. We thank Dr. M. Hans and Mr. N. Souza for proof reading.

References

- [1] W.J. Bartz, The influence of lubricants on failures of bearings and gears, *Tribol. Int.* 9 (1976) 213–224, [http://dx.doi.org/10.1016/0301-679X\(76\)90078-5](http://dx.doi.org/10.1016/0301-679X(76)90078-5).
- [2] D.T. Wasan, Droplets speeding on surfaces, *Science* 80 (291) (2001) 605–606, <http://dx.doi.org/10.1126/science.1058466>.
- [3] M. Hans, F. Müller, S. Grandthyll, S. Hüfner, F. Mücklich, Anisotropic wetting of copper alloys induced by one-step laser micro-patterning, *Appl. Surf. Sci.* 263 (2012) 416–422, <http://dx.doi.org/10.1016/j.apsusc.2012.09.071>.
- [4] M. Hans, C. Gachot, F. Müller, F. Mücklich, Direct laser interference structuring as a tool to gradually tune the wetting response of titanium and polyimide

- surfaces, *Adv. Eng. Mater.* 11 (2009) 795–800, <http://dx.doi.org/10.1002/adem.200900115>.
- [5] D.E. Kataoka, S.M. Troian, Patterning liquid flow on the microscopic scale, *Nature* 402 (1999) 794–797, <http://dx.doi.org/10.1038/45521>.
- [6] Z. Rymuza, Lubrication of miniature systems, in: *Encycl. Tribol.*, Springer US, Boston, MA, 2013, pp. 2101–2110, http://dx.doi.org/10.1007/978-0-387-92897-5_1070.
- [7] M. Morita, T. Koga, H. Otsuka, A. Takahara, Macroscopic-wetting anisotropy on the line-patterned surface of fluoroalkylsilane monolayers, *Langmuir* 21 (2005) 911–918, <http://dx.doi.org/10.1021/la0485172>.
- [8] D. Xia, Z. Ku, S.C. Lee, S.R.J. Brueck, Nanostructures and functional materials fabricated by interferometric lithography, *Adv. Mater.* 23 (2011) 147–179, <http://dx.doi.org/10.1002/adma.201001856>.
- [9] O. Bliznyuk, V. Veligura, E.S. Kooij, H.J.W. Zandvliet, B. Poelsema, Metastable droplets on shallow-grooved hydrophobic surfaces, *Phys. Rev. E* 83 (2011) 041607, <http://dx.doi.org/10.1103/PhysRevE.83.041607>.
- [10] A. Szurdak, A. Rosenkranz, C. Gachot, G. Hirt, F. Mücklich, Manufacturing and tribological investigation of hot micro-coined lubrication pockets, *Key Eng. Mater.* 611–612 (2014) 417–424, <http://dx.doi.org/10.4028/www.scientific.net/KEM.611-612.417>.
- [11] C. Gachot, A. Rosenkranz, L. Reinert, E. Ramos-Moore, N. Souza, M.H. Müser, et al., Dry friction between laser-patterned surfaces: role of alignment, structural wavelength and surface chemistry, *Tribol. Lett.* 49 (2013) 193–202, <http://dx.doi.org/10.1007/s11249-012-0057-y>.
- [12] A.V. Kabashin, P. Delaporte, A. Pereira, D. Grojo, R. Torres, T. Sarnet, et al., Nanofabrication with pulsed lasers, *Nanoscale Res. Lett.* 5 (2010) 454–463, <http://dx.doi.org/10.1007/s11671-010-9543-z>.
- [13] F. Mücklich, A.F. Lasagni, C. Daniel, Laser interference metallurgy – using interference as a tool for micro/nano structuring, *Int. J. Mater. Res.* 97 (2006) 1337–1344, <http://dx.doi.org/10.3139/146.101375>.
- [14] A. Rosenkranz, S. Fleischmann, C. Gachot, F. Mücklich, Anisotropic spreading behavior of PAO oil on laser-patterned stainless steel surfaces, *Adv. Eng. Mater.* 17 (2015) 1645–1651, <http://dx.doi.org/10.1002/adem.201500115>.
- [15] A.F. Lasagni, C. Holzapfel, T. Weirich, F. Mücklich, Laser interference metallurgy: a new method for periodic surface microstructure design on multilayered metallic thin films, *Appl. Surf. Sci.* 253 (2007) 8070–8074, <http://dx.doi.org/10.1016/j.apsusc.2007.02.092>.
- [16] A.F. Lasagni, M. D'Alessandria, R. Giovanelli, F. Mücklich, Advanced design of periodical architectures in bulk metals by means of laser interference metallurgy, *Appl. Surf. Sci.* 254 (2007) 930–936, <http://dx.doi.org/10.1016/j.apsusc.2007.08.010>.
- [17] A. Martini, D. Zhu, Q. Wang, Friction reduction in mixed lubrication, *Tribol. Lett.* 28 (2007) 139–147, <http://dx.doi.org/10.1007/s11249-007-9258-1>.
- [18] T.R. Anthony, H.E. Cline, Surface rippling induced by surface-tension gradients during laser surface melting and alloying, *J. Appl. Phys.* 48 (1977) 3888, <http://dx.doi.org/10.1063/1.324260>.
- [19] Y. Guan, A.J. Pedraza, Synthesis and characterization of self-organized nanostructure arrays generated by laser irradiation, *MRS Proc.* 818 (2004) M11.47.1, <http://dx.doi.org/10.1557/PROC-818-M11.47.1>.
- [20] P. Leibenguth, Evolution of phases and microstructure in rapidly solidified metallic multilayer films: a correlative microscopy study (Ph.D. thesis), Saarland University, 2013.
- [21] D. Quéré, Wetting and roughness, *Annu. Rev. Mater. Res.* 38 (2008) 71–99, <http://dx.doi.org/10.1146/annurev.matsci.38.060407.132434>.
- [22] R. Lucas, Ueber das Zeitgesetz des kapillaren Aufstiegs von Flüssigkeiten, *Kolloid-Zeitschrift* 23 (1918) 15–22, <http://dx.doi.org/10.1007/BF01461107>.
- [23] E.W. Washburn, The dynamics of capillary flow, *Phys. Rev.* 17 (1921) 273–283, <http://dx.doi.org/10.1103/PhysRev.17.273>.
- [24] L.R. Fisher, P.D. Lark, An experimental study of the washburn equation for liquid flow in very fine capillaries, *J. Colloid Interface Sci.* 69 (1979) 486–492, [http://dx.doi.org/10.1016/0021-9797\(79\)90138-3](http://dx.doi.org/10.1016/0021-9797(79)90138-3).
- [25] R.R. Rye, J.a. Mann, F.G. Yost, The flow of liquids in surface grooves, *Langmuir* 12 (1996) 555–565, <http://dx.doi.org/10.1021/la9500989>.
- [26] R.R. Rye, F.G. Yost, E.J. O'Toole, Capillary flow in irregular surface grooves, *Langmuir* 14 (1998) 3937–3943, <http://dx.doi.org/10.1021/la9712247>.
- [27] D. Yang, M. Krasowska, C. Priest, M.N. Popescu, J. Ralston, Dynamics of capillary-driven flow in open microchannels, *J. Phys. Chem. C* 115 (2011) 18761–18769, <http://dx.doi.org/10.1021/jp2065826>.
- [28] D. Yang, M. Krasowska, C. Priest, J. Ralston, Dynamics of capillary-driven liquid–liquid displacement in open microchannels, *Phys. Chem. Chem. Phys.* 16 (2014) 24473–24478, <http://dx.doi.org/10.1039/C4CP03910F>.
- [29] T. Chen, Capillary force-driven fluid flow in open grooves with different sizes, *J. Thermophys. Heat Transf.* 29 (2015) 594–601, <http://dx.doi.org/10.2514/1.T4313>.
- [30] R.N. Wenzel, Resistance of solid surfaces to wetting by water, *Ind. Eng. Chem.* 28 (1936) 988–994, <http://dx.doi.org/10.1021/ie50320a024>.
- [31] A. Rosenkranz, L. Reinert, C. Gachot, H. Aboufadi, S. Grandthyll, K. Jacobs, et al., Oxide formation, morphology, and nanohardness of laser-patterned steel surfaces, *Adv. Eng. Mater.* 17 (2015) 1234–1242, <http://dx.doi.org/10.1002/adem.201400487>.

III Guiding lubricant on stainless steel surfaces by channel-like structures fabricated by roller- and micro-coining

Philipp G. Grützmacher¹, Andreas Rosenkranz², Emre Atalay¹, Adam Szurdak³, Carsten Gachot⁴, Gerhard Hirt³, Frank Mücklich¹

¹ Chair of Functional Materials, Saarland University, 66123 Saarbrücken, Germany

² Department of Mechanical and Aerospace Engineering, Center for Magnetic Memory and Recording, University of California, 92093, La Jolla, United States

³ Institute of Metal Forming, RWTH Aachen, 52056 Aachen, Germany

⁴ Institute for Engineering Design and Technical Logistics, Tribology Division, Vienna University of Technology, 1060, Vienna, Austria

Published in “*Physica A*” (Impact factor (2017): 2.132)

Accessible online at: <https://doi.org/10.1016/j.physa.2018.03.035>

Own contribution:

Project management; scientific discussion; paper writing; data analysis; measurements: lubricant spreading

Abstract:

Guiding lubricant back to the tribological contact or preventing lubricant migration out of the contact zone can be considered as an efficient approach to significantly reduce friction and wear in machine components. This paper aims at studying the spreading behavior of an additive-free lubricant (PAO 4) on coined stainless steel surfaces (AISI 304) under the effect of a controlled temperature gradient of 2 °C/mm. Single channels and multi-channel samples were manufactured by roller coining and hot micro-coining, respectively. A systematic study of the influence of the geometrical parameters on the resulting spreading behavior has been performed. For polished reference samples, a preferential oil spreading parallel to the temperature gradient was observed which can be correlated with Marangoni forces. For single channels, the spreading velocity increases with an increase in structural depth. Multi-channels show a pronounced anisotropic spreading behavior. Lubricant migration towards the colder side of the sample can be prevented if the structures are oriented perpendicular to the temperature gradient. For multi-channel surfaces, the spreading behavior parallel to the temperature gradient is greatly influenced by the periodicity and area density. Samples with a smaller periodicity and greater area density show a higher spreading velocity of a droplet.

Cite this as:

P.G. Grützmacher, A. Rosenkranz, E. Atalay, A. Szurdak, C. Gachot, G. Hirt, F. Mücklich, Guiding lubricant on stainless steel surfaces by channel-like structures fabricated by roller- and micro-coining, *Phys. A Stat. Mech. Its Appl.* **2018**, 505, 482–489. (<http://doi:10.1016/j.physa.2018.03.035>)



Guiding lubricant on stainless steel surfaces by channel-like structures fabricated by roller- and micro-coining

Philipp G. Grützmacher^{a,*}, Andreas Rosenkranz^b, Emre Atalay^a, Adam Szurdak^c, Carsten Gachot^d, Gerhard Hirt^c, Frank Mücklich^a

^a Department of Functional Materials, Saarland University, 66123 Saarbrücken, Germany

^b Department of Mechanical and Aerospace Engineering, Center for Memory and Recording Research, University of California, 92093 La Jolla, United States

^c Institute of Metal Forming, RWTH Aachen, 52056 Aachen, Germany

^d Institute for Engineering Design and Technical Logistics, Tribology Division, Vienna University of Technology, 1060 Vienna, Austria

HIGHLIGHTS

- Manufacturing of single- and multi-channel surfaces on stainless steel by coining.
- Increasing spreading velocity with deeper and wider single channels.
- Multi-channel surfaces can overcome Marangoni force and prevent lubricant migration.
- For multi-channel surfaces, the periodicity has the strongest influence.

ARTICLE INFO

Article history:

Received 13 February 2018

Available online 6 April 2018

Keywords:

Lubricant migration
Anisotropic spreading
Wetting
Surface structures
Micro-coining

ABSTRACT

Guiding lubricant back to the tribological contact or preventing lubricant migration out of the contact zone can be considered as an efficient approach to significantly reduce friction and wear in machine components. This paper aims at studying the spreading behavior of an additive-free lubricant (PAO 4) on coined stainless steel surfaces (AISI 304) under the effect of a controlled temperature gradient of 2 °C/mm. Single channels and multi-channel samples were manufactured by roller coining and hot micro-coining, respectively. A systematic study of the influence of the geometrical parameters on the resulting spreading behavior has been performed. For polished reference samples, a preferential oil spreading parallel to the temperature gradient was observed which can be correlated with Marangoni forces. For single channels, the spreading velocity increases with an increase in structural depth. Multi-channels show a pronounced anisotropic spreading behavior. Lubricant migration towards the colder side of the sample can be prevented if the structures are oriented perpendicular to the temperature gradient. For multi-channel surfaces, the spreading behavior parallel to the temperature gradient is greatly influenced by the periodicity and area density. Samples with a smaller periodicity and greater area density show a higher spreading velocity of a droplet.

© 2018 Elsevier B.V. All rights reserved.

1. Introduction

Surface structuring of metallic surfaces is a promising approach to optimize their tribological or wetting behavior. In terms of tribology, surface structures can be directly applied to the contact area to significantly reduce friction and/or

* Corresponding author.

E-mail address: philipp.gruetzmacher@uni-saarland.de (P.G. Grützmacher).

wear [1–4]. However, those structures are likely to wear off with time thus losing their intended functionality. In contrast to that, applying surface structures in the close proximity of the contact area where they are not subject to wear creates the possibility to indirectly affect the tribological performance by preventing lubricant migration out of the contact area or guiding lubricant back into the contact area [5–7]. It is well known that the temperature in the contact area of a tribological contact increases due to frictional heating. At local contact spots rather high interface temperatures tend to occur. As a consequence, a temperature gradient evolves thus resulting in a surface tension gradient which can lead to lubricant migration out of the contact area and thus to insufficient lubrication [8]. In rotating machine components, centrifugal forces might additionally drive the lubricant out of the contact zone, also leading to lubricant starvation [9,5].

Therefore, a directional spreading behavior on surfaces is of great interest for tribological applications and microfluidic technologies in which a liquid is transported in open channels. In those channels, capillary forces become important for transporting liquid since conventional pumping methods fail [10]. There are many methods to generate such open channels including photolithography, laser surface patterning or mechanical processes like grinding or embossing [7,11,12]. It is worth to emphasize that the directional spreading behavior depends on the material, the surface chemistry and finally the size of the fabricated structures [13,14].

Using standard photolithographic methods, Seemann et al. fabricated grooves with a rectangular cross-section in silicon having a depth between 100 and 900 nm and a width between 400 nm and 3 μm . They demonstrated that the contact line of the liquid droplet is pinned by the edges of the structures which makes it possible to confine the liquid inside the channels and guide it along them [15]. A number of manuscripts deal with the spreading behavior of liquids on laser patterned surfaces [16,7,13]. Rosenkranz et al. showed an anisotropic spreading behavior for channel-like surface patterns fabricated by direct laser interference patterning (DLIP). Thereby, the anisotropy of the spreading behavior increases with decreasing distance between the channels which can be traced back to more structures in contact with the liquid and therefore a stronger pinning of the contact line [16]. Another study deals with the wetting properties of water on micro-grounded silicon surfaces. The grooves on the surfaces lead to an anisotropic spreading behavior with a preferential spreading along the major axis of the grooves whereas the highest anisotropy is reached for the deepest structures. The reason for the observed anisotropy was attributed to a pinning effect perpendicular to the grooves due to sharp micro-groove tops [17].

The flow behavior of Newtonian fluids in open micro-channels can generally be described by the Lucas–Washburn equation [18–20]:

$$l^2 = \frac{\gamma r \cos \theta}{2\eta} t \quad (1)$$

where l is the position of the traveling meniscus along the channel, γ is the surface tension of the liquid, r is the channel radius, θ is the static contact angle of the liquid on the channel wall, η is the dynamic viscosity of the liquid phase and t is the time. This indicates that the velocity of the liquid inside the channels decreases following a \sqrt{t} behavior. A general expression has been found by Rye et al. to describe the fluid behavior in open micro-channels [21]:

$$l^2 = K(\alpha, \theta) \frac{\gamma T}{\eta} t \quad (2)$$

where $K(\alpha, \theta)$ is a geometric term which depends on the groove angle α and the contact angle θ and T is the structural depth. Eq. (2) shows that the structural depth of the grooves represents a decisive factor regarding the influence on the liquid penetration into channels.

The spreading behavior of liquids on surfaces with temperature gradients has also been investigated in the past. Chen et al. explored the droplet migration of several organic liquids on silanized surfaces under the influence of a temperature gradient between 2 and 4 $^\circ\text{C}/\text{mm}$. They verified that the droplets always move towards the colder side of the sample and therefore towards regions with high surface tension due to thermo-capillary forces. Furthermore, they demonstrated that the contact angle hysteresis causes a pinning of the droplet which prevents spreading below a certain droplet radius [22]. The force by an imbalance of the surface tension along the droplet may even be high enough to cause a droplet to move uphill on an inclined surface against the force of gravity. Chaudhury and Whitesides induced such a behavior of a water droplet by chemically generating a gradient in surface free energy on silicon wafers [23]. Grützmaier et al. investigated the spreading behavior of Poly-(alpha)-olefin (PAO) oil on laser-patterned steel surfaces with a temperature gradient of roughly 2 $^\circ\text{C}/\text{mm}$. They demonstrated a spreading behavior of oil from the hot to the colder side of the sample due to Marangoni forces. Thereby, the spreading velocity parallel to the structures was increased with greater structural depths which can be explained with higher capillary forces [7]. Furthermore, if the groove-like patterns are oriented in a direction perpendicular to the temperature gradient, the spreading velocity can be slowed down because of pinning of the droplet at the edges of the structures.

In this study, the effect of micro-coined surface structures on the spreading behavior of an additive-free PAO oil with a kinematic viscosity of 4 cSt (PAO 4) and a viscosity index of 124 on stainless steel surfaces under the influence of an applied temperature gradient is investigated. Thereby, single channels manufactured by roller-coining and multi-channels fabricated by hot micro-coining are studied. In this context, the structural depth as well as width and periodicity of the structures are varied. In order to measure the droplet spreading an especially designed test rig is used which allows for a precise control of the temperature gradient and the recording of the spreading dynamics.

2. Experimental procedure

2.1. Material

Stainless steel substrates (thickness of roughly 1 mm) with the specification AISI 304 were used in order to fabricate channel-like structures by roller coining and hot micro-coining. After coining, all samples were polished in order to remove the oxide scale and to reduce the surface roughness. Prior to spreading experiments, an extensive cleaning procedure was done for all samples in order to remove any contamination, dust or particles. In this context, a multi-step procedure in an ultrasonic bath with cyclohexane, acetone and isopropanol was done for ten minutes each. Those are important steps in order to ensure reproducible testing conditions for the spreading experiments.

2.2. Surface characterization

While light interferometry WLI (*New View 7300*, Zygo) and laser scanning microscopy LSM (*LEXT OLS 4100*, Olympus) were utilized in order to check the as-fabricated channel-like structures in terms of homogeneity and accuracy. In addition, those techniques were used to measure the structural parameters such as depth, width and periodicity as well as selected surface roughness parameters of all samples. For the surface roughness, ten measurements at different locations of the samples were performed in order to calculate mean values and standard deviations.

2.3. Roller coining

The single channels were fabricated by roller coining which is an incremental forming process using a single pre-structured roller. The roller is made of HS 6-5-2 (1.3343) steel and the channel-like structure on the tool was created by mechanical processing. After manufacturing, the tool was hardened to enable the structuring of stainless steel. Furthermore, the roller coining set-up consists of a pneumatic system using a proportional valve and a pneumatic cylinder. The pneumatic cylinder enables to adjust the force continuously since different structures may require different forming forces. In addition, the tool position is self-adjustable which makes the set-up insusceptible against surface asperities. The applied pneumatic pressure is controlled by LabVIEW while the forming force is measured using a load cell. Single channels with different structural depths, namely 10, 15, 30, 35 and 45 μm , were fabricated. For this purpose, the applied forming force was varied between 100 and 390 N. Those forces were sufficient to precisely fabricate the desired structures since the contact area between tool and substrate is rather small for the roller coining process. It is worth to mention that with increasing structural depth, the width of the channel increases from 150 to 190 μm since the structures on the tool do not have upright walls.

2.4. Hot micro-coining

A closed die hot micro-coining setup was used to generate multi-channel structures on steel substrates. The tools which are in contact with the hot sample (punch, cutting rings and die), are made of hardened hot working tool steel X37CrMoV5-1 (AISI H11). The coning structure of the die was fabricated by laser ablation. Conductive heating of the steel sample is required in order to reduce the flow stress of the material. This approach leads to an increased form filling (ratio of coined depth to structure height of the tool) and reduced load on the die. Using a current density of 35 A/mm² and a heating time of 5 s allows to adjust a homogeneous temperature of 1200 °C in the coined area. All micro-coining experiments were conducted with those parameters. More information with regard to the micro-coining process and set-up can be found elsewhere [24,25].

Two dies (die A and die B) with a nominal structural height but varying periodicity and width were used. The main difference between die A and die B is the periodicity which is two times larger for die A. Two different structural depths (20 μm and 30 μm) were fabricated with each die. Since the channel-like structures do not have upright walls the coined width of the channels increases with the coining depth.

2.5. Spreading experiments

In order to study the oil spreading on the fabricated channel-like structures, an experimental set-up developed by Grützmacher et al. was used [7]. For the reader's convenience, a brief description of this set-up is given here. The sample table is made of copper and can be heated on one side by a heating cartridge (*RS Components*). On the other side, the sample can be cooled down which is realized by water cooling thus making it possible to precisely adjust a temperature gradient of 2 °C/mm. The temperatures needed to estimate the temperature gradient are measured with two NiCr-Ni thermocouples placed symmetrically from the center with a distance of 37.75 mm.

For the spreading experiments, a droplet volume of 1.5 μl was selected since any gravitational effects on the droplet shape can be neglected for this volume [13]. Using a pipette (*Eppendorf*), the oil was applied close to the hot side of the sample. An additive-free Poly-(alpha)-olefin with a kinematic viscosity of 3.9 cSt at 100 °C and a viscosity index of 124 was used for all experiments. The respective properties of the oil are given in Table 1. To record the motion of the droplet, a digital camera (*EOS 500 D*, Canon) was utilized. The spreading of the oil and the corresponding spreading velocity were analyzed using an image processing software (*GIMP 2*) after certain times. The distance of the continuous movement of the droplet front from the hot side to the cold side of the sample, was measured. Finally, the spreading velocity of the droplet was estimated.

Table 1

Properties of the used PAO oil as specified by the supplier.

Property	PAO 4
Kinematic viscosity at 100 °C in cSt	3.9
Kinematic viscosity at 40 °C in cSt	16.8
Viscosity index	124
Specific gravity	0.82

Table 2

Summary of the measured surface roughness parameters of the polished reference.

Parameter	$R_a/\mu\text{m}$	$R_q/\mu\text{m}$	R_{sk}
Polished reference	0.02 ± 0.004	0.03 ± 0.05	0.001 ± 0.001

Table 3

Summary of structural depth and width as well as measured skewness for all single-channel structures fabricated by roller coining.

Sample	Coining force/N	Structural depth/ μm	Width/ μm	R_{sk}
D10	100	10.65 ± 0.51	150 ± 10	-1.74 ± 0.09
D15	170	15.54 ± 0.45	160 ± 10	-1.71 ± 0.02
D30	250	29.67 ± 0.22	160 ± 10	-1.69 ± 0.01
D35	320	35.86 ± 0.12	170 ± 10	-1.64 ± 0.01
D45	390	45.21 ± 0.18	190 ± 10	-1.57 ± 0.01

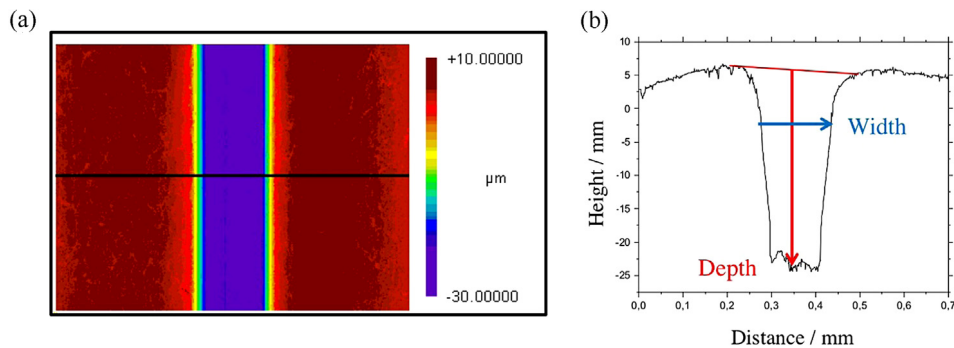


Fig. 1. WLI micrograph (a) and corresponding surface profile (b) measured along the black line in (a) for the single-channel structure with a structural depth of 30 μm .

3. Results and discussion

3.1. Single-channel structures

Prior to the spreading experiments, the surface topography of the polished reference samples and the as-fabricated single-channel structures were studied by WLI. Selected surface roughness parameters were chosen in order to describe the surface topography. Table 2 summarizes the measured values for the polished reference sample.

As can be seen in Table 2, the respective roughness values are in the nanometer range which reflects the mirror-like surface finish and the high surface quality of the reference samples. The measured value for the skewness is around 0. Consequently, no pronounced valleys or peaks can be found which also correlates well with the mirror-like surface finish.

Fig. 1 displays exemplarily the resulting surface topography of the single-channel structure with a structural depth of 30 μm after roller coining.

As can be seen in Fig. 1, the single-channel structures can be fabricated with high accuracy and rather steep wall angles, which make those samples interesting for spreading experiments. In Fig. 1(b), it can be seen that the roller coining leads to a certain material pile-up which, can be explained by severe plastic deformation involved in the manufacturing process.

Table 3 summarizes the structural depth and width as well as the measured skewness of all single-channel structures fabricated by roller coining.

Table 3 demonstrates that the structural depth increases with increasing coining force while keeping the width fairly constant. All presented standard deviations are well below 10% which underlines the high reproducibility and accuracy of the roller coining process. It is possible to observe that the standard deviations are slightly reduced with an increase in coining force. This can be traced back to reduced elastic effects inside the setup [26]. With regard to the measured skewness, it can

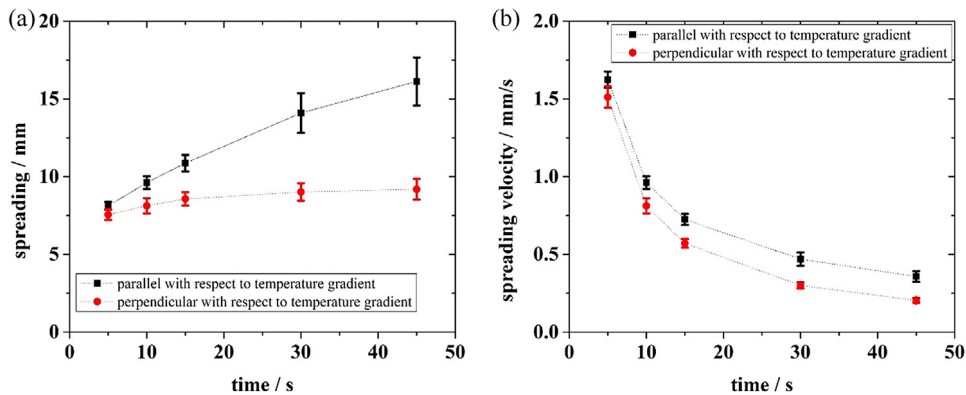


Fig. 2. Spreading behavior (a) and spreading velocity (b) measured parallel and perpendicular with respect to the temperature gradient on a polished reference sample.

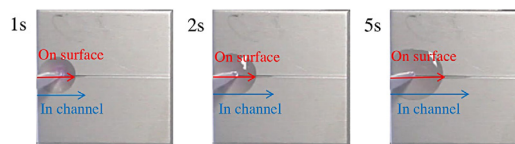


Fig. 3. Temporal evolution of the spreading behavior measured for a single-channel structure with a structural depth of $30\ \mu\text{m}$.

be seen that all single-channel structures have a negative skewness with values ranging between -1.74 and -1.57 . Those values can be well explained by the plateau-like surface topography of the single-channel structures. Additionally, a slight decrease of the skewness with increasing coining force can be noticed.

Before investigating the spreading behavior of the single-channel structures, polished samples were used in order to study the reference state. Since the spreading behavior is studied using a certain temperature gradient, as introduced in Section 2.5, two different directions, namely parallel and perpendicular with respect to the temperature gradient, need to be distinguished. Fig. 2 shows the spreading behavior as well as the respective spreading velocity measured for a polished reference.

The figure clearly reveals that the spreading behavior parallel to the temperature gradient is more pronounced compared to the values observed in the perpendicular direction. This can be well correlated with the applied temperature gradient. It can be noticed that the standard deviations slightly increase over time, which can be explained by a pinning of the contact line which gets more pronounced over time due to a decreasing droplet volume. In addition, the velocity profile of both directions shows an asymptotic behavior with a slightly increased velocity in direction of the temperature gradient over time.

Afterwards, the respective spreading behavior of the single-channels structures was studied with the channels being oriented parallel to the temperature gradient. Fig. 3 shows the temporal evolution of the spreading behavior measured on a single-channel structure with a structural depth of $30\ \mu\text{m}$.

Based upon this figure, it can be seen that the droplet propagation inside the channels is faster than the propagation on the surface. Consequently, it can be concluded that the oil in the channel runs ahead of the oil droplet on the surface. Since it can be assumed that the oil spreading inside the channels and the droplet spreading on the surface are closely connected the lubricant velocity inside the channels (lubricant penetration) is measured.

Fig. 4 presents the spreading behavior and spreading velocity in the channels of all fabricated single-channel structures.

It can be clearly seen that both the spreading behavior and the spreading velocity increase with an increasing structural depth. There seems to be a clear connection between the spreading velocity inside the channels and the radius of the respective channels. To explain the increasing velocity, several factors have to be taken into consideration. First, an increasing capillary radius goes hand in hand with higher capillary forces. This can be well correlated with an enlarged spreading velocity. In addition, the resistance against motion (spreading) in the direction of the temperature gradient due to friction at the channel walls decreases with an increase in capillary diameter since a smaller portion of the liquid is in contact with the channel walls.

Furthermore, a decline in spreading velocity over time can be noticed. This can be attributed to an increase in lubricant viscosity as lubricant migrates towards the colder side of the sample where the temperature drops from roughly $125\ ^\circ\text{C}$ to $51\ ^\circ\text{C}$ (measured at the positions of the thermocouples). Additionally, the capillary length is reduced as liquid travels inside the channels towards the colder side of the sample which results in smaller capillary forces following the Lucas–Washburn-equation (see Section 1). It can be seen from Eq. (1) that there is a \sqrt{t} dependency of the position of the meniscus l or in

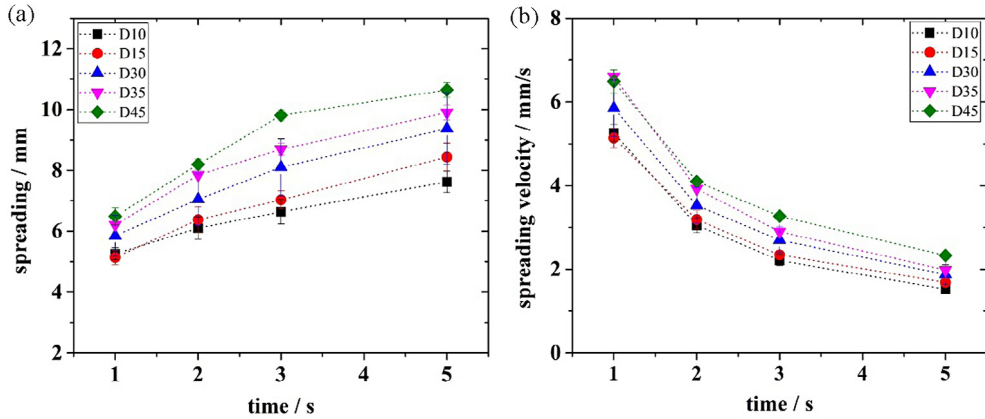


Fig. 4. Spreading behavior (a) and spreading velocity (b) in the channel (parallel to the temperature gradient) measured for all single-channel structures.

Table 4

Summary of structural depth and width as well as periodicity for all multi-channel structures fabricated by hot micro-coining.

Sample	Force/kN	Structural depth/ μm	Width/ μm	Periodicity/ μm
A20	40	22.84 ± 2.18	259 ± 16	795 ± 5
A30	50	33.53 ± 1.76	278 ± 2	799 ± 5
B20	50	21.12 ± 1.41	210 ± 10	493 ± 7
B30	70	30.80 ± 1.52	214 ± 7	496 ± 5

other words on the spreading velocity. This \sqrt{t} behavior can be clearly observed in Fig. 4. The general equation for open micro-channels by Rye et al. (see Eq. (2), Section 1) allows the conclusion that the main influencing factor is the structural depth.

3.2. Multi-channel structures

In a next step, the spreading velocity of multi-channels fabricated by hot micro-coining was investigated to find the most effective structures to either guide lubricant or stop lubricant migration. Thereby, the grooves are oriented perpendicular or parallel to the temperature gradient, respectively.

The geometrical parameters of the micro-coined structures are varied to investigate the influence of the structural depth as well as the structural width and periodicity. As can be seen from the low standard deviations presented in Table 4, the hot micro-coining process is, similar to roller coining, highly accurate.

From Fig. 5, it can be seen that, irrespective of the structure geometry, no lubricant migration along the temperature gradient towards the cold side of the sample can be observed if the micro-coined structures are oriented perpendicular to the temperature gradient. This effect results from the pinning of the droplet's contact line at the sharp edges of the structures [27,28]. This pinning is so pronounced that Marangoni forces acting in direction of the temperature gradient are not sufficient to overcome/overpass a single structure. The droplet is rather elongated along the primary axis of the structures due to capillary forces. Hence, the forces induced by the micro-coined structures dominate the Marangoni forces triggered by the temperature gradient. This indicates that the used structures are suitable to manipulate the lubricant migration and to overcome forces coming from a temperature gradient. Consequently, lubricant migration towards the cold side of the sample can be prevented, if the surface structures are oriented perpendicular to the temperature gradient.

To elicit the possibility of guiding lubricant along the major axis of the micro-coined structures, the samples are oriented in such a way that the structures point in the direction of the temperature gradient. As already seen for the single channels, the lubricant penetration inside the channels is faster than the droplet spreading on the sample surface. Thereby, the liquid inside the channels runs ahead of the droplet thus pulling the droplet over the surface by creating space in the channels as the lubricant migrates inside the channels. It can be assumed that the global spreading behavior is more decisive for most applications. Consequently, this behavior will be discussed in detail for the multi-channel samples in the following section.

Fig. 6 shows the lubricant spreading on different multi-channel samples. It can be observed that the samples which were coined with the same die but a higher coining pressure resulting in a greater structural depth and width show a rather similar spreading behavior. However, comparing samples fabricated with two different dies and having therefore different periodicities, there is a clear tendency for a higher spreading velocities with decreasing periodicity. A smaller periodicity leads to a higher number of surface structures in contact with the liquid considering a similar initial contact area of the droplet with the sample. More surface structures in contact induce higher capillary forces since it can be assumed that capillary forces arising from the individual channels can be summed up. Furthermore, the pinning of the contact line

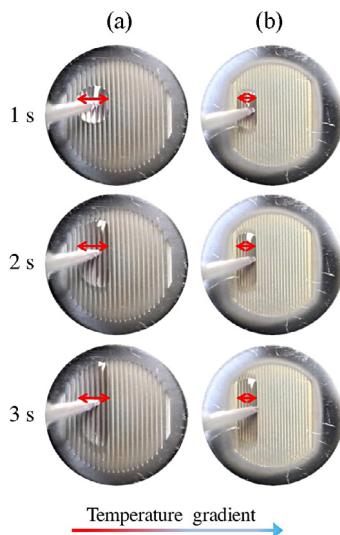


Fig. 5. Temporal evolution of the droplet propagation for A20 (a) and B20 (b) under the influence of a temperature gradient oriented perpendicular to the channel orientation.

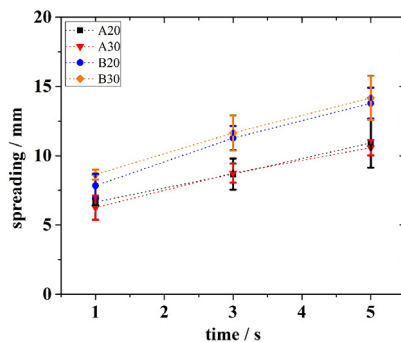


Fig. 6. Spreading behavior versus time for all multi-channel structures with different structural parameters.

increases with smaller periodicities. If the droplet pinning is stronger and thus the liquid spreading across the structures is prevented, a higher amount of liquid is available which can be guided along the channel-like structures thus further increasing the spreading velocity.

Summarizing, the geometrical parameters like structural depth and width seem to have a minor effect on the global spreading behavior of a droplet for the multi-channel samples. In contrast to that, the area density and periodicity of the structures have a significant effect on the spreading behavior.

4. Conclusions

The aim of this study was to investigate the spreading behavior of a lubricant (PAO 4) on micro-coined stainless steel surfaces under the effect of a controlled temperature gradient of 2 °C/mm. Single channels were manufactured by roller coining whereas multi-channel structures were produced by hot micro-coining. For single channels, the coining force was increased successively to increase the structural depth as well as width. For multi-channel structures, two different dies have been used to change the periodicity and thus the area density of the samples. Additionally, the coining force was increased to produce deeper and wider channels. The following conclusions can be drawn based upon the experimental results:

- A preferential oil spreading on a polished reference in the direction of the temperature gradient can be observed. This can be well correlated with Marangoni forces, leading to a lubricant migration towards the colder side of the sample.
- Experiments with single channels demonstrate that the lubricant penetration inside the channels is faster than the droplet spreading on the surface. Thereby, the spreading velocity inside the channels increases with an increasing depth of the single channels. A decline in the spreading velocity inside the channels can be well described with an

increasing lubricant viscosity as the lubricant approaches the colder side of the sample and by the Lucas–Washburn equation which predicts a smaller spreading velocity over time.

- Multi-channels show a pronounced anisotropic spreading behavior. Thereby, lubricant migration towards the colder side of the sample can be prevented if the structures are oriented perpendicular with respect to the temperature gradient. If the structures are oriented parallel to the temperature gradient, the structural depth and width only play a minor role with respect to the spreading behavior whereas the periodicity and therefore the area density have a strong impact on the spreading behavior. Samples with a smaller periodicity and greater area density show a higher spreading velocity of a droplet on the surface.

Acknowledgments

The present work is supported by funding from the Deutsche Forschungsgemeinschaft, Germany (DFG, projects: MU 959/27-2 and HI 790/33-2 within the SPP 1551). Andreas Rosenkranz gratefully acknowledges the Feodor-Lynen Research Fellowship granted by the Alexander von Humboldt foundation.

References

- [1] C. Gachot, A. Rosenkranz, S.M. Hsu, H.L. Costa, A critical assessment of surface texturing for friction and wear improvement, *Wear* 372–373 (2017) 21–41. <http://dx.doi.org/10.1016/j.wear.2016.11.020>.
- [2] A. Rosenkranz, L. Reinert, C. Gachot, F. Mücklich, Alignment and wear debris effects between laser-patterned steel surfaces under dry sliding conditions, *Wear* 318 (2014) 49–61. <http://dx.doi.org/10.1016/j.wear.2014.06.016>.
- [3] D.Z. Segu, S.G. Choi, J.H. Choi, S.S. Kim, The effect of multi-scale laser textured surface on lubrication regime, *Appl. Surf. Sci.* 270 (2013) 58–63. <http://dx.doi.org/10.1016/j.apsusc.2012.12.068>.
- [4] P.G. Grützmaker, A. Rosenkranz, A. Szurdak, C. Gachot, G. Hirt, F. Mücklich, Effects of multi-scale patterning on the run-in behavior of steel-alumina pairings under lubricated conditions, *Adv. Eng. Mater.* (2017) 1700521. <http://dx.doi.org/10.1002/adem.201700521>.
- [5] P. Comanns, G. Buchberger, A. Buchsbaum, R. Baumgartner, A. Kogler, S. Bauer, W. Baumgartner, Directional, passive liquid transport: The Texas horned lizard as a model for a biomimetic “liquid diode”, *J. R. Soc. Interface.* 12 (2015) 20150415. <http://dx.doi.org/10.1098/rsif.2015.0415>.
- [6] A. Rosenkranz, P.G. Gruetzmacher, A. Szurdak, C. Gachot, G. Hirt, F. Mücklich, F. Muecklich, Synergetic effect of laser patterning and micro coining for controlled lubricant propagation, *Surf. Topogr. Metrol. Prop.* 4 (2016) 34008. <http://dx.doi.org/10.1088/2051-672X/4/3/034008>.
- [7] P.G. Grützmaker, A. Rosenkranz, C. Gachot, How to guide lubricants – Tailored laser surface patterns on stainless steel, *Appl. Surf. Sci.* 370 (2016) 59–66. <http://dx.doi.org/10.1016/j.apsusc.2016.02.115>.
- [8] D.T. Wasan, Droplets speeding on surfaces, *Science* 291 (80) (2001) 605–606. <http://dx.doi.org/10.1126/science.1058466>.
- [9] P.G. Grützmaker, A. Rosenkranz, S. Rammacher, C. Gachot, F. Mücklich, The influence of centrifugal forces on friction and wear in rotational sliding, *Tribol. Int.* 116 (2017) 256–263. <http://dx.doi.org/10.1016/j.triboint.2017.07.021>.
- [10] D. Yang, M. Krasowska, C. Priest, J. Ralston, Dynamics of capillary-driven liquid–liquid displacement in open microchannels, *Phys. Chem. Chem. Phys.* 16 (2014) 24473–24478. <http://dx.doi.org/10.1039/C4CP03910F>.
- [11] F.F. Ouali, G. McHale, H. Javed, C. Trabi, N.J. Shirtcliffe, M.I. Newton, Wetting considerations in capillary rise and imbibition in closed square tubes and open rectangular cross-section channels, *Microfluid. Nanofluidics* 15 (2013) 309–326. <http://dx.doi.org/10.1007/s10404-013-1145-5>.
- [12] D. Xia, L.M. Johnson, G.P. López, Anisotropic wetting surfaces with one-dimensional and directional structures: Fabrication approaches, wetting properties and potential applications, *Adv. Mater.* 24 (2012) 1287–1302. <http://dx.doi.org/10.1002/adma.201104618>.
- [13] M. Hans, F. Müller, S. Grandthyll, S. Hüfner, F. Mücklich, Anisotropic wetting of copper alloys induced by one-step laser micro-patterning, *Appl. Surf. Sci.* 263 (2012) 416–422. <http://dx.doi.org/10.1016/j.apsusc.2012.09.071>.
- [14] L. Zhu, Y. Feng, X. Ye, Z. Zhou, Tuning wettability and getting superhydrophobic surface by controlling surface roughness with well-designed microstructures, *Sensors Actuators A* 130–131 (2006) 595–600. <http://dx.doi.org/10.1016/j.sna.2005.12.005>.
- [15] R. Seemann, M. Brinkmann, E.J. Kramer, F.F. Lange, R. Lipowsky, Wetting morphologies at microstructured surfaces, *Proc. Natl. Acad. Sci.* 102 (2005) 1848–1852. <http://dx.doi.org/10.1073/pnas.0407721102>.
- [16] A. Rosenkranz, S. Fleischmann, C. Gachot, F. Mücklich, Anisotropic spreading behavior of PAO oil on laser-patterned stainless steel surfaces, *Adv. Eng. Mater.* 17 (2015) 1645–1651. <http://dx.doi.org/10.1002/adem.201500115>.
- [17] P. Li, J. Xie, J. Cheng, K.K. Wu, Anisotropic wetting properties on a precision-ground micro-V-grooved Si surface related to their micro-characterized, *J. Micromech. Microeng.* 75004 (2014) 75004. <http://dx.doi.org/10.1088/0960-1317/24/7/075004>.
- [18] R. Lucas, Ueber das zeitgesetz des kapillaren aufstiegs von flüssigkeiten, *Kolloid Z.* 23 (1918) 15–22. <http://dx.doi.org/10.1007/BF01461107>.
- [19] E.W. Washburn, The dynamics of capillary flow, *Phys. Rev.* 17 (1921) 273–283. <http://dx.doi.org/10.1103/PhysRev.17.273>.
- [20] T.W. Sowers, R. Sarkar, S.E. Prameela, E. Izadi, J. Rajagopalan, Capillary driven flow of polydimethylsiloxane in open rectangular microchannels, *Soft Matter* 12 (2016) 5818–5823. <http://dx.doi.org/10.1039/c6sm00897f>.
- [21] R.R. Rye, J. a. Mann, F.G. Yost, The flow of liquids in surface grooves, *Langmuir* 12 (1996) 555–565. <http://dx.doi.org/10.1021/la9500989>.
- [22] J.Z. Chen, S.M. Troian, A. a. Darhuber, S. Wagner, Effect of contact angle hysteresis on thermocapillary droplet actuation, *J. Appl. Phys.* 97 (2005) 14906. <http://dx.doi.org/10.1063/1.1819979>.
- [23] M.K. Chaudhury, G.M. Whitesides, How to make water run uphill, *Science* 256 (1992) 1539–1541. <http://dx.doi.org/10.1126/science.256.5063.1539>.
- [24] A. Szurdak, A. Rosenkranz, C. Gachot, G. Hirt, F. Mücklich, Manufacturing and tribological investigation of hot micro-coined lubrication pockets, *Key Eng. Mater.* 611–612 (2014) 417–424. <http://dx.doi.org/10.4028/www.scientific.net/KEM.611-612.417>.
- [25] A. Szurdak, G. Hirt, Finite element analysis of manufacturing micro lubrication pockets in high strength steels by hot micro-coining, *Steel Res. Int.* 86 (2015) 257–265. <http://dx.doi.org/10.1002/srin.201300475>.
- [26] A. Szurdak, G. Hirt, Development and experimental verification of a new roller-coining setup to texture flat and curved surfaces, *Appl. Mech. Mater.* 794 (2015) 128–135. <http://dx.doi.org/10.4028/www.scientific.net/AMM.794.128>.
- [27] A.D. Sommers, A.M. Jacobi, Creating micro-scale surface topology to achieve anisotropic wettability on an aluminum surface, *J. Micromech. Microeng.* 16 (2006) 1571–1578. <http://dx.doi.org/10.1088/0960-1317/16/8/018>.
- [28] D. Quéré, Wetting and roughness, *Annu. Rev. Mater. Res.* 38 (2008) 71–99. <http://dx.doi.org/10.1146/annurev.matsci.38.060407.132434>.

IV Lubricant migration on stainless steel induced by bio-inspired multi-scale surface patterns

Philipp G. Grützmacher¹, Andreas Rosenkranz², Adam Szurdak³, Carsten Gachot⁴, Gerhard Hirt³, Frank Mücklich¹

¹ Chair of Functional Materials, Saarland University, 66123 Saarbrücken, Germany

² Department of Mechanical and Aerospace Engineering, Center for Magnetic Memory and Recording, University of California, 92093, La Jolla, United States

³ Institute of Metal Forming, RWTH Aachen, 52056 Aachen, Germany

⁴ Institute for Engineering Design and Technical Logistics, Tribology Division, Vienna University of Technology, 1060 Vienna, Austria

Published in “*Materials and Design*” (Impact factor (2017): 4.525)

Accessible online at: <https://doi.org/10.1016/j.matdes.2018.04.035>

Own contribution:

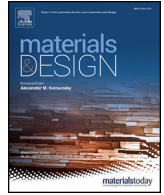
Project management; scientific discussion; paper writing; data analysis; design of test rig; sample preparation; laser surface patterning; measurements: lubricant spreading, laser scanning microscopy

Abstract:

This manuscript aims at investigating the spreading dynamics of an additive-free Poly-(alpha)-olefin (PAO) oil on stainless steel surfaces (AISI 304) having multi-scale surface patterns with and without an applied temperature gradient. For this purpose, single-scale patterns were fabricated by micro-coining, direct laser interference patterning and ultrashort-pulse laser patterning. In a second step, multi-scale patterns were realized by superimposing micro-coined surfaces with the respective laser patterns. In order to precisely adjust the temperature gradient and to study the lubricant's migration on the patterned surfaces, a specially designed test rig was used. Experiments without temperature gradient demonstrated a preferential lubricant spreading parallel to the pattern for all samples. In this context, the multi-scale samples showed a faster lubricant spreading compared to the single-scale patterns, which can be attributed to additional capillary forces and an increased roughness. In case of an applied temperature gradient, purely micro-coined samples showed an increased rate of lubricant spreading compared to the other single-scale samples due to the larger volume to surface area ratio. The multi-scale surfaces demonstrated again the fastest lubricant spreading, which clearly underlines the ability to actively guide lubricant by multi-scale patterning.

Cite this as:

P.G. Grützmacher, A. Rosenkranz, A. Szurdak, C. Gachot, G. Hirt, F. Mücklich, Lubricant migration on stainless steel induced by bio-inspired multi-scale surface patterns, *Mater. Des.* **2018**, 150, 55–63. (<http://doi:10.1016/j.matdes.2018.04.035>)



Lubricant migration on stainless steel induced by bio-inspired multi-scale surface patterns

Philipp G. Grützmacher^{a,*}, Andreas Rosenkranz^b, Adam Szurdak^c, Carsten Gachot^d, Gerhard Hirt^c, Frank Mücklich^a

^a Department of Functional Materials, Saarland University, 66123 Saarbrücken, Germany

^b Department of Mechanical and Aerospace Engineering, Center for Memory and Recording Research, University of California, 92093 La Jolla, United States

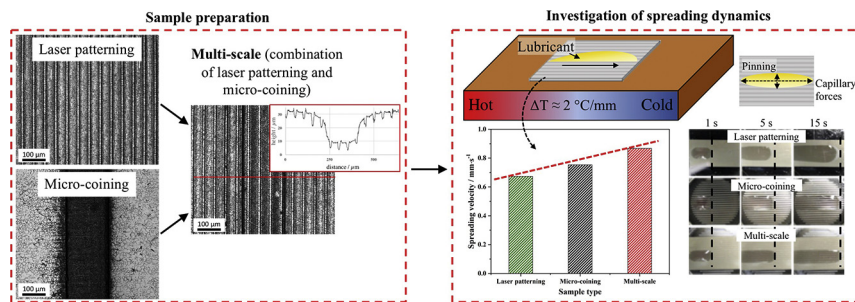
^c Institute of Metal Forming, RWTH Aachen, 52056 Aachen, Germany

^d Institute for Engineering Design and Technical Logistics, Tribology Division, Vienna University of Technology, 1060 Vienna, Austria

HIGHLIGHTS

- Accurate manufacturing of multi-scale surfaces on stainless steel by combining laser patterning and micro-coining.
- Higher capillary forces and increased roughness lead to fastest preferential lubricant spreading for multi-scale surfaces.
- Experiments with additional temperature gradient were performed on a specially designed experimental setup.
- Similar to the experiments without temperature gradient, the multi-scale samples show the fastest lubricant spreading.

GRAPHICAL ABSTRACT



ARTICLE INFO

Article history:

Received 28 December 2017

Received in revised form 10 April 2018

Accepted 12 April 2018

Available online 13 April 2018

Keywords:

Lubricant spreading
Micro-coining
Laser patterning
Multi-scale
Wetting

ABSTRACT

This manuscript aims at investigating the spreading dynamics of an additive-free Poly-(alpha)-olefin (PAO) oil on stainless steel surfaces (AISI 304) having multi-scale surface patterns with and without an applied temperature gradient. For this purpose, single-scale patterns were fabricated by micro-coining, direct laser interference patterning and ultrashort-pulse laser patterning. In a second step, multi-scale patterns were realized by superimposing micro-coined surfaces with the respective laser patterns. In order to precisely adjust the temperature gradient and to study the lubricant's migration on the patterned surfaces, a specially designed test rig was used. Experiments without temperature gradient demonstrated a preferential lubricant spreading parallel to the pattern for all samples. In this context, the multi-scale samples showed a faster lubricant spreading compared to the single-scale patterns, which can be attributed to additional capillary forces and an increased roughness. In case of an applied temperature gradient, purely micro-coined samples showed an increased rate of lubricant spreading compared to the other single-scale samples due to the larger volume to surface area ratio. The multi-scale surfaces demonstrated again the fastest lubricant spreading, which clearly underlines the ability to actively guide lubricant by multi-scale patterning.

© 2018 Elsevier Ltd. All rights reserved.

1. Introduction

Over thousands and millions of years of evolution, nature has created human beings, animals and insects with outstanding properties,

* Corresponding author.

E-mail address: philipp.gruetzmacher@uni-saarland.de (P.G. Grützmacher).

which are able to adapt to extreme conditions. An impressive example is the lotus leaf, which combines superhydrophobic properties with self-cleaning. In order to achieve that, hierarchical structures are covered with a wax to modify the surface topography and the surface chemistry at the same time [1–3]. The gecko foot is another example in the context of functional multi-scale surfaces [4–6]. More examples based upon hierarchical surface topographies such as the non-fogging and super-hydrophobic eyes of mosquitos [7] or the colorful wings of butterflies [8–10] can be found in nature.

Moreover, nature provides unique solutions to adapt to extreme conditions such as moisture harvesting in very arid regions. The skin of the Texas horned lizard consists of capillaries on different size scales, which induce a preferential flow of water towards the snout of the lizards [11]. It is straight forward to postulate that creating surfaces, which mimic natural surfaces with outstanding properties in terms of guiding liquids and adjusting specific wetting properties, can have a huge impact in mechanical components dealing with microfluidic phenomena. In this context, the key aspect is to understand the connection between the material's properties, the surface structure on different scales (ranging from the nano- to the macro-scale) as well as the resulting macroscopic properties [12]. Regarding wetting properties, it is well known that wetting depends on the surface chemistry and the surface roughness [13–16].

Numerous manuscripts have been published dealing with different experimental techniques to fabricate multi-scale surfaces and their impact on the resulting wetting properties. Cha et al. created superhydrophobic silicon surfaces by combining deep reactive ion and plasma etching [17]. A similar approach was presented by Kwon et al. ending up in contact angles of larger than 173° and small tilting angles of about 0.6° [18]. Using embossing and femtosecond laser processing, Zhang et al. demonstrated that self-organized conical spikes with nano-scale roughness can greatly affect the wettability and the degree of anisotropy [19]. Besides that, surface structures with a preferential orientation can strongly affect the wetting properties. Chen et al. fabricated superhydrophobic 200 μm wide strips on silicon to tune the pinning behavior of water droplets [20]. Hans et al. patterned copper alloys by direct laser interference patterning (DLIP) and proved an anisotropic wetting behavior for line-like surface patterns with features sizes on the micron scale [21]. In addition, Rosenkranz et al. pointed out that the periodicity and the aspect ratio (structural depth divided by periodicity) of laser patterned surfaces are the most influencing factors with regard to the anisotropic spreading behavior [22]. Based upon [22], Rosenkranz et al. created multi-scale surfaces by combining DLIP and micro-coining. They demonstrated that multi-scale surfaces showed the greatest anisotropic spreading behavior [23]. All these studies aim at fabricating channel-like structures with a preferential orientation, which pin the droplet's front in the direction perpendicular to the structures and elongate the droplet by inducing capillary forces parallel to the structures [24–26]. Thereby, the pinning of the droplet's front increases with a decreasing periodicity of the structures as well as deeper structures with sharper edges [22,24,27]. Similarly, the capillary forces increase with an increasing capillary radius or structural depth as well as smaller periodicity since this results in a larger number of channels in contact to the liquid [22,27,28].

An interesting application for surfaces with an anisotropic spreading behavior are lubricated tribological components on which a temperature gradient evolves with time. As a result of frictional heating a temperature gradient and thus a surface tension gradient arises on the surface [29]. In these contacts, the acting Marangoni forces lead to a migration of lubricant from hotter to colder regions and therefore to a migration of lubricant out of the tribological contact where it is most urgently needed [30–33].

The aim of this study is to investigate the effect of multi-scale patterns on the spreading behavior of an additive-free Poly-(alpha)-olefin (PAO) oil with a dynamic viscosity of 3.19 mPa.s (PAO 4) and a viscosity index of 124. Therefore, stainless steel (AISI 304) was patterned by a

combination of micro-coining and DLIP as well as by micro-coining and ultrashort-pulse laser patterning (UPLP). To study the effect of a temperature gradient on the lubricant migration the experiments were performed on an especially designed test rig, which allows for a precise adjustment of the temperature gradient on the sample's surface.

2. Experimental procedure

2.1. Materials

Flat, mirror-polished stainless steel specimens (AISI 304) with a thickness of approximately 1 mm and a diameter of 25 mm were used as a base material. The chemical composition of the steel is summarized in Table 1.

After micro-coining, a gentle polishing treatment was done to lower the surface roughness. After each individual fabrication step (micro-coining and laser patterning), the samples were cleaned using a multi-step procedure in an ultrasonic bath. The procedure was started with cyclohexane, followed by acetone thus ending up in isopropanol. The cleaning time for each step was kept constant at 10 min. This procedure ensures the removal of any polar and non-polar contamination as well as of dust and other particles.

For the spreading experiments, a synthetic Poly-alpha-olefin oil (provided by Castrol) was used. Since this oil does not contain any additives, the potential influence of said additives on the resulting spreading properties can be neglected. A summary of the physical properties of the oil used is given in Table 2.

2.2. Analysis of the surface topography

The resulting surface topography of the laser patterned, the micro-coined as well as the multi-scale samples was investigated by laser scanning microscopy LSM (*LEXT OLS 4100, Olympus*). Special emphasis was laid on the homogeneity and accuracy of the as-fabricated samples. Structural parameters of all specimens such as periodicity, depth and width as well as surface roughness parameters such as the root-mean-square roughness and skewness were evaluated. Ten measurements at randomly selected positions of the sample were conducted to calculate mean values and standard deviations.

2.3. Direct laser interference patterning (DLIP)

A pulsed solid-state Nd:YAG laser (*Quanta Ray PRO 290, Newport Spectra Physics*) with a fundamental wavelength of 1064 nm, an average power of 20 W, a pulse duration of 10 ns and a frequency of 10 Hz was used to fabricate channel-like structures with features sizes in the lower micron regime. For the laser patterning, the wavelength was set to 532 nm and the samples were produced under normal atmospheric conditions using just one laser shot. The laser patterning using the ns-laser was based upon an interference approach. First, the primary beam passed through an attenuator, a shutter system and a lens (focal length 2000 mm) in order to adjust the laser power precisely, to select individual laser pulses and to increase the power density, respectively. Afterwards, the primary beam was split into two beams by means of a suitable beam-splitter. A mirror system guided the individual sub-beams to the surface where both sub-beams interfered with each other. The laser power and laser fluence were kept constant for all specimens at 4.4 W and 50 J/cm², respectively. Thereby, a sample area of 15 mm × 20 mm was patterned. Further details related to DLIP have already been published elsewhere [34,35]. Based upon previous research

Table 1

Chemical composition of the steel in wt% as specified by the supplier.

Specimens	Cr	Ni	Mn	Si	C	Fe
Stainless steel (AISI 304)	18	10	2	1	0.1	Balance

Table 2
Properties of the used PAO oil as specified by Castrol.

Property	PAO 4
Dynamic viscosity at 100 °C in mPa.s	3.19
Dynamic viscosity at 40 °C in mPa.s	13.73
Viscosity index	124
Specific gravity	0.82

work published by the authors studying the anisotropic spreading of oil on laser patterned surfaces [22,23], samples with a periodicity of 5 μm and a structural depth of 1 μm were selected for the current study.

2.4. Ultrashort-pulse laser patterning (UPLP)

A passively mode-locked Ti:Sa ultra-short pulse laser (*Spitfire, Newport Spectra Physics*) with a repetition rate of 1 kHz and a wavelength of 800 nm was used to produce channel-like structures with different structural parameters. The underlying physical principle of this laser system is based upon chirped pulse amplification, which enables the production of pulses with pulse durations in the range of pico- or femtoseconds. The pulse duration (FWHM) measured and controlled by autocorrelation was kept constant at 130 ± 20 fs for all fabricated samples. The primary beam with a diameter of approximately 10 mm was focused using a lens having focal length of 100 mm onto the specimen's surface. The steel substrate was located in the focal point and mounted on an automatic translation table (x-y-stage), which was synchronized with the laser. In contrast to DLIP, the laser patterning performed by the fs-laser is more comparable to sequential laser writing. Consequently, individual channels were fabricated separately based upon the interconnection of the translation stage and the controllable laser output (on/off times). Two different periodicities, namely 50 and 100 μm , were fabricated while keeping the structural depth and width constant at 4 and 16 μm , respectively. In order to generate a structural depth of 4 μm , the individual channel needed to be overpassed four times while keeping the velocity of the translation stage constant at 10 mm/s. The laser power and the resulting laser fluence were set to 60.4 mW and 13.3 J/cm², respectively. As for the DLIP samples an area of 15 mm \times 20 mm was patterned.

2.5. Micro-coining

In order to fabricate micro-coined samples, a closed die hot micro-coining setup was used. The coining tool (punch, ring and die) was made of hardened steel X37CrMoV5-1 (AISI H11) and the structure of the die was generated by laser ablation. Prior to micro-coining, the steel sample was conductively heated to lower the flow stress of the material. In addition, the load on the die was reduced due to heating thus reducing the risk of tool damage. A current density of 35 A/mm² and heating time of 5 s were selected to adjust a temperature to 1200 °C in a short period of time. The experimental parameters were kept constant for all samples fabricated by micro-coining. A die with a nominal structural height of 100 μm was used to produce the micro-coined samples with a structural depth of 22 μm and a structural width of 260 μm . The respective structural depth was adjusted by changing the coining force. In this manner, samples with an outer diameter of 25 mm were produced whereby an area of 20 mm in diameter was covered with the line-like pattern. More information regarding the process and the set-up can be found elsewhere [36,37].

2.6. Spreading experiments

The resulting spreading behavior of lubricant on all surfaces was studied using an experimental set-up developed by Grützmaier et al., which is schematically shown in Fig. 1 (a) [27]. The underlying principle shall be described briefly. A precisely adjustable temperature

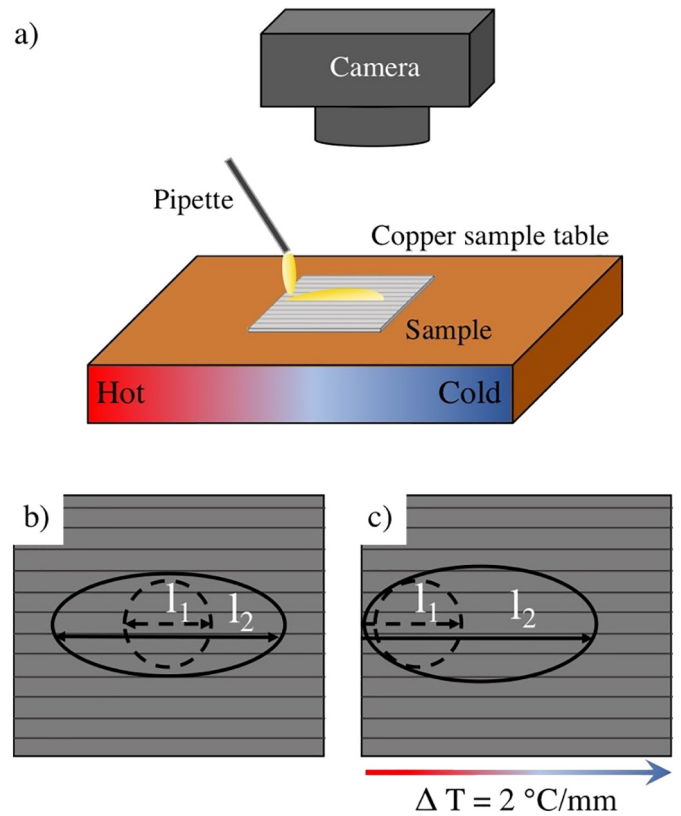


Fig. 1. (a) Schematic illustration of the experimental set-up as well as the measuring strategy in order to characterize the lubricant spreading (b) without and (c) with temperature gradient. The dotted line in (b) and (c) represents the initial droplet with a length l_1 parallel to the pattern directly after deposition. The solid line shows the droplet after a certain time with an increased droplet length l_2 .

gradient was realized by a heating cartridge (*RS Components*) on one side and water cooling on the other side of the sample stage made of copper. Consequently, a temperature gradient of 2 °C/mm was set. Further details have already been published elsewhere [27].

For the spreading experiments, a lubricant droplet was applied to the specimen using a pipette (*Eppendorf*). In this context, a droplet volume of 1.5 μl was selected in order to avoid any influence of gravitation [21]. The motion of the droplet was recorded by a digital camera (*EOS 500 D, Canon*). The spreading of the lubricant was analyzed using an image processing software (*GIMP 2*) after certain times. For preliminary tests without temperature gradient, the length of the droplet parallel to the pattern was measured. In contrast, the distance of the continuous movement of the droplet front from the hot side to the cold side of the sample was measured for the experiments with temperature gradient. The two different measuring strategies for experiments with and without temperature gradient are schematically shown in Fig. 1 (b) and (c), respectively.

3. Results and discussion

3.1. Spreading experiments without an applied temperature gradient

In order to investigate the possibility to guide lubricant over the fabricated samples, experiments without a temperature gradient were performed. Since the droplet propagation along the structures is of interest, only the length of the droplet parallel to the structures was considered.

In a first step, only single-scale patterns were investigated. Prior to the experiments, the samples' topography was characterized by LSM. The respective images are summarized in Fig. 2.

As can be observed from Fig. 2, all produced samples show a homogeneous height distribution as well as a regular distance between the

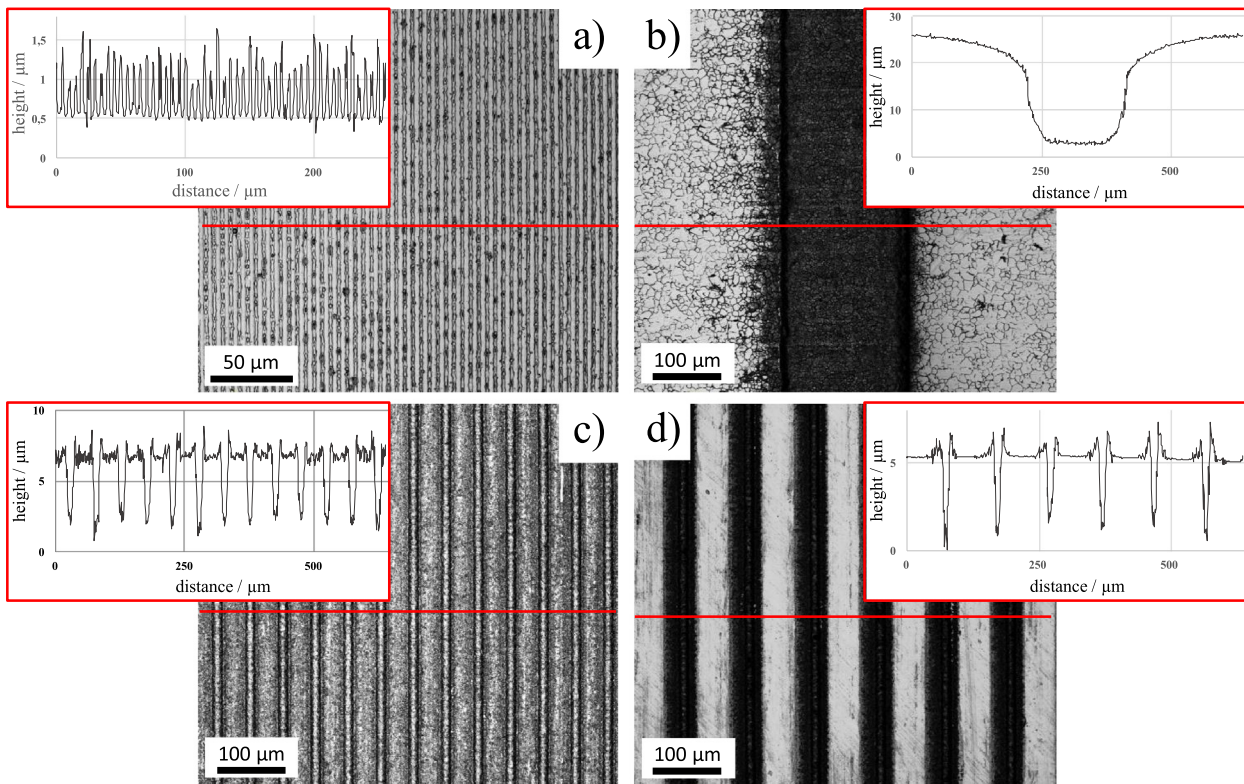


Fig. 2. Overview of all single-scale samples as well as their respective profiles perpendicular to the patterns along the red line measured by LSM. Shown are samples produced by (a) DLIP, (b) micro-coining and (c and d) UPLP. For UPLP, two different periodicities, namely (c) 50 μm (d) and 100 μm , were fabricated. (For interpretation of the references to colour in this figure legend, the reader is referred to the web version of this article.)

structural features according to the desired periodicity. This is also reflected by selected surface parameters and their respective standard deviations given in Table 3.

The standard deviations measured for the structural depth, the width and the periodicity are below 10%, which reflects the high homogeneity of the produced surfaces. The differences in the structural parameters in terms of size can be attributed to a variation in the production process. Thereby, micro-coining is a forming process, which is capable to produce the largest structures of the used techniques in a fast and reliable way [36]. The differences between the patterns created by DLIP and UPLP can be explained by different experimental set-ups and different underlying laser-matter interactions. For UPLP, the laser beam is merely focused onto the sample's surface whereas DLIP creates smaller structures by overlapping two sub-beams, which interfere with each other. Due to the pulse duration of 10 ns, DLIP is based upon melting and resolidification. In contrast, UPLP leads to a direct ablation of the material and therefore prevents the formation of molten material [38]. This makes it possible to create deeper structures by UPLP. The roughness of the samples increases by definition with the structural depth of the samples. Regarding the skewness S_{sk} , it can be observed that all samples, except for the sample patterned by DLIP, show a negative skewness. Those values account for a rather plateau-like surface topography, which is reasonable considering the unstructured portions between the channels. On the other hand, the

sample patterned by DLIP shows a positive skewness, which results from the peaky surface topography without plateaus between the channels (see Fig. 2). As already outlined in the introduction, wetting properties and consequently lubricant spreading are determined by both surface topography and surface chemistry. In this context, it is worth to mention that the polished reference is covered by a native oxide scale, which is typically a mixture of iron and chromium oxide (solid solution) [39]. After DLIP, it could be shown that the resulting oxide scale increased and consisted of two well-separated layers. On top of the surface, an iron oxide layer can be found, which is followed by chromium oxide layer. This observation can be well correlated with the high temperatures involved in DLIP and the thermal stability of iron and chromium oxide [39]. With respect to UPLP, Raillard et al. demonstrated for steel surfaces that UPLP leads to an increase of the iron oxide layer thickness by a factor of roughly 2 [40]. Since the used pulse duration in this study is comparable with the one Raillard et al. used, it is reasonable to assume that the UPLP samples are covered with an oxide layer. Due to the high temperatures involved in micro-coining, those samples are also covered by a similar oxide scale. Consequently, it can be stated that the surface chemistry of all samples is assumed to be comparable. Observed changes in the lubricant spreading can therefore mainly traced back to differences in the surface topography.

After characterizing the surface topography, the propagation of the liquid's meniscus position for all single-scale patterns over time was

Table 3
Summary of selected surface parameters of all single-scale samples measured by LSM.

Sample	Structural depth/ μm	Width/ μm	Periodicity/ μm	$S_q/\mu\text{m}$	S_{sk}
Micro-coined (A)	22.84 ± 2.18	259 ± 16	795 ± 5	8.75 ± 0.27	-0.85 ± 0.02
5 μm DLIP	0.80 ± 0.04	3.77 ± 0.06	4.94 ± 0.06	0.30 ± 0.01	0.29 ± 0.29
50 μm UPLP	4.15 ± 0.00	16.70 ± 0.35	51.43 ± 0.64	1.78 ± 0.05	-1.15 ± 0.02
100 μm UPLP	4.02 ± 0.01	16.23 ± 0.83	100.73 ± 0.55	1.18 ± 0.04	-2.09 ± 0.07

investigated without any temperature gradient. Camera images captured at 1, 5 and 15 s after the deposition of the droplet are shown in Fig. 3. It can be clearly seen that the lubricant shows a preferential spreading parallel to the channels for all samples. This can be traced back to capillary forces induced by the channels, which act parallel to the channels. Furthermore, the channels function as pinning centers, which prevent lubricant propagation perpendicular to the pattern. After 15 s, the elongation of the droplet is the greatest for the 50 μm UPLP sample while the width for this sample is the smallest compared to all other samples.

A more detailed illustration of the results including mean values and standard deviations is given in Fig. 4.

As in Fig. 3, the smallest lubricant spreading can be observed for both the samples fabricated by DLIP and micro-coining. Comparing both samples with each other reveals that the structural depth of the micro-coined sample is increased by a factor of roughly 30 while the periodicity is also increased by a factor of 160 (see Table 3). Consequently, the number of structural features in contact is greatly reduced for the micro-coined pattern and therefore despite its significantly increased depth a comparable pinning effect as well as comparable capillary forces can be observed for both samples. Both UPLP samples demonstrate a faster lubricant spreading than the DLIP and the micro-coined sample, which can be traced back to a larger structural depth and a smaller periodicity. Thereby, a faster lubricant spreading can be observed for the UPLP sample with a periodicity of 50 μm even though both samples have nearly the same structural depth and width (see Table 3 and Fig. 2). Nevertheless, as demonstrated in previous studies by Rosenkranz et al. as well as Grützmacher et al., the periodicity of the patterns plays a decisive role [22,27]. A smaller periodicity results in a higher number of pinning centers as well as higher accumulated capillary forces due to a greater number of channels in contact with the oil. Consequently, this leads to a greater anisotropic droplet distortion and therefore faster lubricant spreading. Since the comparison between the two UPLP samples shows more pronounced effects for the sample with a periodicity of 50 μm , this pattern was used in the following for the multi-scale patterning combining micro-coining and UPLP.

Fig. 5 shows two multi-scale surfaces fabricated by a combination of micro-coining and either DLIP (A + ns) or UPLP (A + fs). In this context, it is worth to mention that micro-coining is the first step followed by the respective laser patterning [41]. Thereby, the laser patterns are not

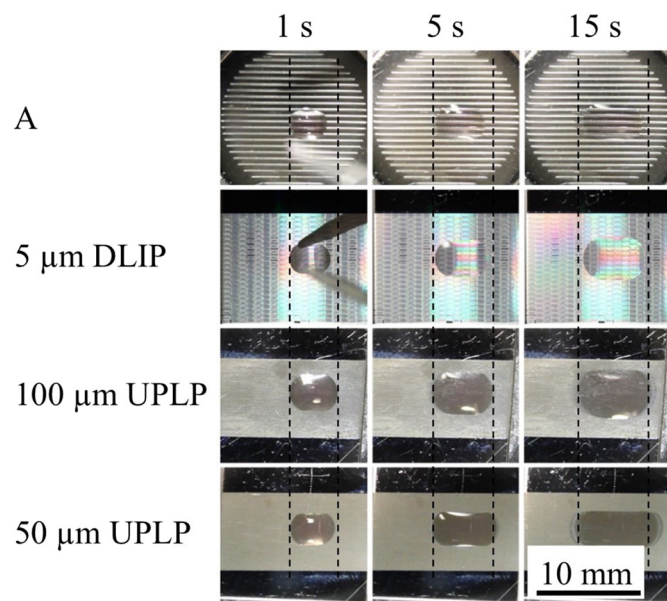


Fig. 3. Temporal evolution of the fluid front measured for the DLIP sample (5 μm ns), the two UPLP samples (50 μm and 100 μm fs) and the micro-coined sample (A) without any temperature gradient.

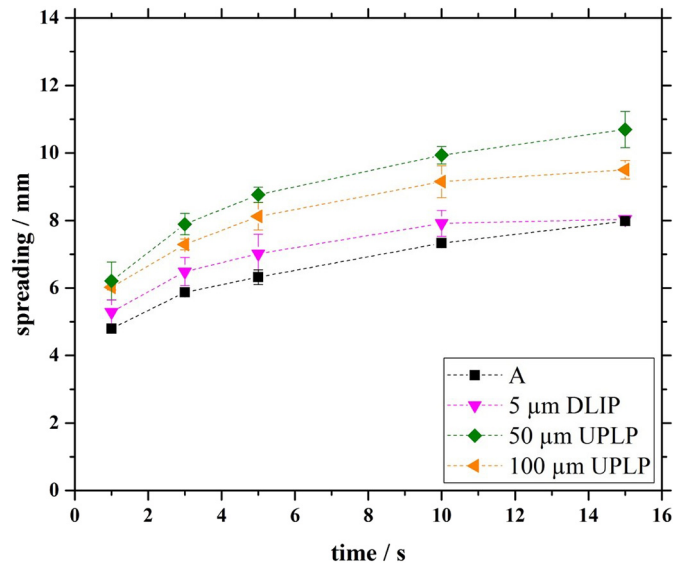


Fig. 4. Temporal evolution of the droplet propagation for the micro-coined (A), the DLIP (5 μm ns) and the two UPLP samples (50 μm UPLP, 100 μm UPLP) without any temperature gradient.

destroyed by the coining process and are homogeneously distributed over the entire sample surface with features on the fillets between the channels as well as inside the channels. Due to the large scale differences between the DLIP pattern and the micro-coined pattern, the line-like laser pattern is barely visible. However, a closer look reveals the laser pattern in the LSM image as well as in the profile plot (Fig. 5 (a)). On the other hand, the UPLP pattern is clearly visible on the larger micro-coined pattern due its larger structural depth and periodicity and shows a homogeneous height distribution over the entire surface of the sample (Fig. 5 (b)).

It is worth mentioning that the roughness of the multi-scale samples increases compared to the purely coined sample due to the additional superimposed laser pattern (see Tables 3 and 4). The skewness of both multi-scale samples is almost identical compared to the purely micro-coined pattern, which underlines the topographical dominance of the micro-coined pattern.

Fig. 6 shows the temporal evolution of the fluid front for both multi-scale samples. As for the single-scale patterns, a clear preferential spreading can be observed. Thereby, this effect is even more pronounced for the sample combining micro-coining and UPLP (A + fs).

By comparing the droplet propagation of the multi-scale samples with that of the single-scale patterns (Fig. 7), it can be seen that both multi-scale samples (A + ns and A + fs) show a faster lubricant spreading than the respective single-scale patterns. Thereby, especially the sample produced by a combination of micro-coining and UPLP (A + fs) shows the fastest lubricant spreading of all tested samples.

In order to explain these findings, different aspects need to be taken into consideration. First of all, the additional laser pattern increases the droplet pinning and thus inhibits the droplet propagation perpendicular to the pattern. This reduces the lubricant spreading perpendicular to the pattern and increases in turn the lubricant spreading parallel to the pattern. Secondly, due to the additional channels of the laser pattern in contact with the oil the capillary forces are increased, which further accelerates the lubricant spreading along the channels. In this context, these effects are stronger for deeper channels, which promotes the fastest lubricant spreading for the multi-scale sample produced by UPLP. Finally, according to the theory by Wenzel, the increased roughness due to the additional laser pattern results in a smaller contact angle and therefore a greater tendency to oil spreading on the sample surface [42]. Bearing in mind that the contact angle θ between the liquid's meniscus and the channel walls affects the capillary forces F_K

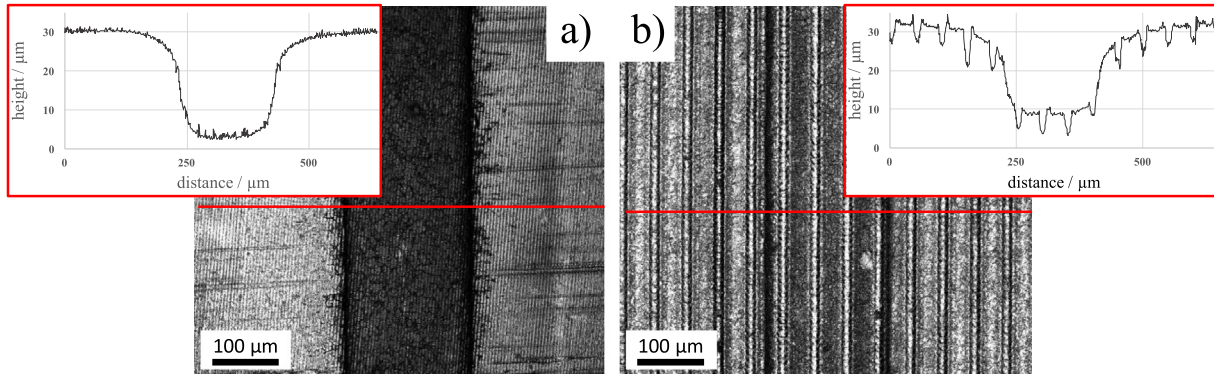


Fig. 5. Overview of the two multi-scale samples (a) A + ns and (b) A + fs as well as their respective profiles perpendicular to the patterns along the red line measured by LSM. (For interpretation of the references to colour in this figure legend, the reader is referred to the web version of this article.)

following the equation [43]:

$$F_K = p\gamma \cos\theta, \quad (1)$$

with γ being the surface tension of the liquid and p the channel perimeter, it becomes clear that the reduced contact angle increases the capillary forces and thus the lubricant spreading.

It is worth mentioning that the velocity of lubricant spreading decreases for all samples over time (decreasing slope over time, which can be observed in Figs. 4 and 7). This behavior is consistent with the behavior of liquids in capillaries, which can be described by the Lucas-Washburn equation [44,45]. Rye et al. modified the Lucas-Washburn equation and came up with a general equation [46]:

$$l^2 = K(\alpha, \theta) \frac{\gamma T}{\eta} t, \quad (2)$$

where l is the position of the travelling meniscus along the channel, $K(\alpha, \theta)$ is a geometric term, which depends on the groove angle α and the contact angle θ , γ is the surface tension of the liquid, η is the dynamic viscosity of the liquid phase, T is the structural depth and t is the time. As can be seen from Eq. (2) the velocity of the liquid flow in capillaries is predicted to decrease proportional to $1/\sqrt{t}$, which is reflected by the curve shapes in Figs. 4 and 7 [47].

3.2. Spreading experiments with an applied temperature gradient

Subsequently, the spreading dynamics of a lubricant along the produced structures were investigated using an applied temperature gradient of $2^\circ\text{C}/\text{mm}$. Since the experiments without temperature gradient demonstrated that the sample with a periodicity of $50\ \mu\text{m}$ was the more effective pattern with respect to UPLP, only this pattern was further investigated.

Similar to the experiments without temperature gradient, a preferential lubricant spreading parallel to the pattern can be observed from the evolution of the fluid fronts in Fig. 8. Thereby, the elongation due to capillary forces and the pinning effect perpendicular to the patterns is especially pronounced for the multi-scale samples. In contrast to the experiments without temperature gradient, there is a lubricant migration from the hotter side of the sample (left-hand side) to colder regions (right-hand side) due to Marangoni forces.

Table 4
Summary of selected surface parameters of the multi-scale samples measured by LSM.

Sample	$S_q/\mu\text{m}$	S_{sk}
Multi-scale (A + ns)	9.86 ± 0.92	-0.77 ± 0.04
Multi-scale (A + fs)	9.16 ± 0.58	-0.76 ± 0.02

In Fig. 9, the temporal evolution of the droplet propagation under the effect of a temperature gradient is shown.

The experimental trends observed in the experiments without temperature gradient can be only partially confirmed. Especially the micro-coined sample (A) shows a much faster lubricant spreading in case of an applied temperature gradient. Compared to the experiments without temperature gradient, additional Marangoni forces lead to a droplet migration towards the cold side of the sample. The capillary and Marangoni forces are balanced by the viscous drag force (wall friction) [28,48]. The Reynolds number of the fluid is even for the fastest velocities smaller than 10^{-2} , representing laminar flow. The flow profile can thus be assumed “Poiseuille-like” and the friction depends on the geometry of the channel [49]. The influence of the wall friction of the respective samples can be discussed by relating the volume of the channels to their real surface area (measured by LSM). Those measurements are summarized in Table 5 and demonstrate that the ratio of volume to surface area for the micro-coined sample is increased by a factor of 18 compared to the DLIP sample and by a factor of 7 compared to the UPLP sample. Consequently, the viscous drag force for the micro-coined sample is smaller than that for the laser patterned samples, which leads to a faster lubricant spreading.

Nevertheless, the differences in lubricant spreading between the UPLP and the DLIP sample became much smaller compared to the experiments without temperature gradient. This can be explained by the greatly enhanced roughness of the UPLP pattern. For the fast lubricant spreading, the spiky surface topography of the UPLP sample parallel to the pattern leads to an additional pinning effect in this direction thus impeding droplet migration. Furthermore, the smaller differences between these patterns may be explained by the variation in the measurement procedure. In case of an applied temperature gradient, the droplet migration is only measured in one direction (towards the cold side of

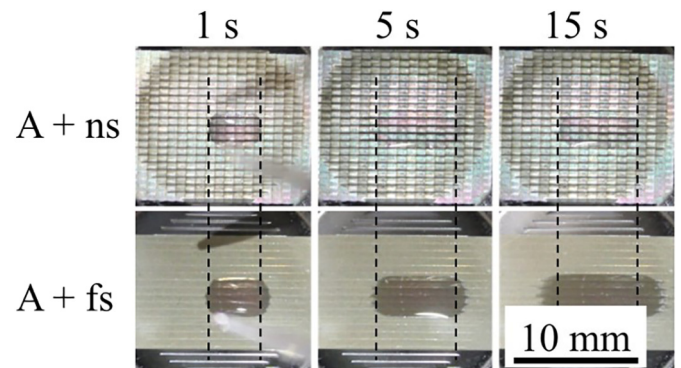


Fig. 6. Temporal evolution of the fluid front for the two multi-scale samples (A + ns and A + fs) without any temperature gradient.

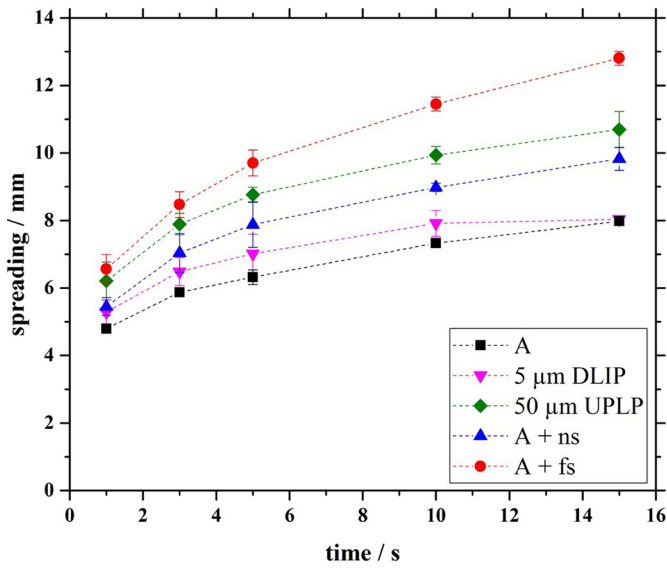


Fig. 7. Temporal evolution of the droplet propagation for the micro-coined (A), the DLIP (5 μm ns), the UPLP (50 μm fs) as well as the two multi-scale samples (A + ns and A + fs) without any temperature gradient.

the sample) whereas for the experiments without temperature gradient the droplet length is measured. Therefore, the capillary forces induced by the surface structures also act in the direction opposite to the droplet's motion and thus the direction of measurement. This leads to a smaller difference between the DLIP and UPLP samples since the UPLP pattern induces higher capillary forces.

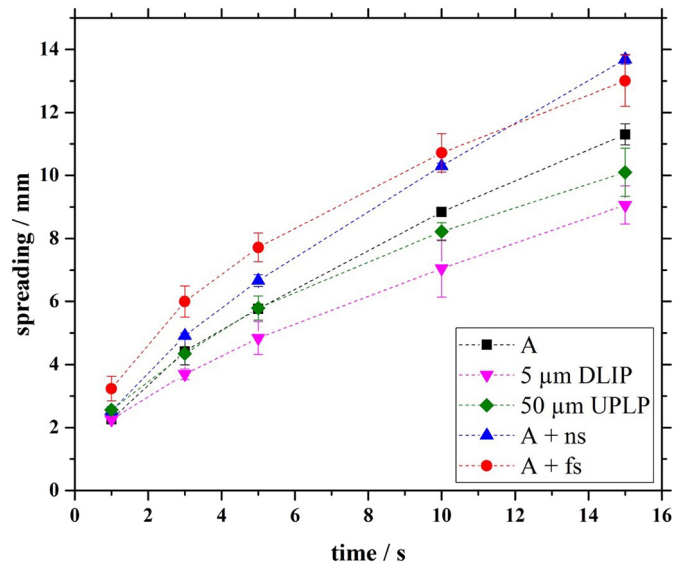


Fig. 9. Temporal evolution of the droplet propagation under the effect of a temperature gradient for the micro-coined (A), the DLIP (5 μm ns), the UPLP (50 μm fs) and the two multi-scale samples (A + ns and A + fs).

Similar to the experiments without temperature gradient, the multi-scale samples show a faster lubricant spreading than the respective single-scale patterns, which can be traced back again to a stronger pinning, greater capillary forces and a higher tendency for spreading due to the additional laser pattern. Especially the multi-scale sample fabricated by micro-coining and DLIP (A + ns) demonstrates a faster lubricant spreading compared to the experiments without a temperature gradient. This can be mainly traced back to the smaller wall friction and thus smaller resistance against Marangoni forces of the purely micro-coined pattern. In accordance with the experimental findings for single-scale laser patterns, the differences between the two multi-scale samples with respect to the lubricant spreading also decrease in case of an applied temperature gradient. This can be again explained by the increased roughness of the UPLP pattern as well as greater capillary forces for the A + fs sample acting against the droplet's propagation. This leads especially towards the end of the experiment to a greater depletion of oil volume which increases the droplet pinning [27].

4. Conclusions

In this study, the spreading behavior of a lubricant (PAO 4) on micro-coined, laser patterned as well as multi-scale stainless steel surfaces was investigated. The possibility to guide lubricants over surfaces is particularly interesting for lubricated, tribological components to improve their lubricating condition and to avoid lubricant migration. In that case, a base oil such as the one in this study with additives such as antioxidant or high-pressure additives can be used. Two different laser patterning techniques (DLIP and UPLP) were used to create single-scale patterns. With each of those techniques a multi-scale pattern was created by combining micro-coining with the respective laser patterning technique. The spreading experiments were conducted with and without a controlled temperature gradient of 2 °C/mm. Based upon the presented results, the following conclusions can be drawn:

- Irrespective of the manufacturing technique, all patterns can be produced with high accuracy and homogeneity in terms of structural depth, width and periodicity. The multi-scale patterns show a homogeneous distribution of the secondary laser patterns over the entire micro-coined surfaces.
- Experiments without a temperature gradient show a preferential

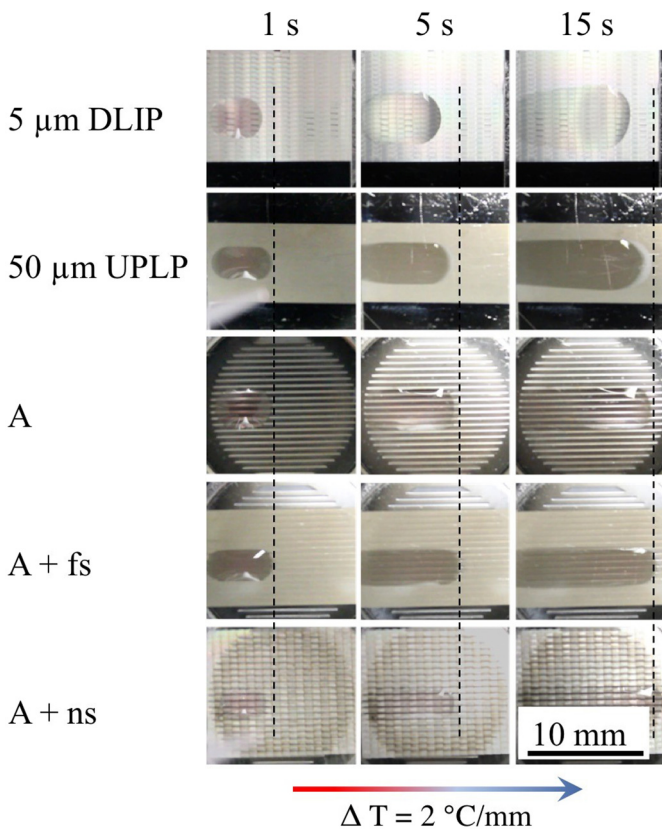


Fig. 8. Temporal evolution of the fluid front for the DLIP sample (5 μm ns), the UPLP sample (50 μm fs), the micro-coined sample (A), as well as the two multi-scale samples (A + ns and A + fs) under the effect of a temperature gradient.

Table 5

Channel area, channel volume as well as the ratio of channel volume to channel area for the all samples. The measurements were performed by LSM for an area of $313 \times 313 \mu\text{m}$.

Sample	Channel area/ μm^2	Channel volume/ μm^2	Volume to area ratio
Micro-coined (A)	$0.12 \cdot 10^6 \pm 1.20 \cdot 10^3$	$1.20 \cdot 10^6 \pm 0.91 \cdot 10^3$	9.62 ± 0.09
5 μm DLIP	$0.11 \cdot 10^6 \pm 5.43 \cdot 10^3$	$0.06 \cdot 10^6 \pm 17.37 \cdot 10^3$	0.57 ± 0.11
50 μm UPLP	$0.13 \cdot 10^6 \pm 4.28 \cdot 10^3$	$0.17 \cdot 10^6 \pm 6.10 \cdot 10^3$	1.37 ± 0.07
Multi-scale (A + ns)	$0.15 \cdot 10^6 \pm 2.89 \cdot 10^3$	$1.57 \cdot 10^6 \pm 5.67 \cdot 10^3$	10.67 ± 0.21
Multi-scale (A + fs)	$0.15 \cdot 10^6 \pm 2.80 \cdot 10^3$	$1.53 \cdot 10^6 \pm 11.83 \cdot 10^3$	10.09 ± 0.18

lubricant spreading parallel to the pattern for all samples. Thereby, the slowest lubricant spreading is observed for the DLIP and the purely micro-coined sample due to their low structural depth and high periodicity, respectively. The UPLP samples show the fastest lubricant spreading for all single-scale patterns. In particular, the UPLP sample with the smaller periodicity possesses the fastest lubricant spreading as a result of a higher number of channels in contact to the lubricant. Both multi-scale samples show a faster lubricant spreading compared to the respective single-scale patterns. This can be attributed to additional capillary forces induced by the superimposed laser patterns as well as a higher tendency for lubricant spreading due to an increased roughness.

- For experiments with an additional temperature gradient, the purely micro-coined sample shows a faster lubricant spreading in relation to the other single-scale samples. LSM measurements proved that the volume to surface area ratio is higher for the micro-coined samples, which results in less wall friction and therefore a smaller resistance against the Marangoni forces induced by the temperature gradient. Similar to the experiments without temperature gradient the lubricant spreads faster on the two multi-scale surfaces than on the respective single-scale patterns.

Acknowledgements

The present work is supported by funding from the Deutsche Forschungsgemeinschaft (DFG, projects: MU 959/27-2 and HI 790/33-2 within the SPP 1551). A. Rosenkranz gratefully acknowledges the Alexander von Humboldt foundation for the financial support of his post-doctoral fellowship (Feodor Lynen research fellowship).

References

- [1] A. Marmur, The lotus effect: Superhydrophobicity and metastability, *Langmuir* 20 (2004) 3517–3519, <https://doi.org/10.1021/la036369u>.
- [2] N.A. Patankar, Mimicking the lotus effect: influence of double roughness structures and slender pillars, *Langmuir* 20 (2004) 8209–8213, <https://doi.org/10.1021/la048629t>.
- [3] L. Gao, T.J. McCarthy, The “lotus effect” explained: two reasons why two length scales of topography are important, *Langmuir* 22 (2006) 2966–2967, <https://doi.org/10.1021/la0532149>.
- [4] M.D. Kern, Y. Qi, R. Long, M.E. Rentschler, Characterizing adhesion between a micropatterned surface and a soft synthetic tissue, *Langmuir* 33 (2017) 854–864, <https://doi.org/10.1021/acs.langmuir.6b03643>.
- [5] K. Autumn, Y.A. Liang, S.T. Hsieh, W. Zesch, W.P. Chan, T.W. Kenny, R. Fearing, R.J. Full, Adhesive force of a single gecko foot-hair, *Nature* 405 (2000) 681–685, <https://doi.org/10.1038/35015073>.
- [6] A.K. Geim, S.V. Dubonos, I.V. Grigorieva, K.S. Novoselov, A.A. Zhukov, S.Y. Shapoval, Microfabricated adhesive mimicking gecko foot-hair, *Nat. Mater.* 2 (2003) 461–463, <https://doi.org/10.1038/nmat917>.
- [7] X. Gao, X. Yan, X. Yao, L. Xu, K. Zhang, J. Zhang, B. Yang, L. Jiang, The dry-style anti-fogging properties of mosquito compound eyes and artificial analogues prepared by soft lithography, *Adv. Mater.* 19 (2007) 2213–2217, <https://doi.org/10.1002/adma.200601946>.
- [8] R.A. Potyrailo, H. Ghiradella, A. Vertiatichkh, K. Dovidenko, J.R. Cournoyer, E. Olson, Morpho butterfly wing scales demonstrate highly selective vapour response, *Nat. Photonics* 1 (2007) 123–128, <https://doi.org/10.1038/nphoton.2007.2>.
- [9] R.E. Rodríguez, S.P. Agarwal, S. An, E. Kazzyak, D. Das, W. Shang, R. Skye, T. Deng, N.P. Dasgupta, Biotemplated morpho butterfly wings for tunable structurally colored photocatalysts, *ACS Appl. Mater. Interfaces* 10 (2018) 4614–4621, <https://doi.org/10.1021/acsami.7b14383>.
- [10] Y. Zheng, X. Gao, L. Jiang, Directional adhesion of superhydrophobic butterfly wings, *Soft Matter* 3 (2007) 178–182, <https://doi.org/10.1039/b612667g>.
- [11] P. Comanns, G. Buchberger, A. Buchsbaum, R. Baumgartner, A. Kogler, S. Bauer, W. Baumgartner, Directional, passive liquid transport: the Texas horned lizard as a model for a biomimetic “liquid diode”, *J. R. Soc. Interface* 12 (2015), 20150415, <https://doi.org/10.1098/rsif.2015.0415>.
- [12] F. Xia, L. Jiang, Bio-inspired, smart, multiscale interfacial materials, *Adv. Mater.* 20 (2008) 2842–2858, <https://doi.org/10.1002/adma.200800836>.
- [13] T. Sun, L. Feng, X. Gao, L. Jiang, Bioinspired surfaces with special wettability, *Acc. Chem. Res.* 38 (2005) 644–652, <https://doi.org/10.1021/ar040224c>.
- [14] J.T. Woodward, H. Gwin, D.K. Schwartz, Contact angles on surfaces with mesoscopic chemical heterogeneity, *Langmuir* 16 (2000) 2957–2961, <https://doi.org/10.1021/la991068z>.
- [15] M. Ramiasa-MacGregor, A. Mierczynska, R. Sedev, K. Vasilev, Tuning and predicting the wetting of nanoengineered material surface, *Nano* 8 (2016) 4635–4642, <https://doi.org/10.1039/C5NR08329j>.
- [16] Y. Liang, L. Shu, W. Natsu, F. He, Anisotropic wetting characteristics versus roughness on machined surfaces of hydrophilic and hydrophobic materials, *Appl. Surf. Sci.* 331 (2015) 41–49, <https://doi.org/10.1016/j.apsusc.2014.12.071>.
- [17] T.G. Cha, J.W. Yi, M.W. Moon, K.R. Lee, H.Y. Kim, Nanoscale patterning of microtextured surfaces to control superhydrophobic robustness, *Langmuir* 26 (2010) 8319–8326, <https://doi.org/10.1021/la9047402>.
- [18] Y. Kwon, N. Patankar, J. Choi, J. Lee, Design of surface hierarchy for extreme hydrophobicity, *Langmuir* 25 (2009) 6129–6136, <https://doi.org/10.1021/la803249t>.
- [19] D. Zhang, F. Chen, G. Fang, Q. Yang, D. Xie, G. Qiao, W. Li, J. Si, X. Hou, Wetting characteristics on hierarchical structures patterned by a femtosecond laser, *J. Micromech. Microeng.* 20 (2010) <https://doi.org/10.1088/0960-1317/20/7/075029>.
- [20] F. Chen, D. Zhang, Q. Yang, X. Wang, B. Dai, X. Li, X. Hao, Y. Ding, J. Si, X. Hou, Anisotropic wetting on microstrips surface fabricated by femtosecond laser, *Langmuir* 27 (2011) 359–365, <https://doi.org/10.1021/la103293j>.
- [21] M. Hans, F. Müller, S. Grandthyll, S. Hüfner, F. Mücklich, Anisotropic wetting of copper alloys induced by one-step laser micro-patterning, *Appl. Surf. Sci.* 263 (2012) 416–422, <https://doi.org/10.1016/j.apsusc.2012.09.071>.
- [22] A. Rosenkranz, S. Fleischmann, C. Gachot, F. Mücklich, Anisotropic spreading behavior of PAO oil on laser-patterned stainless steel surfaces, *Adv. Eng. Mater.* 17 (2015) 1645–1651, <https://doi.org/10.1002/adem.201500115>.
- [23] A. Rosenkranz, P.G. Grützmaier, A. Szurdak, C. Gachot, G. Hirt, F. Mücklich, F. Muecklich, Synergetic effect of laser patterning and micro coining for controlled lubricant propagation, *Surf. Topogr. Metrol. Prop.* 4 (2016), 34008, <https://doi.org/10.1088/2051-672X/4/3/034008>.
- [24] D. Quéré, Wetting and roughness, *Annu. Rev. Mater. Res.* 38 (2008) 71–99, <https://doi.org/10.1146/annurev.matsci.38.060407.132434>.
- [25] D. Yang, M. Krasowska, C. Priest, M.N. Popescu, J. Ralston, Dynamics of capillary-driven flow in open microchannels, *J. Phys. Chem. C* 115 (2011) 18761–18769, <https://doi.org/10.1021/jp2065826>.
- [26] Q. Dai, W. Huang, X. Wang, Micro-grooves design to modify the thermo-capillary migration of paraffin oil, *Meccanica* 52 (2017) 171–181, <https://doi.org/10.1007/s11012-016-0413-3>.
- [27] P.G. Grützmaier, A. Rosenkranz, C. Gachot, How to guide lubricants – tailored laser surface patterns on stainless steel, *Appl. Surf. Sci.* 370 (2016) 59–66, <https://doi.org/10.1016/j.apsusc.2016.02.115>.
- [28] D. Yang, M. Krasowska, C. Priest, J. Ralston, Dynamics of capillary-driven liquid-liquid displacement in open microchannels, *Phys. Chem. Chem. Phys.* 16 (2014) 24473–24478, <https://doi.org/10.1039/C4CP03910F>.
- [29] A. Karbalaei, R. Kumar, H.J. Cho, Thermocapillarity in microfluidics—a review, *Micromachines* 7 (2016) 1–41, <https://doi.org/10.3390/mi7010013>.
- [30] D.T. Wasan, Droplets speeding on surfaces, *Science* 80 (291) (2001) 605–606, <https://doi.org/10.1126/science.1058466>.
- [31] Q. Dai, M. Li, M.M. Khonsari, W. Huang, X. Wang, The thermocapillary migration on rough surfaces, *Lubr. Sci.* (2018) 1–8, <https://doi.org/10.1002/ls.1419>.
- [32] Q. Dai, W. Huang, X. Wang, M.M. Khonsari, Ringlike migration of a droplet propelled by an omnidirectional thermal gradient, *Langmuir* 34 (13) (2018) 3806–3812, <https://doi.org/10.1021/acs.langmuir.7b04259>.
- [33] G. Karapetsas, N.T. Chamakos, A.G. Papathanasiou, Thermocapillary droplet actuation: effect of solid structure and wettability, *Langmuir* 33 (2017) 10838–10850, <https://doi.org/10.1021/acs.langmuir.7b02762>.
- [34] F. Mücklich, A.F. Lasagni, C. Daniel, Laser interference metallurgy – using interference as a tool for micro/nano structuring, *Int. J. Mater. Res.* 97 (2006) 1337–1344, <https://doi.org/10.3139/146.101375>.
- [35] A.F. Lasagni, C. Gachot, K.E. Trinh, M. Hans, A. Rosenkranz, T. Roch, S. Eckhardt, T. Kunze, M. Bieda, D. Günther, V. Lang, F. Mücklich, Direct laser interference patterning, 20 years of development: from the basics to industrial applications, *iProc. SPIE* 10092, Laser-based Micro- and Nanoprocessing XI, 1009211, , 2017 <https://doi.org/10.1117/12.2252595>.

- [36] A. Szurdak, A. Rosenkranz, C. Gachot, G. Hirt, F. Mücklich, Manufacturing and tribological investigation of hot micro-coined lubrication pockets, *Key Eng. Mater.* 611–612 (2014) 417–424, <https://doi.org/10.4028/www.scientific.net/KEM.611-612.417>.
- [37] A. Szurdak, G. Hirt, Finite element analysis of manufacturing micro lubrication pockets in high strength steels by hot micro-coining, *Steel Res. Int.* 86 (2015) 257–265, <https://doi.org/10.1002/srin.201300475>.
- [38] B.N. Chichkov, C. Momma, S. Nolte, F. von Alvensleben, A. Tünnermann, Femtosecond, picosecond and nanosecond laser ablation of solids, *Appl. Phys. A Mater. Sci. Process.* 63 (1996) 109–115, <https://doi.org/10.1007/s003390050359>.
- [39] A. Rosenkranz, L. Reinert, C. Gachot, H. Aboufadi, S. Grandthyll, K. Jacobs, F. Müller, F. Mücklich, Oxide formation, morphology, and nanohardness of laser-patterned steel surfaces, *Adv. Eng. Mater.* 17 (2015) 1234–1242, <https://doi.org/10.1002/adem.201400487>.
- [40] B. Raillard, L. Gouton, E. Ramos-Moore, S. Grandthyll, F. Müller, F. Mücklich, Ablation effects of femtosecond laser functionalization on steel surfaces, *Surf. Coat. Technol.* 207 (2012) 102–109, <https://doi.org/10.1016/j.surfcoat.2012.06.023>.
- [41] C. Gachot, A. Rosenkranz, B. Wietbrock, G. Hirt, F. Mücklich, Advanced design of hierarchical topographies in metallic surfaces by combining micro-coining and laser interference patterning, *Adv. Eng. Mater.* 15 (2013) 503–509, <https://doi.org/10.1002/adem.201200295>.
- [42] R.N. Wenzel, Surface roughness and contact angle, *J. Phys. Colloid Chem.* 53 (1949) 1466–1467, <https://doi.org/10.1021/j150474a015>.
- [43] M. Stange, M.E. Dreyer, H.J. Rath, Capillary driven flow in circular cylindrical tubes, *Phys. Fluids* 15 (2003) 2587–2601, <https://doi.org/10.1063/1.1596913>.
- [44] R. Lucas, Ueber das Zeitgesetz des kapillaren Aufstiegs von Flüssigkeiten, *Kolloid Z.* 23 (1918) 15–22, <https://doi.org/10.1007/BF01461107>.
- [45] E.W. Washburn, The dynamics of capillary flow, *Phys. Rev.* 17 (1921) 273–283, <https://doi.org/10.1103/PhysRev.17.273>.
- [46] R.R. Rye, J.A. Mann, F.G. Yost, The flow of liquids in surface grooves, *Langmuir* 12 (1996) 555–565, <https://doi.org/10.1021/la9500989>.
- [47] T.W. Sowers, R. Sarkar, S.E. Prameela, E. Izadi, J. Rajagopalan, Capillary driven flow of polydimethylsiloxane in open rectangular microchannels, *Soft Matter* 12 (2016) 5818–5823, <https://doi.org/10.1039/c6sm00897f>.
- [48] J. Berthier, D. Gosselin, A. Pham, F. Boizot, G. Delapierre, N. Belgacem, D. Chaussy, Spontaneous capillary flows in piecewise varying cross section microchannels, *Sensors Actuators B Chem.* 223 (2016) 868–877, <https://doi.org/10.1016/j.snb.2015.10.023>.
- [49] J. Berthier, D. Gosselin, N. Villard, C. Pudda, F. Boizot, G. Costa, G. Delapierre, The Dynamics of Spontaneous Capillary Flow in Confined and Open Microchannels, *Sensors & Transducers*, 183, 2014 123–128.

V Effects of Multi-Scale Patterning on the Run-In Behavior of Steel–Alumina Pairings under Lubricated Conditions

Philipp G. Grützmacher¹, Andreas Rosenkranz¹, Adam Szurdak², Carsten Gachot³, Gerhard Hirt², Frank Mücklich¹

¹ Chair of Functional Materials, Saarland University, 66123 Saarbrücken, Germany

² Institute of Metal Forming, RWTH Aachen, 52056 Aachen, Germany

³ Institute for Engineering Design and Technical Logistics, Tribology Division, Vienna University of Technology, 1060 Vienna, Austria

Published in “*Advanced Engineering Materials*” (Impact factor (2018): 2.576)

Accessible online at: <https://doi.org/10.1002/adem.201700521>

Own contribution:

Project management; scientific discussion; paper writing; data analysis; sample preparation: laser surface patterning; measurements: white light interferometry, laser scanning microscopy, tribological testing

Abstract:

In nature, many examples of multi-scale surfaces with outstanding tribological properties such as reduced friction and wear under dry friction and lubricated conditions can be found. To determine whether multi-scale surfaces positively affect the frictional and wear performance, tests are performed on a ball-on-disk tribometer under lubricated conditions using an additive-free poly-alpha-olefine oil under a contact pressure of around 1.29 GPa. For this purpose, stainless steel specimens (AISI 304) are modified by micro-coining (hemispherical structures with a structural depth of either 50 or 95 μm) and subsequently by direct laser interference patterning (cross-like pattern with 9 μm periodicity) to create a multi-scale pattern. The comparison of different sample states (polished reference, laser-patterned, micro-coined, and multi-scale) shows a clear influence of the fabrication technique. In terms of the multi-scale structures, the structural depth of the coarser micro-coining plays an important role. In case of lower coining depths (50 μm), the multi-scale specimens show an increased coefficient of friction compared to the purely micro-coined surfaces, whereas larger coining depths (95 μm) result in stable and lower friction values for the multi-scale patterns.

Cite this as:

P.G. Grützmacher, A. Rosenkranz, A. Szurdak, C. Gachot, G. Hirt, F. Mücklich, Effects of Multi-Scale Patterning on the Run-In Behavior of Steel-Alumina Pairings under Lubricated Conditions, *Adv. Eng. Mater.* **2018**, 20, 1700521. (<http://doi:10.1002/adem.201700521>)

Effects of Multi-Scale Patterning on the Run-In Behavior of Steel–Alumina Pairings under Lubricated Conditions

Philipp G. Grützmacher,* Andreas Rosenkranz, Adam Szurdak, Carsten Gachot, Gerhard Hirt, and Frank Mücklich

In nature, many examples of multi-scale surfaces with outstanding tribological properties such as reduced friction and wear under dry friction and lubricated conditions can be found. To determine whether multi-scale surfaces positively affect the frictional and wear performance, tests are performed on a ball-on-disk tribometer under lubricated conditions using an additive-free poly-alpha-olefine oil under a contact pressure of around 1.29 GPa. For this purpose, stainless steel specimens (AISI 304) are modified by micro-coining (hemispherical structures with a structural depth of either 50 or 95 μm) and subsequently by direct laser interference patterning (cross-like pattern with 9 μm periodicity) to create a multi-scale pattern. The comparison of different sample states (polished reference, laser-patterned, micro-coined, and multi-scale) shows a clear influence of the fabrication technique. In terms of the multi-scale structures, the structural depth of the coarser micro-coining plays an important role. In case of lower coining depths (50 μm), the multi-scale specimens show an increased coefficient of friction compared to the purely micro-coined surfaces, whereas larger coining depths (95 μm) result in stable and lower friction values for the multi-scale patterns.


1. Introduction

Friction, a multi-scale phenomenon, is affected by various factors such as adhesion, deformation, fracture, and third-body interaction on different scales ranging from nanometer- up to millimeter.^[1] The features which influence friction extend from atoms up to asperities and the surface itself.^[1] This scale dependency is well known and gets obvious when measuring the coefficient of friction (COF) at nano- and macro-scale.^[2,3] The

P. G. Grützmacher, Dr. A. Rosenkranz,
Prof. Dr.-Ing. F. Mücklich
Department of Functional Materials, Saarland
University, 66123 Saarbrücken, Germany
E-mail: philipp.gruetzmacher@uni-saarland.de

A. Szurdak, Prof. Dr.-Ing. G. Hirt
Institute of Metal Forming, RWTH Aachen, 52056
Aachen, Germany

Prof. Dr.-Ing. C. Gachot
Tribology Division, Institute for Engineering
Design and Technical Logistics, Vienna University
of Technology, 1060 Vienna, Austria

 The ORCID identification number(s) for the author(s) of this article can be found under <https://doi.org/10.1002/adem.201700521>.

DOI: 10.1002/adem.201700521

question that arises is how to overcome this multi-scale phenomenon and to manipulate friction on different scales. Nature found a smart way to deal with that by creating hierarchical surface patterns.^[1,4–6] In bio-mimetics, this design idea is used to create well-defined surfaces with specially tailored frictional properties, which are transferred from nature to applications.^[7]

The tribological effectiveness of single-scale surface features has been demonstrated in numerous research works including dry and lubricated conditions.^[8–11] In terms of dry friction, the beneficial effects of surface structures can be mainly traced back to the storage of wear debris and a reduced contact area.^[12,13] Considering lubricated conditions, the improvements can be attributed to the storage of produced wear particles,^[14] a reservoir effect for lubricants,^[15] and an additional hydrodynamic pressure build-up.^[16]

There are various methods to manufacture artificial topographies with variable pattern parameters such as structural depth, pitch, diameter, or area density including lithographic methods,^[17] embossing/coining,^[18] and laser surface texturing.^[19] Laser surface texturing and in particular direct laser interference patterning (DLIP) is a suitable technique to structure various materials with patterns having μm and even sub- μm features.^[20] In order to modify surfaces coated with tetrahedral amorphous carbon, Roch et al. used DLIP and could demonstrate an either reduced or increased COFs under dry sliding conditions depending on the pattern periodicity (varied between 2 and 10 μm). The observed differences were attributed to an interplay between decreased hardness (higher COF) and a reduction of the effective contact area (lower COF).^[21] In another study, Rosenkranz et al. could show under mixed lubrication a significant increase of the oil film lifetime (i.e., the time until the COF increases significantly) by using cross-like patterns fabricated by DLIP on steel substrates. The best effects were achieved, if the structural depth of the pattern is in the range of the oil film thickness. Those experimental findings were explained by the storage of oil, as well as wear particles in the topographical minima positions and an additional hydrodynamic pressure.^[8]

In order to produce larger feature sizes on metallic substrates (micro-) coining/embossing seems to be a viable process route,

which also offers the capability for mass production.^[22] Fabricating hemispherical dimples with varying area densities and depths, Rosenkranz et al. studied the effect of the pattern parameters on the frictional response on the COF under lubricated conditions. Beneficial effects of the induced structures in terms of friction reduction could be shown, while the greatest effects (friction reduction by a factor of ≈ 4) were achieved with small area densities and structural depths.^[23] Furthermore, Koszela et al. could show a significant improvement in wear resistance by structuring bronze samples with circular-shaped oil pockets. The best results could be achieved with the biggest dimple depth of 115 μm .^[24]

Despite the fact that nature demonstrates plenty of beneficial effects for multi-scale surface patterns, those patterns have, in contrast to single-scale structures, only been rarely investigated in terms of their frictional and wear behavior. Most of the tested patterns are rather “multishape” structures combining at least two pattern geometries with rather similar dimensions. In this way, Segu et al. used laser surface texturing to create circular and elliptical dimples on steel. They showed a reduced COF with more pronounced effects for deeper dimples, which was attributed to an increased hydrodynamic lubrication effect.^[25] Wang et al. studied multi-scale surfaces with indeed structures on two different scales for silicon carbide sliding under water lubrication. Those surfaces showed a higher critical load for multi-scale samples compared to single-scale and unstructured specimens.^[26] This study proves the great potential of artificially produced multi-scale patterns to obtain beneficial tribological effects even though not all structural aspects have been considered.

Therefore, the goal of this research work is to investigate the frictional and wear performance of multi-scale surfaces (steel AISI 304) combining a larger micro-coined surface pattern with a cross-like laser surface pattern (DLIP). The tribological behavior of the produced multi-scale surface patterns is compared to single-scale micro-coined and laser patterns, as well as to a polished reference using a ball-on-disk setup in rotational sliding mode.

2. Materials and Methods

2.1. Materials

For the experiments, stainless steel (AISI 304) blanks with a thickness of 1 mm and a polished surface (root mean square roughness R_q of 30 nm) were used. **Table 1** summarizes the chemical composition of the used steel measured by energy-dispersive X-ray spectroscopy (EDS). The samples were cleaned prior to the tribological testing using a multi-step cleaning procedure in an ultrasonic bath to remove polar and non-polar

Table 1. Chemical composition of the used steel samples in wt% as specified by the supplier and confirmed by EDS.

Used steel specimens	Fe	Cr	Ni	Mn	Si	C	Mo
Stainless steel (AISI 304)	68.9	18	10	2	1	0.1	/

contaminants. As solvents cyclohexane, acetone, and isopropanol were used. The samples were submerged in each of the solvents for 10 min in the given order.

2.2. Micro-Coining

Micro-coining is a forming process in which a pre-structured tool is used to imprint the pattern of the tool into the surface of a workpiece. Regarding the used forming force, different form filling levels (ratio of structure depth of the workpiece to structure height of the tool) can be obtained. In order to coin high strength materials, like stainless steel (AISI 304), the workpiece needs to be heated up to reduce the flow stress, thus decreasing the load on the die.^[22,23,27] Without this pre-heating, the tool stresses would become too high during the coining process, which could lead to tool damages. In Szurdak et al., the influence of the coining temperature on the maximum tool stress was studied by FEM simulations.^[28] Temperatures higher than 540 °C were determined, in which the tool stresses will not induce plastic deformation of the tool. Therefore, the heating parameters that result in the lowest load on the die were used in this study. Consequently, the current density and heating time were set to 35 A mm^{-2} and 5 s, respectively. This leads to a maximum sample temperature of approx. 1200 °C.

The used closed die hot micro-coining setup, as well as the coining die are described in detail in refs.^[22,23] Basically, the hot micro-coining process can be subdivided into three steps: heating, cutting, and coining. First, the sample is heated by conductive heating. Afterwards, the sample gets cut and coined in one tool movement with a constant tool velocity of 5 mm s^{-1} . The cutting of the sample is required in order to obtain a closed forming area thus preventing material flow out of the forming area and improving the form filling homogeneity of the coined sample. A variation of the coining force enables the manufacturing of structures with different levels of form filling or pocket depths, respectively.

Thus, circular dimples with structural depths of 50 and 95 μm , diameters of 181 and 212 μm , as well as a pitch of 558 μm were fabricated by hot micro-coining (hereinafter called A2 and A3, respectively). The selection of those structural parameters was chosen based upon an earlier study. In this study, one of these patterns (A2) showed beneficial effects compared to a polished reference and the other (A3) showed no improvement or even a slightly worsened behavior regarding the frictional behavior.^[23] Consequently, the influence of the multi-scale patterning on a possible improvement or downgrading (friction and wear) can be addressed.

It is well known that hot micro-coining leads to a significant change of the microstructure underneath the surface due to the involved plastic deformation and the used heat treatment. In order to allow for reproducible tribological testing conditions, the polished reference samples were coined with a flat die keeping all coining parameters constant. This ensures a similar temperature and deformation history of the reference samples compared to the micro-coined ones. Those reference samples were also used for the subsequent treatment with DLIP.

2.3. Direct Laser Interference Patterning

A high-power pulsed solid-state Nd: YAG laser (*Quanta Ray Pro 290, Newport Spectra Physics*) with a pulse duration of 10 ns, a wavelength of 355 nm and a repetition rate of 10 Hz was used. The optical setup, consisting of a shutter, an attenuator, a lens, a beam splitter, and a mirror through which the primary laser beam travels to create interference is described in ref.^[29] The periodicity of the laser patterns is defined by the laser wavelength λ and the angle between two interfering beams.^[20,30,31] By using two interfering sub-beams, a line-like surface topography is induced. Using DLIP, a well-defined, cross-like surface topography with a periodicity of 9 μm and a structural depth of 1 μm was produced by DLIP on steel blanks, as well as superimposed on the previous micro-coined samples in order to produce the multi-scale surfaces. The choice of those structural parameters is highly correlated to the homogeneity of the resulting surface pattern. Surface patterns with an intermediate periodicity, around 10 μm , can be produced with the highest homogeneity.^[29]

In order to create a cross-like pattern, the samples are structured with two line-like patterns which are rotated by 90° relative to each other. To produce a well-defined and homogeneous surface pattern, the laser fluence was kept constant at 29 J cm⁻² for all samples. DLIP was performed under ambient conditions using a single laser pulse. Further details about the DLIP have been already published elsewhere.^[20,30,31]

2.4. Production of Multi-Scale Patterns

The multi-scale surfaces are produced by the two aforementioned methods. Thereby, the samples are first coined and subsequently superimposed by a cross-like laser pattern in order to prevent damaging of the laser pattern by the coining process.^[27]

2.5. Topographical Analysis

The topography of the samples was characterized by white light interferometry (WLI: *New View 7300, Zygo*) and laser scanning microscopy (LSM: *LEXT OLS 4100, Olympus*) after each fabrication step (DLIP and micro-coining) in order to study the surface roughness and the quality of the patterns. Structure-dependent parameters such as periodicity and structural depth were chosen to describe the surface topography of the produced surfaces. Furthermore, said characterization techniques were used to image the samples prior to and after the tribological tests.

2.6. Tribological Experiments

The tribological tests were done using a ball-on-disc tribometer (*CSM Instruments microtribometer*) in rotational sliding mode with a constant normal force of 5 N and track radius of 5 mm. The tribological counter body was an Al₂O₃ ball (surface roughness $R_q \approx 150$ nm and hardness 1800 HV1) with a

Table 2. Properties of the PAO oil used as specified by the supplier (Castrol).

Property	PAO 40
Kinematic viscosity at 100 °C/cSt	39.6
Viscosity index	147
Specific gravity	0.85

diameter of 6 mm. Due to the high hardness of alumina (around 1800 HV1 or 17.65 GPa), plastic deformation and wear of the counter body are negligible during the tribological tests. The estimated Hertzian contact pressure is about 1.29 GPa. The sample is located in a rotating lubricant containment which is filled with 7 ml unformulated Poly-alpha-olefine (PAO 40) oil in order to ensure reproducible testing conditions. The properties of the oil used are summarized in **Table 2**. The tribometer is embedded in a climatic chamber to control temperature (25 °C) and relative humidity (45%). The friction force was measured by linear variable differential transducers. A sliding velocity of 0.01 ms⁻¹ was selected for this study. This sliding velocity reflects, for the polished reference specimen, the transition from mixed to full film EHL.^[23]

3. Results and Discussion

3.1. Topographical Characterization

The coined surfaces are analyzed prior to and after DLIP using LSM. The corresponding overviews are given in **Figure 1**. As can be seen in Figure 1 c and d, the small structures with a depth of around 1 μm created by DLIP are homogeneously distributed over the entire sample with features on the fillets between the dimples, as well as inside the dimples. To produce a pattern without gaps the laser pattern has to be overlapped at certain areas, as can be seen in Figure 1 c and d by the line-like interruptions in the pattern. However, it is worth mentioning that the size of those overlapping areas has been optimized to be as small as possible.

The two different coined patterns are produced with the same die but varying coining pressures. By increasing the coining pressure, the structural depth can be increased from about 50 μm (A2) to roughly 95 μm (A3), as can be seen in the respective profiles displayed in Figure 1. Since the walls of the hemispherical tool structures are not perfectly upright, also the area density is slightly increased from 8.3 to 11.3% when increasing the pocket depth.

3.2. Friction and Wear Behavior

Figure 2 summarizes the temporal evolution of the COF for the polished reference, the purely coined (A2, depth 50 μm) and laser-patterned (cross-pattern with 9 μm periodicity) samples. Besides that, the figure shows the frictional behavior of the corresponding multi-scale sample (A2 combined with 9 μm cross-pattern).

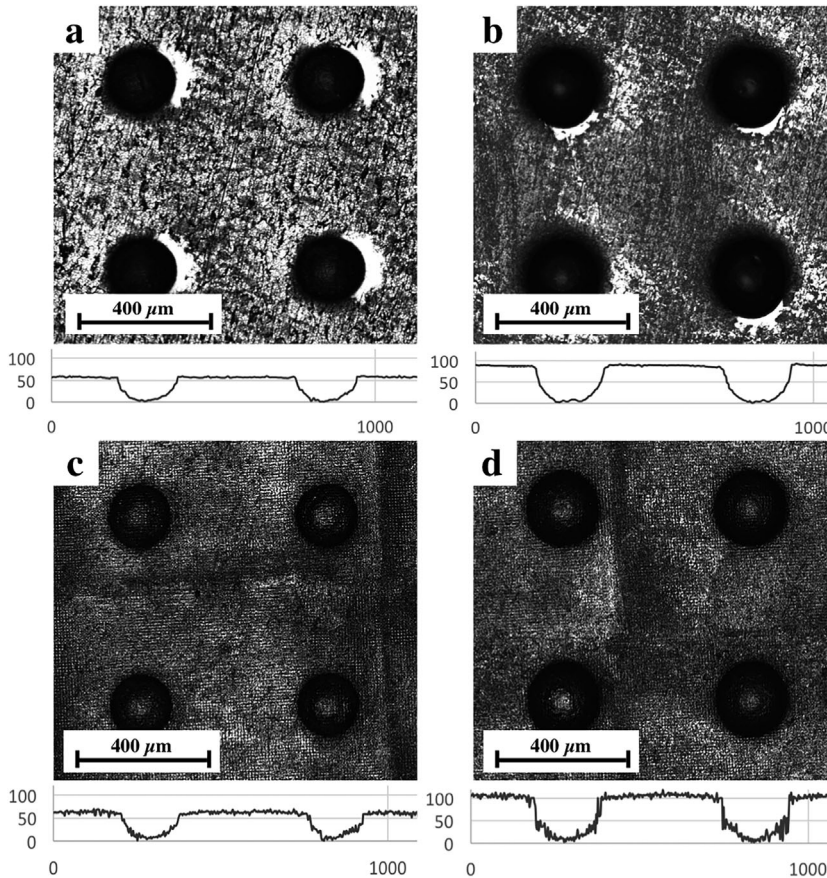


Figure 1. Overview as well as profile information of the coined samples A2 and A3 with a depth of 50 a), c) and 95 μm b), d), respectively. The top view as well as the profiles are shown before a), b) and after laser patterning c), d). All data are given in micron.

The polished reference sample starts with a COF of roughly 0.11 and stays constant over the entire measuring time of 200 sliding cycles. The smooth trend of the COF without any increase combined with the fact that no pronounced wear tracks can be observed for the reference (Figure 3) at a sliding velocity of 0.01 m s^{-1} leads to the conclusion that the prevailing lubrication regime can be assigned to EHL. This goes hand in hand with the estimated nominal Hertzian contact pressure of 1.29 GPa. This implies that elastic deformation of the rubbing surfaces and a viscosity increase with pressure become relevant. This correlates well with results published in ref.^[23]

As can be seen in Figure 2, the COF of the laser-patterned sample starts at around 0.20 and shows a decrease in the first 75 sliding cycles. Afterwards the sample reaches steady-state conditions. The observed effects can be attributed to the wearing-off of the highest surface asperities during run-in and a degradation of the laser pattern.^[10] The increased surface roughness and spiky surface topography increase the contact pressure, which makes a transition from full-film EHL (observed for the reference) to mixed lubrication likely.^[8] Furthermore, the load bearing capacity of the laser-patterned surface is reduced compared to the plateau-like surface of the reference, which can also lead to more pronounced wear features and an increased wear rate (see the severe wear marks in Figure 4b). Said effects of

the laser pattern lead to the generation of wear particles and a modified contact area, which results in a higher COF over the entire measuring time compared to all other samples.^[32,33] Summarizing, the higher contact pressure as well as the reduced load bearing capacity lead rather to increased friction as well as wear and consequently to a downgraded tribological behavior of the purely laser-patterned samples.

The COF of A2 starts at roughly 0.07 and shows a slight increase in the first sliding cycles. According to Blau, this can be explained by an initial high wear rate in which the sharpest asperities are worn off and the surface becomes smoother.^[34] After a certain decrease of the COF in the subsequent cycles, the COF remains fairly constant at around 0.05. Compared to the polished reference, A2 leads to a friction reduction by a factor of roughly 2. It can be assumed that the acting lubrication regime can be associated with full film EHL. The significant friction reduction can be explained by a pressure build-up and an additional oil supply induced by the surface structures.^[23] Considering this significant friction reduction measured for the purely micro-coined sample, the idea was to investigate whether a further friction reduction can be achieved by superimposing a cross-like laser pattern and thereby creating a multi-scale pattern.

However, as can be seen in Figure 2, the respective multi-scale pattern (coining A2 + laser) shows a worsened frictional behavior compared to the purely coined sample. The

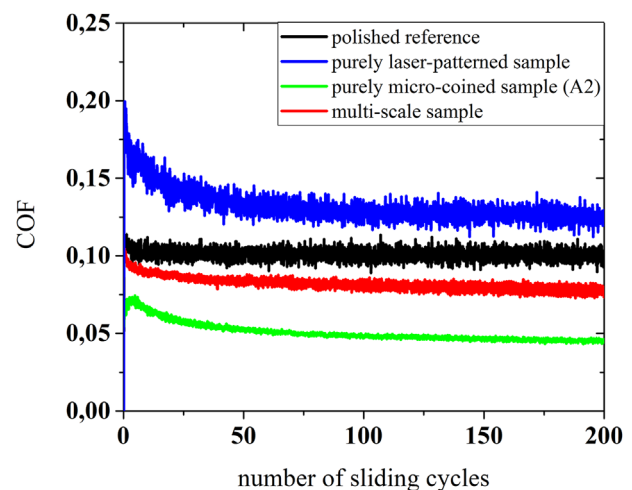


Figure 2. Temporal evolution of the COF of the polished reference, the purely coined sample (A2), the purely laser-patterned sample (cross-pattern with $9 \mu\text{m}$ periodicity) and the multi-scale sample combining coining and DLIP.

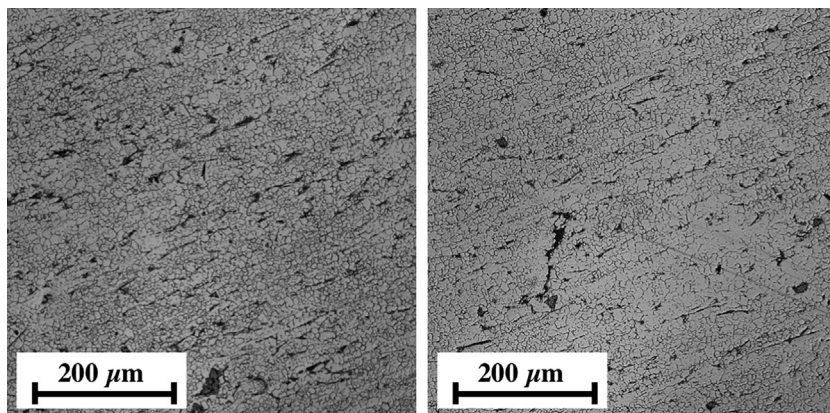


Figure 3. Surface of the polished reference after 200 sliding cycles at two different positions imaged by LSM.

initial COF is around 0.10 and afterwards, the COF slightly decreases over sliding time to end up in a final value of roughly 0.08. With respect to the value of the polished reference, the multi-scale surface leads to an improvement in the frictional behavior by roughly 20%. However, compared to the purely micro-coined surface, the COF of the multi-scale pattern is increased by roughly 60%.

In order to explain the worsened frictional behavior of the multi-scale surface, the wear behavior of those samples needs to be taken into consideration. The purely coined sample just demonstrated rather tiny wear scars with negligible depth and volume, which is in good agreement with^[23] and are, therefore, not displayed here. **Figure 5** shows the entire wear track of the multi-scale surface (combining A2 and the laser pattern), as well as a magnified image of an individual structure imaged by LSM. The arrow in the figure represents the relative motion between the ball and the sample surface. As can be seen in **Figure 5**, the multi-scale surface demonstrates a well-pronounced wear track. As a consequence, it can be assumed that the additional

cross-pattern results in an increased contact pressure due to the spikier and less plateau-like surface topography compared to the micro-coined samples. This can lead to undesired edge effects and stress raisers. Furthermore, changes in the lubrication regime as well as a reduced load bearing capacity may be induced thus increasing the COF. The observed friction reduction with regard to the polished reference can be attributed to the additional oil supply coming from the secondary oil effect induced by the multi-scale surface.

Interesting to note is the deflection of the tribological counter body during the encounter with the deeper coined structures. The deviation from its spherical path is clearly visible in both depicted images. Apparently, the ball is always pushed in the direction away

from the structure (see blue colored rectangle 1a in **Figure 5**). The deflection of the ball might demonstrate a force acting on the tribological counter body, which is generated by a pressure build-up due to the structures. This pressure build-up is due to a converging gap which is formed between the ball and the structure. In the region marked by the blue rectangle (1a) in **Figure 5**, the ball is pushed toward the left when it runs over the first coined dimple on its path, since this dimple lies on the right-hand side of the wear track and the force acts in the opposite direction. In contrast to that, the three subsequent dimples which lie on the left-hand side of the wear track push the ball to the right. Looking at the colored regions in **Figure 5**, it becomes apparent that this deflection behavior is not coincidental since it appears at opposite sides of the wear track. This phenomenon can especially be seen at the top, bottom, and side positions, where the wear track is guided over several of the coined dimples lying in a straight line instead of being guided along a track between those dimples.

Figure 6 summarizes the temporal evolution of the COF of the reference, the purely coined (A3, depth 95 μm), and the laser-patterned (cross-pattern with 9 μm periodicity) samples. In addition to that, the figure shows the frictional behavior of the corresponding multi-scale sample (A3 combined with cross 9 μm).

It is noticeable in **Figure 6** that the initial COF of the coined sample A3 is roughly 0.17. After a pronounced decrease in the first 100 sliding cycles, the COF stays fairly constant at around 0.11. Compared to A2, the COF of A3 is enlarged over the entire measuring time. With respect to the polished reference, the COF of sample A3 is significantly increased in the first 50 sliding cycles. In the following sliding cycles, the COF of the reference and A3 are rather similar without a pronounced friction reduction. Due to the steep dimple geometry, positive effects (additional pressure build-up) might be overcompensated by edge effects and stress concentrations. Moreover,

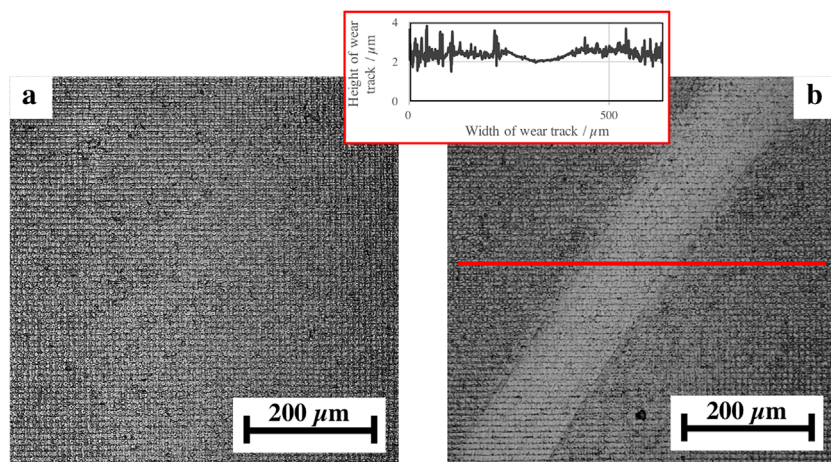


Figure 4. Images of the purely laser-patterned sample captured by LSM before a) and after the friction experiment with 200 cycles. The inset in the red box shows the wear track along the red line.

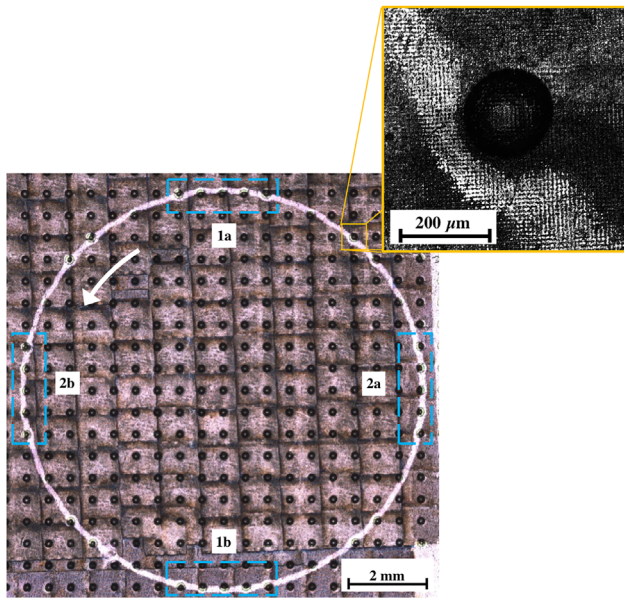


Figure 5. Overview of the entire wear track of multi-scale sample (laser + coining A2) recorded by LSM. Additionally, a magnified LSM-micrograph of an individual multi-scale structure is given. The colored regions show interesting areas of the wear track with a similar behavior on opposite sides. The arrow indicates the relative motion between ball and the sample surface.

surface structures with a larger structural depth have a higher probability for cavitation, thus reducing the oil film thickness and load bearing capacity.^[23,35] Taking the worsened frictional behavior of A3 into consideration, the idea was to check whether the additional laser pattern leads to an improved frictional performance.

The initial COF of the multi-scale surface is about 0.11. After a less pronounced decrease in the COF, the COF remains constant

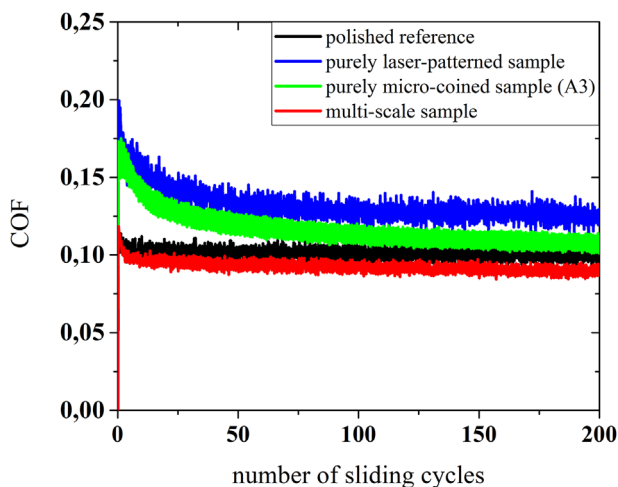


Figure 6. Temporal evolution of the COF of the polished reference, the purely coined sample with a depth of $95\ \mu\text{m}$ (A3), the purely laser-patterned sample (cross-pattern with $9\ \mu\text{m}$ periodicity) and the multi-scale sample.

at roughly 0.10. Regarding the purely coined sample as well as the purely laser-patterned sample, the multi-scale surface leads to a friction reduction over the entire sliding time. It can be assumed that the cross-pattern helps to reduce pronounced cavitation due to a better lubricant distribution in the contact zone. By reducing cavitation, a larger local oil film thickness can be present in the tribological contact thus improving the load bearing capacity and reducing the COF. Therefore, the tribological behavior is improved compared to the purely coined sample.

Considering **Figure 7**, which shows the wear behavior of the multi-scale pattern (combining A3 and the laser cross-pattern) imaged by LSM, a similar behavior as already discussed for the other multi-scale pattern in **Figure 5** can be observed. The deflection of the alumina ball from its track is again most prominent at those positions, where it encounters several coined dimples in a row. The rather similar wear behavior of both multi-scale patterns is not surprising, since both samples have a similar deformation and temperature history as well as a comparable geometry. Furthermore, the COF of both multi-scale patterns is rather similar with values of roughly 0.10 (see **Figure 2, 6**). Compared to the purely laser-patterned samples, the multi-scale patterns show a greatly reduced wear with a still intact laser pattern after 200 sliding cycles. Those differences in wear behavior can be traced back to different lubrication regimes for the laser-patterned samples (mixed lubrication) and the multi-scale surfaces (mixed EHL).

The aim of this paper was to address the run-in behavior of the multi-scale surfaces. We are completely aware that after 200 sliding cycles the COF of the single-scale laser pattern still increases and that the multi-scale surfaces has not reached its

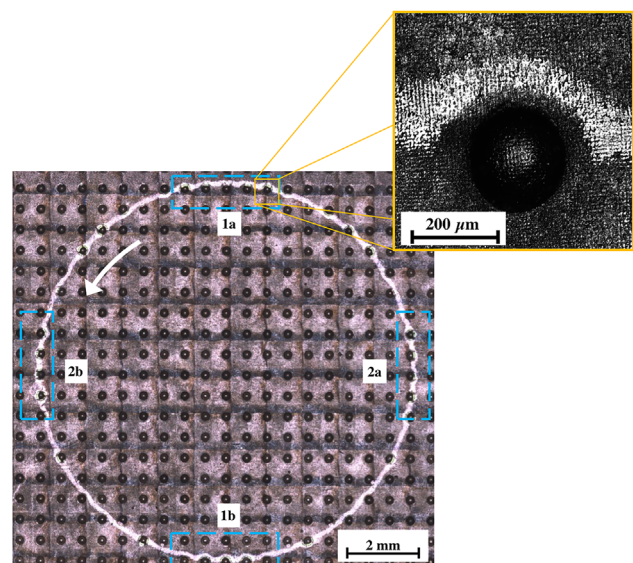


Figure 7. Overview of the entire wear track of multi-scale sample (laser + coining A3) recorded by LSM. Additionally, a magnified LSM-micrograph of an individual multi-scale structure is given. The colored regions show interesting areas of the wear track with a similar behavior on opposite sides and the arrow indicates the relative motion between ball and the sample surface.

lowest COF value. For this reason, as well as to study the stability of those multi-scale surfaces, long-term experiments are an ongoing research topic. The results of those experiments will be presented in a follow-up paper.

4. Conclusions

For the specific testing conditions, materials, patterning methods, and lubrication conditions used in this study, the following conclusions were obtained:

- 1) The measured COF under fully-flooded conditions strongly depends on the used patterning technique and the structural parameters of the respective pattern. Consequently, it can be stated that the depth of the coined structures plays an important role whether the multi-scale patterns show either beneficial or detrimental frictional effects. Thereby, the COF of the multi-scale pattern is decreased for deep structures (95 μm) and increased for shallower ones (50 μm).
- 2) The purely laser-patterned sample starts with rather high friction values and shows a slight decrease afterwards ending up in steady-state conditions. This behavior can be attributed to the wearing-off of the laser pattern and the highest surface asperities during run-in. The laser-patterned sample shows an increased COF over the entire time compared to all other samples. This can be traced back to the spiky surface topography of the laser pattern which increases the contact pressure and makes the transition from full-film EHL to mixed lubrication likely. This is supported by severe wear marks observed by LSM.
- 3) For the purely micro-coined surfaces, lower coining depths of around 50 μm lead to the best tribological performance under full-film EHL due to a pressure build-up in the lubricant and an additional oil supply from the coined pockets. In contrast to that, the corresponding multi-scale sample shows a worsened behavior compared to the only micro-coined samples due to an increased surface roughness and thus stronger edge effects, as well as accompanied stress raisers.
- 4) For larger structural depths around 95 μm , the purely micro-coined surfaces are less efficient over the entire measuring time because the deeper dimples are more prone to pronounced cavitation and do not allow for a sufficient pressure build-up. The multi-scale surfaces show advantageous effects and are characterized by a stable, as well as relatively low COF. The additional laser patterns assist in reducing cavitation, and therefore contribute to an enhanced lubrication in the contact zone which results in an enhanced frictional behavior.
- 5) The wear behavior of the tested samples also changes with the used patterning technique. The laser-patterned samples show pronounced wear scars with a completely destroyed pattern after 200 sliding cycles, whereas the purely micro-coined samples just demonstrate tiny, negligible wear marks. In case of the multi-scale surfaces, again more pronounced wear features can be found which can be traced back to an increased contact pressure induced by the spikier surface topography of the laser pattern.

Acknowledgements

The present work is supported by funding from the Deutsche Forschungsgemeinschaft (DFG, projects: MU 959/27-2 and HI 790/33-2 within the SPP 1551). Henara Costa is gratefully acknowledged for further discussions.

Conflict of Interest

The authors declare no conflict of interest.

Keywords

Laser surface patterning, micro-coining, multi-scale surfaces, friction reduction

Received: June 17, 2017
Revised: August 16, 2017
Published online: September 1, 2017

- [1] M. Nosonovsky, B. Bhushan, *Mater. Sci. Eng. R Rep.* **2007**, *58*, 162.
- [2] E. Broitman, *Friction* **2014**, *2*, 40.
- [3] J. R. Barber, *Tribol. Lett.* **2013**, *49*, 539.
- [4] Z. Guo, W. Liu, B. L. Su, *J. Colloid Interface Sci.* **2011**, *353*, 335.
- [5] B. Bhushan, Y. C. Jung, *Prog. Mater. Sci.* **2011**, *56*, 1.
- [6] B. Bhushan, *Philos. Trans. R. Soc. A Math. Phys. Eng. Sci.* **2009**, *367*, 1445.
- [7] H. Kasem, A. Tsipenyuk, M. Varenberg, *Soft Matter* **2015**, *11*, 2909.
- [8] A. Rosenkranz, T. Heib, C. Gachot, F. Mücklich, *Wear* **2015**, *334–335*, 1.
- [9] I. Etsion, *Tribol. Lett.* **2004**, *17*, 733.
- [10] C. Gachot, A. Rosenkranz, L. Reinert, E. Ramos-Moore, N. Souza, M. H. Müser, F. Mücklich, *Tribol. Lett.* **2013**, *49*, 193.
- [11] W. Tang, Y. Zhou, H. Zhu, H. Yang, *Appl. Surf. Sci.* **2013**, *273*, 199.
- [12] A. Amanov, R. Tsuboi, H. Oe, S. Sasaki, *Tribol. Int.* **2013**, *60*, 216.
- [13] B. Zhang, W. Huang, J. Wang, X. Wang, *Tribol. Int.* **2013**, *65*, 138.
- [14] A. Kovalchenko, O. Ajayi, A. Erdemir, G. Fenske, *Wear* **2011**, *271*, 1719.
- [15] A. Borghi, E. Gualtieri, D. Marchetto, L. Moretti, S. Valeri, *Wear* **2008**, *265*, 1046.
- [16] D. Gropper, L. Wang, T. J. Harvey, *Tribol. Int.* **2016**, *94*, 509.
- [17] U. Pettersson, S. Jacobson, *Tribol. Lett.* **2004**, *17*, 553.
- [18] H. Ike, M. Plancak, *J. Mater. Process. Technol.* **1998**, *80–81*, 101.
- [19] I. Etsion, *J. Tribol.* **2005**, *127*, 248.
- [20] F. Mücklich, A. F. Lasagni, C. Daniel, *Int. J. Mater. Res.* **2006**, *97*, 1337.
- [21] T. Roch, D. Benke, S. Milles, A. Roch, T. Kunze, A. F. Lasagni, *Diamond Relat. Mater.* **2015**, *55*, 16.
- [22] A. Szurdak, A. Rosenkranz, C. Gachot, G. Hirt, F. Mücklich, *Key Eng. Mater.* **2014**, *611–612*, 417.
- [23] A. Rosenkranz, A. Szurdak, C. Gachot, G. Hirt, F. Mücklich, *Tribol. Int.* **2016**, *95*, 290.
- [24] W. Koszela, P. Pawlus, L. Galda, *Wear* **2007**, *263*, 1585.
- [25] D. Z. Segu, S. G. Choi, J. H. Choi, S. S. Kim, *Appl. Surf. Sci.* **2013**, *270*, 58.
- [26] X. Wang, K. Adachi, K. Otsuka, K. Kato, *Appl. Surf. Sci.* **2006**, *253*, 1282.
- [27] C. Gachot, A. Rosenkranz, B. Wietbrock, G. Hirt, F. Mücklich, *Adv. Eng. Mater.* **2013**, *15*, 503.
- [28] A. Szurdak, G. Hirt, *Steel Res. Int.* **2014**, *85*, 1.
- [29] A. Rosenkranz, S. Fleischmann, C. Gachot, F. Mücklich, *Adv. Eng. Mater.* **2015**, *17*, 1645.
- [30] A. F. Lasagni, C. Holzapfel, T. Weirich, F. Mücklich, *Appl. Surf. Sci.* **2007**, *253*, 8070.

- [31] A. F. Lasagni, M. D'Alessandria, R. Giovanelli, F. Mücklich, *Appl. Surf. Sci.* **2007**, 254, 930.
- [32] P. G. Grützmacher, A. Rosenkranz, S. Rammacher, C. Gachot, F. Mücklich, *Tribol. Int.* **2017**, 116, 256.
- [33] A. Rosenkranz, L. Reinert, C. Gachot, F. Mücklich, *Wear* **2014**, 318, 49.
- [34] P. J. Blau, *Tribol. Int.* **2005**, 38, 1007.
- [35] M. B. Dobrica, M. Fillon, M. D. Pascovici, T. Cicone, *Proc. Inst. Mech. Eng. Part J J. Eng. Tribol.* **2010**, 224, 737.

VI From lab to application - Improved frictional performance of journal bearings induced by single- and multi-scale surface patterns

Philipp G. Grützmacher¹, Andreas Rosenkranz², Adam Szurdak³, Florian König⁴, Georg Jacobs⁴, Gerhard Hirt³, Frank Mücklich¹

¹ Chair of Functional Materials, Saarland University, 66123 Saarbrücken, Germany

² Department of Mechanical and Aerospace Engineering, Center for Memory and Recording Research, University of California, 92093, La Jolla, United States

³ Institute of Metal Forming, RWTH Aachen, 52056 Aachen, Germany

⁴ Institute for Machine Elements and Systems Engineering, RWTH Aachen, 52062, Aachen, Germany

Published in "Tribology International" (Impact factor (2017): 3.246)

Accessible online at: <https://doi.org/10.1016/j.triboint.2018.06.036>

Own contribution:

Project management; scientific discussion; paper writing; data analysis; sample preparation: laser surface patterning; measurements: white light interferometry, laser scanning microscopy

Abstract:

The present study experimentally examines the effect of selected single-scale and multi-scale surface patterns fabricated by roller-coining and/or direct laser interference patterning on the frictional performance of journal bearings. For this purpose, surface patterns showing beneficial effects in preliminary laboratory tests were selected and fabricated onto the shaft of journal bearings made of stainless steel (AISI 304). The frictional performance of these patterns was evaluated on a special test rig by recording Stribeck-like curves. The results show greatly reduced coefficients of friction and a shift in the transition from mixed to hydrodynamic lubrication to smaller rotational speeds for all patterned samples compared to the reference sample. The observed friction reduction matches well with results observed in the previous laboratory tests.

Cite this as:

P.G. Grützmacher, A. Rosenkranz, A. Szurdak, F. König, G. Jacobs, G. Hirt, F. Mücklich, From lab to application - Improved frictional performance of journal bearings induced by single- and multi-scale surface patterns, *Tribol. Int.* **2018**, 127, 500–508. (<http://doi:10.1016/j.triboint.2018.06.036>)



From lab to application - Improved frictional performance of journal bearings induced by single- and multi-scale surface patterns

Philipp G. Grützmacher^{a,*}, Andreas Rosenkranz^b, Adam Szurdak^c, Florian König^d, Georg Jacobs^d, Gerhard Hirt^c, Frank Mücklich^a

^a Department of Functional Materials, Saarland University, 66123, Saarbrücken, Germany

^b Department of Mechanical and Aerospace Engineering, Center for Memory and Recording Research, University of California, 92093, La Jolla, United States

^c Institute of Metal Forming, RWTH Aachen, 52056, Aachen, Germany

^d Institute for Machine Elements and Systems Engineering, RWTH Aachen, 52062, Aachen, Germany



ARTICLE INFO

Keywords:

Journal bearing
Micro-coining
Laser patterning
Friction reduction

ABSTRACT

The present study experimentally examines the effect of selected single-scale and multi-scale surface patterns fabricated by roller-coining and/or direct laser interference patterning on the frictional performance of journal bearings. For this purpose, surface patterns showing beneficial effects in preliminary laboratory tests were selected and fabricated onto the shaft of journal bearings made of stainless steel (AISI 304). The frictional performance of these patterns was evaluated on a special test rig by recording Stribeck-like curves. The results show greatly reduced coefficients of friction and a shift in the transition from mixed to hydrodynamic lubrication to smaller rotational speeds for all patterned samples compared to the reference sample. The observed friction reduction matches well with results observed in the previous laboratory tests.

1. Introduction

Tribology, involving friction, wear and lubrication, is an important aspect in our daily life since it can be directly connected with energy efficiency, maintenance intervals and costs of machine components but also with quality of life. The latter can be realized when thinking about tribological problems occurring in contact lenses or artificial joints both being addressed in bio-tribology [1–3]. Historically, tribology is associated with moving mechanical components under a certain normal load such as bearings, piston rings or cam followers. In this context, friction and wear greatly influence the efficiency and lifetime of these components. In passenger cars, roughly one third of the entire energy is needed to overcome frictional losses [4]. A similar picture can be found in mining industry, where roughly 38% of the energy is used to compensate friction and wear losses [5]. Holmberg et al. estimated that the friction and wear losses can be reduced by approximately 60% when using advanced next-generation technologies. Those technologies comprise new coatings, modern surface engineering, improved lubricants, new material systems as well as a better mechanical design [4,5]. It is straight forward to conclude that this would have a tremendous impact on aspects such as energy efficiency and reliability but also sustainability and CO₂-emissions [6].

During the last 20 years, surface engineering, in particular surface

patterning, has emerged as an interesting approach to precisely tailor tribological properties. Starting with the pioneering work by Etsion et al. [7], numerous manuscripts have been published demonstrating the successful use of surface patterning to improve friction and wear under dry and lubricated conditions including boundary, mixed, elasto-hydrodynamic and hydrodynamic lubrication [8–10]. Depending on the experimental conditions and the underlying lubrication regime, different aspects contribute to the observed friction and wear reduction. In this context, the reduction of the real contact area [11], the trapping of wear particles [12–15], the reduction of stress raisers and edge effects [16], the storage of lubricant [12–14], the build-up of an additional hydrodynamic pressure [12,13,17] can be named as potential contributions. Over time, several techniques such as laser surface patterning, embossing/micro-coining, lithographic methods and many more, have been used to fabricate patterns on different scales [9,18]. Thereby, the selection of the appropriate technique depends on the respective frictional characteristics and contact conditions of the corresponding tribological system [9]. Taking the available techniques into consideration, it can be stated that laser surface patterning and embossing/micro-coining are fast, reliable and environmentally-friendly methods, which enable the fabrication of patterns with variable pattern geometries and feature sizes on different scales.

One of the components, which is responsible for frictional losses in

* Corresponding author.

E-mail address: philipp.gruetzmacher@uni-saarland.de (P.G. Grützmacher).

Table 1
Surface roughness parameters measured prior to and after machining and burnishing using a tactile measuring device.

Process step	$R_a/\mu\text{m}$		$R_q/\mu\text{m}$		$R_z/\mu\text{m}$		$R_{Sk}/\mu\text{m}$					
Initial bar	0.88	±	0.18	1.14	±	0.24	6.04	±	1.17	–1.21	±	0.30
Machining	0.44	±	0.01	0.53	±	0.01	2.60	±	0.14	0.01	±	0.06
Burnishing	0.16	±	0.02	0.20	±	0.02	1.07	±	0.09	–0.67	±	0.20

mechanical systems, are bearings [19,20]. For instance, journal bearings are used in many applications such as combustion engines, turbomachinery, construction and oil-field equipment [20–22]. Those bearings especially suffer from high friction and wear if start-stop-cycles occur during operation [20]. Furthermore, bearings installed in heavy-duty machinery often work under mixed or even boundary lubrication and therefore show a tendency for increased friction and/or wear [22]. It could be shown that the surface roughness has a significant effect on the performance of journal bearings [23]. As a consequence, there have been increasing efforts to modify the surface roughness (i.e. by introducing surface patterns) to understand the influence of the roughness on the resulting performance, and to further reduce friction and wear in journal bearings. Lu and Khonsari fabricated dimples on the inner surface of the journal bearing's bushings by machining and chemical etching [24]. Their results showed that friction in a journal bearing can be reduced by an appropriate selection of the pattern geometry. Tala-Ighil and Fillon qualitatively verified the results of Lu and Khonsari by a numerical study [19]. Furthermore, they showed that an improved frictional performance is strongly linked with the operating conditions. Moreover, they proved that larger dimples (diameter = 4 mm) are more effective than smaller ones. Sinanoğlu et al. investigated the effect of shafts' surface patterns on the frictional performance in journal bearings [25]. They concluded that the load bearing capacity for shafts with a trapezoidal profile is better than for saw profiles. Additionally, greater profile heights have a positive effect on the load bearing capacity. Brizmer and Kligerman theoretically examined the use of micro-dimples manufactured by laser surface patterning to improve the performance of journal bearings [26]. Their main finding is that partial patterning can, in contrast to a patterning of the entire surface, improve the bearing's performance. Due to the substantial improvements in terms of the frictional and wear behavior due to surface patterning, it can be expected that especially the surface topography will be the focus of future design guidelines for those bearings [19,27].

The goal of this study is to experimentally investigate the effect of selected single-scale and multi-scale surface patterns on the frictional performance of journal bearings. For this purpose, surface patterns showing beneficial effects in preliminary lab-experiments were selected. Those patterns were fabricated onto the shaft of a journal bearing and the tribological performance was tested on a special test rig by recording Stribeck-like curves. Thereby, the rotational velocity was changed to adjust mixed and hydrodynamic lubrication as well as to record the transition between those regimes.

The results of preliminary tests in which micro-coined, laser-patterned and multi-scale (combining micro-coining and DLIP) samples have been tested using a ball-on-disc tribometer have been published in Refs. [14,16,28]. For the reader's convenience, a short summary of these results shall be given here. It could be demonstrated that the patterned samples usually led to a friction and wear reduction compared to a polished reference irrespective of the patterning method used. Nevertheless, the effectiveness of the patterns strongly depended on the used fabrication technique and geometry of the respective samples. Thereby, micro-coined samples with the lowest area densities (10%) and structural depths (25 μm) showed the best frictional behavior with a maximum friction reduction by a factor of 4 compared to the polished reference [16]. Regarding the laser-patterned samples, it was verified that cross-like patterns with smaller periodicities are more

beneficial [14]. Finally, multi-scale patterns consisting of deeper micro-coined dimples (depth of 50 μm) superimposed by a cross-like surface pattern showed an improved frictional behavior compared to the purely micro-coined samples. In contrast, the coefficient of friction (COF) was increased for multi-scale patterns if micro-coined samples having lower depths (25 μm) were superimposed with an additional laser pattern [28].

2. Experimental procedure

2.1. Material and preprocessing

The shafts were fabricated by machining and burnishing of cold drawn bars made of stainless steel (AISI 304). The burnishing tool EG5T (Ecoroll, Germany) was used to improve the surface roughness after machining. In order to achieve a low surface roughness of the shaft, the roughness before burnishing and the axial displacement of the tool had to be low. Additionally, a high number of overpasses was required. With regard to the burnishing force, a low force is not sufficient to smoothen the surface whereas a high force can possibly increase the roughness again. Consequently, the burnishing force was varied between 1.1 and 2.3 kN taking the material's hardness of 386 ± 16 HV3 into account. This hardness is typical for a work hardened material. The axial movement of the burnishing tool was set to 0.1 mm/turn and the circumferential speed was 90 min^{-1} . Prior to burnishing, the samples were thoroughly cleaned with ethanol. In total, three passes with a constant burnishing force were done whereby PAO40 oil was used as a lubricant. The lowest surface roughness was achieved for a burnishing force of 1.5 kN after three overpasses (see Table 1).

2.2. Analysis of the surface topography

To control the burnishing process and the roller-coining, the surface topography was measured using a digital light microscope (*Keyence VHX-1000*). Additionally, the surface roughness was determined with a tactile measuring device (*Mahr MarSurfPS1*). The measurements of the surface roughness were performed according to DIN EN ISO 4288. The wear marks as well as the geometry of the produced patterns were imaged by laser scanning microscopy LSM (*LEXT OLS 4100, Olympus*) and white light interferometry WLI (*New View 7300, Zygo*). Ten measurements at randomly selected positions of the sample were conducted to calculate mean values and standard deviations.

2.3. Direct laser interference patterning (DLIP)

To fabricate laser patterns with features sizes in the lower micron range, a pulsed solid-state Nd:YAG laser (*Quanta Ray PRO 290, Newport Spectra Physics*) with a fundamental wavelength of 1064 nm, an average power of 20 W, a pulse duration of 10 ns and a frequency of 10 Hz was used. By harmonic generation, a wavelength of 532 nm can be produced. This wavelength was used to fabricate surface patterns under normal atmospheric conditions. For this purpose, the primary laser beam was split up into two sub-beams and then these sub-beams were overlapped again with each other on the sample's surface thus inducing interference. Thereby, the primary beam passed through an attenuator, a shutter system and a lens (focal length 2000 mm) to adjust the respective laser power precisely, to select individual laser pulses and to

increase the power density, respectively. The optical element, which split the primary beam into two beams, was a suitable beam-splitter. Finally, a mirror system guided the individual sub-beams to the surface. By overlapping two beams, a sinusoidal intensity distribution was obtained, which in turn led to a line-like surface topography on the sample in just one shot. The laser fluence was kept constant for all specimens at 1.96 J/cm^2 , respectively. Further details related to DLIP have already been published elsewhere [29,30]. In order to fabricate cross-like surface patterns two line-like surface patterns were overlapped whereas the sample was turned by 90° after the first patterning step.

The generation of surface patterns by DLIP on curved surfaces such as the used shaft of the journal bearing required the incorporation of a rotation motor into the experimental setup. The motor needed to have an adequate precision to connect the individual laser pulses to a seamless pattern. The motor was controlled by an Arduino and therefore could be synchronized with the other parts of the setup. The radius of the shaft was not a crucial factor since the Nd:YAG laser has a high coherence length and small differences in focus distance can be considered as negligible. Possible deviations in the periodicities account for less than 6% [31].

2.4. Roller-coining

Since surface patterns with a depth over $2 \mu\text{m}$ and a width over $30 \mu\text{m}$ cannot be fabricated by DLIP, these micro-dimples were fabricated by roller-coining. The roller-coining set-up consisted of a pneumatic system to control the forming force and a coining tool to fabricate the required pattern [32]. The pneumatic system is shown in Fig. 1. A computer-controlled proportional valve (SENTRONIC D, Asco) and a pneumatic cylinder (DSNU, Festo) were used. Thus, the setup allowed to continuously adjust the forming force by changing the pneumatic pressure as well as to self-adjust the tool-position to overcome asperities without changing the forming force and therefore pocket depth.

The roller-coining tool was made of tool steel HS6-5-2 (1.3343). After machining the tool into a tapered shape, it was vacuum-hardened and structured by laser ablation (Photonik-Zentrum Kaiserslautern). Due to the tapered shape only one dimple is coined simultaneously during the roller-coining process, which increases the flexibility and the control of the entire process. Two tools with different structures, namely A1 and A2, were fabricated based upon results of previously published work [16,28]. Following the preliminary results obtained by laboratory tests the tools had a depth of $22.9 \mu\text{m}$ (A1) and $44.3 \mu\text{m}$ (A2) as well as an area density of 10%.

The roller-coining set-up was integrated into a conventional turning machine to pattern the shafts. In order to control and to measure the pneumatic pressure, a self-developed LabVIEW code and a NI USB-6009 DAQ system were used. Additionally, an HBM C2 load cell was used to measure the forming force. A close positioning of the load cell to the tool allowed for drawing conclusions with respect to the coined depth

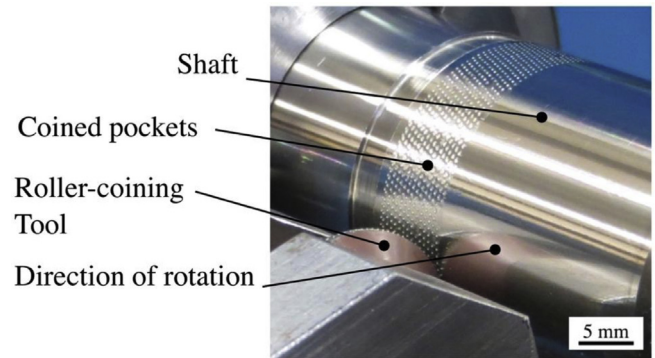


Fig. 2. Roller-coining of a shaft made of stainless steel (AISI 304).

and thus on the quality of the pattern without the influence of stick-slip generated by the pneumatic cylinder. Apart from the pocket depth, the axial distance between the coined pockets was important since this parameter affects the area density. Thereby, the tangential distance (parallel to the tool rolling direction) was determined by the tool and cannot be varied during the process whereas the axial distance (perpendicular to the tool rolling direction) was determined by the movement of the turning machine. The roller-coining process is shown in Fig. 2.

2.5. Journal bearing test rig

The frictional behavior of the shafts was investigated using a special test rig for journal bearings, which is schematically shown in Fig. 3.

For this purpose, turned journal bearings (CuSn12NiC-GCB) with a diameter of 25 mm and a width of 20 mm were used. The average hardness was about $122.5 \pm 7.5 \text{ HBW } 5/250$. The bearings were individually manufactured for each shaft to achieve a relative clearance of 1.4‰. The roughness was about $R_a 0.4 \mu\text{m}$ ($R_z 4 \mu\text{m}$). The bearings were lubricated with an additive-free Poly-alpha-olefin oil. A base oil without additives allowed to avoid chemical reactions between the oil and the rubbing surfaces. Additionally, tribolayer formation as observed in a previous study with additive-rich oil and similar materials can be neglected [33]. The properties of the oil used as well as the testing parameters are summarized in Table 2. In order to reduce the impact of local heating, the bearing system was preheated to 40°C utilizing circumferentially positioned heating cartridges located in the bearing housing. In this study, the shaft speed was reduced stepwise from 600 to 25 rpm (equivalent to a decrease in linear speed from $0.785 \text{ m}\cdot\text{s}^{-1}$ to $0.033 \text{ m}\cdot\text{s}^{-1}$) with a holding time of 120 s for each rotational speed to study the frictional behavior under mixed and hydrodynamic lubrication.

The stationary pressure was kept constant at $1 \text{ N}\cdot\text{mm}^{-2}$ for all

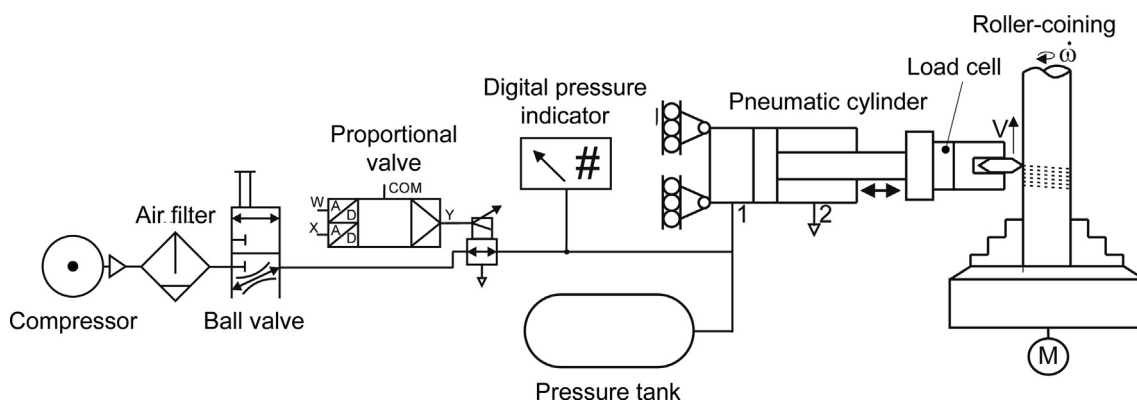


Fig. 1. Circuit diagram of the roller-coining setup consisting of a pneumatic system and the coining tool.

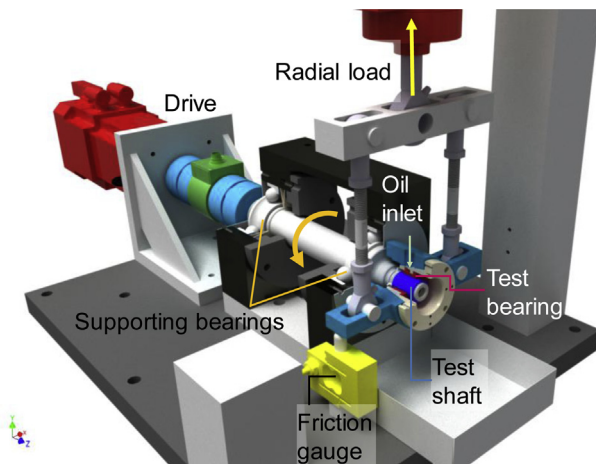


Fig. 3. Schematic representation of the journal bearing test-rig.

Table 2
Properties of the used PAO oil and summary of the testing parameters.

Lubricant	PAO 4
Kinematic viscosity (40 °C)/mm ² ·s ⁻¹	16.8
Kinematic viscosity (100 °C)/mm ² ·s ⁻¹	3.9
Testing parameters	
Bearing temperature/°C	40
Oil inlet pressure/bar	2
Stationary pressure/N·mm ⁻²	1
Rotational speed/rpm	25–600
Linear speed/m·s ⁻¹	0.033–0.785
Relative clearance/%	1.4

experiments conducted. The radial load was applied to the housing of the bearing using a flexible load unit [34]. A friction gauge, which is connected directly to the housing of the bearing, was used to determine the frictional force. The drive speed, radial load, friction force, inlet- and bearing temperature were continuously measured during the experiments. The bearing COF was calculated from the measured friction torque M_F accordingly: $\text{COF} = M_F \cdot (F_R \cdot r)^{-1}$, where F_R is the radial load and r is the radius of the bearing. In order to compare the frictional behavior of different surface patterns, Stribeck-like curves were derived by averaging the COF of each speed step using data from the three cycles.

3. Results and discussion

3.1. Fabrication of surface patterns by roller-coining

Roller-coining experiments with varying pneumatic pressure (i.e. forming force) were performed to determine the process parameters that ensure a high homogeneity of the patterns as well as high form filling (ratio of coined pocked depth to tool height). In Fig. 4a, the deviation of the pneumatic pressure and forming force is shown for roller-coining of A1.

It can be seen that the pneumatic pressure and coining force only vary by 2 and 7%, respectively. The higher deviation of the forming force is caused by stick-slip phenomena of the pneumatic cylinder. The maximum deviation of the coining depth is about 1.3 μm. Based upon this figure and the presented deviations, it can be emphasized that the roller-coining set-up allows for high reproducibility (see also Table 3).

In Fig. 4b, the form filling over the forming force is shown for both samples (A1 and A2). Similar to hot micro-coining an asymptotic curve was determined [16]. However, in contrast to hot micro-coining, a complete form filling was not obtained due to large elastic deformations. These elastic deformations can be correlated with the cold

forming process and additional work hardening of the shaft during burnishing. Both leading to a higher strength of the material thus increasing elastic deformation. The forming forces were selected to be 108 N and 188 N to fabricate A1 and A2, respectively. The form filling is about 65% for A1 and 78% for A2.

After the coining process, the bulges produced at the edges of the dimples were removed by a final burnishing step. Due to the plastic deformation the pocket depth was slightly reduced.

3.2. Topographical characterization

All surfaces were characterized prior to and after the respective patterning steps. The goal of this research work is to study the frictional behavior of promising surface patterns, determined in preliminary laboratory tests, under more realistic conditions in a journal bearing. Therefore, particular consideration is given to the homogeneity of the produced patterns. The example of a multi-scale surface combining the micro-coined pattern A1 and the cross-like laser pattern, as shown in Fig. 5, demonstrates a geometrically well-defined dimple on the shaft's curved surface. Furthermore, the cross-like laser pattern is homogeneously distributed over the entire surface.

An overview of the resulting surface topography of all fabricated samples as well as their respective profiles is given in Fig. 6. Due to the wall angle, which can be seen in the surface profiles, an increasing structural depth simultaneously leads to an enlarged dimple diameter. The multi-scale samples show a homogenous distribution of the laser pattern over the entire sample surface with features inside the dimples as well as between them (Fig. 6 (d) and (f)).

Table 3 summarizes the structural parameters of the fabricated samples and shows the high reproducibility of both patterning techniques. The standard deviations of all parameters are, with exception of the depth of the laser pattern, well below 10%. Thereby, the absolute value of the deviation in depth is with 0.2 μm still very small.

3.3. Tribological results

To investigate the effectiveness of surface patterns that have been studied in preliminary laboratory tests [14,16,28] under more realistic conditions in a mechanical component, the patterns were successfully fabricated on shafts of journal bearings. Subsequently, the frictional response of the patterned shafts was evaluated on a special test rig for journal bearings. In these experiments, the rotational speed was decreased stepwise from 600 rpm to 25 rpm (equivalent to a decrease in linear speed from 0.785 m·s⁻¹ to 0.033 m·s⁻¹) while keeping all other parameters constant. Fig. 7 shows exemplarily the temporal evolution of the COF for three repetitions for the laser-patterned, the micro-coined (A1) and the multi-scale (A1 + L) sample. As can be seen in this figure, the COF of all samples is fairly stable for all rotational speeds and repetitions. Additionally, the evolution of the COF can be considered as reproducible since no significant differences can be observed between the different repetitions.

For these rotational speeds and the materials used, the system's eccentricity of the unpatterned journal bearing was calculated according to DIN 31652-2. The resulting film thickness ratio is depicted in Fig. 8. For rotational speeds higher than 100 rpm, the minimum lubricant gap height h_{\min} becomes thicker than the combined surface roughness of the rubbing surfaces $h_{\text{lim}} \left(\sqrt{R_{z,\text{shaft}}^2 + R_{z,\text{bearing}}^2} \approx 4.1 \mu\text{m} \right)$, which induces a significant friction reduction.

In accordance with the calculated film thickness, the burnished reference demonstrates a Stribeck-like behavior with a rather high COF of 0.23 for the lowest velocities, as can be seen in Fig. 9. With increasing rotational speed (> 100 rpm), a gradual decrease in the COF is observed, which can be traced back to a further separation of the rubbing surfaces. This is in good agreement with the calculated film thickness

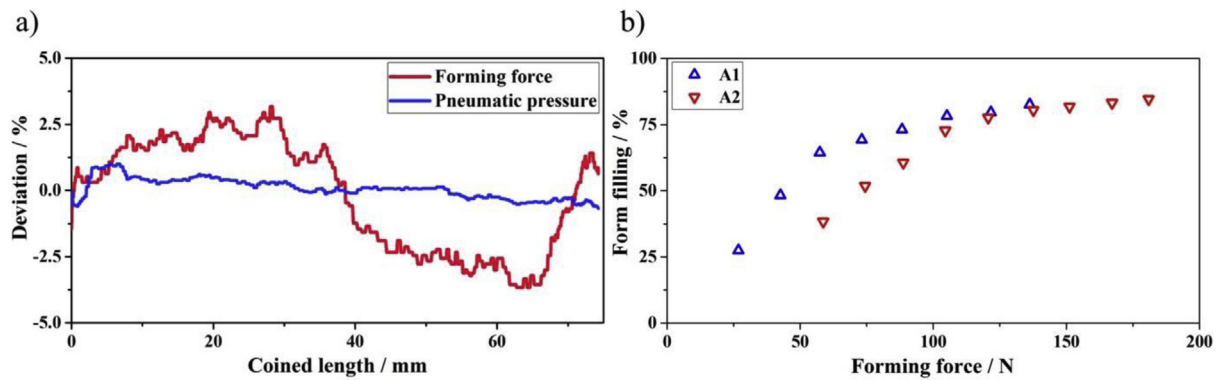


Fig. 4. (a) Deviation of the coining force and pneumatic pressure over coined length during roller-coining of A1 and (b) form filling (ratio of coined pocked depth to tool height) versus forming force of both samples A1 and A2.

ratio, which shows that the film thickness exceeds the combined surface roughness for rotational speeds greater than 100 rpm. Due to the occurrence of wear marks on the shaft's surface it can be assumed that the acting lubrication regime at the lowest rotational speed can be associated with mixed lubrication. For the highest rotational speeds (> 500 rpm), the COF is rather constant with values of approximately 0.12. In addition, the calculated film thickness ratio exceeds values of 3. Taking these two aspects into consideration with the low contact pressure of 1 MPa, it is highly likely that this can be correlated with the transition from mixed to hydrodynamic lubrication.

Compared to the burnished reference, all patterned samples show a reduced COF over the entire range of rotational speeds. For the lowest rotational speed of 25 rpm, the patterned samples demonstrate a COF between 0.16 (micro-coined) and 0.19 (multi-scale), which accounts for a friction reduction of about 20–30% compared to the burnished reference. With increasing rotational speed, a sudden drop in COF can be observed for all patterned samples whereas the COF of the burnished reference only slightly decreases. For rotational speeds larger than 150 rpm (equivalent to 0.4 m s^{-1}), all patterned samples show a constant and low COF of roughly 0.05. This decrease in COF can be traced back to a transition from mixed to hydrodynamic lubrication. Based upon Fig. 9, it can be observed that this transition for all patterned samples is shifted to smaller rotational speeds. Since the patterned samples show the transition to hydrodynamic lubrication at considerably lower rotational speeds, the COF of these samples is reduced by a factor of 2–2.5 compared to the burnished reference. It is worth mentioning that, for the purely micro-coined sample A1, this transition takes place at the lowest speed. Several studies have also observed a shift in the lubrication regime to smaller velocities and/or higher normal loads induced by surface patterning in lab experiments [12,13,17]. Kovalchenko et al. performed tests with laser-patterned steel disks on a pin-on-disk tribometer and concluded that laser patterning can expand the hydrodynamic lubrication regime [12,13]. Wang et al. found a 20% increase in the critical load for laser-patterned SiC disks during cylinder-on-disk sliding tests [17]. Additionally, our preliminary laboratory tests also showed a transition from mixed to hydrodynamic lubrication at lower sliding speeds for purely micro-

coined samples [16]. The improved frictional behavior of the patterned samples can be traced back to the build-up of an additional hydrodynamic pressure thus leading to a greater separation of the rubbing surfaces and an increased load bearing capacity. Furthermore, the patterned surfaces can act as oil reservoirs feeding lubricant into the contact area, which is beneficial especially for lower relative velocities (i.e. in mixed lubrication) [15,16]. It is worth to emphasize that the reduction in the COF compared to the reference is greatest in the transition zone with factors of up to 3. The friction reduction for both lubrication regimes is similar to the preliminary laboratory tests published by Rosenkranz et al. [16], which underlines the possibility to transfer these results to real application. Comparing the patterned samples with each other shows that the differences in the COF between those samples are rather small. In this context, the laser-patterned sample demonstrates the highest COFs and the transition to hydrodynamic lubrication at the highest rotational speed. Interestingly, the multi-scale sample shows an intermediate COF between the micro-coined and laser-patterned samples and thus a slightly downgraded frictional behavior compared to the purely micro-coined sample. Higher COFs measured for multi-scale patterns due to an additional laser pattern have already been observed in our preliminary laboratory tests [28]. It can be assumed that the spikier and less plateau-like surface topography of the laser pattern leads to an increased contact pressure thus inducing undesired edge effects and stress raisers. Consequently, the load bearing capacity decreased, which leads to an increased COF of the multi-scale sample.

Similar to the lab tests published in Refs. [16,28], micro-coined samples with an increased structural depth (A2) and the respective multi-scale samples (A2 + L) were tested. As can be seen from Fig. 10, there is a significant reduction in the COF with factors up to 4.6 compared to the reference sample and a shift in the transition from mixed to hydrodynamic lubrication to smaller rotational speeds. The beneficial effects compared to the reference can be again traced back to a reduced real contact area, the possibility to store lubricant as well as the ability to trap wear particles in the patterns and to the build-up of an additional hydrodynamic pressure.

Comparing the patterned samples reveals that the purely micro-

Table 3

Summary of the structural parameters of all fabricated samples measured by WLI. Summarized are the structural depth d and width w as well as the periodicity (for multi-scale patterns the periodicity of the primary micro-coined pattern is given).

Sample	Depth/ μm	Width/ μm	Periodicity/ μm	Area density/%	Aspect ratio (d/w)
Laser-patterned L	0.64 ± 0.2	5.8 ± 0.2	5.7 ± 0.1	–	0.11
Micro-coined A1	16.3 ± 0.5	116.9 ± 3.0	591.5 ± 47.2	2.9	0.14
Micro-coined A2	35.3 ± 2.1	155.2 ± 5.0	577.5 ± 24.6	5.7	0.23
Multi-scale A1 + L	17.1 ± 0.7	124.5 ± 3.5	565.4 ± 14.4	3.2	0.14
Multi-scale A2 + L	35.3 ± 1.3	155.8 ± 2.3	553.9 ± 18.8	6.0	0.23

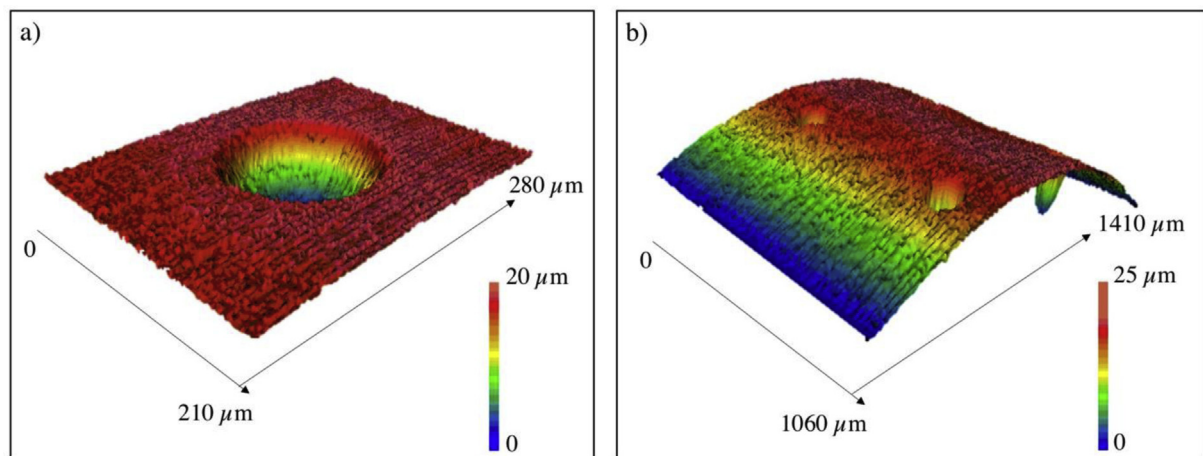


Fig. 5. 3D image of the multi-scale surface (A1 + L) on the shaft's curved surface captured by WLI. (a) Shows a single dimple with the superimposed laser pattern and (b) the shaft's surface in a lower magnification where the curvature of the shaft is clearly visible.

coined sample demonstrates the highest COF for rotational speeds up to 100 rpm. In contrast, the laser pattern and the multi-scale surface show a friction reduction by 30% compared to the micro-coined sample A2. In addition, the multi-scale sample and the laser pattern demonstrate a rather similar frictional behavior for these speeds. For higher rotational speeds (200–600 rpm), hydrodynamic lubrication prevails and the single-scale samples (purely micro-coined and purely laser-patterned) show a comparable frictional behavior with almost identical COFs. In contrast, the multi-scale sample leads to a significant friction reduction by a factor of 2 and 4.6 compared to the two single-scale patterns and the reference, respectively. Regarding the reference sample, these differences can be mostly traced back to differences in the acting lubrication regime, since the patterned samples work under hydrodynamic lubrication at rotational speeds greater than 200 rpm, whereas the reference sample shows the transition from mixed to hydrodynamic lubrication at considerably higher rotational speeds.

Especially under mixed lubrication (low rotational speeds), the purely micro-coined sample A2 shows a downgraded frictional behavior compared to the corresponding micro-coined sample A1 with a shallower structural depth. This correlates well with the preliminary experiments, which also showed higher COFs for deeper micro-coined patterns [16]. It is likely that the steeper wall angles of sample A2 lead to stress raisers due to pronounced edge effects, which results in a smaller load bearing capacity and thus higher COFs. The improved frictional behavior observed for the laser-patterned and multi-scale sample under mixed lubrication can be correlated with the smaller structural depth of the laser pattern. It has been found that friction is highly reduced when the structural depth is in the same range the oil film thickness thus leading to reduced COFs for the shallower patterns [14,35]. Furthermore, the laser pattern is in contrast to the micro-coined pattern distributed over the entire sample's surface, which makes it easier to store wear particles.

As pointed out in Refs. [36] and [16], patterns with an increased structural depth are more prone to induce cavitation under hydrodynamic lubrication. This results in a reduced load bearing capacity thus downgrading the frictional behavior for deeper coined patterns such as A2. Additionally, larger structural depths are also known to generate a recirculation zone (flow vortex) in the dimples, which results in a local reduction of the pressure gradient and thus a decrease in load bearing capacity [37]. For the multi-scale surface, reduced cavitation

phenomena can be assumed due to a better distribution of the oil in the contact zone. The reduction of cavitation leads to an increased load bearing capacity and thus lower COFs under hydrodynamic lubrication. Additionally, the distribution of the lubricant on the sample and the lubricant's flow inside the dimples may be changed by the additional laser pattern, which potentially reduces the recirculation zone and therefore increases the load bearing capacity. The observed friction reduction by superimposing an additional laser pattern on deeper micro-coined dimples correlates well with the preliminary laboratory tests [28]. These tests likewise showed an improvement for multi-scale patterns with larger micro-coined depths.

4. Conclusions

The goal of this study was to experimentally investigate the effect of selected single-scale and multi-scale surface patterns on the frictional performance of journal bearings. For this purpose, surface patterns showing beneficial effects in preliminary lab-experiments were selected and fabricated onto the shaft of journal bearings. Based upon Stribeck-like curves measured on a specially designed test rig for journal bearings, the following conclusions can be drawn:

- Despite the curvature of the shaft's surface, single- and multi-scale surface patterns are homogeneously fabricated with a high accuracy and reproducibility.
- The burnished reference demonstrates a Stribeck-like behavior with a high COF of 0.23 for the lowest velocities and a gradual decrease of the COF for higher rotational speeds. These results are in good agreement with the calculated film thickness ratio.
- Compared to the burnished reference, all patterned samples show a reduced COF over the entire range of rotational speeds. In addition, the transition from mixed to hydrodynamic lubrication is shifted to smaller rotational speeds for all patterned samples. For the lowest rotational speed of 25 rpm, the patterned samples demonstrated a friction reduction of about 20–30%. With increasing rotational speed, a sudden drop in COF is observed for all patterned samples whereas the COF of the burnished reference only slightly decreases. For rotational speeds larger than 150 rpm, all patterned samples show a rather constant and low COF. The maximum friction reduction by a factor of 4.6 compared to the burnished reference is

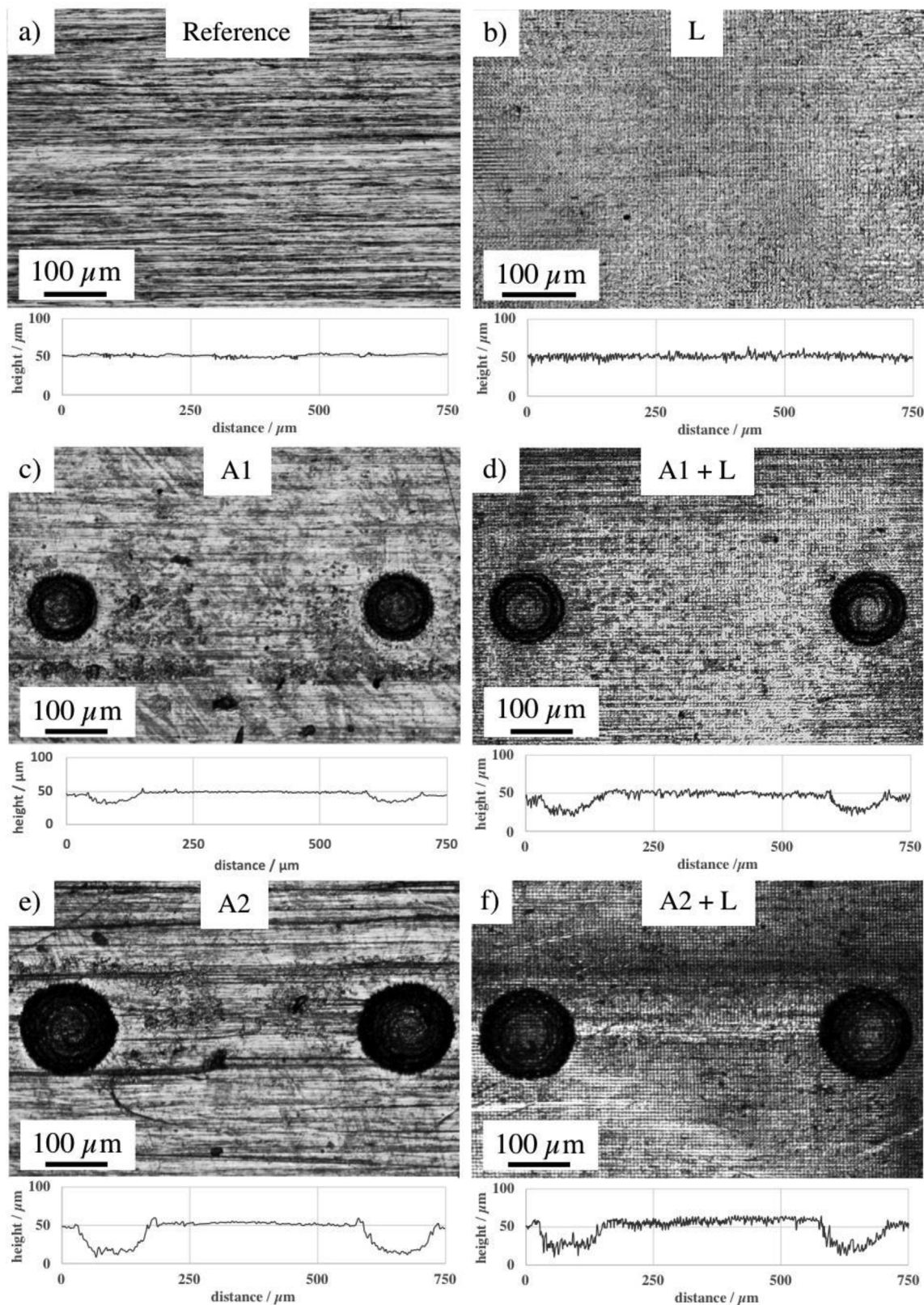


Fig. 6. Overview of all fabricated patterns as well as their respective profiles measured by LSM. Shown are the surfaces of (a) the unpatterned reference shaft as well as both micro-coined shafts (c) A1 and (e) A2 prior to laser patterning. Additionally, the shafts' surfaces after laser patterning are shown with (b) being the purely laser patterned sample L and (d) and (f) the micro-coined and laser-patterned samples A1 + L and A2 + L, respectively.

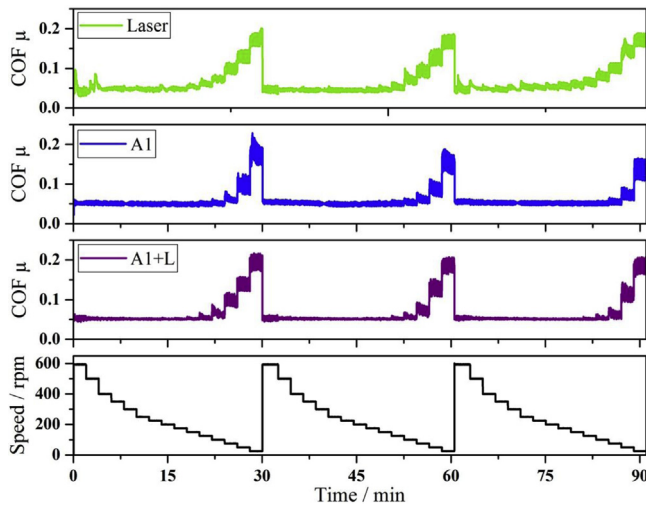


Fig. 7. Temporal evolution of the COF versus rotational speed (decreased from 600 to 25 rpm), exemplarily shown for the laser-patterned, the micro-coined (A1) and the multi-scale (A1 + L) sample.

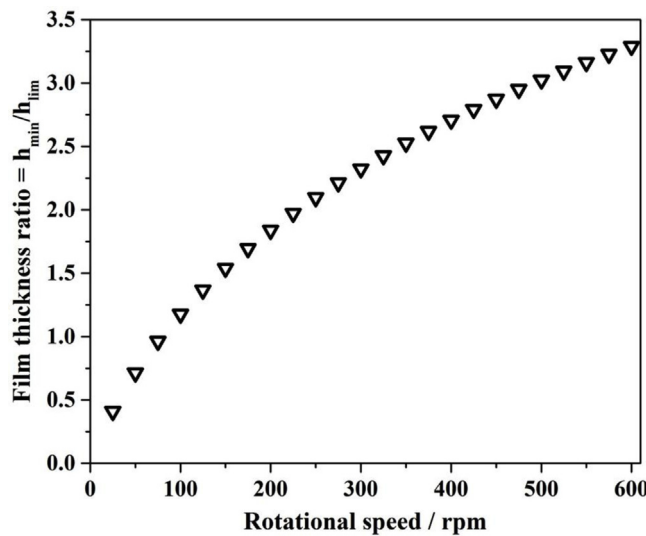


Fig. 8. Film-thickness ratio versus rotational speed based upon the calculation of the film thickness according to DIN 31652-2.

found for the multi-scale sample (A2 + L) combining deeper micro-coined dimples with a cross-like surface pattern.

- The observed friction reduction under mixed lubrication (roughly a factor of 2–3) and hydrodynamic lubrication (up to a factor of 4.6) matches very well with results observed in previous laboratory tests. This underlines the unique possibility to directly transfer results obtained on a simplified ball-on-disk test rig to journal bearings working under more realistic conditions.

Acknowledgements

The present work is supported by funding from the Deutsche Forschungsgemeinschaft (DFG, projects: MU 959/27-2 and HI 790/33-2 within the SPP 1551). A. Rosenkranz gratefully acknowledges the Alexander von Humboldt foundation for the financial support of his postdoctoral fellowship (Feodor Lynen research fellowship). F. König and G. Jacobs gratefully acknowledge the DFG for the funding of the graduate school GRK 1856 „Integrated Energy Supply Modules for Roadbound E-Mobility”.

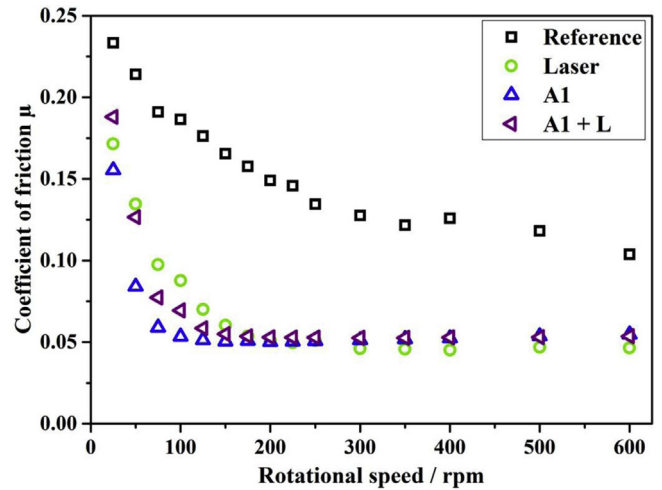


Fig. 9. Evolution of the COF as a function of rotational speed. Shown are results for the burnished reference, the purely coined sample A1, the purely laser-patterned sample and the multi-scale sample combining coining and DLIP (A1 + L).

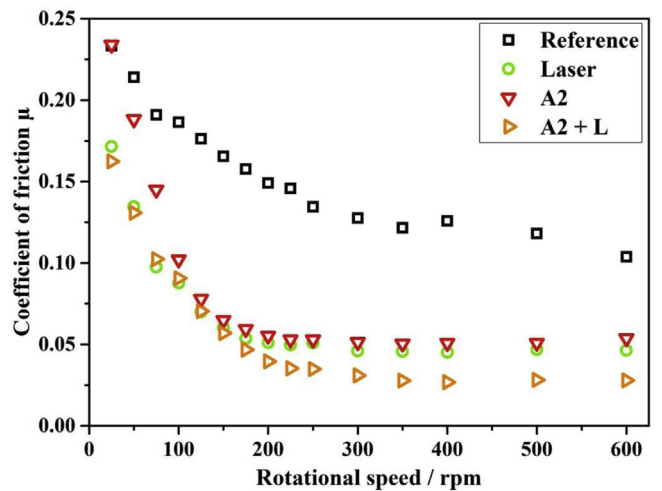


Fig. 10. Evolution of the COF as a function of rotational speed. Shown are results for the burnished reference, the purely micro-coined sample A2, the purely laser-patterned sample (cross pattern with 6 μm periodicity) and the multi-scale sample combining coining and DLIP.

References

- [1] Dunn AC, Tichy JA, Uruenà JM, Sawyer WG. Lubrication regimes in contact lens wear during a blink. *Tribol Int* 2013;63:45–50. <http://dx.doi.org/10.1016/j.triboint.2013.01.008>.
- [2] Fisher J, Dowson D. Tribology of total artificial joints. *Proc Inst Mech Eng Part H J. Eng. Med* 1991;205:73–9. http://dx.doi.org/10.1243/PIME_PROC_1991_205_271_02.
- [3] Di Puccio F. Biotribology of artificial hip joints. *World J Orthoped* 2015;6:77. <http://dx.doi.org/10.5312/wjo.v6.i1.77>.
- [4] Holmberg K, Andersson P, Erdemir A. Global energy consumption due to friction in passenger cars. *Tribol Int* 2012;47:221–34. <http://dx.doi.org/10.1016/j.triboint.2011.11.022>.
- [5] Holmberg K, Kivikytö-Reponen P, Härkisaari P, Valtonen K, Erdemir A. Global energy consumption due to friction and wear in the mining industry. *Tribol Int* 2017;115:116–39. <http://dx.doi.org/10.1016/j.triboint.2017.05.010>.
- [6] Holmberg K, Erdemir A. Influence of tribology on global energy consumption, costs and emissions. *Friction* 2017;5:263–84. <http://dx.doi.org/10.1007/s40544-017-0183-5>.
- [7] Etsion I. Improving tribological performance of mechanical seals by laser surface texturing.pdf. *Proceeding 17th int. Pump user symp. Symp. 2000*. p. 17–21.
- [8] Etsion I. State of the art in laser surface texturing. *J Tribol* 2005;127:248–53. <http://dx.doi.org/10.1115/1.1828070>.
- [9] Gachot C, Rosenkranz A, Hsu SM, Costa HL. A critical assessment of surface texturing for friction and wear improvement. *Wear* 2017;372–373:21–41. <http://dx.doi.org/10.1016/j.wear.2017.05.010>.

- doi.org/10.1016/j.wear.2016.11.020.
- [10] Neumann S, Eng M, Jacobs PG. Reducing friction and leakage by means of micro-structured sealing surfaces – example mechanical face seal. 10th int. Fluid power conf. 2016. p. 493–506.
- [11] Rosenkranz A, Reinert L, Gachot C, Mücklich F. Alignment and wear debris effects between laser-patterned steel surfaces under dry sliding conditions. *Wear* 2014;318:49–61. <http://dx.doi.org/10.1016/j.wear.2014.06.016>.
- [12] Kovalchenko A, Ajayi O, Erdemir A, Fenske G, Etsion I. The effect of laser texturing of steel surfaces and speed-load parameters on the transition of lubrication regime from boundary to hydrodynamic. *Tribol Trans* 2004;47:299–307. <http://dx.doi.org/10.1080/05698190490440902>.
- [13] Kovalchenko A, Ajayi O, Erdemir A, Fenske G, Etsion I. The effect of laser surface texturing on transitions in lubrication regimes during unidirectional sliding contact. *Tribol Int* 2005;38:219–25. <http://dx.doi.org/10.1016/j.triboint.2004.08.004>.
- [14] Rosenkranz A, Heib T, Gachot C, Mücklich F. Oil film lifetime and wear particle analysis of laser-patterned stainless steel surfaces. *Wear* 2015;334–335:1–12. <http://dx.doi.org/10.1016/j.wear.2015.04.006>.
- [15] Pettersson U, Jacobson S. Influence of surface texture on boundary lubricated sliding contacts. *Tribol Int* 2003;36:857–64. [http://dx.doi.org/10.1016/S0301-679X\(03\)00104-X](http://dx.doi.org/10.1016/S0301-679X(03)00104-X).
- [16] Rosenkranz A, Szurdak A, Gachot C, Hirt G, Mücklich F. Friction reduction under mixed and full film EHL induced by hot micro-coined surface patterns. *Tribol Int* 2016;95:290–7. <http://dx.doi.org/10.1016/j.triboint.2015.11.035>.
- [17] Wang X, Kato K, Adachi K, Aizawa K. The effect of laser texturing of SiC surface on the critical load for the transition of water lubrication mode from hydrodynamic to mixed. *Tribol Int* 2001;34:703–11. [http://dx.doi.org/10.1016/S0301-679X\(01\)00063-9](http://dx.doi.org/10.1016/S0301-679X(01)00063-9).
- [18] Bruzzone AAG a G, Costa HLL, Lonardo PMM, Lucca DA a. Advances in engineered surfaces for functional performance. *CIRP Ann - Manuf Technol* 2008;57:750–69. <http://dx.doi.org/10.1016/j.cirp.2008.09.003>.
- [19] Tala-Ighil N, Fillon M. A numerical investigation of both thermal and texturing surface effects on the journal bearings static characteristics. *Tribol Int* 2015;90:228–39. <http://dx.doi.org/10.1016/j.triboint.2015.02.032>.
- [20] Mufti RA, Priest M. Theoretical and experimental evaluation of engine bearing performance. *Proc Inst Mech Eng Part J J. Eng. Tribol* 2009;223:629–44. <http://dx.doi.org/10.1243/13506501JET487>.
- [21] He M, Cloud CH, Byrne JM. Fundamentals of fluid film journal bearing operation and modeling. *Proc. Thirty-fourth turbomach. Symp.* 2005. p. 155–75.
- [22] (Jane) Wang Q, Shi F, Lee SC. A mixed-TEHD model for journal-bearing conformal Contact—Part II: contact, film thickness, and performance analyses. *J Tribol* 1998;120:206. <http://dx.doi.org/10.1115/1.2834411>.
- [23] Tala-Ighil N, Fillon M, Maspeyrot P. Effect of textured area on the performances of a hydrodynamic journal bearing. *Tribol Int* 2011;44:211–9. <http://dx.doi.org/10.1016/j.triboint.2010.10.003>.
- [24] Lu X, Khonsari MM. An experimental investigation of dimple effect on the scribebeck curve of journal bearings. *Tribol Lett* 2007;27:169–76. <http://dx.doi.org/10.1007/s11249-007-9217-x>.
- [25] Sinanoğlu C, Nair F, Karamiş MB. Effects of shaft surface texture on journal bearing pressure distribution. *J Mater Process Technol* 2005;168:344–53. <http://dx.doi.org/10.1016/j.jmatprotec.2005.02.252>.
- [26] Brizmer V, Kligerman Y. A laser surface textured journal bearing. *J Tribol* 2012;134:31702. <http://dx.doi.org/10.1115/1.4006511>.
- [27] Priest M, Taylor CM. Automobile engine tribology—approaching the surface. *Wear* 2000;241:193–203. [https://doi.org/10.1016/S0043-1648\(00\)00375-6](https://doi.org/10.1016/S0043-1648(00)00375-6).
- [28] Grützmacher PG, Rosenkranz A, Szurdak A, Gachot C, Hirt G, Mücklich F. Effects of multi-scale patterning on the run-in behavior of steel-alumina pairings under lubricated conditions. *Adv Eng Mater* 2018;20. <http://dx.doi.org/10.1002/adem.201700521>. 1700521.
- [29] Mücklich F, Lasagni AF, Daniel C. Laser interference metallurgy – using interference as a tool for micro/nano structuring. *Int J Mater Res* 2006;97:1337–44. <http://dx.doi.org/10.3139/146.101375>.
- [30] Lasagni AF, Holzapfel C, Weirich T, Mücklich F. Laser interference metallurgy: a new method for periodic surface microstructure design on multilayered metallic thin films. *Appl Surf Sci* 2007;253:8070–4. <http://dx.doi.org/10.1016/j.apsusc.2007.02.092>.
- [31] Bieda M, Schmädicke C, Wetzig A, Lasagni AF. Direct laser interference patterning of planar and non-planar steels and their microstructural characterization. *Met. Mater. Int* 2013;19:81–6. <http://dx.doi.org/10.1007/s12540-013-1013-6>.
- [32] Szurdak A, Hirt G. Development and experimental verification of a new roller-coining setup to texture flat and curved surfaces. *Appl Mech Mater* 2015;794:128–35. <http://dx.doi.org/10.4028/www.scientific.net/AMM.794.128>.
- [33] Paulus A, Jacobs G. Tribolayer formation on bronze CuSn12Ni2 in the tribological contact between cylinder and control plate in an axial piston pump with swashplate design. 10th int. Fluid power conf. 2016. p. 251–62.
- [34] Peels JA, Meesters CJM. Ontwerp en constructieve aspecten van een 2kN- glijlageropstelling. *Constr Met (CTICM)* 1996;34:40–3.
- [35] Ramesh A, Akram W, Mishra SP, Cannon AH, Polycarpou AA, King WP. Friction characteristics of microtextured surfaces under mixed and hydrodynamic lubrication. *Tribol Int* 2013;57:170–6. <http://dx.doi.org/10.1016/j.triboint.2012.07.020>.
- [36] Dobrica MB, Fillon M, Pasovic MD, Cicone T. Optimizing surface texture for hydrodynamic lubricated contacts using a mass-conserving numerical approach. *Proc Inst Mech Eng Part J J. Eng. Tribol* 2010;224:737–50. <http://dx.doi.org/10.1243/13506501JET673>.
- [37] Cupillard S, Cervantes MJ, Glavatskih S. Pressure buildup mechanism in a textured inlet of a hydrodynamic contact. *J Tribol* 2008;130. <http://dx.doi.org/10.1115/1.2805426>. 21701.

VII Surface texturing in machine elements - a critical discussion for rolling and sliding contacts

Andreas Rosenkranz¹, **Philipp G. Grützmacher**², Carsten Gachot³, Henara L. Costa⁴

¹ Department of Chemical Engineering, Biotechnology and Materials, FCFM, Universidad de Chile, Santiago, Chile

² Chair of Functional Materials, Saarland University, 66123 Saarbrücken, Germany

³ Institute of Engineering Design and Product Development, Tribology Research Group, TU Wien, 1060 Vienna, Austria

⁴ School of Engineering, Universidade Federal de Rio Grande, Campus Carreiros, 96203 900 Rio Grande, RS, Brazil

Submitted to “Advanced Engineering Materials”

Own contribution:

Scientific discussion; paper writing

Abstract:

Surface texturing has the ability to reduce friction and/or wear under different lubrication conditions which makes it particularly interesting for machine elements since they may experience different conditions during their operation or sometimes even over one cycle/stroke. Therefore, surface texturing has gained significant attention over the last three decades in the tribological. However, despite the great effort by both researchers and industry to introduce surface texturing in machine elements, many questions remain unclear regarding the optimal design of textures, as well as the positive and negative effects on the component's performance. The aim of this review article is to critically summarize the state of the art of surface texturing applied to machine elements, with a special emphasis on piston rings, seals, roller bearings and gears. After a brief introduction, the first section focuses on surface texturing in sliding components (piston rings and seals), whereas the second section deals with surface texturing in rolling components (roller bearings and gears). Based upon the main evidence from the literature, the final section provides more general design guidelines for surface texturing in machine elements.

Cite this as:

A. Rosenkranz, P.G. Grützmacher, C. Gachot, H. Costa, Surface texturing in machine elements - a critical discussion for roll-ing and sliding contacts, *Adv. Eng. Mater.* **2019**, submitted.

Surface texturing in machine elements - a critical discussion for rolling and sliding contacts

*Andreas Rosenkranz**, Philipp G. Grützmacher, Carsten Gachot, Henara L. Costa

Prof. A. Rosenkranz

Department of Chemical Engineering, Biotechnology and Materials, FCFM, Universidad de Chile, Santiago, Chile

Email: arosenkranz@ing.uchile.cl

P. G. Grützmacher

Chair of Functional Materials, Department of Materials Science and Engineering, Saarland University, 66123 Saarbrücken, Germany

Prof. C. Gachot

Institute of Engineering Design and Product Development, Tribology Research Group, TU Wien, 1060 Vienna, Austria

Prof. H. L. Costa

School of Engineering, Universidade Federal de Rio Grande, Campus Carreiros, 96203 900 Rio Grande, RS, Brazil

Keywords: Surface texturing; piston rings; seals; roller bearings; gears

Abstract: Surface texturing has gained great attention in the tribological community since precisely defined surface features can help to reduce friction and/or wear irrespective of the acting lubrication regime. The ability to positively influence tribological performance under different lubrication conditions makes surface texturing

particularly interesting for machine elements since they may experience different conditions over the lifetime or sometimes even over one cycle/stroke. However, despite the great effort by both researchers and industry to introduce surface texturing in machine elements, many questions remain unclear regarding the optimal design of surface textures, as well as the positive and negative effects on the component's performance. The aim of this review article is to critically summarize the state of the art of surface texturing applied to machine elements, with a special emphasis on piston rings, seals, roller bearings and gears. After a brief introduction, the first section focuses on surface texturing in sliding components (piston rings and seals), whereas the second section deals with surface texturing in rolling components (roller bearings and gears). Based upon the main evidence from the literature, the final section provides more general design guidelines for surface texturing in machine elements.

1. Introduction

In times of globally increasing population and energy consumption, decreasing resources for fossil fuels as well as more consciousness about the anthropogenic greenhouse effect (global warming), energy efficiency and sustainability are considered as key aspects.¹ Bearing in mind that fossil fuels (oil and coal) may be depleted in the next 50 - 100 years,²⁻⁴ and that the average temperature possibly increases by several degrees in the next 80 years,⁵ the desire for more efficient and sustainable processes and components is stronger than ever before. Consequently, new approaches to tackle this increasing energy demand need to be developed. According to the important work carried out by Holmberg and collaborators, under the auspices of the International Energy Agency,^{6,7} the annual worldwide energy consumption is about 549 EJ, whereas about 27 % of this energy is

used for transportation, especially road transportation using cars and trucks.^{8,9} Thereby, it is astonishing to note that about 20 % of this energy is needed to overcome friction and wear losses, underlining the tremendous impact of these aspects in a global context.^{6,8-10}

To efficiently reduce friction and wear, several aspects can be considered. The easiest approach is to use lubricants (oil or solid lubricant) to separate both rubbing surfaces thus avoiding solid-solid contact and decreasing friction as well as wear. This is reflected in the annual usage of lubricant (mainly oil) of about 40 million tons.¹¹ However, the main problem with this approach is that the lubricants' disposal is mostly toxic and therefore harmful to the environment. Moreover, lubricant additives can cause further harm to the environment. For example, the anti-wear additive ZDDP leads to the formation of phosphorus oxides, sulfur oxides and ash, which reduce the effective life of exhaust catalysts. This has led to legislation that strongly restricts the use of ZDDP in lubricants, but no commercial anti-wear additive has so far been able to successfully replace ZDDP.¹² Taking additionally the diminishing resources for raw oil into consideration, it becomes obvious that the use of lubricants cannot be the only preferred long-term solution to reduce friction and wear. Holmberg et al. suggested that friction and wear can be significantly improved when considering new materials, modified mechanical designs, environmentally-friendly biologically-degradable lubricants and advanced surface engineering strategies.^{6,8-10} The latter can be subdivided into advanced coating systems and novel approaches to modify surface topography such as the generation of well-defined surface features known as surface texturing.

In the last 70 years, the modification of the surface topography/roughness has proven to be a successful approach to effectively reduce friction and wear under dry and lubricated conditions. The first experimental evidences go back to Hamilton et al. and Anno et al. in the 1960's.^{13,14} In the 1990's, the pioneering work of Etsion et al. related to laser surface

texturing (LST) can be considered as the renaissance of this topic.^{15,16} Since then, surface texturing has gained increased attention in the tribological community. Lots of experimental and numerical studies have been published in the last two decades trying to assess the underlying mechanisms of surface texturing in terms of potential friction and wear reduction. Depending on the acting lubrication regime, different aspects have to be considered.

Under dry conditions, surface texturing helps to lower the real area of contact, which reduces the resulting friction force and hence the coefficient of friction (COF).¹⁷ In addition, surface textures store wear particles, produced during rubbing, thus reducing abrasion and lowering friction.¹⁸ In the presence of a lubricant, the effects of surface texturing strongly depend on the prevailing lubrication regime. Thereby, the well-known Stribeck curve and the λ -ratio (resulting oil film thickness divided by the combined surface roughness of both rubbing surfaces) can be used to distinguish between different lubrication regimes. For λ -ratios smaller than 1, boundary lubrication is predominant with pronounced solid-solid contact and a strong influence with formed monolayers. In this lubrication regime, surface textures reduce the real area of contact and trap wear debris.^{19,20} In addition, surface texturing can also help to induce the formation of pressure-induced tribolayers under boundary lubrication.²¹ For $1 < \lambda < 3$, the lubricant regime is typically assigned to mixed lubrication, in which the normal load is partly carried by the oil film and partly by the surface asperities.²² In this lubrication regime, surface textures act as an oil reservoir thus inducing a secondary oil effect, trap wear debris and contribute to an additional hydrodynamic pressure.²³⁻²⁶ For $\lambda > 3$, the lubrication regime is full-film hydrodynamic lubrication, where both rubbing surfaces are completely separated by a thick oil film. Surface texturing typically aims at generating an additional hydrodynamic pressure thus generating a significant contribution to the load bearing capacity.²⁷⁻²⁹ As

can be noticed, different effects contribute to improved frictional and wear properties induced by surface textures. The underlying mechanisms have been extensively studied from an experimental and numerical point of view. Comprehensive reviews summarizing the fundamental effects of surface texturing related to friction and wear reduction in laboratory experiments have been published by Gropper et al. and Gachot et al.^{30,31} Gachot et al. pointed out that it is almost impossible to create design guidelines for surface textures to be effective under a wide range of experimental conditions, even using idealistic laboratory set-ups and test rigs.³⁰ Moreover, it has been emphasized in the literature the need to carefully study and characterize the individual tribological system with respect to operating and lubrication conditions. Using such approach, design recommendation for surface textures to reduce friction and wear can be derived for individual systems, set-ups, test-rigs and conditions.

Transportation, as one of the main sources for energy consumption, greatly involves tribological aspects. In this field, tribological problems are a perfect source for further optimization that could lead to improved friction and wear performance and hence energy efficiency. A detailed analysis by Holmberg et al. on the engine and transmission system of cars directly identifies bearings, piston rings, gears and seals as main machine elements largely contributing to frictional losses.⁹ These elements work under different operating conditions regarding loads, velocities, and lubrication conditions. Recalling the difficulties to derive general design guidelines for surface texturing even in highly simplified laboratory set-ups and test-rigs makes obvious the need for a detailed analysis of the tribological system under realistic conditions. Only with such approach, design recommendation for surface textures aiming at reducing friction and wear in specific machine elements present in transportation systems may be derived.

This review article critically evaluates the potential of surface texturing in four machine elements, namely the piston-ring system, seals, roller bearings and gears. For seals and the piston-ring system, the contact is conformal thus resulting in relatively small contact pressures. In contrast, roller bearings and gears present non-conformal contacts with contact pressures on the order of 1 to 4 GPa. The effect of surface texturing is significantly different between conformal and non-conformal contacts. Thus, the influence of surface texturing for conformal components (piston rings and seals) will be first presented, followed by the non-conformal components (roller bearings and gears). Each section summarizes the main functions of the component and highlights the challenges and problems related to the use of surface texturing. Afterwards, the use of surface texturing for the respective machine elements is critically discussed. Cases for which surface texturing is beneficial or even detrimental are identified. Based upon this analysis, general design guidelines for surface textures are derived for each component.

2. Surface texturing in sliding contacts

2.1. Introduction

The majority of the research literature reporting on the use of surface texturing in machine elements is related to situations involving sliding motion of fairly conformal surfaces.³⁰ Particular emphasis has been given to the use of surface texturing in sliding bearings, where the textures are believed to increase film thickness and load bearing capacity thus reducing friction. Gropper's review provides a broad perspective on the main mechanisms involved in the tribological behavior of textured sliding bearings (parallel, inclined and journal bearings), derived from both numerical and experimental studies.³¹ This section

will review the most relevant aspects related to the surface texturing of two other important conformal, sliding contacts: piston rings and seals.

Contact pressures are relatively low in piston rings and seals, often leading to the presence of a full film separating the surfaces under lubricated conditions, although for piston rings the variable velocity along the piston stroke gives rise to mixed or even boundary lubrication at the dead centers. Thus, the ability of the textures to boost lubricant supply and generate lift is highly relevant for this component. Another aspect is that textures may lead to a full film separating the surfaces at lower speeds or higher loads than smooth surfaces. The relevance of each mechanism, as well as an overview of the main advantages and drawbacks of surface texturing in piston rings and seals are summarized in this section.

2.2. Effect of surface texturing in the piston-ring system

The piston ring cylinder liner contact is very important for the overall car's energy efficiency since it accounts for up to 60 % of the engine's frictional losses and largely determines the oil as well as the fuel consumption.^{9,32} It can be estimated that a reduction of the frictional losses by 6 % would result in a reduction of fuel consumption by 1 %.³² This is highly relevant when taking into account more stringent guidelines for the exhaust emissions (NO_x, CO and CO₂) as well as the desire to design more efficient and environmentally friendly engines. To tackle this problem, the lubrication conditions of the piston ring pack need to be carefully studied. Tian demonstrated that hydrodynamic lubrication is the predominant regime for almost the entire cycle/stroke.³³ However, as the system experiences variations of the angular velocity during one cycle, near the top dead center (TDC) and the bottom dead center (BDC), the decreasing velocity reduces

film thickness, so that mixed and boundary lubrication prevail. Moreover, axial motion of the piston ring as well as thermal and elastic deformation need to be considered. Finally, the inhomogeneous distribution of lubricant over the circumference of the cylinder surface as well as insufficient lubrication occurring at the TDC and BDC further complicate the problem. To reduce frictional losses and to improve the lubrication conditions especially close to the TDC and BDC, different aspects such as the lubrication supply mechanisms, the rheological properties of the lubricant and the modification of the surface topography by surface texturing can be taken into account. In this context, since different lubrication regimes ranging from boundary to hydrodynamic lubrication depending on the position of the piston along the stroke can be found for this system, the use of surface textures is especially promising since it has been shown to improve the tribological performance under different lubricated conditions.

The performance of surface texturing in this system has been investigated both experimentally and numerically. This section aims at revising the most relevant findings. First, studies that combine experimental and numerical analyses are summarized, since this combination is considered as a powerful tool to understand the mechanisms involved. In sequence, experimental works that have provided significant information despite lacking analytical or numerical analysis are described. Finally, relevant numerical investigations without experimental support are presented. Together, they help creating a broader picture of the effects of surface texturing on the tribological performance in the piston-ring system.

2.2.1 Combined experimental and numerical work

Pioneering experimental and numerical work for textured piston rings have been presented by Etsion and his co-workers. Kligerman et al. developed an analytical model to investigate the benefits of laser-textured piston rings. By solving the Reynolds equation and simultaneously considering the radial motion of piston rings, benefits of full and partial surface texturing were evaluated. For partial texturing, they verified that the texture's position had only a minor influence on friction. Related to the texture's geometry, friction was not significantly affected by the dimples' diameter, but continuously decreased with increasing area density. A maximum friction reduction was found for a textured portion of 60 %.³⁴ Following Kligerman's predictions, Ryk et al. experimentally verified the beneficial effects of partially textured piston rings. Frictional tests under full and starved lubrication conditions using hemispherical textures (depth of 7 μm , area density of 50 % and textured portion of 60 %) demonstrated a maximum friction reduction of 45 % for partially textured piston rings.³⁵ Moreover, Ryk et al. compared the performance of a textured piston ring with an untextured barrel-shaped piston ring, which is considered as the optimum shape for conventional piston rings. Partially textured piston rings reduced friction by 25 % compared to the barrel-shaped one as can be seen in **Figure 1**.³⁶

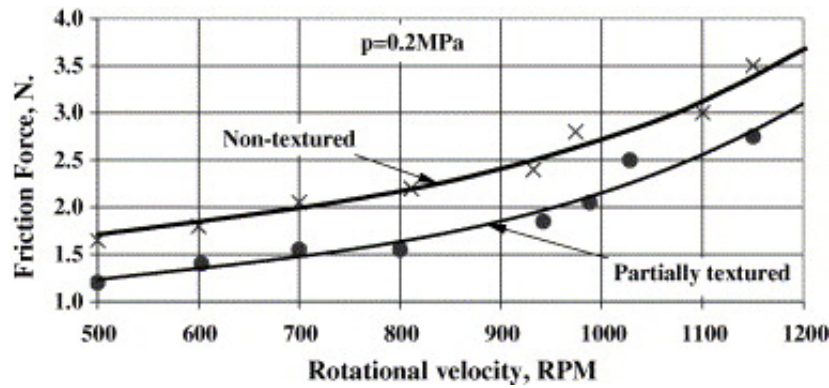


Figure 1. Comparison of the averaged friction force versus rotational velocity for a non-textured barrel-shaped and a partially textured piston ring having the ideal structural parameters predicted by Kligerman. Reproduced with permission.³⁶ 2016, Elsevier.

Etsion and Sher studied the fuel efficiency of partially textured piston rings using a 2500 cm³ four-cylinder Diesel engine with a total engine running time of 1800 h. Using the texture parameters predicted by Kligerman et al. and verified by Ryk et al., a 4 % reduction in fuel consumption was verified for partially textured piston rings.³⁷

Using a simplified 1-D model, Tomanik studied effects of LST in terms of friction reduction for the bore, top and oil control piston rings considering flat and barrel-shaped geometries.³⁸ In accordance with Etsion et al., Tomanik verified beneficial effects of partial texturing, especially when using small pitch distances (high densities). Tomanik proved that LST can significantly improve the hydrodynamic performance of flat oil control rings thus reducing friction and wear. Surface textures with dimple sizes of a few micrometers placed in the middle of the stroke and close to the TDC were effective.³⁸ Profito et al. expanded Tomanik's work to a 3-D deterministic mixed lubrication model considering mass-conservative cavitation to study friction and wear of oil control rings. Surface roughness parameters prior to and after 100 h engine tests for textured surfaces were used as input parameters for the Greenwood-Tripp model to account for changes in

the surface topography and potential effects of wear. Profito's model allowed to study global and local effects of wear on hydrodynamic pressure, shear stress and asperity contact pressure depending on the position in the stroke. After 100 h engine time, the hydrodynamic pressure significantly increased compared to the initial unworn stage, which was explained by a pronounced reduction in cavitation and an increased wetted area.³⁹

Significant contributions related to laser-textured piston rings have been presented by the tribology group at Imperial College London. Vladescu et al. developed a reciprocating test-rig to simulate the contact between the liner and the piston's top ring. Ultra-fast picosecond LST was used to fabricate grooves, chevrons and cross-hatches with a constant depth of about 8 μm and widths between 60 and 80 μm . Using a fully formulated SAE 40 engine oil and different oil temperatures, experiments were conducted under full-film, mixed and boundary lubrication. For full-film lubrication, the frictional force increased towards the middle of the stroke and LST showed detrimental effects with increased friction values. For mixed and boundary lubrication, the frictional response over the stroke angle reflected a U-shape due to a squeeze effect and LST showed a friction reduction of up to 50 % for chevrons and transversely oriented grooves. In terms of average power loss, transverse grooves led to an overall reduction of 55 %.⁴⁰ To shed more light onto the involved mechanisms, Vladescu et al. studied transient effects when individual grooves (spacing of 3.3 mm, breadth of 80 μm and depth of 8 μm) crossed the tribological contact. In case of boundary and mixed lubrication, the frictional force was reduced when the pockets crossed the contact due to an abrupt change in film thickness and reduced asperity contact. In contrast, individual grooves increased friction and the non-textured reference outperformed the textured surfaces under full-film lubrication.⁴¹ To study the effect of surface texturing on wear, Vladescu et al. fabricated grooves with

variable breadth (40, 80 and 300 μm) and tested them under high load, low speed conditions using an additive-free mineral oil. Initially, the non-textured reference showed the lowest frictional force. However, after 5 minutes, a significant friction reduction for the textured surfaces was observed showing the best performance for the textures with the highest depth and density (**Figure 2**).⁴²

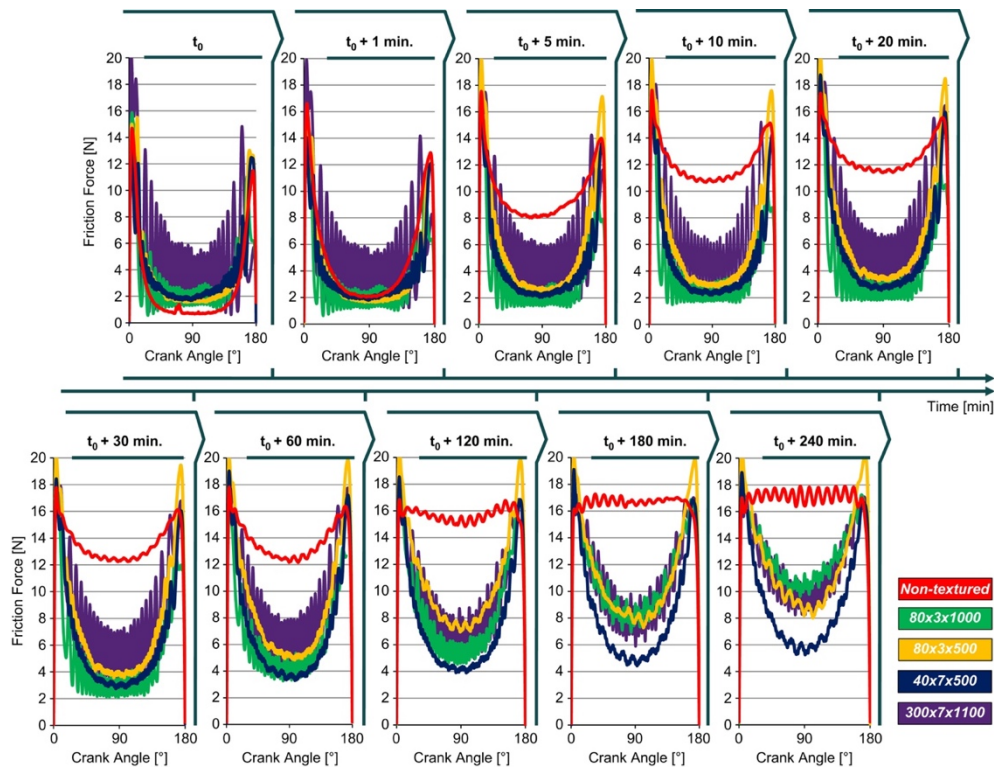


Figure 2. Temporal evolution of the frictional force for the non-textured reference and selected surface textures (width x depth x separation all given in micrometers). Reproduced with permission.⁴² 2016, Elsevier.

The wear volume of textured surfaces correlated well with the oil volume supplied to the contact in each stroke.⁴² To fundamentally understand the involved mechanisms, Vladescu et al. developed an out-of-contact ultrathin-film interferometry approach using multiple wavelengths to study oil film formation in the cylinder liner contact. This set-up

allowed for the first time to study film formation under full-film, mixed and even boundary lubrication in a cylinder liner contact with high accuracy. Under full-film lubrication, an increased frictional force in the middle of each stroke was related to increased oil film thickness and thus increased shearing forces. For mixed lubrication, surface texturing helped to increase oil film thickness thus reducing asperity contact and hence the frictional force.⁴¹ Moreover, the use of this set-up coupled with laser induced fluorescence enabled to study the effect of surface texturing on lubricant distribution and cavitation. The authors impressively demonstrated cavitation phenomena at the reversal points for non-textured samples. They proved that surface textures prevent the oil flow away from the wear track and ensure fully-flooded conditions even at the reversal points, which significantly reduced cavitation and improved the lubricant's distribution.⁴³ The experimental results of Vladescu et al. were numerically supported by modeling of transient effects of grooves carried out by Profito et al.. Hydrodynamic contributions were modeled based upon the averaged Reynolds equation using flow factors following the Patir and Cheng's approach. An asperity contact model using the Greenwood-Tripp approach was used to account for asperity interactions under boundary and mixed lubrication.⁴⁴ This work enabled a direct comparison of the resulting frictional response and the acting oil film thickness for different lubrication regimes, which is of utmost importance to explain the fundamental mechanisms. The simulated COF and oil film thickness for different lubrication regimes are given in **Figure 3**.

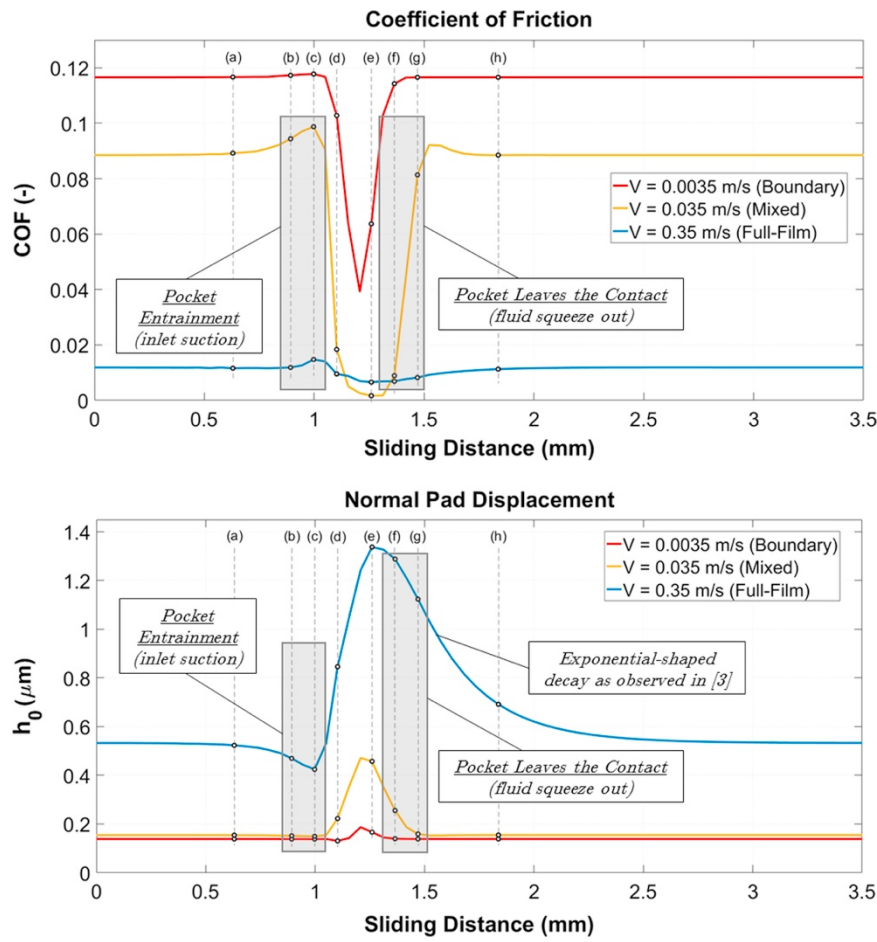


Figure 3. Simulated evolution of the COF and oil film thickness when an individual texture feature passes through the contact for boundary, mixed and hydrodynamic lubrication.⁴⁴ 2017, open access, Elsevier.

Under boundary conditions, the sudden friction reduction, when a texture entered the contact, was traced back to an increase in the local oil film thickness and a significant reduction in the effective contact area. For mixed lubrication, a small friction peak appeared when the texture entered the contact due to the film's rupture thus reducing hydrodynamic support. This frictional increase was then overcompensated due to inlet suction thus increasing the oil film and reducing friction again. Similar to other studies, no beneficial effects of surface textures were observed under full-film lubrication.⁴⁴

Khonsari et al. put considerable effort to optimize surface texturing in piston rings designing textures with different shapes, area densities, depths and diameters. They applied the textures at the piston ring's inlet and outlet (**Figure 4**) thus proposing a new design especially suited for reciprocating sliding conditions.⁴⁵

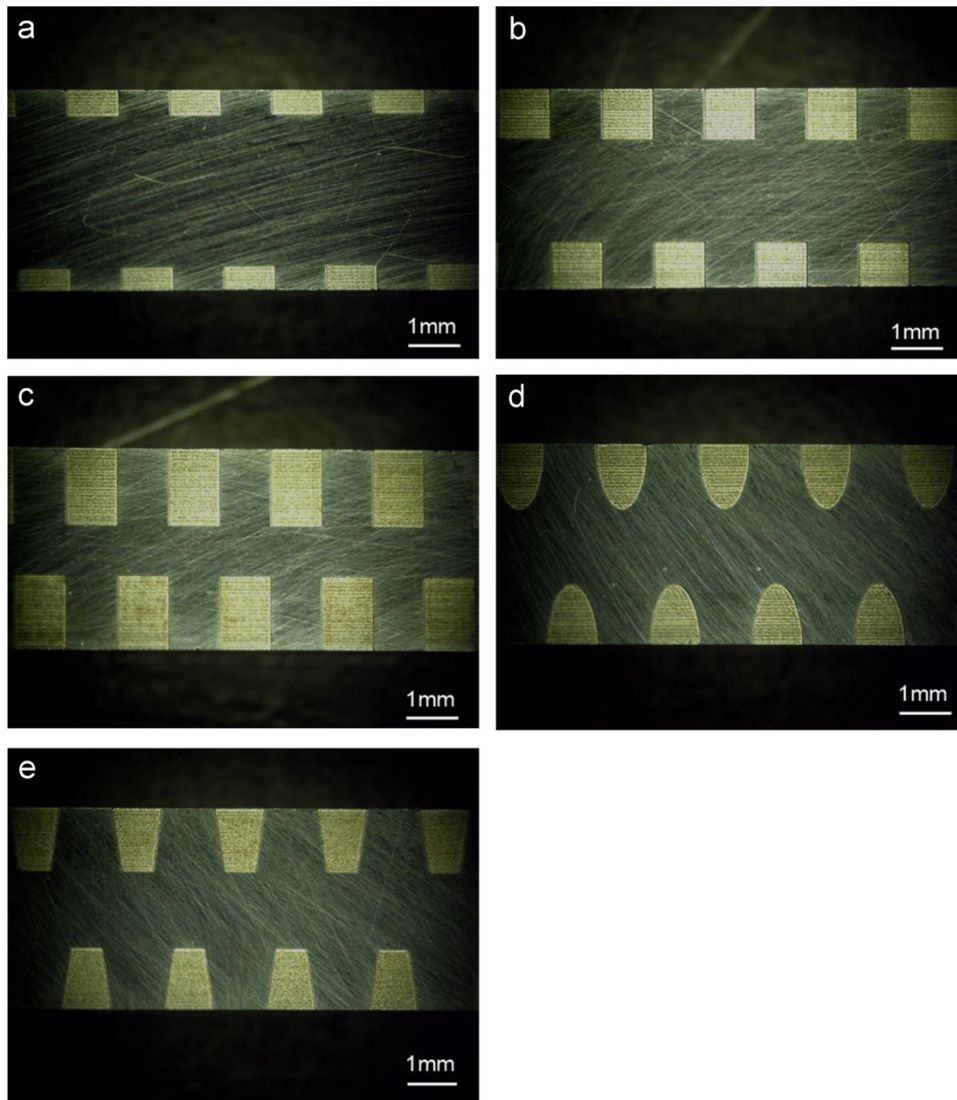


Figure 4. Texture design with features at the inlet and outlet especially suited for reciprocating machine elements. Reproduced with permission.⁴⁵ 2016, Elsevier.

They demonstrated that intermediate area densities (25 %) led to the best performance thus reducing friction by up to 52 %. Surface textures with the smallest depth (5.3 μm) experienced the lowest COF, while textures with the largest depth (25 μm) showed detrimental effects with increased COFs. They verified a significant friction reduction for all shapes with the best results obtained for trapezoid textures.⁴⁵ Moreover, they developed a set-up to mimic radial motion, elastic deformation and a potential twist between the cylinder liner and the piston rings thus reflecting more realistic working conditions. A trapezoid texture (in terms of the texture's cross-section) led to a significant friction reduction, which was more pronounced for higher viscosities and lower speeds. Additionally, this optimized texture showed beneficial effects in terms of power loss as well as better sealing characteristics.⁴⁶ Additionally, this group presented an innovative approach by combining surface texturing and plasma coating, which led to a reduced run-in time and lower frictional forces (initial and steady-state).⁴⁷

Morris et al. developed a novel numerical tool considering asperity and hydrodynamic contributions as well as transient thermal effects to effectively predict lubricant's temperature and viscosity for piston ring cylinder liner contacts. Neglecting thermal effects, the lubrication regime was mainly associated with full-film lubrication (except at the TDC). Taking thermal effects into consideration, mainly mixed or boundary lubrication were found for the entire stroke.⁴⁸ Inspired by textures tested by Costa and Hutchings,²⁷ Morris et al. studied chevrons fabricated by LST both experimentally and numerically and found optimal chevron depth of about 3 μm with an inclusion angle of 80°. Moreover, they concluded that the area density should be as high as possible and that the arrangement of the chevrons had a significant effect on friction reduction. Compared to the results published by Costa and Hutchings,²⁷ the optimized chevrons further reduced friction by 4 %.⁴⁹ Morris et al. numerically studied the influence of textures placed at the

TDC on friction and cross-correlated their results with in-situ real time friction measurements based upon a floating liner set-up. The lubricant's dynamic viscosity was calculated for each crank angle and a gas flow model was included to evaluate the pressure on the inner rim of the compression ring. Under these more realistic conditions, chevrons with a depth of 1 μm were shown to be more effective in terms of friction reduction, which led to the recommendation to use shallower textures thus avoiding extensive oil loss.⁵⁰

2.2.2 Experimental work

Grabon et al. fabricated hemispherical textures (density of 13 %, depth of 5 μm and diameter between 150 and 200 μm) by plateau honing and burnishing on the liner surface and studied the frictional response under different lubricated conditions. In case of a sufficient oil supply, the burnished surfaces induced a friction reduction by a factor of 2, whereas under starved lubrication, a 15 % friction reduction was observed.⁵¹ Furthermore, Grabon et al. investigated the effects of honing process parameters on the tribological efficiency in short-term experiments using a fully formulated oil preheated to 80 °C. They concluded that lower honing angles result in reduced COF. The obtained results correlated well with surface roughness parameters (cylinder roughness height) measured by WLI.⁵¹⁻⁵⁴ Similar results were also observed for tribological experiments studying the evolution of the cylinder liner topography under low temperatures (-20 °C).⁵⁴

Koszela et al. studied the combination of texturing and coating (diamond-like carbon) on liner surfaces. The liner surfaces were plateau-honed, textured by plastic deformation and then DLC coated (thickness of 1.5 μm). The textures (diameter between 250 and 350 μm and depth between 4 and 6 μm) were located in each cylinder bore between the piston's

top and bottom dead center. It was shown that the maximum power increase was found for liners presenting both surface texturing and DLC coating.⁵⁵

2.2.3 Numerical work

Apart from contributions made by Tomanik and Profito, further numerical work has paved the way to obtain more realistic models for the piston ring cylinder liner contact considering cavitation, mass conservation and asperity contact. Lubrecht et al. developed a simplified 1-D model (neglecting inertia) to study transient effects of cross-textures placed in the high-velocity regime in the middle of the stroke. The authors demonstrated that the pressure around and in the textures can be greatly reduced, which significantly alters the film thickness.³² El Mansori et al. presented a 3-D hydrodynamic model to investigate frictional effects of grooved textures placed on cylinder surfaces (middle of the stroke) also considering their real surface topography. By solving the Reynolds equation and integrating the results, they demonstrated that a minimum width of 20 μm and an optimal groove density exist to significantly reduce COF.⁵⁶ Zhou et al. presented a theoretical model using computational fluid dynamics (CFD), which takes into account the velocity and the pressure depending on the crank angle. Intermediate area densities (16 - 22 %) demonstrated to be more beneficial for low velocities, while low densities were favorable for higher velocities. The aspect ratio did not depend on the acting velocity, so that the authors advised that it should be kept constant at 0.1.⁵⁷ These authors came up with an optimal surface texture design with variable texture parameters over the entire cylinder length as schematically shown in **Figure 5**.

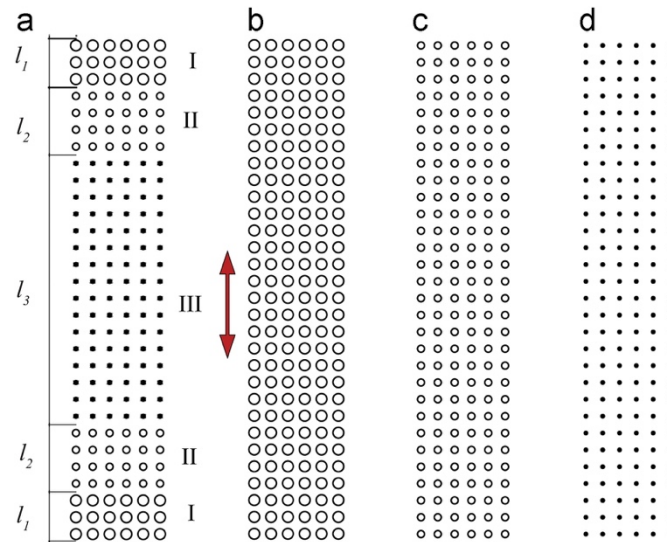


Figure 5. Optimized surface texturing for piston rings taking into consideration the respective velocities over the stroke length. Reproduced with permission.⁵⁷ 2012, Elsevier.

The theoretical model developed by Zhou et al. verified the superior behavior of this new design in terms of dimensionless film thickness compared to surfaces with fixed structural parameters.⁵⁷

Usman and Park presented a 2-D transient mixed lubrication model for partially textured barrel-shaped piston rings (dimples and grooves) considering shear rate effects and warm internal combustion engine conditions. Shallow grooves oriented perpendicular to the sliding direction gave the best frictional performance over 90 % of the entire stroke. Shallow micro-dimples turned out to be beneficial at the TDC and BDC. Furthermore, they pointed out that deep micro-textures tended to have detrimental effects irrespective of their geometry.⁵⁸ Additionally, Usman and Park investigated the tribological performance of partially textured piston rings in contact with deformed liner surfaces under realistic working conditions using a mixed lubrication model considering cavitation and mass conservation. They verified that neglecting the deformation of the bore surface

led to unrealistic computational results and to an overestimation of the minimum oil film thickness. Moreover, they demonstrated that transverse grooves led to improved lubrication conditions under high velocities and shortened durations of asperity contact.⁵⁹

Checo et al. developed a cavitation model considering mass conservation for textured liners in contact with barrel-shape piston rings, which allows for the study of transient effects of elliptical textures moving through the contact. The simulation was performed under fully flooded, low load conditions as a function of the curvature radius of the piston ring. The authors showed that the effect of texturing largely depends on the piston ring's profile. In this context, the larger the curvature and thus the more conformal the contact, the greater the friction reduction induced by surface texturing. A decrease in the average COF of up to 73 % as well as an increase in the film thickness by 86 % were demonstrated. In contrast, for smaller curvatures, even detrimental effects of surface texturing were verified.⁶⁰ Similar results were presented by Biboulet and Lubrecht using a simplified analytical model.⁶¹ Zavos et al. developed a 2-D CFD model for textured piston rings based upon the full Navier-Stokes equations considering a realistic free ring model but neglecting cavitation. In this context, it needs to be stated that the free ring model predicts lower pressures at the ring's outlet due to possible leakage. Zavos et al. clearly demonstrated the beneficial effects of surface texturing for free and secured rings with a maximum friction reduction of 59 % for rectangular textures with the highest number of dimples. The optimal value for the aspect ratio in terms of friction reduction varied between 0.2 and 0.28.^{62,63} Recently, Hu et al. presented an efficient mixed lubrication model for cross-hatched surface textures considering mass conservation, flow continuity and the plateau roughness. In this approach, the lubricant stored in each texture was considered as an additional lubricant supply. By considering flow continuity between the three piston rings, the authors demonstrated that the minimum oil film thickness was

greatly reduced for the first two rings. Furthermore, they numerically verified that the lubricant stored in the textures significantly improved the lubricant conditions, thus reducing asperity contact and frictional forces as well as wear.⁶⁴

2.2.4 Summarizing remarks

The piston ring cylinder liner contact is a highly sophisticated tribological sub-system due to the changing lubrication conditions and kinematics along the stroke. The use of surface textures to reduce friction and wear in this system requires advanced methods to in-situ record the resulting oil film thickness. New methods and experimental work presented by Vladescu et al. have paved the way for a more detailed understanding of the effect of surface texturing in this system under full-film, mixed and boundary lubrication.^{40-43,65} Related to the test-rigs used, more emphasis needs to be put in facilitating set-ups mimicking the real kinematics occurring in a piston ring cylinder liner contact. The strategy to place different textures' geometry along the stroke depending on the respective lubricated conditions seems to be promising and more research work should be dedicated in this direction. In addition, placing surface textures at the inlet and outlet of the piston ring is considered to be a smart way to improve the lubrication conditions in linearly reciprocating contacts. The design of new texture's shape such as trapezoid textures or the combination of surface texturing with coatings is another way to further improve the tribological performance of this system. A combination of the aforementioned aspects may be highly interesting and innovative to induce further friction and wear reduction. It is strongly recommended that experimental studies should be complemented by numerical simulations trying to assess the effects of surface texturing in this system. In this regard, the use of 3-D models considering cavitation,

mass-conservation, real kinematic conditions such as radial motion, vibrations and fluttering as well as potential wear need to be included. Models presented by Profito et al. have shown very promising results.^{39,44}

2.3. Effect of surface texturing in seals

When a shaft passes from one fluid-containing vessel to another, mechanical seals, such as rotating shaft seals, are needed to prevent fluid leakage. Sealing is achieved by two components whereby one is stationary and the other rotates against it. Reduced friction and wear and thus longer lifetimes are achieved using thick lubricant films to avoid contact between the rubbing surfaces. In contrast, leakage is minimized by reducing the clearance between the surfaces. A compromise between both aspects is essential to reduce both leakage and friction.⁶⁶ Surface texturing can improve friction and leakage of mechanical seals thus enhancing the load-capacity, which ensures sealing of conformal contacts with low uniform clearances.⁶⁷

Pioneering work by Fogg demonstrated the existence of fluid films between seal-like mating surfaces such as those found in thrust bearings.⁶⁸ Later, it was shown that these oil films can exist without any leakage occurring.⁶⁹ Based upon Fogg's findings, Denny carried out experiments with plane thrust surfaces for radial-face seals and verified a lubricating film between the surfaces, which generated significant pressure build-up.⁶⁹ Since then, many attempts have been made to efficiently separate the seal surfaces and to improve their tribological performance. The underlying mechanisms comprise hydrostatic, hydrodynamic and thermal effects, which all are greatly affected by the surfaces' topography.⁷⁰ The basic surface geometries initially investigated were flat parallel surfaces, wavy surfaces, surfaces with angular misalignment and coned surfaces.

Thereby, sinusoidal or wavy surfaces showed an increased hydrodynamic pressure, thus improving the load carrying capacity coming from an asymmetric pressure distribution induced by cavitation.⁷⁰⁻⁷²

Rotary-shaft seals were the first lubricated machine elements that were textured to improve their tribological performance. In 1966, Hamilton et al. applied protruding asperities on a stator surface by photoetching and found that these asperities increased hydrodynamic pressure and thus load carrying capacity.¹⁴ Similarly, Anno et al. investigated the effect of photoetched asperities on load support and leakage.^{13,73} All tested shapes led to a similar increase in load support, but leakage reduction induced by texturing was superior for etched depressions (dimples) than for protruding asperities.¹³

Three decades later, Etsion and Burstein presented a numerical model to investigate the effects of pores and dimples on the seal's performance.¹⁶ An optimum area density of 20 % and diameters between 5 and 75 μm , depending on viscosity, sealed pressure and area density led to an optimized frictional and leakage performance. Later, Etsion et al. suggested an optimum value of 0.05 for the aspect ratio (depth/width).⁷⁴ Their experimental findings were validated using numerical results based upon the 2-D, steady-state Reynolds equation for an incompressible Newtonian fluid assuming laminar flow.¹⁵ Using this simplified model, they showed the major influence of the aspect ratio regarding the resulting pressure distribution, whereas the other geometrical parameters were of minor importance. Kligerman and Etsion numerically investigated the effects of LST for dry gas seals and demonstrated a maximum friction reduction of up to 40 %.⁷⁵ In contrast to oil-lubricated seals, the use of smaller aspect ratios (0.02) was recommended. These results were experimentally validated whereby a maximum reduction in friction torque by 40 % and a drop in face temperature of 20 °C were demonstrated.⁷⁶ Etsion and Halperin used LST to partially texture high-pressure hydrostatic mechanical seals with a higher

area density close to the high-pressure side, whereas the low-pressure side remained untextured.⁷⁷ Partial surface texturing generated a hydrostatic lift with similar effects compared to a Rayleigh step or for face coning (inclined faces), as shown in **Figure 6 a**. Additional hydrodynamic lift can be generated due to a converging contact with different film thicknesses across the faces.³¹ Experimental studies and numerical work proved the possibility to increase the sealing pressure capability and to reduce the friction torque by up to 50 % (see Figure 6 b).

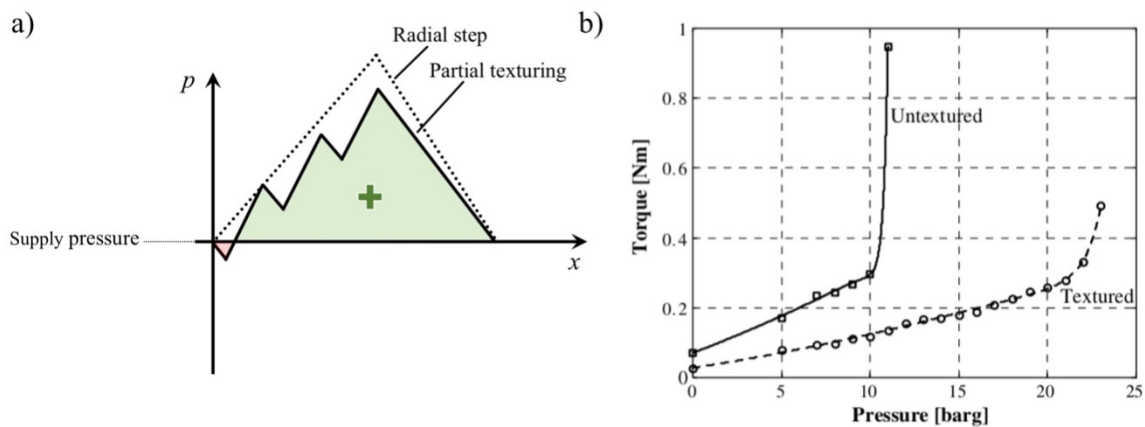


Figure 6. Effects of partial texturing: a) Function principle and net positive pressure distribution due to partial texturing. The effect is similar to that achieved with a radial step.³¹ 2016, open access, Elsevier. b) reduction in friction torque and increase in sealed pressure capability by using partially textured hydrostatic mechanical seals compared to untextured, original seals. Reproduced with permission.⁷⁸ 2004, Springer Nature.

Similarly, Etsion's group demonstrated the effectiveness of partial texturing in hydrostatic gas seals to improve load carrying capacity;⁷⁹ and to maximize gas film stiffness.⁸⁰ Again, an additional hydrodynamic pressure was attributed to the similarity between partial texturing and a radial step. The best performance was achieved for area densities between 50 and 70 %.^{79,80} In addition, they observed a reduced daily leakage (20 %) in field tests, attributed to a better mechanical integrity of the textured seal.⁸¹

Furthermore, a reduction in friction torque of 65 % was verified due to an increased hydrodynamic pressure thus inducing a greater separation of the surfaces and an increased fluid film stiffness.⁸¹

After the pioneering work of Etsion et al., various studies have been published assessing the effects of surface texturing on the seal's performance. Several aspects have been taken into consideration such as an increase in hydrodynamic pressure and thus load carrying capacity,^{82,83} potential wear reduction,⁸² a reduction in leakage,⁷⁹ and a reduction in surface temperature.⁷⁶ The mechanisms behind performance improvement, optimum geometric parameters and shapes as well as accurate modeling approaches have been extensively investigated, which are summarized in the following sections.

2.3.1 Optimum geometric parameters

Wang et al. textured SiC seals with hemispherical textures with area densities between 2.8 and 22.5 % while keeping depth and diameter constant. Tribological tests under water lubrication demonstrated an increase of 20 % in the critical load for the transition from full-film to mixed lubrication for textures with the smallest area density.⁸⁴ However, a later parametric study verified that higher area densities and greater depths were more beneficial to increase the critical load (up to three-fold increase).^{85,86} The authors concluded that the additional supply of water from the dimples favored a tribochemical reaction that led to the formation of silicic acid, thus lowering friction. Moreover, they emphasized that the main effect induced by the textures in this study was to provide sufficient water for the tribochemical reactions.⁸⁶ However, these results were not supported by a detailed analysis of the surface chemistry in the worn areas. Wan and Dang-Sheng generated dimples (200 μm diameter, 10 μm depth, 10 % area density) in

steel discs and found an increased critical load (by a factor of 2.5) and critical speed (by a factor of 1.4) until the COF suddenly increased.⁸⁷ This was traced back to an additional oil supply, but without further experimental evidence. Chen et al. used ultrashort-pulse LST to fabricate micro-stripes on SiC mechanical seals resulting in a COF reduction of 20 %.⁸⁸ Wang et al. studied the effect of LST on friction and temperature of two-phase mechanical face seals (sealed liquid partially vaporized) with hemispherical dimples having a depth of 10 or 40 μm , a diameter of 1000 or 2000 μm and a constant area density of 20 %. For most textured seal rings, a significant reduction in friction and temperature without any leakage was observed due to an increased load carrying capacity. However, if both diameter (2000 μm) and depth (40 μm) were too large, excessive vaporization started to occur thus leading to increased temperature and higher friction.⁸⁹

Yu et al. investigated the temperature rise in laser-textured SiC rings (diameter of 90 μm , depth of 25 μm , area density of 20 %) sliding against carbon seal rings. Apart from a friction reduction, they demonstrated that the temperature in the textured SiC ring could be reduced by roughly 40 % by surface texturing.⁹⁰ It should be emphasized that the temperature rise in mechanical seals is a serious problem since excessive frictional heat can significantly degrade the seal as well as the lubricant, thus inducing leakage and a change in the lubrication regime.

2.3.2 Optimum shape and orientation

The effects of circular, square, diamond, hexagonal and triangular textures were numerically investigated by Siripuram and Stephens. They showed that the texture's shape had only a minor effect on the resulting COF, whereas the area density greatly affected the COF. However, the optimum area density depended on the texture's shape.⁹¹

In contrast, Shi et al. numerically demonstrated a significant influence of the texture shape (micro-grooves vs. micro-dimples) on the load carrying capacity of gas seals. For small area densities, micro-grooves showed an improved performance, while micro-dimples outperformed micro-grooves for higher area densities. The greatest load carrying capacity was found for elliptical micro-dimples with an area density of about 40 %.⁹²

Qiu and Khonsari also studied friction and wear of circular and elliptical textures fabricated by LST on seal rings.⁹³ They showed an optimum aspect ratio for a fixed area density (0.1 and 0.138 for an area density of 25 and 40 %, respectively) as well as an optimum area density for a given aspect ratio (increasing area density leads to lower COFs), which agrees well with their additional numerical work.⁹⁴ One particularly interesting aspect of their work is the visualization of cavitation inside the dimples with a high-speed camera, which is depicted in **Figure 7**. Additionally, they demonstrated that circumferentially-oriented elliptical dimples outperform other dimple shapes or orientations.⁹³ Despite the improvements in COF, Qiu and Khonsari also verified an increase in wear for the laser textured rings, which potentially reduces the component's lifetime.

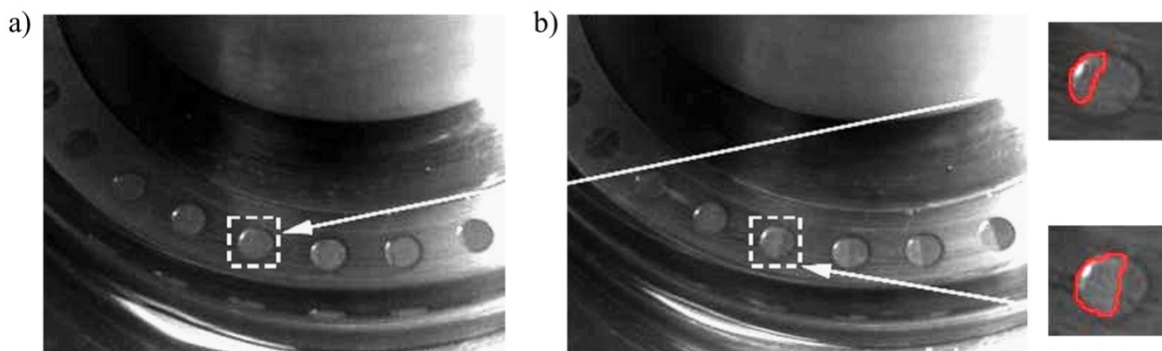


Figure 7. Increasing size of cavitation areas inside dimples with increasing sliding speed: a) 100 rpm; b) 200 rpm. Cavitation inside the dimples increased film thickness and thus reduced COF. Reproduced modified with permission.⁹³ 2011, Elsevier.

Xie et al. studied the tribological performance in water of SiC rings with circular and triangular textures (20% area density, 7 μm depth). They found that the triangular textures experience a strong frictional anisotropy. If the triangular textures pointed against the sliding direction, its apex was located in the convergent region and friction was minimal. In contrast, friction was maximum if the triangular textures pointed in the opposite direction. The circular textures showed intermediate friction values.⁹⁵ Numerical studies helped to explain the experimental findings and verified a higher resistance to outlet fluid flow if the apex was in the convergent region, which generated greater pressures and thicker films.⁹⁵ Meng et al. numerically investigated the sealing capability of different seals having diamond, elliptical, rectangular and triangular textures. Based upon their simulations, the sealing performance depended on the dimples' inclination as well as on the dimple's depth and diameter. Rectangular textures offered the best sealing performance due to a maximum additional pressure build-up. In addition, it is worth to mention that all shapes demonstrated negligible leakage.⁹⁶ Bai et al. numerically investigated the influence of texture shape for gas seals and found that elliptical dimples could improve the opening force by 20 % compared to circular dimples. Nevertheless, leakage was shown to simultaneously increase with greater opening force.⁹⁷ A later work found that the COF of surfaces with double-row elliptical dimples having different inclinations decreased by 59 % and the face temperature rise decreased by 58 % compared to single-row elliptical dimples having the same inclination angle.⁹⁸ This was attributed to an accumulation of lubricant between the dimple rows and thus stronger hydrodynamic effects. In a recent study, Shen and Khonsari first used a mathematical optimization method to find the optimum texture shape and subsequently evaluated optimum texture shapes experimentally. It was demonstrated that chevron-like textures created the maximum load carrying capacity by increasing the hydrodynamic pressure. This reduced

COF values and expanded the hydrodynamic lubrication regime.⁹⁹ Similarly, Wang et al. used a multi-objective optimization approach and found that the optimum shape in terms of load carrying capacity and leakage for gas seals is an asymmetric chevron shape.¹⁰⁰ Furthermore, they concluded that it is not recommendable to increase the load carrying capacity to its maximum since the leakage rate may simultaneously increase drastically. This interdependency between load carrying capacity and leakage rate is shown in **Figure 8**.

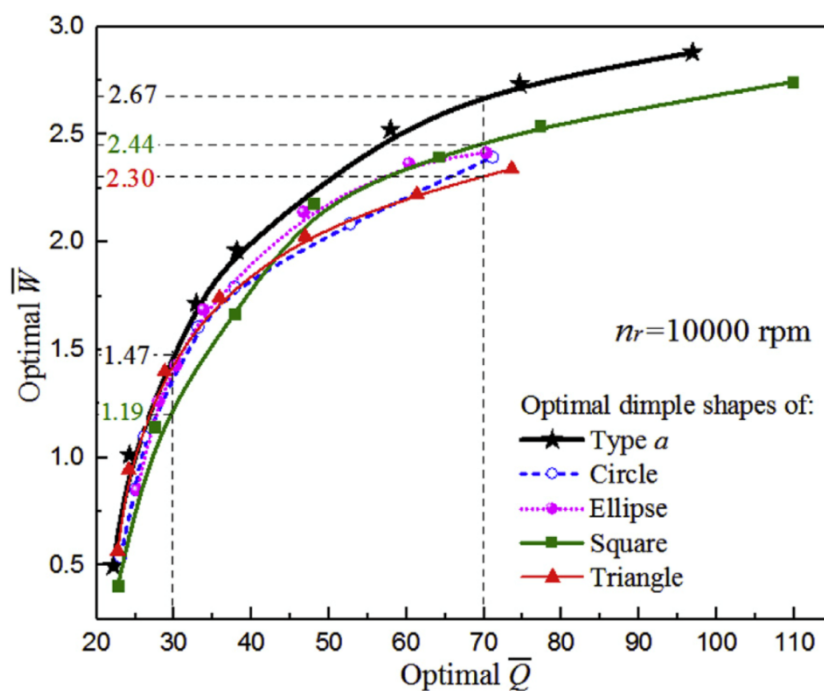


Figure 8. Dimensionless load carrying capacity \bar{W} plotted against dimensionless leakage rate \bar{Q} . An increase in load carrying capacity simultaneously leads to an increase in the leakage rate. “Type a” corresponds to the optimum asymmetric chevron shape which exhibits the greatest load carrying capacity under the same leakage rate. Reproduced with permission.¹⁰⁰ 2018, Elsevier.

Brunetière et al. developed a numerical model to investigate the influence of the texture’s shape (e.g. cylinder, square, truncated pyramid, triangle) on the seal’s performance.^{101, 102} They demonstrated that triangles had the greatest load carrying capacity with a significantly decreased leakage. The numerical results were experimentally confirmed

showing a reduction in friction of around 50 % and improvements in terms of temperature rise by roughly 40 %.¹⁰³ Moreover, they analyzed the effects of a deviation of the real texture's shape from a perfect shape since real textures show roughness and other defects, which are typically not considered in numerical studies.¹⁰⁴ The authors verified that leakage was greatly affected by roughness and the real dimple shape (e.g. deformed dimple edges) whereby either beneficial or detrimental effects in terms of leakage can be induced depending on the dimple's shape. In addition, the film thickness depended on the real dimple shape. Finally, they concluded that a proper control of the texture shape is crucial for surface texturing and an accurate study requires consideration of the real texture shape.

2.3.3 Modeling

Hamilton used the half-Sommerfeld model to study the effect of textured surfaces in mechanical seals. In this model, the Reynolds equation was solved analytically whereby the negative pressure was eliminated.¹⁴ Etsion et al. used this approach for their earlier studies on mechanical seals.¹⁶ Later, they developed an improved model by using the Reynolds cavitation model (Swift–Stieber model).¹⁵

More recently, it has been emphasized that models using non-mass-conserving cavitation boundary conditions cannot accurately predict the load carrying capacity of textured surfaces.^{31,101} This was demonstrated by Qiu and Khonsari by comparing two non-mass-conserving cavitation models with a mass-conserving Jakobsson-Floberg-Olsson (JFO) model for fully-textured, smooth mechanical face seals. In contrast to non-mass-conserving models, the JFO model accounts for rupture and reformation of the lubricant film.¹⁰⁵ The results proved that the JFO model gives lower peak and overall pressure as

well as load-carrying capacity, which can be explained by the higher pressure build-up for non-mass-conserving models. Hence, it is not recommended to use Swift–Stieber or half-Sommerfeld models for textured surfaces.¹⁰⁵ The textures modeled by Qiu and Khonsari had smooth surfaces outside the pockets. Since their results showed very limited load generation for the textured seals, they contradicted experimental observations in the literature, which often show a significant enhancement in load generation. Thus, they added roughness by using flow factors following the Patir and Cheng formulation.⁹⁴ They found that roughness had a positive but limited effect on load-carrying capacity. Additionally, optimum texture parameters (aspect ratio and dimple density) were identified, which greatly depended on rotational speed and cavitation pressure. Maximum load carrying capacity was achieved for an aspect ratio of around 0.005 for lower sliding speeds and about 0.015 for higher sliding speeds. Furthermore, the load carrying capacity was also affected by the area density whereby the optimum area density (between 40 and 65 %). According to their results, leakage was highly dependent on both roughness and texture depth whereby larger depths or surface roughness led to increased leakage.

Based upon work by Qiu and Khonsari,⁹⁴ Brunetière et al. also considered roughness between the dimples by solving the Reynolds equation coupled with a mass-conserving algorithm, as presented in **Figure 9**.¹⁰¹ Surface roughness generated a load-carrying capacity above a certain threshold of velocity.¹⁰⁶ Regarding the pressure distribution, there was good correlation with results presented by Qiu and Khonsari. For smooth surfaces outside the textured area, the opening force generated by surface texturing was too small to balance the closing forces and therefore unable to separate both contacting surfaces. Thereby, especially the generated net force was very small since the local pressure was attenuated by negative effects of the cavitation area. A global pressure effect completely separating the surfaces was not observed. In contrast, the authors showed a

significant increase in hydrodynamic pressure and thus a friction reduction under mixed and hydrodynamic lubrication if roughness was added to the dimpled surfaces. Furthermore, an area density higher than 10 % and an aspect ratio greater than 0.04 were suggested to allow for the maximum friction reduction.¹⁰¹ The seals' performance under mixed lubrication was also studied by Brunetière et al. by considering asperity contact (Hertz contact model), since optimal performance for mechanical seals is typically obtained at the transition from mixed and hydrodynamic lubrication. When roughness was considered, friction could be decreased significantly not only under hydrodynamic but also under mixed lubrication.^{102,107}

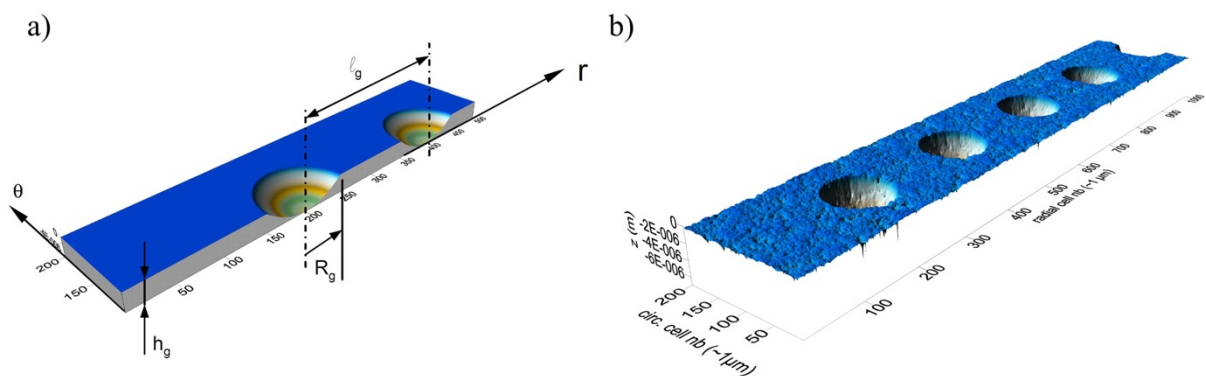


Figure 9. Models for a perfectly flat textured surface vs. a rough textured surface. Reproduced with permission.¹⁰¹ 2012, Elsevier.

2.3.4. Summarizing remarks

Mechanical seals are an essential component used in conjunction with almost all mechanical equipment. Thereby, the lifetime of other components in the system, like bearings, might be limited by the seal's integrity.⁶⁶ In this context, surface texturing can be a viable method to reduce friction and wear and as a consequence increase the seal's and the component's lifetime. Seal-type contacts are ideal for applying surface textures

due to their conformal contact conditions as well as small requirements in terms of load carrying capacity. In this context, pioneering work on mechanical seals by Etsion et al. found an optimum area density of 20 % with oil lubrication. Furthermore, the aspect ratio is considered as the most significant texture's parameter, which needs to be optimized with respect to the seal's operation conditions.⁷⁸ Friction, wear, leakage and surface temperature can be significantly reduced if optimized texture parameters such as depth, width, area density, aspect ratio, shape and texture orientation are considered. The textures' optimization should be carried out with the highest possible caution to avoid detrimental effects such as stress concentration or higher leakage induced by surface textures. Modeling approaches using mass-conserving codes can give accurate results and thus facilitate the texture design/optimization. However, a precise implication of the textures' shape and surface roughness should be performed since flat surfaces and perfect shapes as usually used in modeling rarely exist in real applications. In summary, it can be stated that considerable research work has been dedicated to understand the underlying mechanisms and effects of surface texturing in mechanical seals with respect to the potential increase in the load bearing capacity and hydrodynamic pressure. However, until today, the underlying phenomena have not been entirely understood and explored, which paths the way for further research activities in this field.

3. Surface texturing in rolling contacts

3.1. Introduction

Although the effects of surface texturing for sliding components have been largely reported in literature, studies regarding the influence of surface texturing for rolling components are scarcer. There are important reasons for the more restricted use of surface

textures in rolling machine elements. First, rolling components present non-conformal contacts, and thus the contact areas are rather small.¹⁰⁷ Since texturing methods have limitations in terms of the texture's sizes,¹⁰⁸ it is difficult to ensure that individual texture's features are smaller than the contact areas.¹⁰⁹ Consequently, the lubricant may escape from the contact because textures guide the lubricant away from the contact.^{27,109} Second, rolling machine elements rely on elastohydrodynamic lubrication (EHL) to form a lubricant film between the contacting surfaces. Thereby, one of the main mechanisms involved in EHL, which favorably influences the tribological behavior is the large increase in viscosity due to high contact pressures (typically between 1 and 4 GPa).¹¹⁰ Deep surface textures can reduce the pressure in the lubricant, thus reducing beneficial effects coming from the increased viscosity in EHL contacts.¹¹¹ Third, rolling machine elements are prone to the occurrence of rolling contact fatigue (RCF).¹¹² Smooth non-conformal contacts loaded below the yield stress and in the absence of any tractive force would have a stress field near the contact just given by the Hertzian pressure distribution. This still holds true to a reasonable extent if the surface presents surface topography but the lubrication regime results in thick films, since surface traction is negligible for large λ -ratios. However, if the lubricant film is thin, traction is present and rough surfaces change the contact's stress distribution, generating increased and localized stresses near the asperities.¹¹³ Cracks can initiate at these high stress locations and lead to contact fatigue.¹¹² Because of that, the general design principle for rolling elements is that they should be as smooth as possible and that any type of surface topography (as opposed to a perfectly smooth surface) could be detrimental to RCF. Therefore, the possibility of surface texturing promoting RCF has been a frequent concern for rolling machine elements, particularly among industrial manufacturers.

In case of gears, the whole situation is further complicated as the contact is neither pure sliding nor rolling. The minimum sliding friction can be found at the characteristic pitch point of a gear whereas maximum sliding occurs at the tip interface. Due to high loads and roughness requirements involved, the introduction of surface textures in gear parts is quite challenging.¹¹⁴ Another relevant point is that gear parts are mostly case-carburized components and the interaction of such a hardened material with laser sources can be seen critical with regard to microstructural changes in particular by reducing hardness thus limiting the applicability of LST.¹¹⁵ In addition, another fundamental question is where to apply surface textures on gear tooth surfaces due to complex geometries involved with narrow tolerances. The maximum load is shared by gear teeth surfaces around the pitch point, where rolling action dominates and due to the high load in these regions no textures should be introduced as they may wear off fast. It is however reasonable to locate surface textures in high slip areas i.e. off-locations to the pitch point where frictional losses can be up to 15 %.¹¹⁴ The problem associated with the location of surface textures in high slip zones can be associated with accelerated wear due to insufficient lubrication.

It will be shown that despite the challenges for surface texturing in rolling components, the use of surface texturing has potential to decrease RCF and improve lubrication of rolling machine elements. Therefore, surface texturing in rolling machine elements has regained interest from researchers and manufacturers in recent years.

3.2. Effect of surface texturing in roller bearings

Roller bearings are largely used in mechanical systems to reduce friction between rotating parts. From a tribological point of view, the contacting surfaces under relative motion are the inner raceway, the outer raceway, the rollers (balls, cylinders or cones) and the roller

cage. In terms of manufacturing, surface texturing of roller bearings is more difficult and is mostly carried out on the surfaces of either the outer raceway or rollers.

The effects of surface texturing on the tribological behavior of roller bearings will be analyzed from two viewpoints. First, the main findings related to RCF life of textured roller bearings will be summarized thus extracting the main mechanisms involved. Despite the conventional view that surface texturing is detrimental for RCF, some cases will be presented where surface texturing helped to increase RCF life. Then, the effects of surface texturing on lubrication will be reviewed. However, it is important to emphasize that both phenomena (RCF and lubrication) are in fact intertwined and that the effects of surface texturing cannot be treated completely separately, as some of the work will show.

3.2.1 Effects on rolling contact fatigue (RCF)

RCF involves the initiation of microscopic fatigue cracks in the contacting surfaces or within the sub-surface due to cyclic shear stresses. The coalescence and growth of these cracks lead to material removal from the surface.¹¹⁶ Surface roughness alters significantly the contact's pressure distribution. Due to the cyclic nature of the movement in roller bearings, local cyclic plastic deformation occurs at the vicinity of the surface asperities.¹¹² Consequently, contact fatigue phenomena are strongly related to surface roughness/topography.

A numerical model was proposed to account for the effects of roughness on RCF life, based upon the damage accumulation theory. Different surface topographies were produced by three manufacturing processes. The surface topographies produced by each

process were measured and input into the numerical model. The results indicated that surface roughness induced significant fluctuations in the contact pressure, in turn resulting in variations in the stress field close to the surface. Effective stress factors were calculated for these processes, which rose substantially at the near-surface layer. The depth for the high values of effective stress factors was only around 0.1 - 0.2 of the Hertzian contact width, suggesting that surface roughness increases fatigue risk only within a thin surface or near-surface layer.¹¹³ In another model, the effects of a single hemispherical bump as well as of numerically generated 3-D complex rough surfaces on RCF life were investigated, showing similar findings in terms of stresses near the surface.¹¹⁶ A fatigue life model predicted reduction in fatigue life as a consequence of the high stresses near the surface.

The negative impact of surface roughness on contact fatigue has led to the common sense that perfectly smooth surfaces, such as polished surfaces, should present optimal RCF life,¹¹⁷ which has delineated manufacturing technologies of roller bearings. In this context, it is worth to emphasize that Zhang et al. have made considerable research contributions in the field of developing grinding and polishing methods to achieve a surface roughness in the range of a few nanometers.^{118,119} Nevertheless, the potential for surface textures containing arrays of depressions (pockets) rather than protruding features to improve RCF life of roller bearings has been largely suggested in the literature, although in many cases not proved.¹²⁰ One rationale for this possible improvement is that an array of depressions may potentially decrease the interaction between asperities, which may increase the fatigue life.¹²¹ Another possibility is the introduction of residual stresses when the texturing method involves intense plastic deformation, such as localized blasting, since surface compressive stresses can increase RCF life.¹²¹ In addition, microstructural changes that might result from surface texturing could affect RCF.

Microstructural changes accompanying surface texturing are particularly relevant for methods involving localized removal of material by high temperature methods, such as laser surface texturing. After pico- and femtosecond-laser texturing of roller bearings raceways, a martensitic microstructure was found in near-surface zones, whereas martensitic-bainitic and bainitic microstructures were observed in the areas surrounding the pockets.¹²² This was traced back to ongoing phase transformations occurring during the crystallization of the liquid phase formed during laser texturing. The author suggested that these microstructural changes may help to reduce friction and increase RCF life of roller bearings, but no experimental evidence was presented.

One of the pioneering studies showing beneficial effects of depressions on the RCF life was presented by Akamatsu et al. They produced small randomly-distributed indentations on smooth needle rollers and rings and measured RCF life for different lubrication conditions (λ -ratios varying from 0.64 to 2.10).¹²³ The surfaces were characterized using the parameter R_{sk} (skewness), which represents the asymmetry of the height distribution curve. Positive values of R_{sk} indicate a surface composed of plateau-peaks, *i.e.*, presenting protruding features, whereas negative values of R_{sk} represent a surface consisting of plateau-valleys, *i.e.*, presenting depressions. The roller bearings with more negative skewness values presented longer RCF life. For lower λ -ratios, fatigue life increased by more than 13 times. However, for higher λ -ratio values (thicker EHL films), life increase was smaller (around three times).

The aforementioned results obtained by Akamatsu et al. had an important impact for researchers as well as roller bearing manufacturers and experienced a significant discussion in the scientific community. Zhao et al. modeled the conditions used in Akamatsu's work as an attempt to understand the underlying mechanisms responsible for the improved fatigue life.¹²⁴ As a first approach, they modeled the effects of the

depressions on EHL film thickness, but their results did not demonstrate any increase in film thickness. Afterwards, they discussed how surface texturing can help to reduce friction. They concluded that the main reason for an improved RCF life of textured bearings was the lubricant stored in the pockets, which helped to reduce friction. They proposed that, for low λ -ratios, the texture pockets act as lubricant reservoirs, from where the lubricant is brought into the contacting asperities via hydrostatic and squeeze effects. The reduction of micro-slip among contacting asperities reduces friction, increasing RCF life. Indeed, friction is strongly related to the occurrence of RCF. Tallian et al. showed how friction causes surface-initiated fatigue,¹²⁵ leading to a considerable decrease in contact fatigue life due to an increased shear stress in the near- surface region of roller bearings, which is the main cause for RCF.¹²⁶

The effect of the texture's geometry on RCF has been investigated in the literature, but not to a large extent. Vrbka et al. investigated the effects of surface texturing with arrays of dimples (diameters between 35 and 65 μm ; depths between 0.6 and 1.45 μm ; and area densities between 9 and 32%) on rolling contact fatigue of roller bearings for a slide-to-roll value (SRR) of 0.05. Improvement in RCF life with surface texturing has been shown particularly relevant for textures more densely packed and with shallower features. The fact that denser textures presented longer RCF life was attributed to a reduction in the interaction between the surfaces when the total area of the dimples increased. Moreover, the additional supply of lubricant, which reduces local traction at the asperity contacts, is more effective for denser textures. A further beneficial effect was attributed to the fact that the lubricant entrapped within the dimples goes ahead of it or lags behind it and elastically deforms the rubbing surfaces, further contributing to reduce asperity contact. On the other hand, it was proposed that a film constriction occurs at the leading edge of the dimple, reducing film thickness. This could increase asperity interaction and therefore

reduce RCF. Since this constriction is more significant for deeper dimples, it was suggested that this detrimental effect surpasses the beneficial effects for deeper dimples.

121,127

Recently, a method for calculating the relative fatigue life of textured ball bearings, combining rolling bearing quasi-dynamics, micro-TEHL analysis, non-Gaussian surface simulating techniques and stress analysis by finite element modeling, showed that textures oriented transversely to the movement direction increased fatigue life.¹²⁸ This was attributed to an increase in film thickness and will be further discussed in the next section.

One important point about the studies correlating surface texturing and fatigue life is the statistical significance of the effects. Since fatigue tests are expensive and time consuming, the number of repetitions of the tests is often small and therefore the differences found from RFC life tests may not be statistically significant.¹²¹

3.2.2 Effects on lubrication

Optical interferometry was used to visualize EHL point contacts containing regular arrays of both protruding features and pockets, for different slide-to-roll ratios,¹²⁹ showing how the passage of individual texture features changes film thickness locally in the contact. Similar works can be found in the literature showing either increase or decrease of EHL film thickness in textured surfaces.^{130,131} For example, it has been shown that transverse grooves and ridges increase film thickness, which has been attributed to their contribution on the hydrodynamic pressure in the contact. On the other hand, longitudinal features and regular arrays of bumps typically reduce film thickness, because they channel lubricant away from the contact.

Numerical simulations have also been used to analyze the effect of surface topography on EHL.¹³² Similar to experimental studies, numerical work has proved an increase in film thickness for transversal features and reduction for longitudinal features.¹³³ Micro-cavitation effects have been introduced in recent models and made it possible to predict conditions for which surface textures can increase EHL film thickness.¹³⁴

Experimental studies of textured EHL contacts have shown that very shallow pockets (depth below 1 μm) with lateral dimension smaller than the contact area increase film thickness when they cross the contact. However, deeper pockets lead to collapse of the lubricant film.¹¹¹

Also, surface texturing has only shown to increase film thickness in experimental studies when the texture motifs are substantially smaller than the contact width.^{135,136} Since EHL contacts present small contact areas, the width of the surface features needs to be small to be suitable for EHL contacts.

Most of the aforementioned works showing effects of surface texturing on EHL lubrication are related to sliding conditions, but roller bearings work under conditions of low slide-to-roll ratio (SRR). Fewer studies can be found for effects of surface texturing on lubrication under rolling conditions. For example, optical observation of textured EHL contacts show that the lubricant film's shape present a typical horse-shoe shaped constriction.¹²⁹ In addition, oil entrapment at the asperities in the peripheral region of the contact is often observed. Therefore, the possibility of positive effects of surface texturing on lubrication described for certain sliding conditions could also occur under rolling/sliding conditions. It should be emphasized that the experimental studies in the previous section showing the positive impact of surface texturing on fatigue life used low

sliding-to-roll ratios.^{121,123,127} They mostly attributed the increase in fatigue life to lubrication improvement.

An initial discussion in Akamatsu's pioneering work regarding the improvement of fatigue life of roller bearings containing surface depressions already suggested an improvement in lubrication.¹²³ Zhai's subsequent work pointed out that the mechanism was not just related to an increase in film thickness, but merely to the fact that the depressions stored lubricant, which was released in the contact when needed.¹²⁴

The experiments described above showing an increased EHL film thickness with surface texturing under certain conditions suggest that even under low slide-to-roll conditions, both mechanisms (increase in film thickness and lubricant storage) can help to improve the lubrication conditions and increase the RCF life of roller bearings. This has been proposed by Shi et al. when they modelled life prediction of textured ball bearings. The lubrication model used in their calculations showed that lubricant film formation by hydrodynamic effects was favored for transverse textures placed perpendicularly to the entrainment velocity.¹²⁸

However, surface texturing of roller bearings is challenging since the texture's width and depth should be considerably smaller than those used in conformal contacts. Typically, the width needs to be in the order of only a few micrometers and the depth in the sub-micrometer range. Texturing techniques able to produce such small features are few and generally more expensive.^{30,110}

Another important issue related to lubrication of surface textured roller bearings is the activation of additives present in the lubricant. Commercial cylindrical roller bearings were textured by direct laser interference patterning (DLIP) and tested in tribological tests corresponding to the conditions defined in the standard DIN 51819-3. The tests used a

mineral base oil containing ZDDP additive as lubricant. The textured roller bearings presented lower friction (30%) and significantly lower wear (two orders of magnitude) when compared with untextured bearings.²¹ When the worn surfaces were analyzed by optical (Figure 10 a) and laser scanning microscopy (Figure 10 b), tribofilms were observed near the peaks of the textures. Raman analysis in the regions with and without the tribofilms showed the formation of typical compounds present in ZDDP mechanically activated tribofilms. It seems that localized high pressures induced by the surface texture activated the decomposition of ZDDP and the formation of protective tribofilms thus reducing wear. The decomposition of ZDDP is fundamental for the formation of protective tribofilms.¹² It should be emphasized that the texturing technique (DLIP) used in this work enables the fabrication of surface textures with small features at relatively low cost.³⁰ Since larger features have shown to be detrimental for film formation in EHL contacts, the positive impact of surface texturing of roller bearings on the activation of ZDDP additive could be counterbalanced if texturing methods that produce larger features were used.

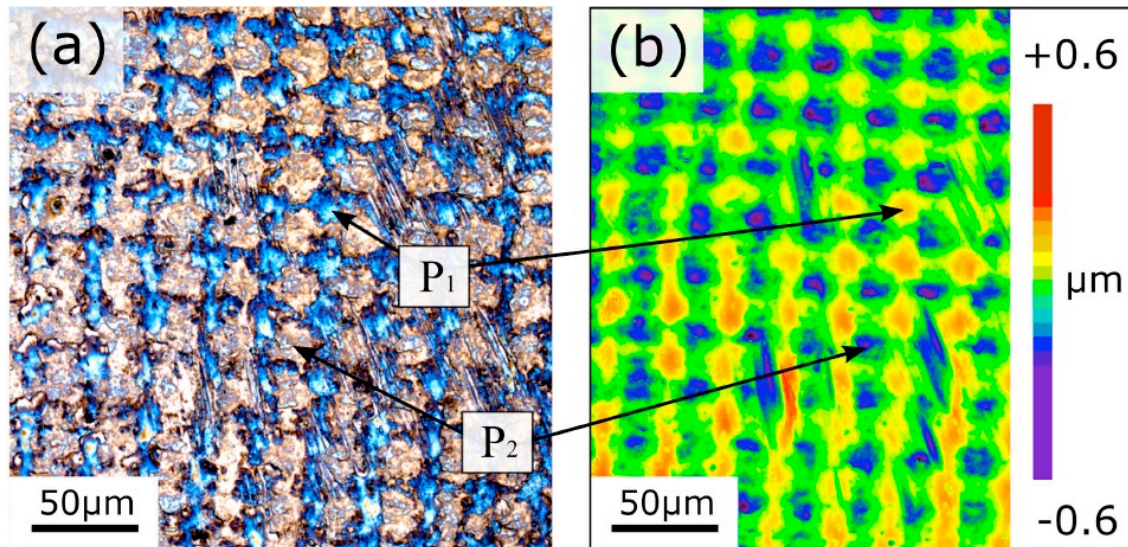


Figure 10. Textured AISI 52100 steel roller bearing surface after rubbing in the presence of mineral oil + ZDDP: (a) optical microscopy; (b) laser scanning microscopy (LSM). P1 marks a position with blue-colored tribofilm on the top of the textures, whereas P2 highlights a region of valleys without blue color.²¹ 2017, open access, MDPI.

3.2.3 Summarizing remarks

This section showed that the use of surface textures in roller bearings is still scarce when compared to other machine elements, in particular sliding components. The main reason is the concern regarding RCF life of textured bearings. Another difficulty is the need for textures with small diameters and depths, which are difficult to manufacture. Despite these restrictions/challenges, it has been shown that textures can improve the lubrication of roller bearings under certain conditions without compromising their RCF. First, the depth of the individual pockets should be in the sub-micrometer range. Second, their width should be substantially smaller than the elastic contact width. Third, channel-like features are generally detrimental, since they can induce lubricant leakage from the contact. Fourth, in the case of directional textures, they should be aligned perpendicularly to the direction of movement. In addition, care should be taken when choosing the

technology to manufacture the textures. It should be able to produce, preferably cheaply, textures with small depths and diameters.

3.3. Effect of surface texturing in gears

Gear transmission represents the most important way of mechanically transmitting rotational motion and torque. Most commonly used gear parts are planetary-, bevel-, helical-, worm-, rack and pinion gears.¹¹⁴ Gears are used in different applications such as industrial machines, vehicles, wind parks or power plants.

A typical gearbox includes a plurality of gear sets all disposed in the gearbox housing. Each gear set includes at least two gears meshing with one another. Figure 11 highlights the most relevant parameters for properly describing gears.¹³⁷

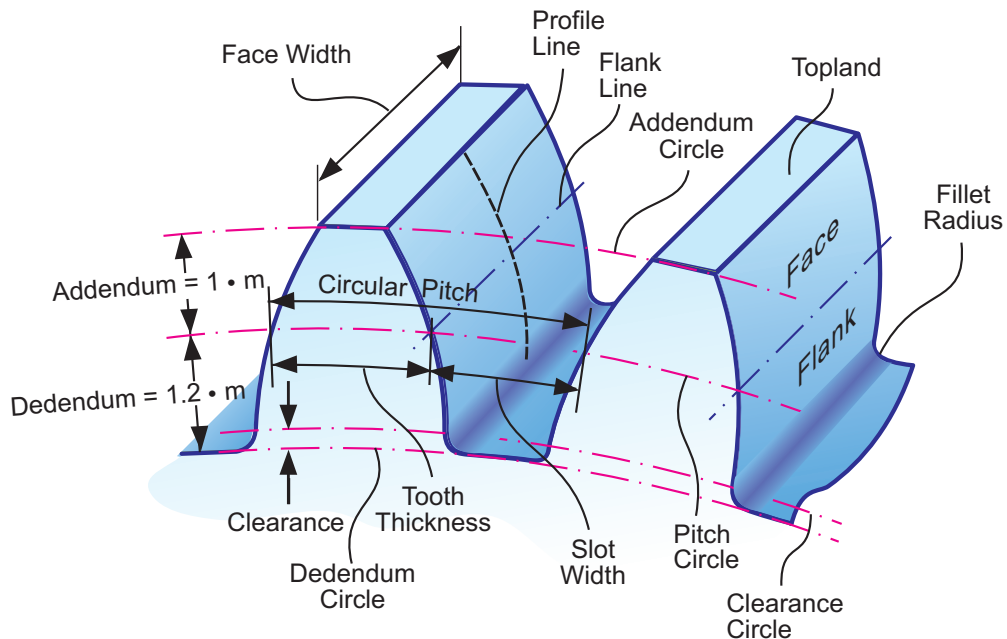


Figure 11. Schematic of gear teeth and their most relevant parameters. Reproduced with permission.¹³⁷

The non-conformal and highly loaded contact (in the range of several GPa) between the gear teeth surfaces usually operates under boundary or mixed lubrication due to poor lubricant retention.¹¹⁴ Even for highly polished gears with low roughness values, the calculated maximum film thickness, assuming the best combination of load, speed and temperature, is less than the peak to valley distance, thus leading to strong asperity interactions.¹³⁸ Because of that, there is an urgent need for techniques that can help to effectively sustain a lubricant film between the meshing gears in a gearbox in order to improve the lubrication conditions. Friction at the sliding and rolling tooth contacts is responsible for the majority of losses in gear pairs.

The different amounts of rolling and sliding occurring at different locations of the gear teeth results in variations in sliding friction, inducing vibration and thus gear failure. Typical gear failures are micro-pitting, pitting and scuffing. Surface fatigue phenomena such as micro-pitting and pitting occur due to cyclic loading of gear parts thus resulting in crack initiation and growth. Micro-pitting refers to a composite of small initial cracks, provoked by insufficient lubrication, which can be recognized by its appearance due to diffuse light scattering at the crack network. Micro-pitted areas can finally result in pitting with small holes in the metallic surface.

Scuffing as a catastrophic failure refers to a sudden damage when sliding surfaces are locally welded together. Due to insufficient lubrication and increasing sliding friction between gear teeth, temperature increases and the protective lubricant film collapses thus welding parts together and leading to material transfer when the gear teeth separate again. Scuffing strongly depends on the applied load, sliding speed, surface quality and lubrication state.¹³⁹ This failure mode mainly occurs during running-in as gear components need some operational time to achieve a smooth surface. In this context, there are many approaches to smoothen gear teeth surfaces efficiently. According to Nakatsuji

and Mori, electrolytically polished gear teeth with an arithmetic surface roughness R_a of about $0.13 \mu\text{m}$ showed reduced pitting tendency by 50 %.¹⁴⁰

In this context, an important finishing technique for gears is superfinishing.¹³⁸ Surface roughness of less than $0.1 \mu\text{m}$ can be achieved by superfinishing. The respective parts are treated by the interaction of non-abrasive ceramic media (mostly alumina-based media) with a reactive chemical (mostly consisting of phosphates, oxalates, sulfates, chromates or even mixtures of them) in a vibratory finishing bowl thus using a dedicated surface leveling/smoothing mechanism to produce gear parts with a reduced surface roughness. The parts to be superfinished are placed in a finishing media, and a reactive chemical is used to form a soft “conversion coating” on the respective surface. This coating is chemically stable but mechanically unstable thus allowing for an easy removal through the interaction with the non-abrasive finishing media. The repeated chemical reaction on the surface and subsequent removal leads to a leveling effect where the chemical also acts as a catalyst reducing the energy required to remove material from the surface of the component while also controlling the refinement speed.¹³⁸ In 1984, Tanaka et al. had already postulated that superfinishing may lead to a higher surface durability because of the mirror-like surface finish leading to a pronounced reduction in asperity interactions.¹⁴¹ Britton et al. showed a decrease in friction of approximately 30 % by superfinishing at maximum load and speed probably due to a significant reduction of asperity interactions.¹³⁸ Krantz et al. studied the influence of superfinishing on surface fatigue for case-carburized gears.¹¹⁵ They present data from NASA Glenn gear fatigue tests, which were run 300 millions of cycles. The direct comparison between ground and superfinished specimens clearly reveals that in case of superfinishing, 7 specimens out of 15 operated for 300 millions of cycles without any damage whereas for the ground samples only 3 out

20 finished the test successfully. The overall superfinishing process has been reviewed by Sroka and Winkelman.¹⁴²

Andersson et al. dedicated a lot of research work to investigate the influence of running-in on the efficiency of superfinished gears.¹⁴³ Their main finding was that superfinished gears demonstrate a higher overall gear efficiency but obviously there is a particular roughness limit up to which the efficiency can be improved. In the same context, Stanley et al. stated that if surfaces are too smooth then adhesive forces may increase and thus friction.¹⁴⁴ Additionally, Zhu and Hu developed a general model for highly concentrated contacts and according to their calculations there is an increased COF for smooth surfaces under boundary lubrication in the speed range between 10-30 mm/s.¹⁴⁵

Apart from methods to smoothen gear surfaces with the aim to increase the gear efficiency and the resistance against surface fatigue, a few attempts have been made to apply surface texturing in gear surfaces. One study dealing with texturing gears was performed by Gupta et al., who studied the tribological performance of dimpled surface textures on spur gear sets.¹¹⁴ The surface textures were produced by chemical etching with non-uniform dimple diameters (250, 400, 500 and 600 μm) and a final dimple density of around 11 %. According to the above-mentioned reasons, the authors located the respective textures on the face and flank regions of the gear teeth, as shown in Figure 12. Larger dimples were produced close to the tip point where maximum sliding occurs based upon a research work by Wang et al., who stated that larger dimple diameters lead to improved tribological properties.⁸³ A controversial aspect is that Wang et al. performed texturing on SiC thrust bearings, so that the tribological conditions may be quite different from those in gear teeth, even if we consider only the regions of the teeth where sliding prevails over rolling.

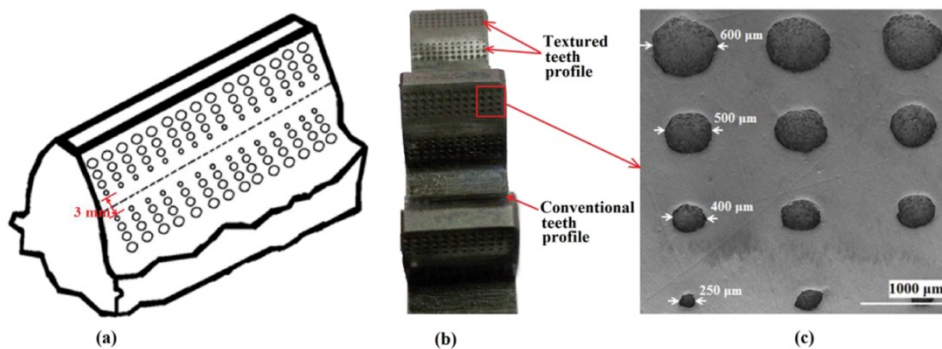


Figure 12. Textured gear teeth produced by chemical etching. Reproduced with permission.¹¹⁴ 2018, Elsevier.

Testing of the textured gears revealed two main findings.¹¹⁴ First, the textured gear sets exhibited less wear compared to the untextured samples and moreover, the textured gear contacts had only a low variation of sliding friction and thus a reduced vibration level, which is decisive for gear applications. The basic mechanisms responsible for these findings are not fully understood in their research work. It is supposed that the presence of surface textures reduces the temperature rise in the contact and moreover wear debris can be effectively trapped thus reducing abrasive contributions.

Tiwari et al. also reported on the use of dimpled textures for wind power gearboxes within a US patent application publication.¹⁴⁶ They cited in their patent texturing methods such as water-, abrasive jet machining, electrochemical methods and laser surface texturing amongst others. Dimple diameters were in the range of 50 - 150 μm with structural depths of about 5 - 10 μm. The textures were located at the face region of the gear teeth contacts, since it is away from the heavily loaded pitch area.

For particular applications such as helicopter gears with flank loads in the range of 1.5 GPa, textures could be beneficial if loss of lubrication occurs. According to EASA

(European Aviation Safety Agency) requirements, a safe operation of the helicopter must be guaranteed for at least 30 minutes after having recognized a severe oil pressure drop in the system.¹⁴⁷ In this case, surface textures could act as emergency backup to maintain functionality of the gearbox.

Summarizing remarks

The texturing strategy obviously plays a vital role for gear parts. It is of utmost importance to locate textures in regions of the gear teeth contacts, in which they can operate most efficiently. In addition to the proper design strategy, it is necessary to consider the material characteristics such as hardness and roughness. The effects of the respective texturing method on the microstructure are highly relevant as it may be detrimental concerning the previous material treatments such as case-carburizing.

On the one hand, LST using a pulse duration of nanosecond as a prominent texturing technique could produce molten bulges in gear regions thus being detrimental for the application by disturbing the lubricant film formation and also with regard to contact fatigue. On the other hand, ultra-short pulsed laser systems (femto- or picosecond systems) show significantly reduced thermal impacts with precise surface textures and thus a better control of lubricant film formation. Avoiding bulges by the application of ultra-short pulsed laser sources is furthermore of interest concerning the gear backlash between gear pairs. Finally, the complex geometries of gears require a precise laser handling system with a laser source of high stability and repeatability concerning the texturing process. The introduction of properly designed surface textures by femto- or picosecond laser must be accompanied by an ongoing development of the automation process including the experimental periphery.

The main drawback for the introduction of surface textures in gears might be due to the high contact loads. Surface textures will probably not withstand this high load scenario thus degrading quickly and therefore losing the ability to sustain a sufficient lubrication of the contact. The precise location of surface textures in less heavily loaded regions is a necessity as textures may degrade fast, losing their functionality.

4. Guidelines for surface texturing in machine elements

The successful use of surface texturing used in the main machine elements of transportation systems faces many challenges. First, the effects of surface texturing on tribological performance strongly depend on the contact conditions and lubrication regime thus making the choice of appropriate textures difficult. Second, the underlying mechanisms are not yet fully understood. Third, even in cases when the underlying mechanisms are well understood, most components do not operate under one single set of tribological conditions. Different parts of the same components may be subjected to different velocities, normal loads, slide-to-roll ratios, lubricant supply conditions, temperatures, etc., thus leading to different lubrication regimes. Therefore, different texture patterns should be applied to different parts. Fourth, the manufacturing technique should be able to texture parts of complex geometry, within the range of sizes most adequate for the lubrication regime involved. Fourth, the technique should be cheap, reproducible and with high resolution, ensuring that texturing in large-scale, industrial conditions is reliable and cost-effective.

Based upon the evidences presented in the literature, this section aims at summarizing texturing guidelines for each component (piston-ring system, seals, roller bearings and gears) in terms of the sizes and shapes of the texture features, location of the textures on

the component surface, texture distribution, and most relevant texturing techniques. However, it is of utmost importance to consider that the effects of surface texturing in real machine elements strongly depend on the operating conditions. Therefore, the points raised should be only considered as initial guidelines. As far as possible, numerical simulations using realistic conditions should help the design of textured machine elements under specific operating parameters.

4.1. Piston-ring system

In the piston-ring system, surface texturing has been carried out on the bores or liners,^{32,38,44,49-53,55-57,60,64} as well as on the rings.^{34-38,41,43,45-47,58,59,62,63} Texturing of the rings has the advantage of resulting in smaller areas to be textured. In contrast, texturing of the bores or liners should allow texturing to last much longer, since wear of the ring is significantly higher than the wear of the bores.³⁸ Another advantage for applying textures on the bores is that since the velocity varies along the stroke, the textures can be tailored according to the lubrication regime. For example, near the dead centers, where mixed or even boundary lubrication prevails, higher area densities should be used, whereas in the middle of the stroke, where a full film separates the surfaces of the rings and cylinders, lower area densities may lead to better performance.⁵⁷ When the rings are textured, partial texturing provides further beneficial effects when compared with full texturing.^{34-38,47,59} The percentage of textured area in case of partial texturing is recommended as around 50-60%.^{34,37}

In terms of texture shapes, features that are able to retain the lubricant within the contact, such as dimples,^{34-38,45,46,55,58,148} chevrons,^{40,49,50} triangles, trapezoids,⁴⁷ and interrupted grooves,^{40,41,43,44,58,59} have generally shown superior performance than long grooves.

Grooves are mostly used when the textures are applied onto the bores or liners, since they are easier to manufacture, but the orientation normally follows a cross hatched pattern to reduce lubricant leakage.^{32,40,43,51-54,56,64} Although the shape of the texture features have not shown a very strong effect on the piston-ring system's performance, small directional features such as chevrons, trapezoids and angular interrupted grooves with their apex aligned with the direction of piston movement seem more beneficial,^{40,47,49,50} apparently due to their ability to direct the flow into the high pressure regions, improving hydrodynamic effects.

Different sizes have been reported in the literature for texture features, based upon experiments and simulation. The width of the features is normally in the range between 30 and 100 μm ,^{34,37,38,41,44,49,50,61,65} although some works have reported values around 350-400 μm .^{46,47,55} Depths of the pockets are in the order of a few micrometers, with values in the literature mostly in the range between 2 to 10 μm . Most of the simulation results show that the aspect ratio between the depth and width of the features is more important than the values of width and depth themselves.^{34,37,58,59} It has been pointed out that higher aspect ratios may entrap more lubricant, leaving less oil for lubrication, thus leading to starvation.

In terms of the texture distribution, most simulations suggest the largest improvements in terms of lubrication and friction for higher area densities, so that it should be only limited by the ability of the texturing technique to produce densely packed pockets or grooves.^{34,37} However, values between 10 and 50% have been successfully used,^{40-43,65} and some simulations suggest that the effect of area density on the piston-ring system performance should be minimal.^{58,59}

Cross-hatched patterns are the easiest and cheapest to be produce and have been in use in commercial cylinders for decades. They are mostly produced by plateau honing,^{51-54,56} but also by laser honing.^{58,59,149} For the production of texture patterns, LST is today the most vastly used technique.^{35-37,40,43,55,65,148} Advances in the technique have largely reduced texturing times. In addition, the occurrence of hard rims around the pockets can be reduced drastically by using pulsed lasers with ultra-short pulse duration, such as femtosecond lasers. However, the challenge for even faster and cheaper technologies is still an issue for a broader use of surface texturing in piston rings. One alternative that seems promising is the use of electrochemical texturing, which does not produce any changes in the material around the pockets, due to its low cost and high texturing speed. For example, the use of soft photolithographic masks at low cost allows cheap and fast texturing of cylindrical surfaces.^{150,151} Another approach consists of electrochemical texturing whereby masking is carried out in the tool rather than in the workpieces, called maskless electrochemical texturing (MECT).¹⁵² This technique has been used to texture gray cast iron cylinders,¹⁵³ presenting the further advantage of exposing the graphite flakes in the matrix, thus inducing further friction reduction due a solid lubrication mechanism.¹⁵⁴

4.2. Seals

Surface texturing is carried out on the sealing face of the seal, which should be only partially textured for further improvement in terms of load capacity, friction and leakage performance.⁷⁹⁻⁸¹

Circular dimples are the most largely used for texturing seals,^{16,78,81,86,87,90,100}. Although some works suggest that the shape of the textures does not seem to have a strong influence

on the seal performance,⁹¹ both numerical simulations and experiments have pointed towards superior performance for directional textures, such as elliptical textures,^{92,93} as well as triangles pointed towards the sliding direction.^{95,101}

Different width values (diameter for circular dimples) have been successfully used in textured seals, from some tens of micrometers,^{16,77,85,90} to hundreds of micrometers,^{85,87}, or even the low millimeter range.⁸⁹ It seems that the width of the textures has only a minor effect, as long as the aspect ratio and the area density are not changed. Depth values are often in the range between 2 and 20 μm , depending on the width of the textures, to ensure aspect ratios normally in the range between 0.05 and 0.1, although some simulations have suggested optimum performance for much lower values of aspect ratios (between 0.005 and 0.015). Simulations have suggested optimum area densities of around 50 %, ⁹⁴ although most works in the literature have shown improved performance for textured seals with area densities between 10 to 20 %.^{86,87,89,90}

LST is again the technique mostly used for textured seals,^{79,80,87,89,90,155} although other techniques have also been suggested, such as reactive ion beam for ceramic materials.^{85,86}

4.3. Roller bearings

It is common sense among manufacturers that the surfaces of roller bearings should be as smooth as possible to improve their rolling contact fatigue.¹¹⁷ However, surface texturing of roller bearings has led to superior performance in terms of lubrication and RCF under specific conditions. Texturing has been mostly carried out on the rolling elements,^{120,121,123,127,129,156} but also on their counterparts,¹³⁶ in particular on the bearing washers.²¹

Small dimples, particularly with circular shapes, have been used in those trials,^{21,121,127} although short interrupted grooves have also been used.¹⁵⁶ There is some evidence in the literature that directional features, such as triangles, could lead to lower friction for the texturing of cylinders in line contacts, when compared to isotropic features, such as circular and square dimples.¹⁵⁷ However, the effects of directional texturing on roller bearings has not yet been tested under more realistic, sliding-rolling conditions.

From the lubrication point of view, the textures need to be shallow, so that positive results have been mostly observed for texture depths below 2 μm .^{21,121,127,156} In terms of width of the textures (diameter for circular dimples), the textures are also smaller when compared with those used under sliding conditions, since the contact areas in non-conformal contacts are small. From the point of view of reducing asperity contact, which can directly improve RCF, larger width and area densities are more beneficial.¹²¹ Since it is difficult to manufacture wide and shallow textures, the guideline has been to use shallow textures with intermediate width values. Most works in the literature show values of width in the range 30 - 40 μm .^{21,121,127,156} To reduce the amount of asperity contact, the strategy should be to increase the area density without compromising the load support.

The choice of texturing technology for roller bearings is a difficult task. In their pioneering work to use surface texturing in roller bearings, Akamatsu et al. used a machining process involving tumbling of barrels to remove the asperities of conventional rollers, leaving behind depressions in the surface.¹²³ Nanosecond laser ablation may be restricted to produce very shallow features and may lead to problems by creating rims around the pockets, thus strongly compromising their RCF life. In laboratory studies, slow techniques such as by producing individual indentations have been used,^{121,127,156} but they are not applicable at industrial scale. One promising technique is DLIP¹⁵⁸ since it does not involve ablation, but material is moved to create the textures as a result of the

interference of at least two laser beams. The features produced are shallow, normally in the range between 0.5 and 2 μm . Shallow textures are essential to ensure relatively thick films between the surfaces, thus not compromising the RCF life of the roller bearings.

4.4. Gears

Traditionally, the surface of gears is improved by superfinishing.^{115,138,142} The use of surface texturing in gears is still very incipient. When used, surface texturing has been applied to the face and flank regions of the gear teeth. Texturing should be avoided around the pitch point because it withstands the highest load, thus textures could wear off quickly.¹¹⁴

Since there is very little work dedicated to evaluate the tribological performance of textured gears, guidelines regarding optimized surface texturing conditions cannot be drawn yet. So far, circular dimples have been used, with diameter between 50 and 650 μm , depth between 5 and 50 μm . It might be advisable to use different texture geometries at different locations of the gear teeth, with larger diameters closer to the teeth tip. However, further numerical and experimental work are highly recommended before optimized surface textures can be identified for gears.

Another issue is the adequate choice of surface texturing technique. The use of laser texturing techniques faces the challenge of a complex geometry of the gear teeth, this requiring sophisticated positioning systems. In addition, ultra-short pulsed lasers should be used to avoid rims around the pockets that could compromise the RCF life of the gears. One potential technique is electrochemical texturing, particularly using soft

photolithographic masks.^{151,159} This should overcome the challenge of texturing complex-shape components and should also avoid the formation of hard rims around the pockets.

Conflict of Interest: The authors declare no financial/commercial conflict of interest.

Acknowledgements

A. Rosenkranz greatly acknowledges the financial support given by Conicyt (Fondecyt 11180121) as well as the continuous support of the academic direction and the Department of Chemical Engineering, Biotechnology and Materials of the University of Chile. C. Gachot would like to thank the Government of Lower Austria (WST3) for financially supporting the endowed professorship tribology at the TU Wien. H. L. Costa is grateful to CNPq/Brazil for financial support.

Received: ((will be filled in by the editorial staff))

Revised: ((will be filled in by the editorial staff))

Published online: ((will be filled in by the editorial staff))

References

- 1 IEA, *CO2 emissions from fuel combustion 2017*, OECD/IEA International Energy Agency, Paris **2017**.
- 2 J. Wang, L. Feng, X. Tang, Y. Bentley, M. Höök, *Futures* **2017**, *86*, p.58-72.
- 3 S. Shafiee, E. Topal, *Energy Policy* **2009**, *37*, p.181-189.
- 4 S. H. Mohr, J. Wang, G. Ellem, J. Ward, D. Giurco, *Fuel* **2015**, *141*, p.120-135.
- 5 R. B. Alley, J. Marotzke, W. D. Nordhaus, J. T. Overpeck, D. M. Peteet, R. A. Pielke, R. T. Pierrehumbert, P. B. Rhines, T. F. Stocker, L. D. Talley, J. M. Wallace, *Science* **2003**, *299*, p.2005-2010.
- 6 K. Holmberg, A. Erdemir, *FME Trans* **2015**, *43*, p.181-185.
- 7 IEA, *Key World Energy Statistics 2013*, OECD/IEA International Energy Agency, Paris, **2013**.
- 8 K. Holmberg, P. Andersson, N.-O. Nylund, K. Mäkelä, A. Erdemir, *Tribol Int* **2014**, *78*, p.94-114.
- 9 K. Holmberg, P. Andersson, A. Erdemir, *Tribol Int* **2012**, *47*, p.221-234.
- 10 K. Holmberg, P. Kivikytö-Reponen, P. Härkisaari, K. Valtonen, A. Erdemir, *Tribol Int* **2017**, *115*, p.116-139.
- 11 W. Dressel, *Lubricants and lubrication*, John Wiley & Sons **2007**.
- 12 H. Spikes, *Tribol Lett* **2004**, *17*, p.469-489.
- 13 J. N. Anno, J. A. Walowit, C. M. Allen, *Trans ASME, J Lubr Tech* **1969**, *91*, p.726-731.
- 14 D. B. Hamilton, J. A. Walowit, C. M. Allen, *J Basic Eng-Trans ASME* **1966** 177-185.
- 15 I. Etsion, Y. Kligerman, G. Halperin, *Tribol Trans* **1999**, *42*, p.511-516.
- 16 I. Etsion, L. Burstein, *Tribol Trans* **1996**, *39*, p.677-683.
- 17 C. Gachot, A. Rosenkranz, L. Reinert, E. Ramos-Moore, N. Souza, M. H. Müser, F. Mücklich, *Tribol Lett* **2013**, *49*, p.193-202.
- 18 A. Rosenkranz, L. Reinert, C. Gachot, F. Mücklich, *Wear* **2014**, *318*, p.49-61.
- 19 A. Erdemir, *Tribol Int* **2005**, *38*, p.249-256.
- 20 U. Pettersson, S. Jacobson, *Tribol Int* **2003**, *36*, p.857-864.
- 21 C.-J. Hsu, A. Stratmann, A. Rosenkranz, C. Gachot, *Lubricants* **2017**, *5*, p.39.
- 22 H. A. Spikes, *Lubr Sci* **1997**, *9*, p.221-253.
- 23 A. Kovalchenko, O. Ajayi, A. Erdemir, G. Fenske, I. Etsion, *Tribol Int* **2004**, *47*, p.299-307.
- 24 A. Kovalchenko, O. Ajayi, A. Erdemir, G. Fenske, I. Etsion, *Tribol Int* **2005**, *38*, p.219-225.
- 25 D. Braun, C. Greiner, J. Schneider, P. Gumbsch, *Tribol Int* **2014**, *77*, p.142-147.
- 26 A. Rosenkranz, T. Heib, C. Gachot, F. Mücklich, *Wear* **2015**, *334-335*, p.1-12.
- 27 H. L. Costa, I. M. Hutchings, *Tribol Int* **2007**, *40*, p.1227-1238.
- 28 M. Fowell, A. V. Olver, A. D. Gosman, H. A. Spikes, I. Pegg, *J Tribol* **2006**, *129*, p.336-347.
- 29 M. T. Fowell, S. Medina, A. V. Olver, H. A. Spikes, I. G. Pegg, *Tribol Int* **2012**, *52*, p.7-16.
- 30 C. Gachot, A. Rosenkranz, S. M. Hsu, H. L. Costa, *Wear* **2017**, *372-373*, p.21-41.
- 31 D. Gropper, L. Wang, T. J. Harvey, *Tribol Int* **2016**, *94*, p. 509-529.
- 32 M. Organisciak, G. Cavallaro, A. A. Lubrecht, in *Tribology and Interface Engineering Series*. Vol. 48 (Dowson D, Priest M, Dalmaz G, Lubrecht AA eds.) Elsevier **2005**. p. 573-583.
- 33 T. Tian, *Proc IMech Part J: J Eng Tribol* **2002**, *216*, p.209-228.
- 34 Y. Kligerman, I. Etsion, A. Shinkarenko, *J Tribol* **2005**, *127*, p.632-638.
- 35 G. Ryk, Y. Kligerman, I. Etsion, A. Shinkarenko, *Tribol Trans* **2005**, *48*, p.583-588.
- 36 G. Ryk, I. Etsion, *Wear* **2006**, *261*, p.792-796.
- 37 I. Etsion, E. Sher, *Tribol Int* **2009**, *42*, p.542-547.
- 38 E. Tomanik, *Tribol Int* **2013**, *59*, p.90-96.
- 39 F. J. Profito, E. Tomanik, D. C. Zachariadis, *Tribol Int* **2016**, *93*, p.723-732.
- 40 S.-C. Vladescu, A. V. Olver, I. G. Pegg, T. Reddyhoff, *Tribol Int* **2015**, *82, Part A*, p.28-42.

- 41 S.-C. Vlădescu, S. Medina, A. V. Olver, I. G. Pegg, T. Reddyhoff, *Tribol Int* **2016**, *98*, p.317-329.
- 42 S.-C. Vlădescu, A. V. Olver, I. G. Pegg, T. Reddyhoff, *Wear* **2016**, *358-359*, p.51-61.
- 43 S.-C. Vlădescu, A. Ciniero, K. Tufail, A. Gangopadhyay, T. Reddyhoff, *Tribol Int* **2017**, *115*, p.140-153.
- 44 F. J. Profito, S.-C. Vlădescu, T. Reddyhoff, D. Dini, *Tribol Int* **2017**, *113*, p.125-136.
- 45 C. Shen, M. M. Khonsari, *Tribol Int* **2016**, *101*, p.273-283.
- 46 C. Shen, M. M. Khonsari, *Tribol Lett* **2016**, *64*, p.26.
- 47 A. Akbarzadeh, M. Khonsari, *Coatings* **2018**, *8*, p.110.
- 48 N. Morris, R. Rahmani, H. Rahnejat, P. D. King, B. Fitzsimons, *Tribology International* **2013**, *59*, p.248-258.
- 49 N. Morris, M. Leighton, M. De la Cruz, R. Rahmani, H. Rahnejat, S. Howell-Smith, *Proceedings of the Institution of Mechanical Engineers, Part J: Journal of Engineering Tribology* **2015**, *229*, p.316-335.
- 50 N. Morris, R. Rahmani, H. Rahnejat, P. D. King, S. Howell-Smith, *Journal of Tribology* **2015**, *138*, p.703-711.
- 51 W. Grabon, W. Koszela, P. Pawlus, S. Ochwat, *Tribol Int* **2013**, *61*, p.102-108.
- 52 W. Grabon, P. Pawlus, S. Wos, W. Koszela, M. Wieczorowski, *Tribol Int* **2017**, *113*, p.137-148.
- 53 W. Grabon, P. Pawlus, S. Wos, W. Koszela, M. Wieczorowski, *Tribol Int* **2018**, *127*, p.545-556.
- 54 W. Grabon, P. Pawlus, S. Wos, W. Koszela, M. Wieczorowski, *Tribol Int* **2018**, *121*, p.148-160.
- 55 W. Koszela, P. Pawlus, R. Reizer, T. Liskiewicz, *Tribol Int* **2018**, *127*, p.470-477.
- 56 S. Mezghani, I. Demirci, H. Zahouani, M. El Mansori, *Precis Engr* **2012**, *36*, p.210-217.
- 57 Y. Zhou, H. Zhu, W. Tang, C. Ma, W. Zhang, *Tribol Int* **2012**, *52*, p.1-6.
- 58 A. Usman, C. W. Park, *Tribol Int* **2016**, *99*, p.224-236.
- 59 A. Usman, C. W. Park, *Tribol Int* **2017**, *105*, p.148-157.
- 60 H. M. Checo, R. F. Ausas, M. Jai, J.-P. Cadalen, F. Choukroun, G. C. Buscaglia, *Tribol Int* **2014**, *72*, p.131-142.
- 61 N. Biboulet, A. A. Lubrecht, *Tribol Int* **2016**, *96*, p.269-278.
- 62 A. Zavos, P. G. Nikolakopoulos, *Intl J Structl Integr* **2015**, *6*, p.300-324.
- 63 A. B. Zavos, P. G. Nikolakopoulos, *Lubr Sci* **2015**, *27*, p.151-176.
- 64 Y. Hu, X. Meng, Y. Xie, *Tribol Int* **2018**, *119*, p.443-463.
- 65 S.-C. Vlădescu, S. Medina, A. V. Olver, I. G. Pegg, T. J. T. L. Reddyhoff, **2016**, *62*, p.19.
- 66 A. O. Lebeck, *Principles and Design of Mechanical Face Seals*. New York, NY: John Wiley & Sons, Inc., **1991**.
- 67 I. Etsion, *Friction* **2013**, *1*, p.195-209.
- 68 A. Fogg, *Proc Inst Mech Engrs* **1946**, *155*, p.49-67.
- 69 D. F. Denny, *Wear* **1961**, *4*, p.64-83.
- 70 I. Etsion, *J Mech Eng Sci* **1980**, *22*, p.59-64.
- 71 J. G. Pape, *ASLE Trans* **1968**, *11*, p.302-309.
- 72 M. E. Salama, *Proc Inst Mech Engr* **1950**, *163*, p.149-161.
- 73 J. N. Anno, J. A. Walowit, C. M. Allen, *J Tribol* **1968**, *90*, p.351-355.
- 74 I. Etsion, G. Halperin, Y. Greenberg, Increasing Mechanical Seal Life with Laser-Textured Seal Faces. in *15th Int Conf Fluid Seal*; Maastricht. BHR Group, **1997** **1997**. p. 3-11.
- 75 Y. Kligerman, I. Etsion, *Tribol Int* **2001**, *44*, p.472-478.
- 76 A. D. McNickle, I. Etsion, *J Tribol* **2004**, *126*, p.788-788.
- 77 I. Etsion, G. Halperin, *Tribol Trans* **2002**, *45*, p.430-434.
- 78 I. Etsion, *Tribol Lett* **2004**, *17*, p.733-737.
- 79 Y. Feldman, Y. Kligerman, I. Etsion, *Tribol Lett* **2006**, *22*, p.21-28.
- 80 Y. Feldman, Y. Kligerman, I. Etsion, *J Tribol* **2007**, *129*, p.407-407.

- 81 I. Etsion, *Improving tribological performance of mechanical seals by laser surface texturing* **2000**, p. 17-21.
- 82 M. Geiger, S. Roth, W. Becker, *Surf Coat Tech* **1998**, 100-101, p.17-22.
- 83 X. Wang, K. Kato, K. Adachi, K. Aizawa, *Tribol Int* **2003**, 36, p.189-197.
- 84 X. Wang, K. Kato, K. Adachi, K. Aizawa, *Tribol Int* **2001**, 34, p.703-711.
- 85 X. Wang, K. Kato, *Tribol Lett* **2003**, 14, p.275-280.
- 86 X. Wang, K. Kato, K. Adachi, *Tribol Trans* **2002**, 45, p.294-301.
- 87 Y. Wan, D. S. Xiong, *J Mat ProcTech* **2008**, 197, p.96-100.
- 88 C. Y. Chen, C. J. Chung, B. H. Wu, W. L. Li, C. W. Chien, P. H. Wu, C. W. Cheng, *Appl Phys A: Mater Sci Proc* **2012**, 107, p.345-350.
- 89 T. Wang, W. Huang, X. Liu, Y. Li, Y. Wang, *Tribol Int* **2014**, 72, p.90-97.
- 90 X. Q. Yu, S. He, R. L. Cai, *J Mat ProcTech* **2002**, 129, p.463-466.
- 91 R. B. Siripuram, L. S. Stephens, *J Tribol* **2004**, 126, p.527-527.
- 92 L. Shi, X. Wang, X. Su, W. Huang, X. Wang, *J Tribol* **2015**, 138, p.021701-021701.
- 93 Y. Qiu, M. M. Khonsari, *Tribol Int* **2011**, 44, p.635-644.
- 94 Y. Qiu, M. M. Khonsari, *J Tribol* **2011**, 133, p.021704-021704.
- 95 Y. Xie, Y. J. Li, Y. M. Wang, S. F. Suo, X. F. Liu, *Sci China: Phys Mech & Astron* **2014**, 57, p.273-279.
- 96 X. Meng, S. Bai, X. Peng, *Tribol Int* **2014**, 77, p.132-141.
- 97 S. Bai, X. Peng, Y. Li, S. Sheng, *Tribol Lett* **2010**, 38, p.187-194.
- 98 L. Bai, S. Bai, *Tribol Trans* **2014**, 57, p.1122-1128.
- 99 C. Shen, M. M. Khonsari, *Tribol Trans* **2016**, 59, p.698-706.
- 100 X. Wang, L. Shi, Q. Dai, W. Huang, X. Wang, *Tribol Int* **2018**, 123, p.216-223.
- 101 N. Brunetière, B. Tournier, *Tribol Int* **2012**, 49, p.80-89.
- 102 M. Adjemout, N. Brunetiere, J. Bouyer, *Surf Topogr: Metr Prop* **2016**, 4, p.14002-14002.
- 103 M. Adjemout, N. Brunetière, J. Bouyer, *Trib Trans* **2018**, 2004, p.1-44.
- 104 M. Adjemout, A. Andrieux, J. Bouyer, N. Brunetière, G. Marcos, T. Czerwiec, *Tribol Int* **2017**, 115, p.409-416.
- 105 Y. Qiu, M. M. Khonsari, *J Tribol* **2009**, 131, p.041702-041702.
- 106 C. Minet, N. I. Brunetière, B. Tournier, *J Tribol* **2011**, 133, p.042203-042203.
- 107 K. L. Johnson, *Contact Mechanics*. Cambridge: Cambridge University Press, **1985**.
- 108 H. L. Costa, I. M. Hutchings, *Proc IMech Part J: J Eng Tribol* **2015**, 229, p.429-448.
- 109 I. Krupka, M. Hartl, P. Svoboda, *Proc IMech Part J: J Eng Tribol* **2010**, 224, p.713-722.
- 110 B. T. Hamrock, D. Dowson, *Ball bearing lubrication: The elastohydrodynamics of elliptical Contacts*. New York: Wiley, **1981**.
- 111 L. Mourier, D. Mazuyer, F. P. Ninove, A. A. Lubrecht, *P I Mech Eng J-J Eng* **2010**, 224, p.697-711.
- 112 A. V. Olver, *Proc IMech Part J: J Eng Tribol* **2005**, 219, p.313-330.
- 113 X. Ai, *J Tribol* **1998**, 120, p.159-164.
- 114 N. Gupta, N. Tandon, R. K. Pandey, *Tribol Int* **2018**, 128, p.376-385.
- 115 T. L. Krantz, M. P. Alanou, H. P. Evans, R. W. Snidle, *J Tribol* **2001**, 123, p.709-716.
- 116 N. Deolalikar, F. Sadeghi, *Tribol Lett* **2007**, 27, p.197-209.
- 117 D. Epstein, L. M. Keer, Q. J. Wang, H. S. Cheng, D. Zhu, *Tribol Trans* **2003**, 46, p.506-513.
- 118 Z. Zhang, J. Cui, J. Zhang, D. Liu, Z. Yu, D. Guo, *Appl Surf Sci* **2019**, 467, p.5-11.
- 119 Z. Zhang, Z. Shi, Y. Du, Z. Yu, L. Guo, D. Guo, *Appl Surf Sci* **2018**, 427, p.409-415.
- 120 B. Karpuschewski, Ouml, C. bberthin, K. Risse, L. Deters, C. Döbberthin, **2017**.
- 121 M. Vrbka, O. Šamánek, P. Šperka, T. Návrat, I. Krupka, M. Hartl, *Tribol Int* **2010**, 43, p.1457-1465.
- 122 W. Napadłek, *Analysis of Selected Properties 100CrMnSi6-4 Surface Layer after Laser Micro-Smelting* **2017**, p. 757.
- 123 Y. Akamatsu, N. Tsushima, T. Goto, K. Hibi, *Trib Trans* **1992**, 35, p.745-750.
- 124 X. Zhai, L. Chang, M. R. Hoeprich, H. P. Nixon, *Tribol Trans* **1997**, 40, p.708-714.

- 125 T. E. Tallian, *J Lubr Tech* **1976**, *98*, p.384-392.
- 126 T. A. Harris, *Rolling bearing analyses*, 3rd ed. New York: Wiley, **1991**.
- 127 M. Vrbka, I. Křupka, O. Šamánek, P. Svoboda, M. Vaverka, M. Hartl, *Meccanica* **2011**, *46*, p.491-498.
- 128 X. Shi, L. Wang, F. Qin, *Tribol Int* **2016**, *101*, p.364-374.
- 129 M. Kaneta, H. Nishikawa, *Proc IMech Part J: J Eng Tribol* **1999**, *213*, p.371-381.
- 130 J. W. Choo, R. P. Glovnea, A. V. Olver, H. A. Spikes, *J Tribol* **2003**, *125*, p.533-542.
- 131 A. V. Olver, G. Guangteng, H. A. Spikes, in *Thinning Films and Tribological Interfaces*, (Dowson Dea ed.) Elsevier **2000**. p. 503-510.
- 132 C. H. Venner, A. A. Lubrecht, *J Tribol* **1994**, *116*, p.751-761.
- 133 R. R. Raghavendra, S. K. Raja, *Indl Lubrn & Tribol* **2007**, *59*, p.285-296.
- 134 L. M. Gao, G. de Boer, R. Hewson, *Tribol Int* **2015**, *90*, p.324-331.
- 135 I. Krupka, M. Hartl, M. Zimmerman, P. Houska, S. Jang, *Tribol Int* **2011**, *44*, p.1144-1150.
- 136 P. Lu, R. Wood, M. Gee, L. Wang, W. Pflöging, *Lubricants* **2016**, *4*, p.26.
- 137 H. J. Stadtfeld, *Gear Tech* **2015**, *June*, p.40-46.
- 138 R. D. Britton, C. D. Elcoate, M. P. Alanou, H. P. Evans, R. W. Snidle, *J Tribol* **1999**, *122*, p.354-360.
- 139 J. Zhang, W. Li, H. Wang, Q. Song, L. Lu, W. Wang, Z. Liu, *Wear* **2016**, *368-369*, p.253-257.
- 140 T. Nakatsuji, A. Mori, *Tribol Int* **1999**, *42*, p.393-400.
- 141 S. Tanaka, A. Ishibashi, S. Ezo, *ASME Publication* **1984**.
- 142 G. J. Sroka, L. Winkelmann, *Gear Tech* **2003**, *20*, p.28-33.
- 143 M. Andersson, M. Sosa, U. Olofsson, *Tribol Int* **2016**, *93*, p.71-77.
- 144 H. M. Stanley, I. Etsion, D. B. Bogy, *J Tribol* **1990**, *112*, p.98-104.
- 145 D. Zhu, Y.-Z. Hu, *Tribol Trans* **2001**, *44*, p.383-390.
- 146 M. Tiwari, P. R. Joshi, N. S. Tambe, M. R. Sridhar, H. Vadari, H. U. S. Gowda, *USA* **2009**.
- 147 G. Gasparini, N. Motta, A. Gabrielli, D. Colombo, *Gearbox Loss of Lubrication Performance: Myth, Art or Science?* **2014**. p. 2-5.
- 148 G. Ryk, Y. Kligerman, I. Etsion, *Tribol Trans* **2002**, *45*, p.444-449.
- 149 Y. H. Fu, Y. X. Ye, Y. K. Zhang, L. Cai, *Key Engineering Materials* **2001**, *202-203*, p.265-270.
- 150 X. Wang, S. M. Hsu, An integrated surface technology for friction control: a new paradigm: effects of geometric shapes on friction. in *4th China International Symposium on Tribology*; China, **2004 Nov 8-11**. p. 12-16.
- 151 S. M. Hsu, Y. Jing, Y. Mo, D. Hua, M. Chan, *Friction reduction for engine components* **2012**.
- 152 H. L. Costa, I. M. Hutchings, *J Mater ProcessTech* **2009**, *209*, p.3869-3878.
- 153 L. da Silva, H. Costa, *Mater Perf Charact* **2017**, *6*, p.96-111.
- 154 L. R. R. da Silva, H. L. Costa, *Wear* **2017**, *under review*, p.
- 155 I. Etsion, *J Tribol* **2005**, *127*, p.248-253.
- 156 F. Ali, I. Křupka, M. Hartl, *Proc Inst Mech Eng, Part J: J Eng Tribol* **2015**, *229*, p.420-428.
- 157 P. Lu, R. J. K. Wood, M. G. Gee, L. Wang, W. Pflöging, *Tribol Int* **2017**, *113*, p.169-181.
- 158 A. F. Lasagni, T. Roch, J. Berger, T. Kunze, V. Lang, E. Beyer, To use or not to use (direct laser interference patterning), that is the question. in *SPIE LASE International Society for Optics and Photonics*, **2015**. p. 9351151-9351157.
- 159 S. M. Hsu, J. Yang, H. Diann, Z. Huan, *J Phys D: Appl Phys* **2014**, *47*, p.335307.



Andreas Rosenkranz is currently professor for material-oriented tribology at the University of Chile, Chile. He obtained his Diploma (2010) and PhD (2015) degrees in Materials Science and Engineering from the Saarland University, Germany. His main research focus lays on the possibility to reduce friction and wear by either surface functionalization or the use of nanoparticles. He has authored more than 60 peer-reviewed journal publications. He is an Alexander von Humboldt Research Fellow and editor for the peer-reviewed journal “Industrial Lubrication and Tribology” of the Emerald Publishing Group Leeds UK.



Philipp Grützmacher received his Bachelor degree in Materials Engineering from the Nuremberg Institute of Technology Georg Simon Ohm, Germany, in 2012 and his Master degree in Advanced Materials Science and Engineering from the Saarland University and

the Polytechnic University of Catalonia in 2014. Since 2015, he pursues his PhD studies at the Chair of Functional Materials under the guidance of Prof. Dr. Frank Mücklich (Saarland University). His current research interests focus on tribology, laser surface texturing, and surface engineering.



Carsten Gachot received his PhD from the Saarland University in Germany in 2012 where he studied the effects of laser interference patterning on the microstructure and topography of metallic surfaces with a focus on tribological applications. He was then academic visitor at the tribology Group at the Imperial College London and is currently the head of the tribology research Group at the Vienna University of Technology. Additionally, he is chief editor of the peer reviewed journal "Industrial Lubrication and Tribology" of the Emerald Publishing Group Leeds UK.



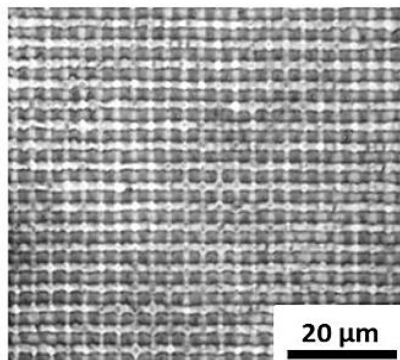
Henara Costa is currently professor at the Federal University of Rio Grande, Brazil. She obtained her B.S. (1992) and M.Sc. (1995) degrees in Mechanical Engineering from Federal University of Uberlândia, Brazil and her PhD from Cambridge University, UK (2005). She has worked with tribology for over 20 years, with a main focus on reducing friction losses by either surface modification or lubrication. She has authored over 130 manuscripts in journals, book chapters and conference proceedings. She is a member of IFToMM and of the editorial boards of a few tribology-related journals. She is also the Brazilian representative at IEA/AMT.

Surface texturing has gained great attention in the tribological community since precisely defined surface features can help to reduce friction and/or wear irrespective of the acting lubrication regime. This review aims at summarizing the latest developments in the field of surface texturing applied to machine components with a special emphasis on piston rings, seals, roller bearings and gears.

Surface texturing

Andreas Rosenkranz*, Philipp G. Grützmacher, Carsten Gachot, Henara L. Costa

Surface texturing in machine elements - a critical discussion for rolling and sliding contacts



5. CONCLUSIONS AND OUTLOOK

The present dissertation aims at improving the tribological behavior of steel surfaces by applying bio-inspired multi-scale surface patterns inside and outside of the contact zone. Additionally, suitable patterns are to be transferred to the application, in the of journal bearings' shafts. For the generation of multi-scale patterns, larger micro-coined patterns are combined with smaller laser patterns. Typical spatial dimensions of the laser patterns comprise periodicities below 50 μm and depths below 5 μm , whereas micro-coining particularly creates patterns with periodicities and depths greater than 500 and 15 μm , respectively. With respect to laser patterning, especially DLIP effectively and precisely creates even smaller patterns (periodicity $< 20 \mu\text{m}$ and depth $< 2 \mu\text{m}$). Hence, the combination of both techniques is suitable to create multi-scale patterns. Especially smaller patterns comprising features smaller than the Hertzian contact width can induce hydrodynamic pressure, whereas larger patterns are particularly effective in entrapping wear particles and creating lubricant reservoirs, thus enhancing the secondary lubrication effect. In this context, multi-scale patterns, applied inside the contact zone, are an interesting approach to improve the tribological behavior of surfaces. Furthermore, multi-scale patterns, applied outside the contact zone, are investigated with the aim of preventing lubricant migration out of the tribological contact or guiding lubricant over the surface. Thus, surface patterns outside the contact area can further improve the tribological behavior by helping to prevent starved lubrication, which leads to significantly increased friction and/or wear.

First of all, reasons for lubricant migration out of the contact zone as well as means to improve lubricant migration by hindering lubricant movement or guiding lubricants over the surface are investigated (**Objective 1**). Secondly, the efficiency and the underlying mechanisms of multi-scale patterns, applied inside the contact zone, are demonstrated in preliminary ball-on-disk laboratory experiments (**Objective 2**). Finally, suitable single-scale and multi-scale surface patterns are selected, transferred onto the curved shafts of journal bearings, and compared with respect to their tribological behavior. In this context, especially the comparability between preliminary laboratory experiments and the patterns' efficiency in a real machine element is of interest (**Objective 3**).

OBJECTIVE 1

Lubricant migration out of the contact zone can be caused by centrifugal forces or temperature gradients. It is found that higher centrifugal forces cause a faster lubricant migration out of the contact, thus decreasing the lifetime of the measured samples. By means of measurements of the solid-solid contact ratio, a transition from mixed to boundary lubrication resulting from lubricant migration is verified, which leads to significantly increased friction and severe wear. This transition is faster for greater centrifugal forces and smaller lubricant viscosities. Hence, the potentially catastrophic consequences of lubricant migration out of the contact zone are demonstrated.

Regarding thermocapillary migration, it is shown that surface patterns oriented perpendicular to the temperature gradient and thus, to the preferential direction of lubricant migration, can effectively hinder the lubricant movement towards colder regions. In this regard, deeper patterns are more effective in pinning the droplet's contact line and thus hinder lubricant migration. It is shown that patterns fabricated by micro-coining can completely prevent thermocapillary lubricant migration, representing a viable method to reduce lubrication migration by applying patterns outside the contact zone. Additionally, channel-like single-scale laser and micro-coined patterns, as well as multi-scale patterns fabricated by a combination of both techniques, are investigated in terms of their ability to guide lubricants over the surface. All patterned surfaces inhibit an anisotropic lubricant spreading behavior with a preferential lubricant spreading parallel to the channel-like patterns, which can be attributed to pinning effects perpendicular to the patterns and capillary forces parallel to the patterns. Besides, the effect of structural parameters is demonstrated, whereby stronger anisotropic spreading is observed with greater structural depths and smaller periodicities. As the multi-scale samples exhibit greater capillary forces and a stronger tendency for spreading induced by a greater roughness, these samples show the strongest anisotropic spreading behavior. In this context, artificially fabricated multi-scale samples are investigated for the first time regarding their influence on lubricant spreading. In case of parallel orientation of the patterns with respect to an applied temperature gradient all patterns again show a faster migration velocity than a polished reference sample. Similar to the experiments without temperature gradient, the multi-scale samples show the fastest migration velocity. Hence, these results demonstrate the possibility to improve lubricant migration by guiding lubricants over the surface. Summarizing, lubricant migration out of the tribological contact zone, which leads to significantly increased friction and severe wear, can be prevented by applying tailored patterns outside the tribological contact. This approach has the additional advantage that the patterns do not wear off with time, which means that they can outlive the component and prolong the lifetime of patterns applied inside the tribologically loaded contact zone. Finally, patterns applied outside the contact zone can contribute to improved friction and wear behavior, thus increasing the lifetime of the element.

OBJECTIVE 2

Multi-scale patterns inspired by nature are accurately fabricated on steel by a combination of micro-coining and DLIP. In this context, the cross-like laser pattern is homogeneously distributed on the primary micro-coined pattern consisting of hemispherical dimples. As shown by ball-on-disk experiments the multi-scale patterns improve the frictional behavior and show smaller COFs compared to the polished reference and the purely laser-patterned sample. However, compared to the purely micro-coined pattern the multi-scale patterning approach can either show detrimental or beneficial effects depending on the depth of the micro-coined pattern with which the laser pattern is combined. For shallow micro-coined patterns, the additional laser pattern increases the COF due to its spikier topography, resulting in higher contact stresses and reduced load-carrying capacity. On the contrary, for

deeper micro-coined patterns combined with the additional laser pattern synergetic effects are observed. This pattern improves the frictional behavior leading to smaller COFs, which can be traced back to a better distribution of lubricant in the contact zone, reduced cavitation effects and thus possibly higher hydrodynamic pressures. Hence, multi-scale patterns applied inside the contact zone can, if appropriately designed, contribute to an enhanced frictional behavior with reduced COFs.

OBJECTIVE 3

Effective single- and multi-scale surface patterns, which have been selected in the preliminary laboratory experiments, are transferred successfully to the shafts of journal bearings. Despite the shaft's curved surface, all patterns are accurately fabricated showing good comparability between the laboratory samples and the shafts. The tribological experiments demonstrate a greatly improved frictional behavior with significantly reduced COFs and a transition from mixed to hydrodynamic lubrication at smaller rotational speeds for all patterned shafts compared to the polished reference shaft. Following the preliminary laboratory experiments, the maximum friction reduction in mixed and hydrodynamic lubrication accounts for 2 - 3 and 4.6, respectively. The positive effects of the patterns can be traced back to an additional hydrodynamic pressure as well as the possibility to create lubricant reservoirs and trap wear particles. The maximum friction reduction of 4.6 is observed for the shaft with the multi-scale pattern comprised of deeper micro-coined hemispherical dimples and an additional cross-like laser pattern. This again reflects the synergetic effects of the multi-scale patterning approach as well as the excellent comparability between preliminary laboratory experiments and the tested journal bearings. In summary, the unique possibility to transfer results from the laboratory into the application, in the form of a journal bearing, is demonstrated. Furthermore, multi-scale patterns inspired by natural occurring surfaces offer great potential to contribute to improved frictional behavior.

ONGOING WORK

As shown in the results, patterns applied outside the contact zone offer the potential to improve lubricant migration by preventing the migration out of the contact zone or by guiding lubricant over the surface. It is subject of ongoing research to apply single- and multi-scale surface patterns to machine elements, such as thrust bearings, to prevent lubricant migration out of the contact thus improving the elements' lifetime. Apart from that, surface patterns outside the tribological contact zone are considered to be beneficial to reduce side leakage of lubricants in journal bearings or mechanical seals.

Another promising approach to maximize the positive effects regarding a tribological improvement is to combine surface patterns applied inside and outside the contact zone. Synergetic effects are to be expected by combining these approaches, thus "directly" and "indirectly" reducing friction and wear. Furthermore, by reducing lubricant migration and retaining the lubricant inside the contact zone, the patterns applied inside the contact zone will exhibit less wear and thus have a longer lifetime.

OUTLOOK

The results of the present dissertation provide fundamental insights into the underlying mechanisms of surface patterns inside and outside the tribological contact zone regarding the improvement of the tribological behavior and lubricant migration. However, to obtain a comprehensive and holistic understanding of the process of friction reduction, supporting simulations are necessary. In this context, the first steps have already been realized within the framework of this thesis by comparing the tribological effects of purely micro-coined dimples under lubricated conditions in ball-on-disk experiments and accompanying simulations [222]. In both, experiments and simulations, the frictional performance could be improved by applying hemispherical micro-coined dimples. It could be shown that the relative position between counter-body and dimple is of great importance, whereby the greatest friction reduction was achieved when the dimple is crossed centrally by the ball. The significant friction reduction by applying micro-coined dimples inside the contact area as well as the excellent comparability between simulations and experiment is shown in **Fig. 20**. Regarding an optimization of the dimples' structural parameters, it was demonstrated that shallow dimples with diameters in the order of the elastically deformed contact zone provide the greatest friction reduction due to the build-up of additional hydrodynamic pressure and an increase in lubricant film thickness.

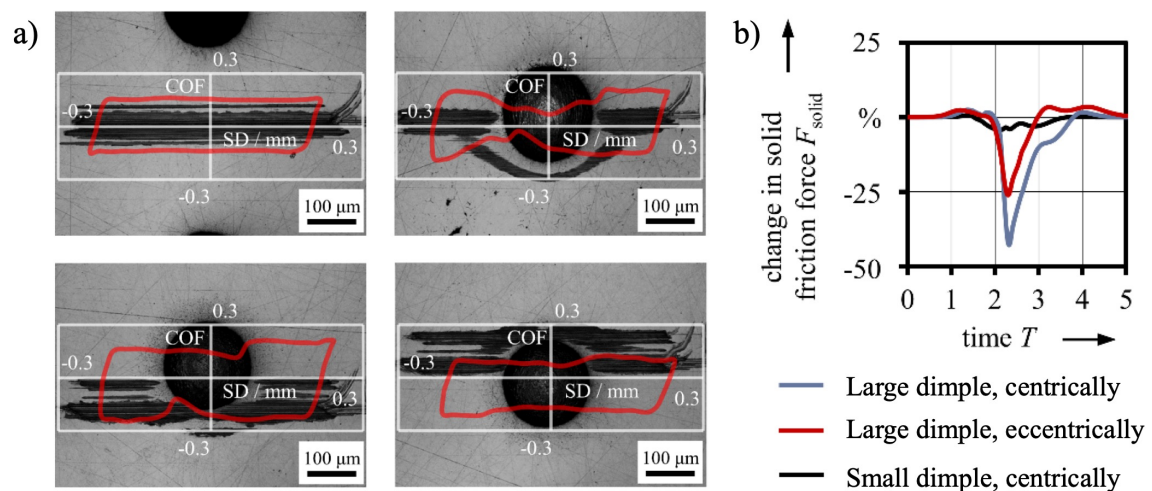


Figure 20: Comparison of the frictional behavior of micro-coined dimples in experiments and simulations. The experiments show a significant friction reduction upon encounter with the micro-coined dimple compared to the reference surface, which is the greatest when the dimple is crossed centrally (a). Likewise, the simulations demonstrate a dependence of the relative position between dimple and counter body with a greater friction reduction for a central alignment (b). Modified from [222].

Simulating the frictional performance of patterns inside the contact zone can be an effective and time-efficient approach to identify optimum structural parameters and pattern geometries. This is especially true when considering patterns in machine elements since these experiments are complicated, time-consuming, and costly. Nevertheless, simulations have to be carefully verified by experiments since simulations can only deliver results that are predetermined by the assumptions on which the

simulation is based. Furthermore, simulations of multi-scale patterns are highly sophisticated. Simulations that capture multiple scales are either very time consuming or not very precise because a small mesh size has to be chosen to capture the effects induced on the smaller scale, which is intensive to compute. Hence, further research must be dedicated to this issue.

Finally, as demonstrated in the final paper of the present dissertation the tribological performance of numerous machine elements can be improved by applying surface patterns. A future challenge will be to integrate patterning tools into existing product lines to apply surface patterns to machine elements. Especially for multi-scale patterns, this is a challenging task. One possible approach to create multi-scale patterns inline is based upon laser processing, which is versatile regarding the substrate materials and possible pattern geometries. Thus, large surface features could be generated by DLW, while smaller features are superimposed in a second step by DLIP.

6. NOT INCLUDED PAPERS

Within the framework of the present dissertation, further research has been conducted which was also published in internationally recognized, peer-reviewed journals. However, since these results contribute only to a minor extent to clarifying the objectives of the dissertation mentioned above, these papers were not included. Nonetheless, they shall be mentioned in the following:

- [1] A. Rosenkranz, **P.G. Grützmacher**, A. Szurdak, C. Gachot, G. Hirt, F. Mücklich, F. Muecklich, Synergetic effect of laser patterning and micro coining for controlled lubricant propagation, *Surf. Topogr. Metrol. Prop.* 4, **2016**, doi:10.1088/2051-672X/4/3/034008.
- [2] C. Gachot, C. Hsu, S. Suárez, **P.G. Grützmacher**, A. Rosenkranz, A. Stratmann, G. Jacobs, Microstructural and Chemical Characterization of the Tribolayer Formation in Highly Loaded Cylindrical Roller Thrust Bearings, *Lubricants.* 4, **2016**, doi:10.3390/lubricants4020019.
- [3] S. Bettscheider, **P.G. Grützmacher**, A. Rosenkranz, Low Friction and High Solid-Solid Contact Ratio — A Contradiction for Laser-Patterned Surfaces?, *Lubricants.* 5, **2017**, doi:10.3390/lubricants5030035.
- [4] L. Reinert, F. Lasserre, C. Gachot, **P.G. Grützmacher**, T. Maclucas, N. Souza, F. Mücklich, S. Suarez, Long-lasting solid lubrication by CNT-coated patterned surfaces, *Sci. Rep.* 7, **2017**, doi:10.1038/srep42873.
- [5] C. Schäfer, L. Reinert, T. MacLucas, **P.G. Grützmacher**, R. Merz, F. Mücklich, S. Suarez, Influence of Surface Design on the Solid Lubricity of Carbon Nanotubes-Coated Steel Surfaces, *Tribol. Lett.* 66, **2018**, doi:10.1007/s11249-018-1044-8.
- [6] A. Rosenkranz, A. Szurdak, **P.G. Grützmacher**, G. Hirt, F. Mücklich, Friction Reduction Induced by Elliptical Surface Patterns under Lubricated Conditions, *Adv. Eng. Mater.* 20, **2018**, doi:10.1002/adem.201700731.
- [7] C. Gachot, **P.G. Grützmacher**, A. Rosenkranz, Laser Surface Texturing of TiAl Multilayer Films—Effects of Microstructure and Topography on Friction and Wear, *Lubricants.* 6, **2018**, doi:10.3390/lubricants6020036.
- [8] H. Kasem, O. Stav, **P.G. Grützmacher**, C. Gachot, Effect of Low Depth Surface Texturing on Friction Reduction in Lubricated Sliding Contact, *Lubricants.* 6, **2018**, doi:10.3390/lubricants6030062.

- [9] **P.G. Grützmacher**, S. Rammacher, D. Rathmann, C. Motz, F. Mücklich, S. Suarez, Interplay between microstructural evolution and tribo-chemistry during dry sliding of metals, *Friction.*, **2019**, doi:10.1007/s40544-019-0259-5.
- [10] M. Marian, **P.G. Grützmacher**, A. Rosenkranz, S. Tremmel, F. Mücklich, S. Wartzack, Designing Surface Textures for EHL Point-Contacts - Transient 3D Simulations, Meta-Modeling and Experimental Validation, *Tribol. Int.*, **2019**, accepted.
- [11] **P.G. Grützmacher**, A. Rosenkranz, A. Szurdak, M. Grüber, C. Gachot, G. Hirt, F. Mücklich, Multi-scale surface patterning – An approach to control friction and lubricant migration in lubricated systems, *Ind. Lubr. Tribol.*, **2019**, accepted.
- [12] A. Rosenkranz, **P.G. Grützmacher**, K. Murzyn, C. Mathieu, F. Mücklich, Multi-scale surface patterning – an approach to tune friction under mixed lubricated conditions, *Appl. Nanosci.*, **2019**, submitted.
- [13] A. Rosenkranz, **P.G. Grützmacher**, R. Espinoza, V.M. Fuenzalida, E. Blanco, N. Escalona, F.J. Gracia, R. Villarroel, L. Guo, R. Kang, F. Mücklich, S. Suarez, Z. Zhang, 2D Carbides (MXENES) as Solid Lubricants - Role of Surface Terminations and Intercalated Water, *Appl. Surf. Sci.*, **2019**, submitted.

REFERENCES

- [1] R. Tyagi, J. P. Davim, Eds. , *Processing Techniques and Tribological Behavior of Composite Materials*, IGI Global, **2015**.
- [2] A. C. Dunn, J. A. Tichy, J. M. Uruenã, W. G. Sawyer, *Tribol. Int.* **2013**, *63*, 45.
- [3] F. Di Puccio, *World J. Orthop.* **2015**, *6*, 77.
- [4] B. Bhushan, *Principles and Applications of Tribology*, John Wiley & Sons, Ltd, The Atrium, Southern Gate, Chichester, West Sussex, PO19 8SQ, UK, **2013**.
- [5] K. Holmberg, A. Erdemir, *Friction* **2017**, *5*, 263.
- [6] K. Holmberg, P. Andersson, A. Erdemir, *Tribol. Int.* **2012**, *47*, 221.
- [7] International Energy Agency, *CO2 Emissions from Fuel Combustion 2017 - Highlights*, IEA, **2017**.
- [8] M. Nosonovsky, B. Bhushan, Eds. , *Green Tribology*, Springer Berlin Heidelberg, Berlin, Heidelberg, **2012**.
- [9] D. Pirro, M. Webster, E. Daschner, *Lubrication Fundamentals, Revised and Expanded*, CRC Press, Boca Raton, FL, USA, **2016**.
- [10] C. Gachot, A. Rosenkranz, S. M. Hsu, H. L. Costa, *Wear* **2017**, *372–373*, 21.
- [11] D. B. Hamilton, J. A. Walowit, C. M. Allen, *J. Basic Eng.* **1966**, *88*, 177.
- [12] M. Priest, C. M. Taylor, *Wear* **2000**, *241*, 193.
- [13] L. Mourier, D. Mazuyer, F. P. Ninove, A. A. Lubrecht, *Proc. Inst. Mech. Eng. Part J J. Eng. Tribol.* **2010**, *224*, 697.
- [14] A. Arslan, H. H. Masjuki, M. A. Kalam, M. Varman, R. A. Mufti, M. H. Mosarof, L. S. Khuong, M. M. Quazi, *Crit. Rev. Solid State Mater. Sci.* **2016**, *41*, 447.
- [15] X. Ai, *J. Tribol.* **1998**, *120*, 159.
- [16] U. Pettersson, S. Jacobson, *Tribol. Lett.* **2004**, *17*, 553.
- [17] J. J. Zhang, J. G. Zhang, A. Rosenkranz, X. L. Zhao, Y. L. Song, *Adv. Eng. Mater.* **2018**, *1700995*, 1.
- [18] A. Szurdak, A. Rosenkranz, C. Gachot, G. Hirt, F. Mücklich, *Key Eng. Mater.* **2014**, *611–612*, 417.
- [19] A. Rosenkranz, A. Szurdak, C. Gachot, G. Hirt, F. Mücklich, *Tribol. Int.* **2016**, *95*, 290.
- [20] I. Etsion, *J. Tribol.* **2005**, *127*, 248.
- [21] A. Rosenkranz, T. Heib, C. Gachot, F. Mücklich, *Wear* **2015**, *334–335*, 1.
- [22] D. Gropper, L. Wang, T. J. Harvey, *Tribol. Int.* **2016**, *94*, 509.
- [23] F. P. Bowden, D. Tabor, *Proc. R. Soc. A Math. Phys. Eng. Sci.* **1939**, *169*, 391.
- [24] X. Wang, K. Kato, K. Adachi, K. Aizawa, *Tribol. Int.* **2003**, *36*, 189.
- [25] X. Wang, K. Kato, K. Adachi, *Tribol. Trans.* **2002**, *45*, 294.
- [26] S. Cupillard, M. J. Cervantes, S. Glavatskih, *J. Tribol.* **2008**, *130*, 021701.

- [27] L. Reinert, F. Lasserre, C. Gachot, P. G. Grützmacher, T. Maclucas, N. Souza, F. Mücklich, S. Suarez, *Sci. Rep.* **2017**, *7*, 42873.
- [28] M. Amiri, M. M. Khonsari, *Entropy* **2010**, *12*, 1021.
- [29] M. F. Ashby, J. Abulawi, H. S. Kong, *Tribol. Trans.* **1991**, *34*, 577.
- [30] G. Karapetsas, K. C. Sahu, K. Sefiane, O. K. Matar, *Langmuir* **2014**, *30*, 4310.
- [31] H. B. Nguyen, J. C. Chen, *Phys. Fluids* **2010**, *22*, 1.
- [32] Q. Dai, W. Huang, X. Wang, *Exp. Therm. Fluid Sci.* **2014**, *57*, 200.
- [33] Q. Dai, W. Huang, X. Wang, *Langmuir* **2015**, *31*, 10154.
- [34] Q. Dai, M. Li, M. M. Khonsari, W. Huang, X. Wang, *Lubr. Sci.* **2018**, 1.
- [35] Q. Dai, W. Huang, X. Wang, *Meccanica* **2017**, *52*, 171.
- [36] A. A. Fote, R. A. Slade, S. Feuerstein, *J. Lubr. Technol.* **1977**, *99*, 158.
- [37] F. Brochard, *Langmuir* **1989**, *5*, 432.
- [38] P. M. Dickens, J. L. Sullivan, J. K. Lancaster, *Wear* **1986**, *112*, 273.
- [39] A. A. A. Fote, R. A. A. Slade, S. Feuerstein, *Wear* **1978**, *51*, 67.
- [40] Z. Rymuza, in *Encycl. Tribol.*, Springer US, Boston, MA, **2013**, pp. 2101–2110.
- [41] M. Nosonovsky, B. Bhushan, *Mater. Sci. Eng. R Reports* **2007**, *58*, 162.
- [42] B. Bhushan, Y. C. Jung, *Prog. Mater. Sci.* **2011**, *56*, 1.
- [43] J. Oeffner, G. V. Lauder, *J. Exp. Biol.* **2012**, *215*, 785.
- [44] X. Pu, G. Li, H. Huang, *Biol. Open* **2016**, *5*, 389.
- [45] C. Greiner, M. Schäfer, *Bioinspiration and Biomimetics* **2015**, *10*, 44001.
- [46] M. J. Baum, L. Heepe, S. N. Gorb, *Beilstein J. Nanotechnol.* **2014**, *5*, 83.
- [47] P. Cuervo, D. A. López, J. P. Cano, J. C. Sánchez, S. Rudas, H. Estupiñán, A. Toro, H. A. Abdel-Aal, *Surf. Topogr. Metrol. Prop.* **2016**, *4*, 1.
- [48] J. Resendiz, P. Egberts, S. S. Park, *Tribol. Lett.* **2018**, *66*, 132.
- [49] D. Z. Segu, S. S. Kim, *Meccanica* **2014**, *49*, 483.
- [50] M. Shafiei, A. T. Alpas, *Appl. Surf. Sci.* **2009**, *256*, 710.
- [51] H. Yu, W. Huang, X. Wang, *Lubr. Sci.* **2013**, *25*, 67.
- [52] P. Lu, R. J. K. Wood, M. G. Gee, L. Wang, W. Pfleging, *Tribol. Lett.* **2018**, *66*, 1.
- [53] X. Wang, W. Liu, F. Zhou, D. Zhu, *Tribol. Int.* **2009**, *42*, 1118.
- [54] P. Blau, *Friction Science and Technology*, CRC Press, Boca Raton, FL, USA, **2008**.
- [55] J. F. Prinz, R. A. de Wijk, L. Huntjens, *Food Hydrocoll.* **2007**, *21*, 402.
- [56] H. L. L. Costa, I. M. Hutchings, *Proc. Inst. Mech. Eng. Part J J. Eng. Tribol.* **2015**, *229*, 429.
- [57] A. F. Lasagni, C. Gachot, K. E. Trinh, M. Hans, A. Rosenkranz, T. Roch, S. Eckhardt, T. Kunze, M. Bieda, D. Günther, V. Lang, F. Mücklich, in *Proc. SPIE 10092, Laser-Based Micro-Nanoprocessing XI*, **2017**, p. 1009211.
- [58] K. Sugioka, M. Meunier, A. Piqué, Eds., *Laser Precision Microfabrication*, Springer Berlin Heidelberg, Berlin, Heidelberg, **2010**.
- [59] J. Pozo, *Laser Tech. J.* **2018**, *15*, 24.

- [60] A. Y. Vorobyev, C. Guo, *Laser Photonics Rev.* **2013**, 7, 385.
- [61] R. F. Haglund, in *Springer Ser. Mater. Sci.*, **2014**, pp. 1–28.
- [62] B. N. Chichkov, C. Momma, S. Nolte, F. von Alvensleben, A. Tünnermann, *Appl. Phys. A Mater. Sci. Process.* **1996**, 63, 109.
- [63] F. Dausinger, H. Hugel, V. Konov, *SPIE proc.* **2003**, 5147, 106.
- [64] Y. L. Yao, H. Chen, W. Zhang, *Int. J. Adv. Manuf. Technol.* **2004**, 26, 598.
- [65] K.-H. Leitz, B. Redlingshöfer, Y. Reg, A. Otto, M. Schmidt, *Phys. Procedia* **2011**, 12, 230.
- [66] T. A. Mai, G. C. Lim, *J. Laser Appl.* **2006**, 16, 221.
- [67] J. Marczak, *Arch. Metall. Mater.* **2015**, 60, 2221.
- [68] S. Prakash, S. Kumar, *IOP Conf. Ser. Mater. Sci. Eng.* **2016**, 149, 1.
- [69] F. Mücklich, A. F. Lasagni, C. Daniel, *Int. J. Mater. Res.* **2006**, 97, 1337.
- [70] A. F. Lasagni, C. Holzapfel, T. Weirich, F. Mücklich, *Appl. Surf. Sci.* **2007**, 253, 8070.
- [71] A. F. Lasagni, M. D'Alessandria, R. Giovanelli, F. Mücklich, *Appl. Surf. Sci.* **2007**, 254, 930.
- [72] C. Gachot, A. Rosenkranz, R. Buchheit, N. Souza, F. Mücklich, *Appl. Surf. Sci.* **2016**, 367, 174.
- [73] D. Günther, D. Scharnweber, R. Hess, C. Wolf-Brandstetter, M. Grosse Holthaus, A. F. Lasagni, in *Laser Surf. Modif. Biomater.*, Elsevier, **2016**, pp. 3–33.
- [74] H. Ike, M. Plancak, *J. Mater. Process. Technol.* **1998**, 80–81, 101.
- [75] A. Szurdak, G. Hirt, *Appl. Mech. Mater.* **2015**, 794, 128.
- [76] C. Gachot, A. Rosenkranz, B. Wietbrock, G. Hirt, F. Mücklich, *Adv. Eng. Mater.* **2013**, 15, 503.
- [77] M. Thome, G. Hirt, B. Rattay, *Adv. Mater. Res.* **2005**, 6–8, 631.
- [78] K. Zhao, B. Wietbrock, G. Hirt, *Prod. Eng.* **2011**, 5, 629.
- [79] K. Zhao, B. Wietbrock, G. Hirt, *Proc. 10th Int. Conf. Technol. Plast.* **2011**, 133.
- [80] A. Szurdak, G. Hirt, *Steel Res. Int.* **2015**, 86, 257.
- [81] H. Ike, *J. Mater. Process. Technol.* **2003**, 138, 250.
- [82] P. G. Grützmacher, A. Rosenkranz, A. Szurdak, F. König, G. Jacobs, G. Hirt, F. Mücklich, *Tribol. Int.* **2018**, 127, 500.
- [83] Y. H. Chae, *Key Eng. Mater.* **2007**, 345–346, 765.
- [84] K. Meine, T. Schneider, D. Spaltmann, E. Santner, *Wear* **2002**, 253, 725.
- [85] J. Zhang, Y. Meng, *J. Mater. Process. Technol.* **2012**, 212, 2133.
- [86] L. R. Rudnick, Ed. , *Lubricant Additives: Chemistry and Applications*, CRC Press (Taylor And Francis Group), Boca Raton, FL, USA, **2009**.
- [87] D. E. Sander, H. Allmaier, M. Witt, A. Skiadas, *MTZ Worldw.* **2017**, 78, 46.
- [88] K. Holmberg, P. Kivikytö-Reponen, P. Härkisaari, K. Valtonen, A. Erdemir, *Tribol. Int.* **2017**, 115, 116.
- [89] A. Ramesh, W. Akram, S. P. Mishra, A. H. Cannon, A. A. Polycarpou, W. P. King, *Tribol. Int.* **2013**, 57, 170.

- [90] M. Adjemout, A. Andrieux, J. Bouyer, N. Brunetière, G. Marcos, T. Czerwiec, *Tribol. Int.* **2017**, *115*, 409.
- [91] A. Kovalchenko, O. Ajayi, A. Erdemir, G. Fenske, I. Etsion, *Tribol. Trans.* **2004**, *47*, 299.
- [92] A. Kovalchenko, O. Ajayi, A. Erdemir, G. Fenske, I. Etsion, *Tribol. Int.* **2005**, *38*, 219.
- [93] F. P. Bowden, D. Tabor, F. Palmer, *Am. J. Phys.* **1951**, *19*, 428.
- [94] J. A. Greenwood, J. B. P. Williamson, *Proc. R. Soc. A Math. Phys. Eng. Sci.* **1966**, *295*, 300.
- [95] Y. Mo, K. T. Turner, I. Szlufarska, *Nature* **2009**, *457*, 1116.
- [96] L. Reinert, *Advanced Self-Lubricating Surfaces Based on Carbon Nanoparticles*, Saarland University, **2018**.
- [97] S. Bettscheider, C. Gachot, A. Rosenkranz, *Tribol. Int.* **2016**, *103*, 167.
- [98] M. Shafiei, A. T. Alpas, *Mater. Sci. Eng. C* **2008**, *28*, 1340.
- [99] A. Rosenkranz, L. Reinert, C. Gachot, F. Mücklich, *Wear* **2014**, *318*, 49.
- [100] C. Gachot, A. Rosenkranz, L. Reinert, E. Ramos-Moore, N. Souza, M. H. Müser, F. Mücklich, *Tribol. Lett.* **2013**, *49*, 193.
- [101] R. Ranjan, D. N. Lambeth, M. Tromel, P. Goglia, Y. Li, *J. Appl. Phys.* **1991**, *69*, 5745.
- [102] B. Zhang, W. Huang, J. Wang, X. Wang, *Tribol. Int.* **2013**, *65*, 138.
- [103] M. Bieda, C. Schmädicke, T. Roch, A. Lasagni, *Adv. Eng. Mater.* **2015**, *17*, 102.
- [104] S. Yuan, W. Huang, X. Wang, *Tribol. Int.* **2011**, *44*, 1047.
- [105] S. Fang, T. Herrmann, A. Rosenkranz, C. Gachot, F. G. Marro, F. Mücklich, L. Llanes, D. Bähre, *Procedia CIRP* **2016**, *42*, 439.
- [106] B. Raillard, L. Gouton, E. Ramos-Moore, S. Grandthyll, F. Müller, F. Mücklich, *Surf. Coatings Technol.* **2012**, *207*, 102.
- [107] R. Catrin, T. Gries, B. Raillard, F. Mücklich, S. Migot, D. Horwat, *J. Mater. Res.* **2012**, *27*, 879.
- [108] A. Kovalchenko, O. Ajayi, A. Erdemir, G. Fenske, *Wear* **2011**, *271*, 1719.
- [109] M. Wakuda, Y. Yamauchi, S. Kanzaki, Y. Yasuda, *Wear* **2003**, *254*, 356.
- [110] T. Ibatan, M. S. Uddin, M. A. K. Chowdhury, *Surf. Coatings Technol.* **2015**, *272*, 102.
- [111] K. E. Trinh, A. Tsipenyuk, M. Varenberg, A. Rosenkranz, N. Souza, F. Mücklich, *Wear* **2015**, *344–345*, 86.
- [112] M. Varenberg, G. Halperin, I. Etsion, *Wear* **2002**, *252*, 902.
- [113] A. A. G. a G. Bruzzone, H. L. L. Costa, P. M. M. Lonardo, D. A. a. Lucca, *CIRP Ann. - Manuf. Technol.* **2008**, *57*, 750.
- [114] N. P. Suh, M. Mosleh, P. S. Howard, *Wear* **1994**, *175*, 151.
- [115] R. Merz, A. Brodyanski, M. Kopnarski, *Conf. Pap. Sci.* **2015**, *2015*, 1.
- [116] P. G. Grützmacher, S. Rammacher, D. Rathmann, C. Motz, F. Mücklich, S. Suarez, *Friction* **2019**, DOI 10.1007/s40544-019-0259-5.
- [117] M. Vardavoulias, *Wear* **1994**, *173*, 105.
- [118] H. L. Costa, I. M. Hutchings, *J. Mater. Process. Technol.* **2009**, *209*, 1175.

- [119] A. Blatter, M. Maillat, S. Pimenov, G. Shafeev, A. Simakin, E. Loubnin, *Wear* **1999**, 232, 226.
- [120] X. Wang, K. Kato, K. Adachi, K. Aizawa, *Tribol. Int.* **2001**, 34, 703.
- [121] X. Lu, M. M. Khonsari, *Tribol. Lett.* **2007**, 27, 169.
- [122] A. A. Voevodin, J. S. Zabinski, *Wear* **2006**, 261, 1285.
- [123] P. Andersson, J. Koskinen, S. Varjus, Y. Gerbig, H. Haefke, S. Georgiou, B. Zhmud, W. Buss, *Wear* **2007**, 262, 369.
- [124] H. Zhang, L. G. Qin, M. Hua, G. N. Dong, K. S. Chin, *Appl. Surf. Sci.* **2015**, 332, 557.
- [125] U. Pettersson, S. Jacobson, *Tribol. Int.* **2003**, 36, 857.
- [126] T. V. Kononenko, S. V. Garnov, S. M. Pimenov, V. I. Konov, V. Romano, B. Borsos, H. P. Weber, *Appl. Phys. A Mater. Sci. Process.* **2000**, 71, 627.
- [127] M. Duarte, A. F. Lasagni, R. Giovanelli, J. Narciso, E. Louis, F. Mücklich, *Adv. Eng. Mater.* **2008**, 10, 554.
- [128] A. Arslan, H. H. Masjuki, M. Varman, M. A. Kalam, M. M. Quazi, K. A. H. Al Mahmud, M. Gulzar, M. Habibullah, *Appl. Surf. Sci.* **2015**, 356, 1135.
- [129] C. Schäfer, L. Reinert, T. MacLucas, P. G. Grützmacher, R. Merz, F. Mücklich, S. Suarez, *Tribol. Lett.* **2018**, 66, 89.
- [130] J. Wang, H. Zhao, W. Huang, X. Wang, *Wear* **2017**, 380–381, 52.
- [131] M. Adjemout, N. Brunetiere, J. Bouyer, *Surf. Topogr. Metrol. Prop.* **2016**, 4, 14002.
- [132] I. Etsion, *Friction* **2013**, 1, 195.
- [133] L. S. Martz, *Proc. Inst. Mech. Eng.* **1949**, 161, 1.
- [134] E. Willis, *Wear* **1986**, 109, 351.
- [135] I. Etsion, L. Burstein, *Tribol. Trans.* **1996**, 39, 677.
- [136] I. Etsion, G. Halperin, Y. Greenberg, in *Proc. 15th Int'l. Conf. Fluid Seal.*, BHR Group, Maastricht, **1997**, pp. 3–11.
- [137] Y. Xie, Y. J. Li, Y. M. Wang, S. F. Suo, X. F. Liu, *Sci. China Physics, Mech. Astron.* **2014**, 57, 273.
- [138] X. Meng, S. Bai, X. Peng, *Tribol. Int.* **2014**, 77, 132.
- [139] A. Rosenkranz, A. Szurdak, P. G. Grützmacher, G. Hirt, F. Mücklich, *Adv. Eng. Mater.* **2018**, 20, 1700731.
- [140] H. L. Costa, I. M. Hutchings, *Tribol. Int.* **2007**, 40, 1227.
- [141] S. C. Vlădescu, A. Ciniero, K. Tufail, A. Gangopadhyay, T. Reddyhoff, *Tribol. Int.* **2017**, 115, 140.
- [142] S.-C. Vlădescu, K. Tufail, A. Gangopadhyay, T. Reddyhoff, *Tribol. Trans.* **2017**, 00, 00.
- [143] S. Neumann, G. Jacobs, A. Feldermann, F. Straßburger, in *10th Int. Fluid Power Conf.*, **2016**, pp. 493–506.
- [144] M. Adjemout, N. Brunetière, J. Bouyer, **2018**, 2004, 1.
- [145] T. D. Ling, P. Liu, S. Xiong, D. Grzina, J. Cao, Q. J. Wang, Z. C. Xia, R. Talwar, *Tribol. Lett.*

- 2013**, 52, 113.
- [146] A. Arslan, H. H. Masjuki, M. Varman, M. A. Kalam, M. M. Quazi, M. H. Mosarof, *J. Mater. Res.* **2016**, 31, 1837.
- [147] C. Sinanoğlu, F. Nair, M. B. Karamiş, *J. Mater. Process. Technol.* **2005**, 168, 344.
- [148] N. Tala-Ighil, P. Maspeyrot, M. Fillon, A. Bounif, *Proc. Inst. Mech. Eng. Part J J. Eng. Tribol.* **2007**, 221, 623.
- [149] Z. Zhang, Y. W. Zhang, H. Gao, *Proc. R. Soc. B Biol. Sci.* **2011**, 278, 519.
- [150] G. Costagliola, F. Bosia, N. M. Pugno, *Phys. Rev. E* **2016**, 94, 063003.
- [151] K. Autumn, A. Dittmore, D. Santos, M. Spenko, M. Cutkosky, *J. Exp. Biol.* **2006**, 209, 3569.
- [152] T. Liskiewicz, A. Morina, A. Neville, in *Des. Nat. IV*, WIT Press, Southampton, UK, **2008**, pp. 263–272.
- [153] Y. C. Jung, B. Bhushan, *Langmuir* **2009**, 25, 14165.
- [154] M. J. Baum, L. Heepe, E. Fadeeva, S. N. Gorb, *Beilstein J. Nanotechnol.* **2014**, 5, 1091.
- [155] X. Wang, K. Adachi, K. Otsuka, K. Kato, *Appl. Surf. Sci.* **2006**, 253, 1282.
- [156] D. Z. Segu, S. G. Choi, J. H. Choi, S. S. Kim, *Appl. Surf. Sci.* **2013**, 270, 58.
- [157] D. Zenebe Segu, P. Hwang, *Tribol. Int.* **2015**, 91, 111.
- [158] X. Wang, J. Wang, B. Zhang, W. Huang, *Proc. Inst. Mech. Eng. Part J J. Eng. Tribol.* **2014**, 229, 538.
- [159] N. Brunetière, B. Tournerie, *Tribol. Int.* **2012**, 49, 80.
- [160] K.-H. Chu, R. Xiao, E. N. Wang, *Nat. Mater.* **2010**, 9, 413.
- [161] A. Rosenkranz, P. G. Grützmaker, A. Szurdak, C. Gachot, G. Hirt, F. Mücklich, F. Muecklich, *Surf. Topogr. Metrol. Prop.* **2016**, 4, 034008.
- [162] F. Chen, D. Zhang, Q. Yang, X. Wang, B. Dai, X. Li, X. Hao, Y. Ding, J. Si, X. Hou, *Langmuir* **2011**, 27, 359.
- [163] Y. Zheng, X. Gao, L. Jiang, *Soft Matter* **2007**, 3, 178.
- [164] L. Feng, S. Li, Y. Li, H. Li, L. Zhang, J. Zhai, Y. Song, B. Liu, L. Jiang, D. Zhu, *Adv. Mater.* **2002**, 14, 1857.
- [165] W. C. Sherbrooke, A. J. Scardino, R. De Nys, L. Schwarzkopf, *Zoomorphology* **2007**, 126, 89.
- [166] P. Comanns, G. Buchberger, A. Buchsbaum, R. Baumgartner, A. Kogler, S. Bauer, W. Baumgartner, *J. R. Soc. Interface* **2015**, 12, 20150415.
- [167] U. Hermens, S. V. Kirner, C. Emonts, P. Comanns, E. Skoulas, A. Mimidis, H. Mescheder, K. Winands, J. Krüger, E. Stratakis, J. Bonse, *Appl. Surf. Sci.* **2017**, 418, 499.
- [168] H. Ke, W. Huang, X. Wang, *Tribol. Int.* **2016**, 93, 318.
- [169] J. B. Fournier, A. M. Cazabat, *Europhys. Lett.* **1992**, 20, 517.
- [170] H. Hu, R. G. Larson, *Langmuir* **2005**, 21, 3972.
- [171] A. Karbalaei, R. Kumar, H. Cho, *Micromachines* **2016**, 7, 13.
- [172] V. Pratap, N. Moumen, R. S. Subramanian, *Langmuir* **2008**, 24, 5185.
- [173] Y. Sui, *Phys. Fluids* **2014**, 26, DOI 10.1063/1.4894077.

- [174] T. Young, *Philos. Trans. R. Soc. London* **1805**, 95, 65.
- [175] D. T. Wasan, *Science (80-.)*. **2001**, 291, 605.
- [176] Q. Dai, W. Huang, X. Wang, M. M. Khonsari, *Langmuir* **2018**, acs. langmuir.7b04259.
- [177] J. B. Brzoska, F. Brochard-Wyart, F. Rondelez, *Langmuir* **1993**, 9, 2220.
- [178] Y.-T. Tseng, F.-G. Tseng, Y.-F. Chen, C.-C. Chieng, *Sensors Actuators A Phys.* **2004**, 114, 292.
- [179] A. A. Fote, R. A. Slade, *Lubr. Eng.* **1976**, 32, 542.
- [180] H. Ke, W. Huang, X. Wang, *Proc. Inst. Mech. Eng. Part J J. Eng. Tribol.* **2016**, 230, 583.
- [181] Q. Dai, W. Huang, X. Wang, *Lubr. Sci.* **2017**, 29, 17.
- [182] H. Bouasse, *Capillarité-Phénomènes Superficiels*, Paris: Librairie Delagrave, **1924**.
- [183] W. J. Bartz, *Tribol. Int.* **1976**, 9, 213.
- [184] J. Z. Chen, S. M. Troian, A. a. Darhuber, S. Wagner, *J. Appl. Phys.* **2005**, 97, 014906.
- [185] N. Bjelobrk, H. L. Girard, S. B. Subramanyam, H. M. Kwon, D. Quéré, K. K. Varanasi, *Phys. Rev. Fluids* **2016**, 1, 1.
- [186] L. Rozeanu, D. Pnueli, *J. Lubr. Technol.* **2010**, 100, 479.
- [187] H. S. Nagaraj, D. M. Sanborn, W. O. Winer, *Wear* **1978**, 49, 43.
- [188] K. Sathyan, *J. Eng. Technol.* **2002**, 2, 27.
- [189] H. Liang, D. Guo, J. Luo, *Tribol. Lett.* **2014**, 56, 491.
- [190] H. Liang, D. Guo, L. Ma, J. Luo, *Tribol. Lett.* **2015**, 59, 1.
- [191] M. M. Khonsari, E. R. Booser, *Applied Tribology: Bearing Design and Lubrication*, John Wiley & Sons, Ltd, Chichester, UK, **2017**.
- [192] M. Kalin, M. Polajnar, *Appl. Surf. Sci.* **2014**, 293, 97.
- [193] Z. Rymuza, *Tribology of Miniature Systems*, Elsevier, Amsterdam, **1998**.
- [194] M. K. Bernett, W. A. Zisman, **2009**, 332.
- [195] Q. Dai, Y. Ji, W. Huang, X. Wang, in *Proc. Asia Int. Conf. Tribol.*, Malaysian Tribology Society, **2018**, pp. 350–352.
- [196] E. V. Zaretsky, *Tribol. Int.* **1990**, 23, 75.
- [197] J. R. Jones, M. J. Jansen, *Proc. Inst. Mech. Eng. Part J J. Eng. Tribol.* **2008**, 222, 997.
- [198] W. Huang, X. Wang, *Colloids Surfaces A Physicochem. Eng. Asp.* **2016**, 497, 167.
- [199] A. P. Semenov, *J. Frict. Wear* **2010**, 31, 469.
- [200] V. G. Fitzsimmons, C. M. Murphy, J. B. Romans, C. R. Singleterry, *J. Am. Soc. Lubr. Eng.* **1968**, 24, 35.
- [201] P. G. Grützmacher, A. Rosenkranz, C. Gachot, *Appl. Surf. Sci.* **2016**, 370, 59.
- [202] A. A. Fote, R. A. Slade, **1977**, 13.
- [203] O. Bliznyuk, H. P. Jansen, E. S. Kooij, H. J. W. Zandvliet, B. Poelsema, *Langmuir* **2011**, 27, 11238.
- [204] M. Hans, F. Müller, S. Grandthyll, S. Hüfner, F. Mücklich, *Appl. Surf. Sci.* **2012**, 263, 416.
- [205] D. E. Kataoka, S. M. Troian, *Nature* **1999**, 402, 794.

- [206] D. Quéré, *Annu. Rev. Mater. Res.* **2008**, *38*, 71.
- [207] A. Rosenkranz, S. Fleischmann, C. Gachot, F. Mücklich, *Adv. Eng. Mater.* **2015**, *17*, 1645.
- [208] P. Li, J. Xie, J. Cheng, K. K. Wu, *J. Micromechanics Microengineering* **2014**, *075004*, 075004.
- [209] D. Xia, L. M. Johnson, G. P. López, *Adv. Mater.* **2012**, *24*, 1287.
- [210] Q. Dai, W. Huang, X. Wang, in *ABM Proc.*, Editora Blucher, São Paulo, **2019**, pp. 4035–4049.
- [211] J. Berthier, D. Gosselin, N. Villard, C. Pudda, F. Boizot, G. Costa, G. Delapierre, *Sensors & Transducers* **2014**, *183*, 123.
- [212] T. Chen, *J. Thermophys. Heat Transf.* **2015**, *29*, 594.
- [213] D. Yang, M. Krasowska, C. Priest, J. Ralston, *Phys. Chem. Chem. Phys.* **2014**, *16*, 24473.
- [214] D. Yang, M. Krasowska, C. Priest, M. N. Popescu, J. Ralston, *J. Phys. Chem. C* **2011**, *115*, 18761.
- [215] R. R. Rye, F. G. Yost, E. J. O’Toole, *Langmuir* **1998**, *14*, 3937.
- [216] R. R. Rye, J. a. Mann, F. G. Yost, *Langmuir* **1996**, *12*, 555.
- [217] R. Lucas, *Kolloid-Zeitschrift* **1918**, *23*, 15.
- [218] E. W. Washburn, *Phys. Rev.* **1921**, *17*, 273.
- [219] D. Zhang, F. Chen, G. Fang, Q. Yang, D. Xie, G. Qiao, W. Li, J. Si, X. Hou, *J. Micromechanics Microengineering* **2010**, *20*, DOI 10.1088/0960-1317/20/7/075029.
- [220] F. Zhang, H. Y. Low, *Langmuir* **2007**, *23*, 7793.
- [221] P. G. Grützmacher, A. Rosenkranz, A. Szurdak, C. Gachot, G. Hirt, F. Mücklich, *Adv. Eng. Mater.* **2018**, *20*, 1700521.
- [222] M. Marian, P. G. Grützmacher, A. Rosenkranz, S. Tremmel, F. Mücklich, S. Wartzack, *Tribol. Int.* **2019**.

FIGURES

- Figure 1:** a) Increasing worldwide CO₂ emissions in tons of CO₂ since 1971 due to the growth in world energy demand from fossil fuels. In b) the CO₂ emissions are broken down by sector. Two-thirds of global emissions are produced by two sectors of which electricity and heat generation is by far the largest with 42 %, followed by transport, accounting for 24 % [7]. 2
- Figure 2:** Scale-like surface topographies of a) shark skin [43] and b) snakeskin [47]. 5
- Figure 3:** Schematic of the laser-material interaction in the case of a) short and b) ultrashort laser pulses [65]. 9
- Figure 4:** Representation of the effect of pulse duration on the thermal penetration depth in steel according to equation (2). The pulse duration is varied from 5 ns down to 100 fs resulting in a significant reduction in the depth of thermal penetration. 10
- Figure 5:** a) Schematic of the DLIP process set-up with the necessary equipment to guide the beam and scan the sample: beam attenuator, shutter, beam splitter, mirrors, mask and translation stage. Here, the beam is split into two beams to create a line-like intensity distribution. b) Generation of a periodic intensity distribution due to constructive (high intensity) and destructive (low intensity) interference of two beams. The periodicity indicates the distance from one intensity maximum to the next and depends on the angle of the two beams as well as the laser wavelength λ . 12
- Figure 6:** Schematic of the micro-coining process showing the different components used for manufacturing micro-patterns. 13
- Figure 7:** Schematic of the photochemical patterning process. Before the process, the substrate is cleaned. Subsequently, a photoresist is applied, which is then exposed to UV light at the positions not covered with the photomask to increase the resistance against the developing solution (negative photoresist). Finally, the photo-resist is dissolved, and the substrate is chemically etched, resulting in surface patterns. 14
- Figure 8:** Stribeck curve showing the different lubrication regimes, boundary, mixed and hydrodynamic lubrication. 16
- Figure 9:** Schematic illustration of the real area of contact and the apparent contact area of contact between two rough surfaces or a surface with deterministic surface topography and a flat surface [96]. 17
- Figure 10:** Reduction of the real area of contact as a result of laser patterning. The images show the real area of contact upon contact of a steel ball (diameter 6 mm) with a polished steel sample (a) and with a laser-patterned sample having a periodicity of 9 μm (b). The ball was loaded onto the sample with 1 N. Modified from [97]. 18
- Figure 11:** Schematic of the entrapment of wear particles in the topographic minima of a patterned surface. During sliding, plastic deformation of the substrate occurs resulting in the generation of wear particles. These particles are entrapped in the surface depressions and hence cannot contribute to further abrasion of the surface. 19

- Figure 12:** Asymmetric pressure distribution due to local cavitation at the patterns' sites. The net pressure is positive since the cavitation pressure of the lubricant limits the negative pressure. Note that additional hydrodynamic pressure can only be generated when the cavitation pressure is inferior to the supply pressure [22]. 21
- Figure 13:** Examples of artificially manufactured multi-scale patterns. Shown are electrodeposited lotus leaf patterns in nickel (a) [50], a combination of large and small dimples in silicon carbide (b) [155] and multi-shaped patterns manufactured by laser patterning on steel (c) [157]. 23
- Figure 14:** Schematic illustration of the flow patterns on the solid-liquid interface and inside a liquid droplet sitting on a surface with a temperature gradient. The advancing (θ_a) and receding (θ_r) contact angles, which are related by Young's equation with the interfacial tensions existing at the solid-liquid (γ_{SL}), solid-gas (γ_{SG}) and liquid-gas (γ_{LG}) interfaces [174], differ as a result of the applied temperature gradient. The droplet moves toward cold regions of the surface. Modified from [175]. 25
- Figure 15:** Schematic illustration of the lubricant's migration out of the hot contact zone toward the colder surrounding areas. The contact zone is heated by frictional heating resulting in a reduction of the interfacial tension and ultimately in the loss of lubricant out of the contact zone. 27
- Figure 16:** Schematic illustration of the lubricant loss from the contact zone due to centrifugal forces in a ball-on-disk experimental set-up. The oil reservoir represents the lubricant film, which is present in excess in the contact zone. Due to the acting centrifugal forces, the surface area of the lubricant film significantly decreases possibly leading to a reduction of lubricant film thickness. Reproduced from [189]. 28
- Figure 17:** A droplet's contact line with the contact angle θ is pinned on an edge as the liquid migrates from left to right. Upon contact with the edge, the contact angle can take any value with respect to the horizontal reference value between θ and $\pi - \phi + \theta$, which is represented by the colored region. Only after exceeding a contact angle of $\pi - \phi + \theta$ the droplet can migrate further to the right. Reproduced from [206]. 30
- Figure 18:** Overview of the respective papers regarding objective 1. Reasons for lubricant migration, the effects of lubricant migration on the tribological behavior, as well as topographical designs to modify it are investigated. 34
- Figure 19:** Overview of the respective papers regarding objective 2 and 3. First, multi-scale patterns are designed and tested for their tribological behavior. Effective patterns are then transferred to the shaft of a journal bearing, and the comparability with the preliminary results is demonstrated. 38
- Figure 20:** Comparison of the frictional behavior of micro-coined dimples in experiments and simulations. The experiments show a significant friction reduction upon encounter with the micro-coined dimple compared to the reference surface, which is the greatest when the dimple is crossed centrally (a). Likewise, the simulations demonstrate a dependence of the relative position between dimple and counter body with a greater friction reduction for a central alignment (b). Modified from [222]. 54